The ROMY Ring Laser Array for Seismology: Instrumental Characterization, Low Noise Limits for Rotations and Seismological Applications

Andreas Brotzer

München 2024

The ROMY Ring Laser Array for Seismology: Instrumental Characterization, Low Noise Limits for Rotations and Seismological Applications

Dissertation
zur Erlangung des Doktorgrades
an der Fakultät für Geowissenschaften
der Ludwig-Maximilians-Universität München

vorgelegt von
Andreas Brotzer

München, den 14.11.2024

Erstgutachter: Prof. Dr. Heiner Igel
Zweitgutachter: Prof. Dr. Karl Ulrich Schreiber
Tag der Zulassung: 14.11.2024
Tag der mündlichen Prüfung: 05.02.2025

Abstract

The field of rotational seismology emerged after advances in ring laser gyroscope (RLG) technology made it possible to observe weak rotational ground motions in seismic wavefields. Large-scale RLGs are challenging to operate, but are currently the only possibility to resolve small rotational motions associated with phenomena in seismology and geodesy, such as the Earth's free oscillations or variations of the Earth's rotation vector. The ROMY ring laser array is an unprecedented instrument for geoscientific observations. By combining four large-scale, triangular-shaped RLGs with high sensitivity, it can provide all three components of weak rotational ground motion.

As part of this thesis, the performance and operational stability of ROMY has been evaluated and improved through various hardware upgrades. For all heterolithic RLGs, a profound understanding of environmental impacts and their mitigation or correction is essential. Therefore, a network of environmental monitoring sensors has been developed and installed for ROMY. This enabled the identification and quantification of instrumental effects caused by environmental influences, such as temperature changes.

The first rotational low noise model was derived and validated with available direct and indirect rotational observations of RLGs and seismic arrays, respectively. Knowledge of the rotational background noise floor contributes to a deeper understanding of our planet and provides a valuable guidance for instrument development. Unique direct observations of ground tilt by ROMY allow the study of ground deformation induced by atmospheric processes at long periods, independent of inertial acceleration contributions. In combination with local barometric pressure observations, compliance functions are obtained and a low noise level at long periods, which is imposed by atmospheric pressure changes, is determined for ROMY.

Successfully operating three RLGs continuously over one year resulted in a valuable dataset. While this dataset acquired with ROMY is used to demonstrate potential six degree-of-freedom (6 DoF) applications, such as seismic source tracking of the secondary microseism, a one-year dataset of a portable 6 DoF station in southern California is used to analyze local and regional seismicity and derive an empirical scaling relation for ground rotations.

Although continuous operation has been demonstrated, further hardware upgrades for ROMY, in order to mitigate identified instrumental effects and enhance the operational stability, are encouraged. Harnessing ROMY's full potential will ultimately provide the observational basis to study and answer many open geoscientific questions.

Acknowledgements

Foremost, I want to thank Heiner Igel for his continuous guidance, support and trust for my endeavors within the scope of my doctoral thesis. This includes all the opportunities to join field work, workshops and conferences, but also to acquire new hardware and instrumentation for ROMY and gain experience in teaching.
I would like to express my deepest gratitude to Ulrich Schreiber to introduce me into the secrets of ring laser gyroscopes. His comprehensive explanations on ring laser physics were immensely enriching, as were his many hours of practical support at ROMY during maintenance jobs.
I want to thank Felix Bernauer for many helpful discussions upon weird signals and bugs, as well as for his practical support during many maintenance jobs.
Many thanks to Sven Egdorf, Jürgen Loos and Marcos Terpoorten for their continuous technical advice and support to keep ROMY operational, setup and integrate new sensors to our observational network, emptying water buckets and realize projects to enhance ROMY step by step. Their enthusiasm, technical knowledge and commitment to contribute to projects made many of the presented results possible.
I am grateful to Jan Kodet for many hours of joined efforts to keep ROMY operational and further harness its potential by upgrading technological aspects.
Many thanks to Simon Stellmer and Jannik Zenner for many fruitful and inspiring discussions, as well as providing technical support for experiments.
I am thankful for many helpful discussions, talks, coffee breaks, trips to conferences and fieldwork that I shared with Sabrina Keil, Felix Bernauer and Fabian Lindner.
I am honored to have been awarded the Jerome M. Paros Scholarship by the American Geophysical Union (AGU), which enabled my research stay at the Scripps Institution of Oceanography in San Diego in 2022, contributing to my research on geophysical instrumentation. This involved and the setup of the 6-DoF station at Piñon Flat Observatory, replacing the former GEOsensor. Thanks to Mark Zumberge and Frank Vernon I had a wonderful stay in San Diego.
I consider myself lucky to have a parents and siblings who provide support of all kinds, whenever needed the most. Last, but not least, I am very grateful to Katharina Maetschke for all her moral support, thorough proofreading and helpful advice along the way.

Abbreviations

AD	Allan Deviation
ADR	Array-Derived Rotations
BFO	Black Forest Observatory
BROMY	BoreholeROMY tiltmeter
BSPF	BlueSeis at Piñon Flat
DAS	Distributed Acoustic Sensing
DoF	Degree of Freedom
EMA	Experimental Modal Analysis
FFT	Fast Fourier Transform
FSR	Free Spectral Range
FUR	broadband seismometer station
GSN	Global Seismic Network
HTP	Humidity, Temperature, Pressure sensors
LDM	Local Deformation Model
LDT	Local Deformation Tilt
MLTI	MuLtimode TrIgger
NHNM	New High Noise Model
NLNM	New Low Noise Model
OMA	Operational Model Analysis
PD	Photo Diode detector
PFO	Piñon Flat Observatory
PMT	Photo Multiplier detector

PROMY	Pressure in ROMY (DPS310 sensor box)
PSD	Power Spectral Density spectrum
RANSAC	RANdom SAmple Consensus regression method
RF	Radio Frequency
RHNM	Rotational High Noise Model
RLNM	Rotational Low Noise Model
ROMY	ROtational Motions in seismologY
ROMYT	ROMYTiltmeter (platform tiltmeter 1)
RLG	Ring Laser Gyroscope
RU	northern ring of ROMY
RV	western ring of ROMY
RW	eastern ring of ROMY
RZ	horizontal ring of ROMY
TROMY	TiltmeterROMY (platform tiltmeter 2)
TWM	Travelling Wave Model
TWT	Traveling Wave Tilt
WROMY	Weather in ROMY WS1-9 (HTP sensor box)

Contents

List of Figures

List of Tables

Chapter 1

Introduction

In seismology, the wavefield gradients, explicitly ground strain and rotation, have largely been ignored in the past due to amplitudes about three orders of magnitude smaller than the translational motions and a sheer lack of instrumentation to provide observations.

In order to study weak rotational ground motions of the seismic wavefield, at this point, only large-scale ring laser gyroscopes (RLGs) provide sufficient sensitivity (e.g., Brotzer et al. 2023). With advancements in large-scale RLG technology (Schreiber & Wells 2013), first observations of teleseismic events (e.g., Pancha et al. 2000, Igel et al. 2005, 2007), and of rotational constituents for toroidal free oscillations of Earth (Schreiber et al. 2014) became possible.

As a result of the accessibility of this new observable, the field of rotational seismology emerged (e.g., Schreiber et al. 2006b,a, Cochard et al. 2006, Zembaty et al. 2021) with a focus on single-station wavefield observations at highest sensitivity.

The combination of co-located observations of rotational and translational motions utilizing six degrees-of-freedom (6 DoF) methodology (e.g., Cochard et al. 2006, Sollberger et al. 2020, 2018, Schmelzbach et al. 2018) exploits local sensitivity (Bernauer, Fichtner & Igel 2012) to obtain seismic phase velocities (e.g., Keil et al. 2021) and backazimuth estimates (e.g., Sollberger et al. 2020, Wassermann et al. 2022, Yuan et al. 2021) for separated seismic wave types (Sollberger et al. 2018). There is also potential in improved moment tensor inversion (e.g., Donner et al. 2016, 2018, Donner 2021), dynamic tilt correction (e.g., Venkateswara et al. 2017, Lin et al. 2011, Bernauer et al. 2020b) and the observation of Earth's eigenmodes (Widmer-Schnidrig & Zurn 2009).

A high-sensitivity single station, with an increased information gain on the seismic wavefield by observing 6 DoF, is especially beneficial wherever the deployment of large amounts of stations or seismic arrays is not feasible. This includes settings with challenging terrain and limited space such as encountered at volcanoes (e.g., Wassermann et al. 2020, 2022), in urban environments (e.g., Keil et al. 2021), at the ocean floor (e.g., Lindner et al.

2017), inside buildings for structural health monitoring (e.g. Zembaty et al. 2016) or on extraterrestrial bodies (e.g., Bernauer et al. 2020a, Guattari et al. 2019).

The availability of portable rotation sensors for field applications is currently limited, and their current resolvability not sufficient to observe all weak ground motions, thus not yet usable for many promising seismological applications (e.g., Bernauer et al. 2021). This becomes evident through a comparison of sensor self-noise levels with the low noise model for rotational ground motions, introduced in this thesis (Sec. 4.1), and provides a benchmark for future instrumental development. As part of this thesis, the applicability of the 6 DoF methodology to local and regional seismicity are demonstrated and current limitations of signal detectability are assessed to serve as guidance for similar experiments (Sec. 4.2).

High-sensitive RLGs possess the potential to provide new insights and Earth-based observations not only for seismology, but in particular for geodesy (e.g., Schreiber et al. 2023a, Schreiber & Wells 2023b) and theoretically for experiments to contribute to fundamental physics (e.g., Stedman 1997, Bosi et al. 2011). In seismology, a complete understanding of the ground deformation due to atmospheric or oceanic loading on the solid Earth is still unresolved. With this in mind, a tilt correction of inertial accelerometers, in particular their horizontal components, is desirable (e.g. Bernauer et al. 2020b, Lin et al. 2011). In this context, a contribution to improved observations of the Earth's eigenmodes (Widmer-Schnidrig & Zurn 2009), and thus to a better understanding of the internal structure of the Earth, is within reach.

Currently, there are only few active, large-scale RLGs operated globally, including ROMY (Germany; Igel et al. (2021)), G-ring (Germany; Schreiber et al. (2009)), the ER-1 (New Zealand; Zou (2021)), GINGERINO (Italy; Belfi et al. (2017)) and the recently established GEORG (Germany). ROMY is unprecedented in design by assembling four large-scale (between 33 m to 36 m perimeter), triangular-shaped rings to a tetrahedron structure. This unique access to three components of weak seismic ground rotations enables to address open scientific questions.

The heterolithic realization of ROMY poses the challenge of mechanical instability of the resonator. Hence, it has a susceptibility to variations in the scale factor as a result of geometric deformation, which is understood to be an instrumental effect that should be avoided. Its proximity to the surface allows studying and quantifying environmental influences on the heterolithic rings. Identified instrument responses to these external influences help to design appropriate countermeasures in order to minimize their impact on the operation (Sec. 3.2).

This thesis consists of four main chapters. Following this introduction, the second chapter summarizes the advancements achieved by upgrading parts of the hardware components or optimizing configurations. Moreover, new instrumentation of ROMY is introduced and described.

The third chapter on the instrumental characterization of ROMY contains an article on the "Automated Quality Assessment of Interferometric Ring Laser Data" published in Sensors (Brotzer et al. 2021) and contributes to the aim of providing high-quality data for the geoscientific community. A second article "On Environmental-related Instrumental Effects of a Multi-component, Heterolithic Ring Laser Array", submitted to Review of Scientific Instruments, identifies and quantifies influences of external drivers, such as temperature and barometric pressure and the response of the ring laser system. With a deeper understanding of the interaction, appropriate countermeasures can be designed and implemented in order to eventually enhance the operational stability further and provide continuous high-quality, multi-component rotation data.

The fourth chapter on rotational seismology contains an article on "Characterizing the Background Noise Level of Rotational Ground Motions on Earth" published in Seismological Research Letters (Brotzer et al. 2023) and a second article "On Single-station, Six Degrees-of-freedom Observations of Local to Regional Seismicity at the Piñon Flat Observatory in Southern California" that is submitted to Seismica.

A final chapter eventually summarizes key findings of this work and provides an outlook for the future of ROMY and its potential to address open scientific questions in a seismological and geodetic context.

Chapter 2

Hardware Upgrades and Performance

Over the past four years (2020 to 2024), efforts have been made to characterize the ring laser array ROMY (Igel et al. 2021) and its instrumental effects (Sec. 3.2). The hardware has been gradually upgraded within the scope of the available budget with the objective to achieve an improved performance and better operational stability, hence more continuous, high-quality rotation data.

In the following sections, the realized hardware upgrades are concisely documented and validated enhancement are reported. First, the advanced hardware setup currently deployed for RZ is summarized. Second, an overview of the recent performance is provided. Next, identified sources of electrical noise are discussed, such as interference between radio frequency antennas, as well as implemented countermeasures. A specifically developed and installed environmental monitoring system and the implemented passive thermal insulation are described and validated. Finally, new instrumentation, comprising a microbarometer station, a barometer array and a tiltmeter is presented and characterized.

Within the scope of an intended major hardware upgrade for ROMY in the future, it is recommended that all four rings of ROMY are equipped with a setup, as described in Section 2.1 and beyond. The insights and suggestions provided in this chapter may contribute to a successful upcoming hardware upgrade.

2.1 Advanced Ring Laser Setup

The instrumental setup illustrated in Figure 2.1 is the most advanced for ROMY to date. This setup is currently deployed for RZ, which has proven to be the most stable to operate and maintain based on previous experience.

Each triangular-shaped, optical ring resonator forms a closed optical beam path using curved dielectric mirrors (Fig. 2.1). Reducing four corners (for square rings) to three is advantageous, since each missing mirror reduces transmission and absorption losses (e.g.,

Schreiber & Wells 2023b), however, also reduces potential detection sites of transmitted light. Optimizing the beam combination and eliminating external influences and interferences is essential to enhance the Sagnac signal and all subsequent signal processing.

Compared to the previous setup of two plane mirrors and a beam combiner prism, a Koester prism is now used to interfere the clockwise and counter-clockwise laser beams and generate the Sagnac interferogram (Fig. 2.1). The prism is mounted on a prism stage with three rotational degrees-of-freedom, which can be adjusted by micrometer screws to provide the required sensitivity. A slim, one-dimensional micrometer translation stage completes the required degrees-of-freedom to optimize the beam alignment for a large interferogram contrast, thus an advantageous detection signal.

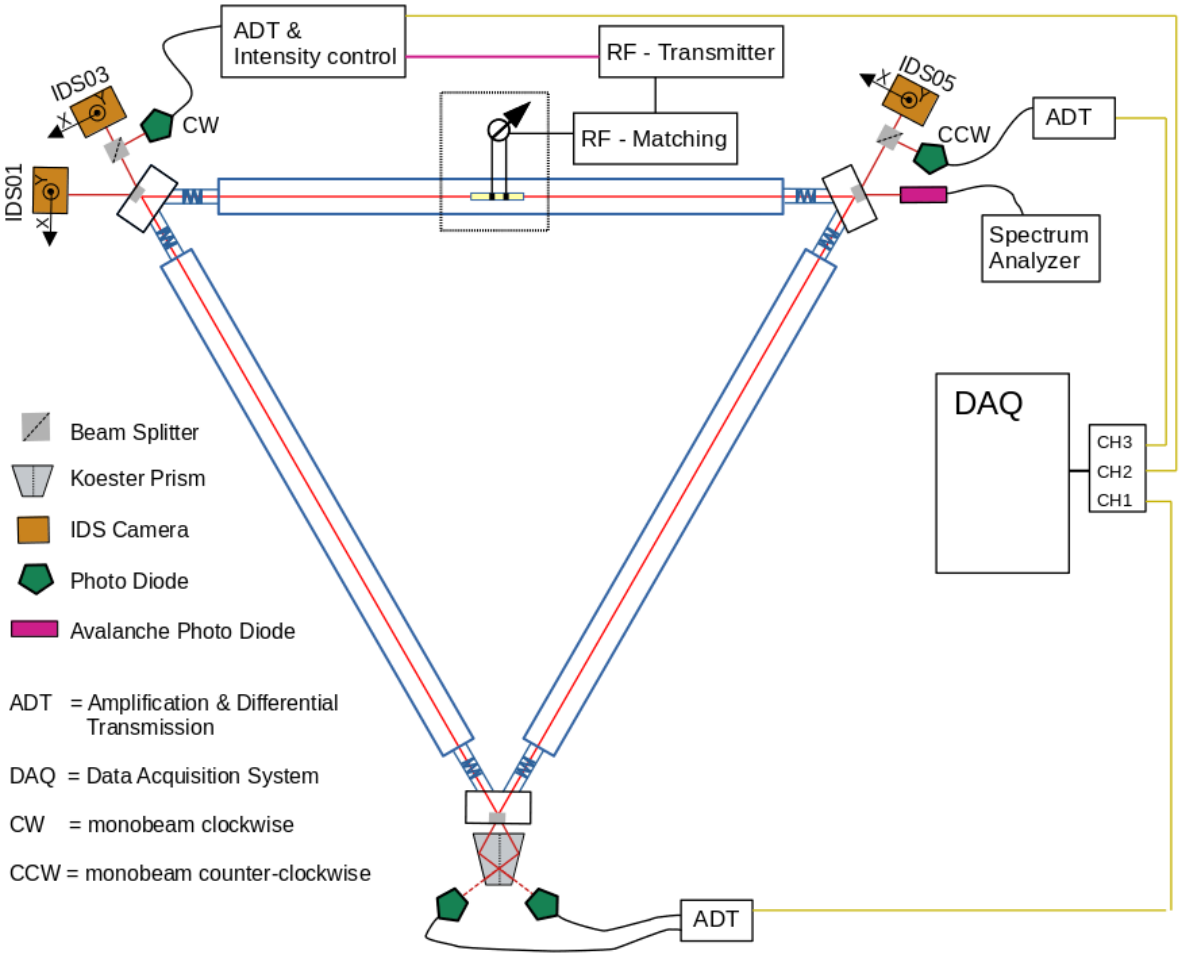

Figure 2.1: Sketch of an advanced ring laser gyroscope instrumentation setup as realized for RZ. Sketch is not to scale.

In contrast to a setup with two mirrors and a beam combiner, a Koester prism can be positioned closer to the corner window. As a result, much of the beam propagation and the beam combination occurs within the prism, reducing asymmetric, free-air propagation

effects on the uncombined beams, such as fluctuations of the refractive index of air, caused for instance by temperature variations (e.g., Schreiber & Wells 2023b). Recording both combined beams leaving the Koester prism and stacking the electronic signal (see Sec. 2.4) allows to reduce incoherent common-mode noise (see Sec. 2.4).

Monochromatic video cameras are mounted on the optical table corner boxes behind the mirror to track laser beam walk. In the setup shown in Figure 2.1 three cameras are included, while a fourth could replace the avalanche photo diode. Beam walk could also be observed using quadrant photodiodes, which can simultaneously record the beam intensity and thus monobeam signals at multiple locations. The camera approach, however, is sufficient to constrain the beam plane deformation caused by geometric variation of the optical resonator (see Sec. 3.2).

This crosstalk between RF-excitation has been observed visually and electronically and is unfavorable for a stable operation and high-quality signals (see Sec. 2.5). A new signal generator (RIGOL DG992) is combined with a linear amplifier (LZY-22+ by Mini-Circuits) to serve as an RF-transmitter (radio frequency transmitter) with adjustable transmission frequency (up to 100 MHz). This allows operating the co-located RF-excitation of RZ and RV at different transmission frequencies (RV=80 MHz and RZ=65 MHz), hence reducing their interference (see Sec. 2.5).

In addition, a Faraday cage was designed and build in cooperation with Jürgen Loos to cover the gain tube of RV and reduce the RF emissions of the antenna, which easily couple to the exposed, co-located electrodes of RZ (see Fig. 2.11a).

The copper electrodes for the gain tube have been upgraded by mounting each onto an adjustable support. This allows to manually set and fix the electrode distance.

Upgrading the plasma ignition mechanism by integrating a beta radiator inside the gain tube is still pending for three rings (RZ, RU, RV), as it is best carried out during gas refill. Compared to the 'sparker units' currently used to manually ignite the plasma at each fade, the beta radiators would provide unsupervised automatic ignition whenever there is sufficient power provided by the RF-antenna, thus reducing maintenance work and downtime.

A new device, called for amplification and differential transmission (ADT), designed for either photodiode and PMT inputs have been realized and tested in cooperation with Jan Kodet (TUM). Two input signals can be stacked for common-mode noise reduction. The device features post-detection amplification of low-amplitude signals of a photo diode (PD) detecting monobeams and transmit the signals to the central data acquisition unit in the central shaft. Generally, differential transmission is advantageous against external interference (see Sec. 2.4).

In the advanced setup, selected PDs (10439-01 and C10439-03 from Hamatasu), based on their fixed gain and low drift characteristics, are used in combination with the ADT devices for monobeam and Sagnac signal detection (Fig. 2.1). Previously used photomultiplier

tubes (PMTs) require a high-voltage power supply, whereas PDs require only 15 V DC. The PDs have a fixed gain and a low temperature drift, while PMTs have a variable gain controlled by the power supply, which needs to be as stable as possible. This is a challenge to ensure, especially with the long transmission cables involved. A sufficiently large aperture to properly capture the approximately 3 mm wide beam, is required and is provided by both, PMT and PD (C10439-08 10x10 mm).

2.2 Performance Characterization

2.2.1 Data Quality Status

The quality of observations for ROMY's RLG is evaluated for 2023 and 2024 (until September) as shown in Figure 2.2, based on a simplified methodology as presented in Section 3.1. One-minute time intervals are classified as good or bad quality, while downtimes refer to a non-operational state of the rings, for instance during maintenance work (see also Sec. 3.2.2). Bad data is mainly dominated by periods where MLTI launches are required to recover from multi-mode operational states.

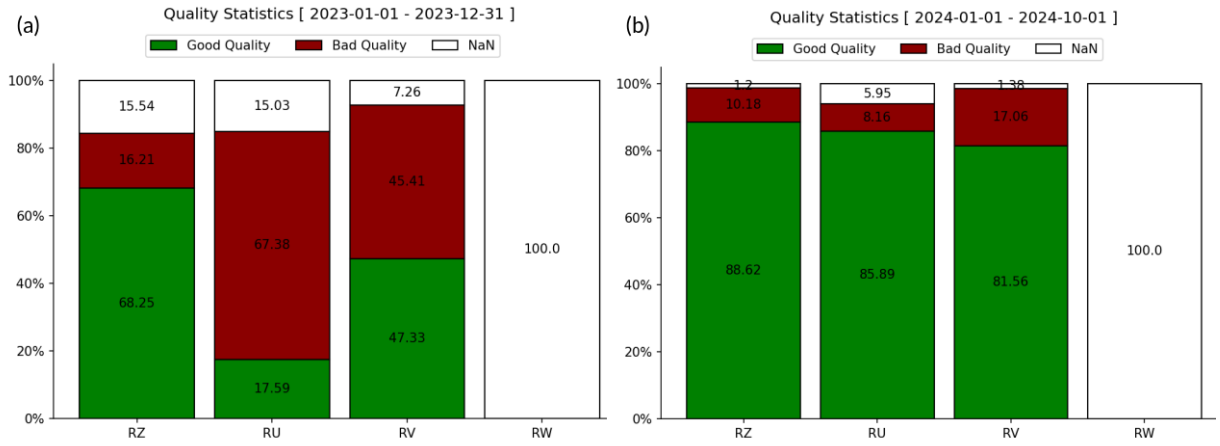

Figure 2.2: Statistical overview of data quality of ROMY's rings for the year (a) 2023 and (b) 2024 (until 2024-09-30) classifying data as good, bad and downtime or erroneous (= N/A).

RW was not operated due to a possibly still existing cavity leak. However, an evacuation test in the spring of 2024 gave no indication of a remaining gas leak. Until August 2024, an unavailable high-quality neon isotope gas mixture prevented an immediate refill of the cavity. After an upcoming refill, a manual realignment of the optical resonator is required before the RLG can be returned into service.

The best performing ring in 2023 was RZ with 68 % of good data, followed by RV (47 %), then RU (18 %). All the ring resonators required re-alignment at least once during the

one-year observation period. An overlapping period of good quality data from all three rings is limited to times after September 23, 2023, when RU was manually re-aligned. The hereafter referenced long-term observation period of three rings of ROMY refers starts on September 23, 2023 and continues until October 2024.

In 2024, three of ROMY's rings have been operated with good data quality in the range of 81 % to 88 % as a result of continuous supervision and maintenance efforts. This demonstrates not only the feasibility but also provides the largest available dataset of three component rotational ground motion observations for ROMY. Shorter periods of multi-component operation between 2017 and 2020 complement this dataset. The individual uptime equal about 70 % of simultaneous operation of RU and RV to obtain horizontal components of ground rotation. In order to achieve more continuous, good quality observations, the operation stability of all rings has to be improved (see Sec. 3.2).

2.2.2 Allan Deviation

The stability and sensitivity for an RLG can be evaluated using the Allan Deviation (AD). In order not to rely on a subjectively selected time period for the analysis, an overlapping Allan Deviation is computed in a statistical approach for 4 h intervals with 50 % overlap between 2024-04-20 and 2024-04-25 (Fig. S.1). This allows a median and minimum percentile value to be computed for each averaging time, and the variation of averaging time that achieves the maximum resolution to be evaluated. Results for the G-ring (= RLAS) are shown instead of data for RW (Fig. S.1d).

The overall superior stability of the G-ring at sub-pico rad/s resolution, is attributed to its monolithic design, the stabilization scheme employed and sophisticated environmental shielding. The difference across averaging times is evident compared to the non-stabilized, heterolithic rings of ROMY. For averaging times above 100 s to 200 s (median values in Fig. S.1), the increasing ADs indicate strong frequency drifts due to non-stabilized resonators.

The best resolution, achieved by RZ, is less than 2 prad s^{-1} for an averaging time between 200 s to 300 s, while the median value amounts to 6 prad s^{-1} for an averaging time of 100 s. A slightly less effective performance is observed when RZ is operated in a phase-locked multi-mode regime during the free-spectral range measurements in September 2024 (Fig. S.2).

RV reveals less variation compared to RZ, with a maximum resolution of around 2 prad s^{-1} and a median value of approximately 5 prad s^{-1} at 200 s. The inferior performance of RU, achieving a average resolution of 20 prad s^{-1} at 90 s, might be linked to the low-quality isotope mix that promotes multi-mode regimes.

When the median ADs are put into perspective with geophysical and geodetic signals observable with large RLGs, the insufficient long-term stability of ROMY to resolve most geodetic signals is evident (Fig. 2.3). Currently, ROMY accomplishes its purpose to provide

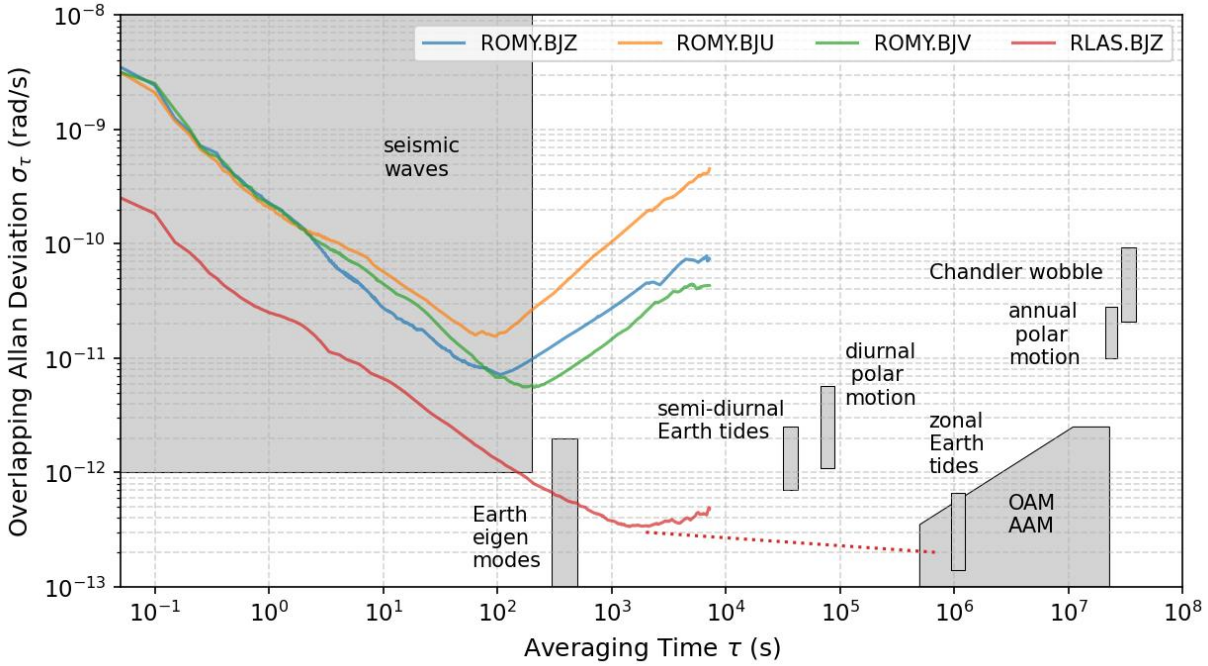

Figure 2.3: Median, overlapping Allan deviations for ROMY's rings RZ, RU, RV and the G-ring, are shown. The red, dotted line indicates the resolution of G-ring based on long datasets underlying the detection length-of-day variations (Schreiber et al. 2023a). The expected range for geoscientific signals, including seismic waves, Earth's eigenmodes, semi-diurnal Earth tides, diurnal and annual polar motion, Chandler wobble, zonal Earth tides and oceanic/atmospheric angular momentum (OAM/AAM) are depicted.

multi-component observations for rotational ground motions of seismic waves. Secondary microseisms are observed (see Fig. S.3) and possibly Earth eigenmodes excited after sufficiently large earthquakes. Considering only its geometrically imposed resolution limit, ROMY could achieve a higher resolution as the G-ring. In order to harness ROMY's full potential and resolve polar motion and length-of-day variations, as achieved by G-ring (Schreiber et al. 2004, 2023a), more effort must be undertaken towards implementing a sophisticated active resonator stabilization system for all of ROMY's rings (see Sec. 3.2).

2.2.3 Resonator Characterization

An optical resonator (or cavity) is commonly characterized by the quality factor $Q = 2\pi c\tau/\lambda$ and the finesse $F = \lambda Q/P$, with P being the perimeter of the ring (P_{RZ}=33.5 m), c the speed of light (c=3 × 10^8 m s^{-1}) and λ the optical wavelength (λ=632.8 nm) for a helium-neon gas mix (Schreiber & Wells 2023b, Igel et al. 2021).

In order to assess the cavity for RZ, measurements of the ring downtime τ or photon lifetime within the optical resonator were conducted on 2020-09-01. A comparison is shown in Figure 2.4. By fitting an exponential function, a ring downtime of 0.67 ms is determined.

This allows computing the quality factor of $Q_Z = 1.996 \times 10^{12}$ and finesse of $F_Z = 37\,699$ for RZ. Using the free spectral range (FSR), defined by the resonator geometry, $FSR = c/P$, a total cavity loss, $L = (\tau \cdot FSR)^{-1}$ of $L = 167\,\text{ppm}$ for RZ is determined, which is about 55 ppm per mirror. The expected losses per mirror amount to about 10 ppm, hence around 30 ppm for the total loss of the resonator. The increased loss can be the result of combined effects: damaged mirror coatings, an extended beam diameter due to beam divergence, dust particles on the mirrors or dust covering the corner windows.

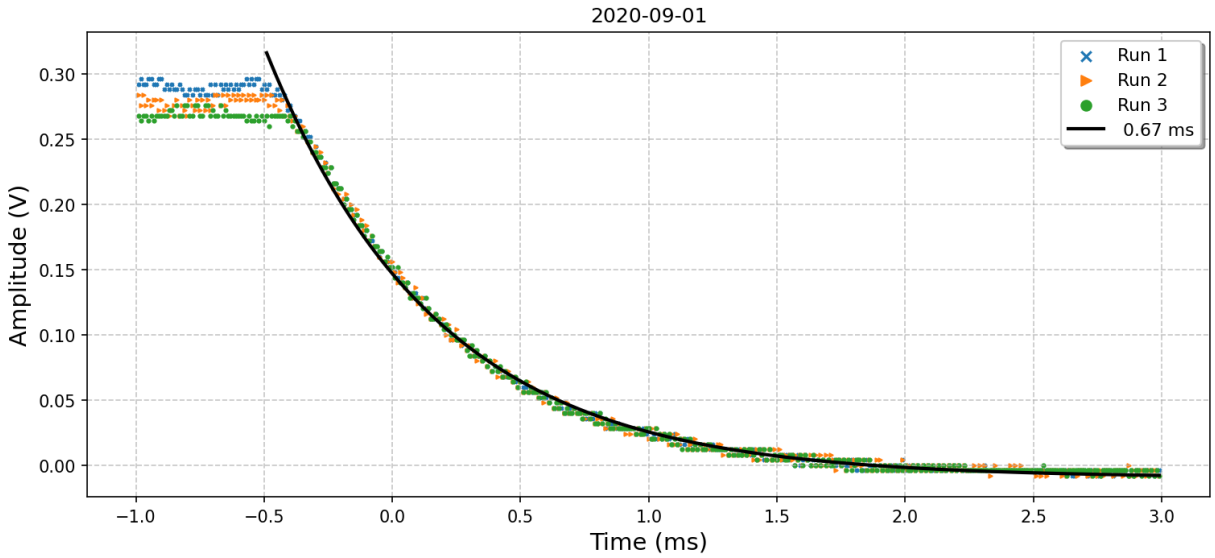

Figure 2.4: Ring downtime measurement for RZ on 2020-09-01. Three measurements are compared and run 1 is modelled using an exponential function to determine the ring downtime τ of 0.67 ms.

Since all ROMY rings have identical hardware components and the same design (see Fig. 3.7b), although slightly larger (P=12 m), comparable characteristics are expected for the slanted rings RU, RV and RW.

The beam power of a beam after combination in a Koester prism was measured with a Thorlabs powermeter on 2023-06-05 over several hours (Fig. 2.5). The ring laser was operated at low intensity to support a single-mode operation regime.

The transmitted beam power amounts to about 15 nW, which gives a monobeam power of about 7.5 nW, assuming equal partitioning of the beam intensity for both propagation directions. Power values around 20 nW have been observed during previous measurements, depending on the explicit settings of the intensity control loop. This provides an assessment of the expected transmission power.

The beam power decrease by about 4 nW over the 5 h of the measurement. The contrast of the Sagnac signal and the peak power spectral density values (PSD_{max}) correspond to this trend and can serve as a proxy for the beam power when no powermeter is set up.

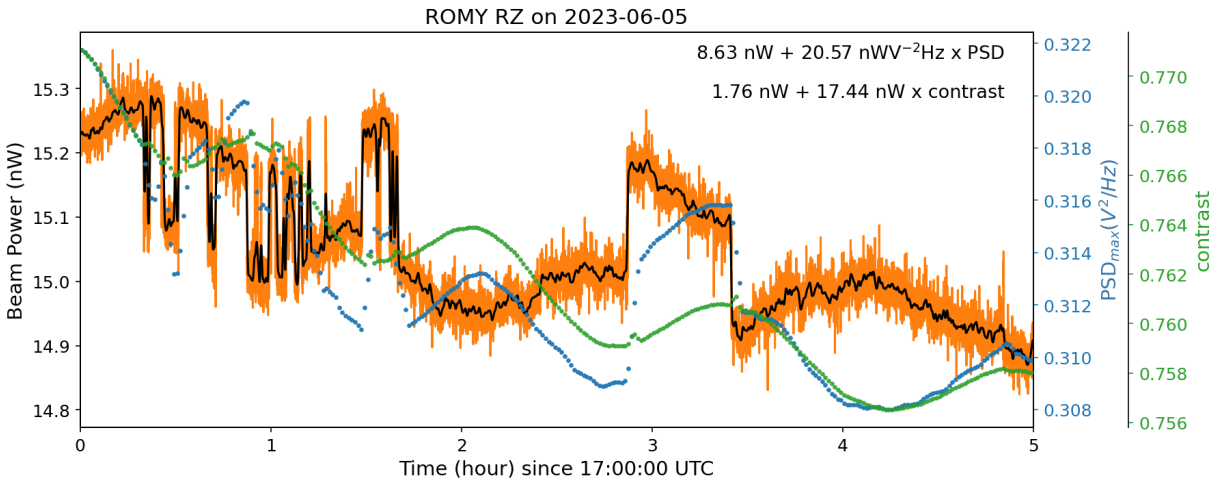

Figure 2.5: Measurement of the beam power (orange) for RZ of a single output after beam combination on 2023-06-05. A moving average is included as a black line. The contrast of the Sagnac interferogram and the PSD maximum are shown on separate y-axes.

Scaling factors of 17.44 nW and 20.57 nW V^{-2} Hz for contrast and PSD_{max}, respectively, are obtained via a linear regression.

2.3 Electronic Noise Sources

The quality of the Sagnac signal also depends on the electrical noise. To achieve good signal quality, the noise floor and pronounced peaks therein have to be minimized. This is especially important for the monobeams, which have only about half the signal power compared to the combined Sagnac signal. A systematic noise analysis at ROMY enabled to attribute several characteristics to various hardware components (Fig. 2.6).

The blue spectrum in Figure 2.6 shows a typical power spectrum for RZ (without interference). Several distinct peaks are visible besides a dominant Sagnac frequency peak at around 553.5 Hz, which is about 200 dB above the noise floor. The most pronounced noise peaks belong to the 50 Hz hum and harmonics thereof.

The self-noise of the data logger unit is characterized using an open channel and is about 100 dB below the signal noise floor, but includes some electronic hum peaks (green; Fig. 2.6). Adding an 50 Ω endpiece (or terminator) to the channel via a short cable (approx. 1 m) to shorten the circuit produces a noise signature with distinct peaks between 10 Hz and 100 Hz (red; Fig. 2.6).

Connecting an unpowered PMT in a corner shaft via long coaxial cables (about 15 m to 20 m) and the electronic boards used for signal monitoring in the acquisition rack adds 1/f noise (brown; Fig. 2.6). The design of the electronic boards may have a grounding issue and thus contribute to the increase in electronic noise. Turning on the PMT, however

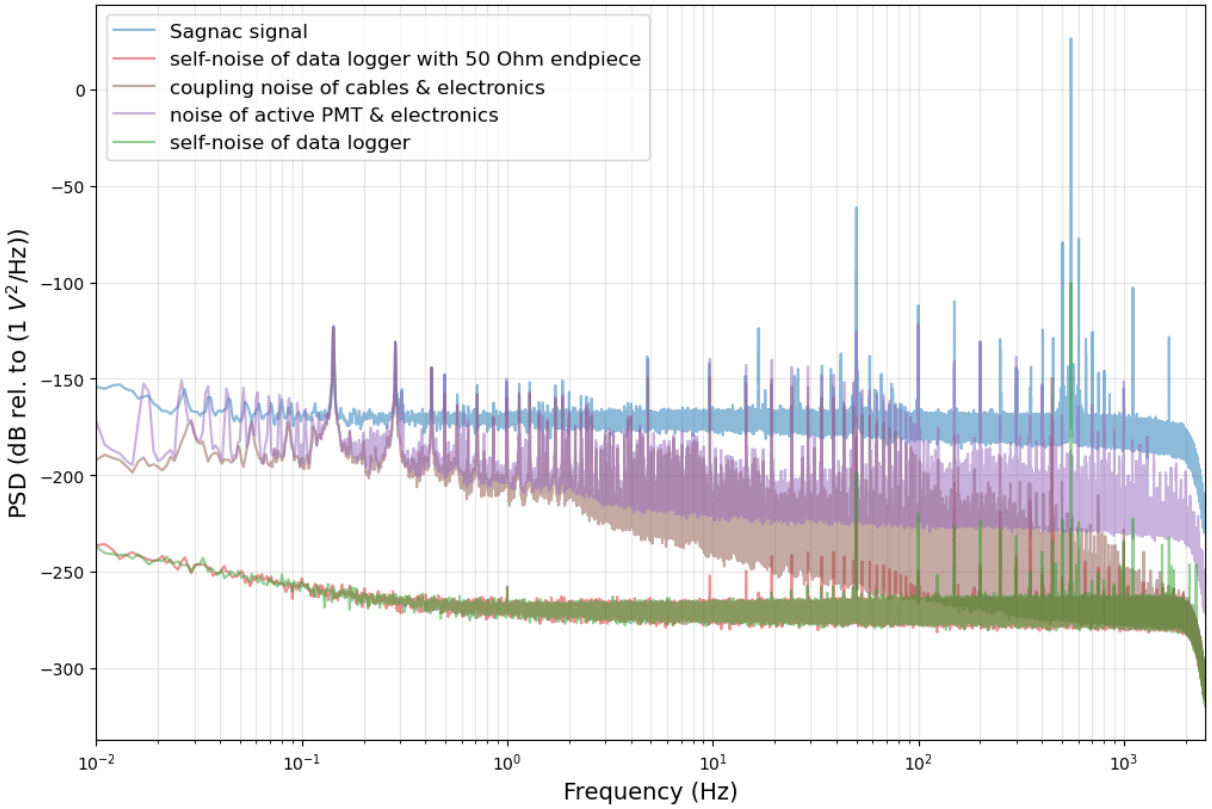

Figure 2.6: Electric noise sources are compared by power spectral density (PSD) characteristics. Data of an open-channel of the data logger unit (green) represents the self-noise level. A short coaxial cable with an 50 Ω endpiece is attached to the data logger (red). An unpowered photomultiplier tube (PMT) detector is connected via a long coaxial cable and electronic boards (brown). The PMT is powered, but covered (purple). Detection of the Sagnac signal with the PMT (blue).

covering its detector to avoid light sensing, boosts the noise floor, in particular for higher frequencies (> 1 Hz).

A second example for RV, now using PDs for signal detection is shown in Figure 2.7. Here, FJV shows the power spectrum for RV without interference signatures and FJW represents the power spectrum for an open channel with only a 1 m coaxial cable with an 50 Ω endpiece attached. The noise level for FJW is about 50 dB below the level of the Sagnac signal (FJV).

A reflection signature between 10 Hz and 100 Hz is present, as well as peaks for the 50 Hz hum and its harmonics. A harmonic peak at 450 Hz is clearly visible in the close-up about 40 dB above the noise floor (Fig. 2.7c). The small peak at the Sagnac frequency of RV is most likely attributed to electronic channel crosstalk. The difference between the Sagnac frequency peak of FJV and the noise floor is about 75 dB to 90 dB (Fig. 2.7c).

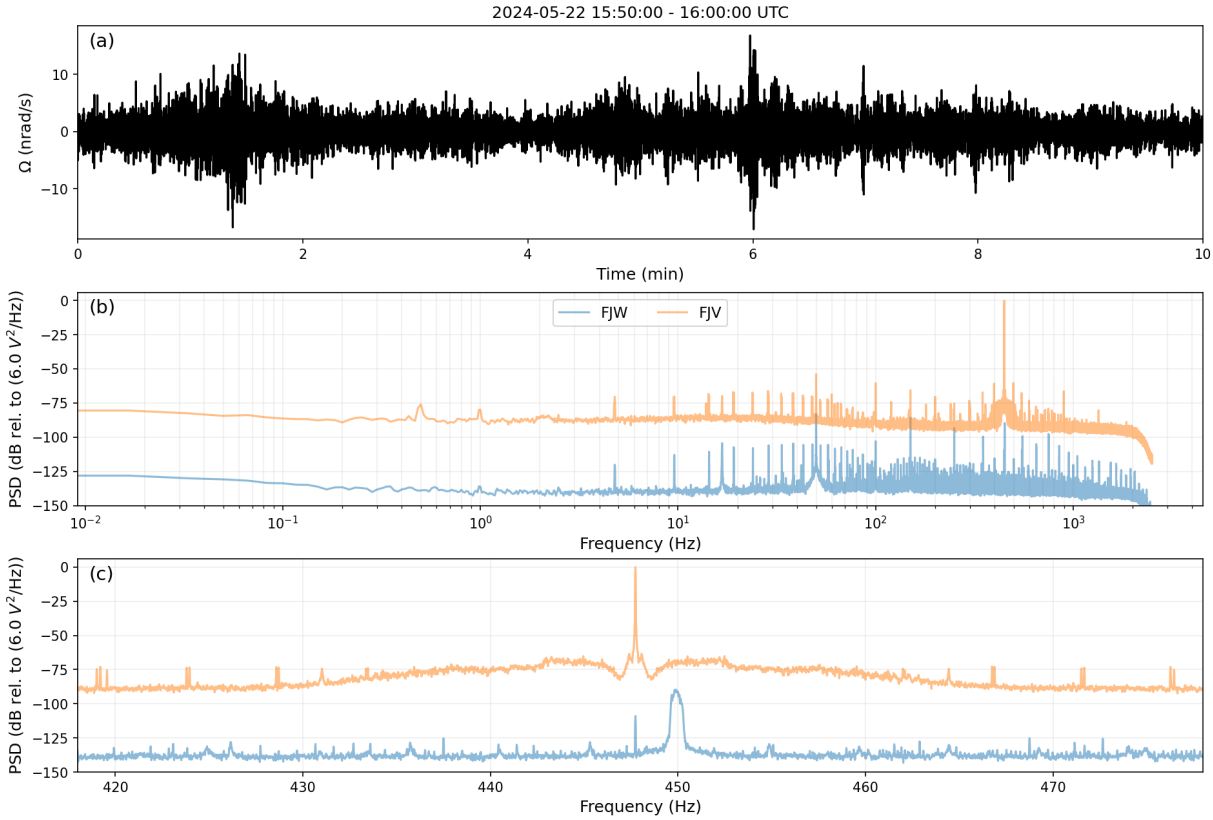

Figure 2.7: (a) A random, low-noise selection for 10 min of rotation rate data of RV. (b) spectra of Sagnac signal data for RV (FJV) and an empty channel of the data logger with a cable and 50 Ω endpiece attached (FJW). (c) represents a zoom-in on the Sagnac frequency peak at around 447.7 Hz. Decibel scale is relative to the Sagnac peak of FJV.

2.4 Differential Transmission

Analog signal transmission is still the default for ROMY to transmit signals from the detection in the corner shafts to the data acquisition unit in the central shaft (02). This is based on single-ended coaxial cables. Differential signal transmission is generally recommended when EMI (electromagnetic interference) or RFI (radio frequency interference) noise is present. To address this issue, electronic boards for signal amplification and differential transmission (ADT) were designed, built and tested in close cooperation with Jan Kodet (TUM). The amplification is required especially before transmitting signals detected by photodiodes with low internal gain and small signals, such as monobeams. The differential transmission relies on twisted, well-shielded RJ45 cables. The intention is to reduce present EMI and RFI noise, although long cable distances remain and are inevitable when using a central data acquisition unit due to ROMY's structure. Three ADT units are currently operated at RZ (see Fig. 2.1).

By stacking both beams leaving the Koester prism (see Fig. 2.1a), the incoherent common-

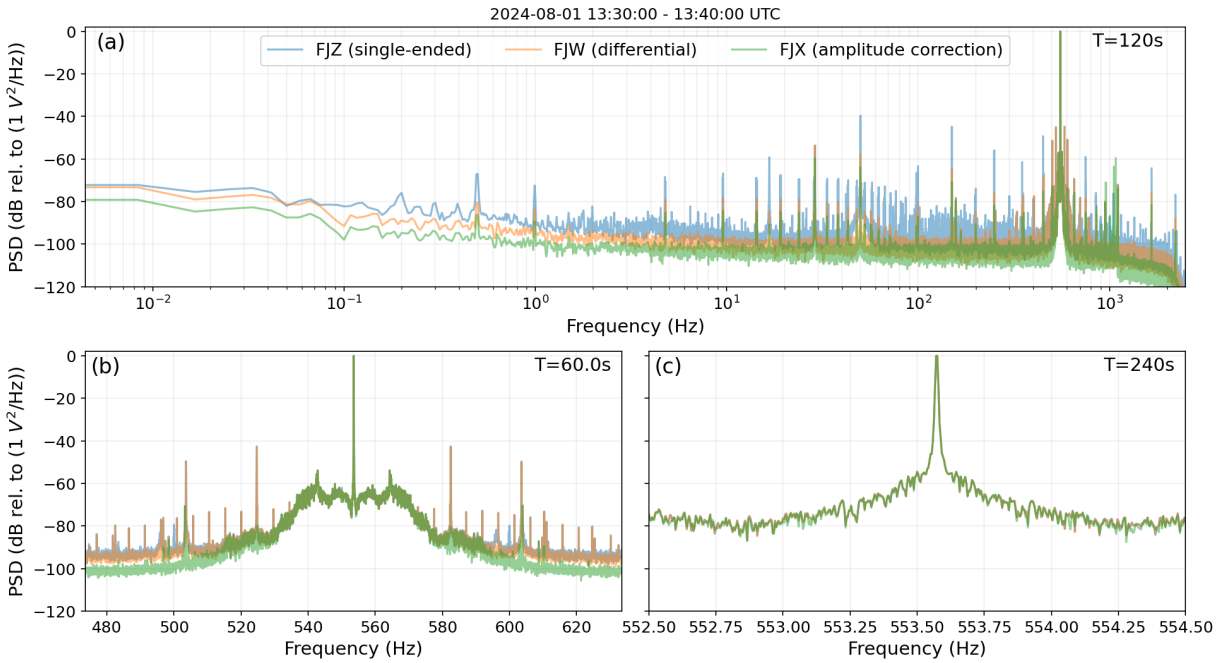

Figure 2.8: (a) Power spectral density for Sagnac signals at RZ for 10 min duration each, comparing: single-ended (blue) and differential (orange) transmission of a combined signal detected by two photodiodes. The waveform of FJW is divided by its envelope to obtain FJX. The maximum is set to zero for all spectra. (b) and (c) present different close-ups of the Sagnac frequency peak at about 553.6 Hz.

mode noise can be successfully reduced (see (Schreiber & Wells 2023b)) by about 10 dB to 20 dB. The comparison of the Sagnac signal between single-ended and differential transmission shows a reduction of the noise floor for the latter of several decibels on average and up to about 11 dB. The Sagnac frequency peak appears unchanged (Fig. 2.8c).

An equalization of the amplitudes of the Sagnac signal is achieved when dividing by the envelope of the signal with pre-whitening value of 0.001. This amplitude correction further enhances the PSD by some decibels and rejects some prominent noise peaks near the Sagnac frequency peak (see Fig. 2.8b). These peak in turn most likely result from amplitude modulation of the signal due to external interference, internal beam intensity fluctuations or the rather low sampling rate of 5 kHz, thus artificially causing amplitude variations.

With regard to a long-term upgrade of ROMY, it is recommended to use differential signal transmission as default. Including a well-defined electrical grounding system in each shaft to ground all devices consistently could further eliminate electrical noise sources. The presence of RFI noise will remain due to several RF-excitation antennas (see Sec. 2.5) since required to operate the active RLGs.

2.5 Antenna Interference

Each of ROMY's four ring lasers uses an RF-excitation scheme at the gain tube to power the plasma for active lasing. The RF-excitation antenna consists of an RF signal generator, amplification unit, impedance matching and electrodes at the gain tube. The gain tubes of RZ and RV are both located in shaft 08 only about 30 cm apart.

Strong interference between the excitation antenna at RV and RZ is evident, both visually in the plasma and in the signal spectra. Whenever only one RF-excitation is operated and the other is off, no interference is present. This can be attributed to the similar transmission frequencies during excitation at about 80 MHz. The precise interference signature depends on the settings of the antenna, such as input and output power. To address this issue, RV has been upgraded with a new signal generator that allows the setting of transmission frequencies and an amplification unit to provide sufficient excitation power.

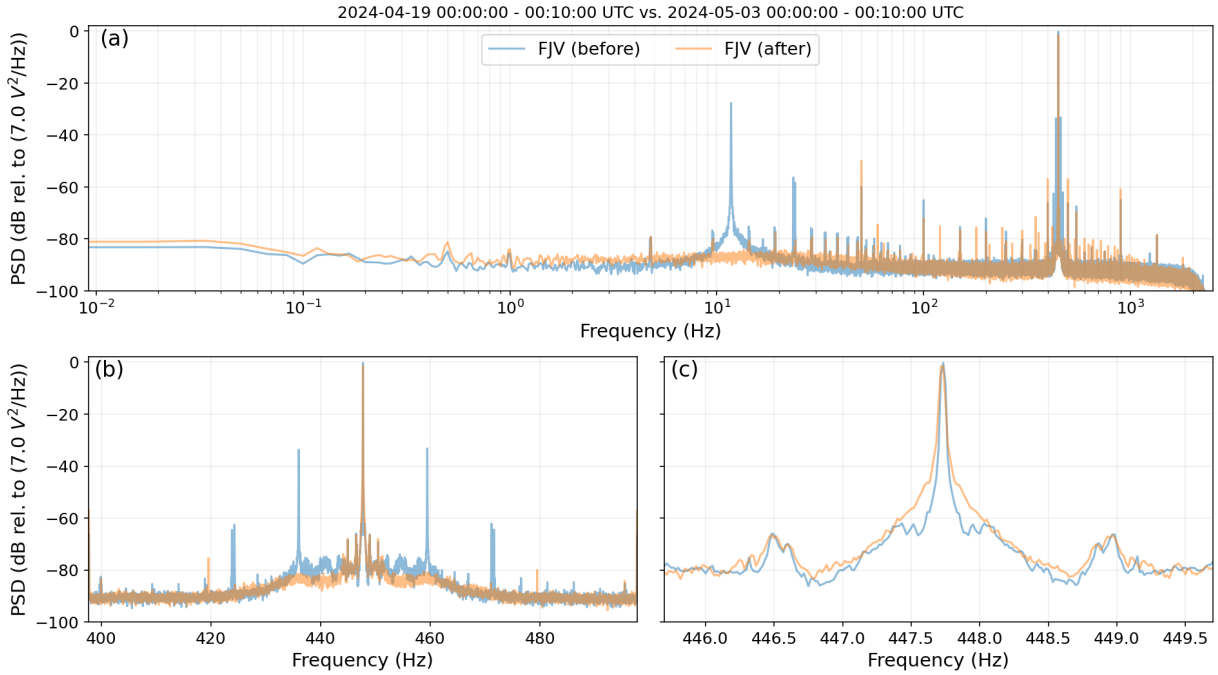

Figure 2.9: (a) Spectra of 10 min of Sagnac signals for ROMY's western ring (RV) are shown as power spectral densities before and after the installation of a new radio frequency excitation system for RV (2024-05-02) to reduce interference with the antenna of RZ. (b) and (c) show a different zoom-in on the Sagnac frequency peak.

Figure 2.9 compares spectra of Sagnac signal data for RV before and after employing the new antenna setup at RV. A pronounced peak at around 11 Hz, as well as a set of symmetrically aligned peaks in the vicinity of the Sagnac frequency peak (447.7 Hz) are identifiable before the new antenna setup is used (blue; Figs. 2.9a and 2.9b). Operating RF-excitation at two different transmission frequencies of 80 MHz and 65 MHz eliminated

the interference signature (Fig. 2.9). In general, less prominent side lobes around the Sagnac frequency indicates less amplitude modulation.

A synthetic frequency modulation approach as used for ratio transmission techniques has been implemented to create and analyze a synthetic Sagnac signal and noise contributions. Real rotation data is modulated on a carrier frequency to produce a synthetic Sagnac signal. Figure 2.10 shows spectra computed for an observed and a synthetic Sagnac signal as well as noise spectra for white frequency and phase modulation noise intended to explain the noise level of the observed data.

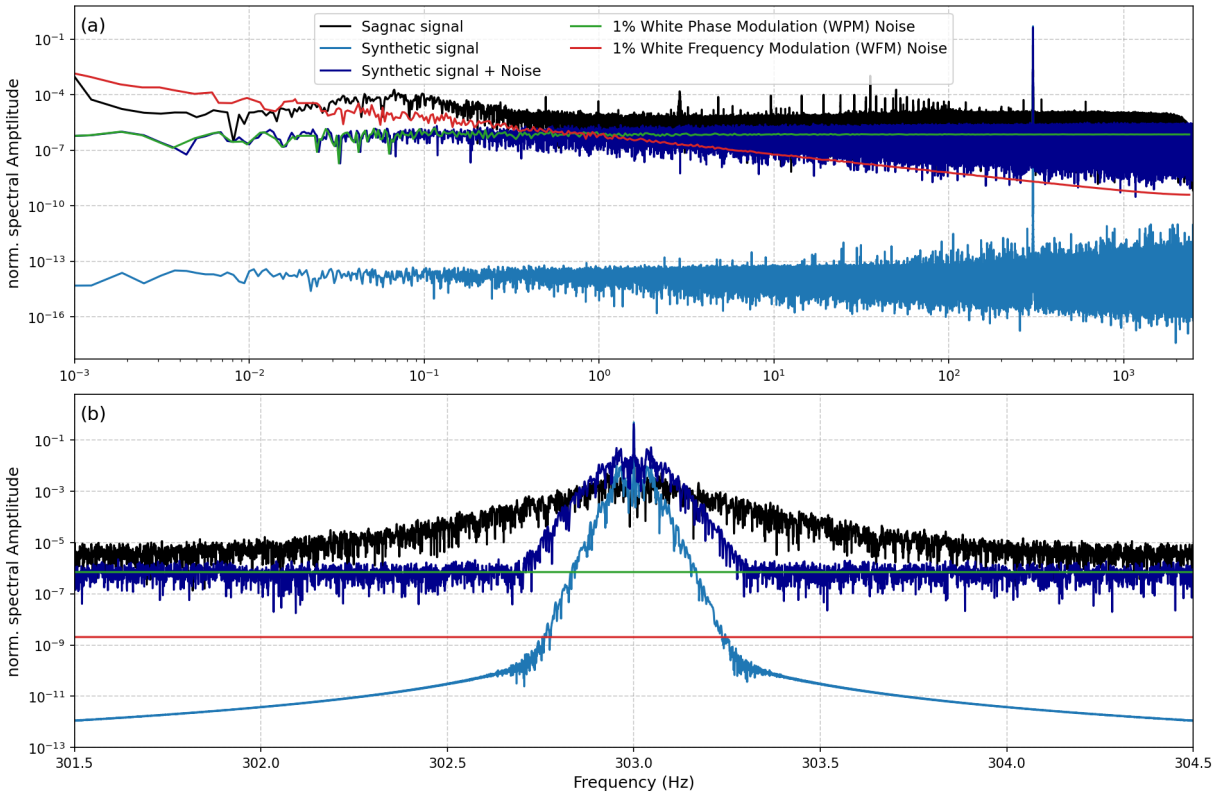

Figure 2.10: (a) Amplitude spectra of real Sagnac data for RU (black), a synthetic Sagnac signal based on frequency modulation (pale blue), synthetic Sagnac signal with white phase noise (dark blue), 1% smoothed white phase modulation noise (green) and smoothed white frequency modulation noise (red). (b) A close-up on the Sagnac frequency peak of RU at about 303 Hz. For the synthetic signal with and without noise, a modulation index of 3 and 1 is used, respectively.

For example, white frequency modulation noise could explain the increase in noise level observed towards low frequencies below 500 mHz. A pure synthetic Sagnac signal shows symmetric side lobes at about 0.1 Hz next to the Sagnac peak, while its general spectral amplitude level is not representative with that of observed Sagnac data (see Fig. 2.10b). By adding white phase modulation to the modulated signal, the overall level better matches

the real observations better. The width of the slope around the Sagnac frequency is not well captured in the synthetic signal, this is mainly controlled by the modulation index.

2.6 Environmental Monitoring System

In order to study the environmental influences on the near-surface ring laser array, causing undesired instrumental effects (see Sec. 3.2), ROMY had to be equipped with an internal environmental monitoring system.

The monitoring system, called Weather in ROMY, abbreviated WROMY, consists of self-assembled sensor boxes in each access shaft, except for shaft 02 and 03. Each sensor box uses a Raspberry Pi computer as data acquisition unit and an HTP sensor to record air humidity (H), air temperature(T) and air pressure (P), as shown in Figures 2.11e and 2.11f.

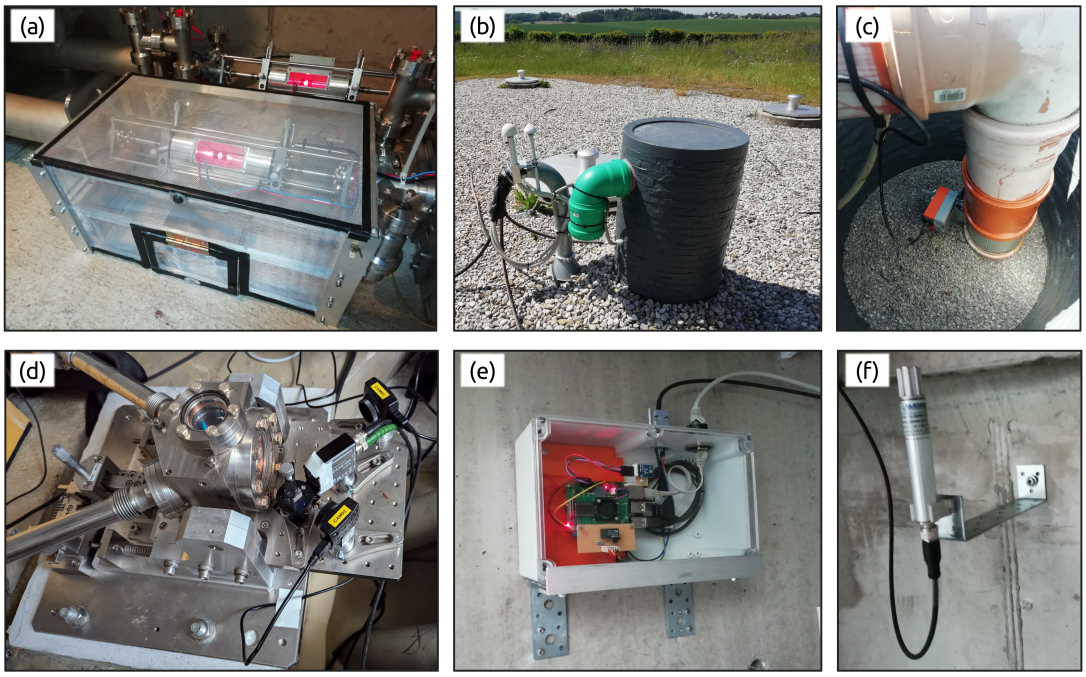

Figure 2.11: (a) A Faraday cage covers the gain tube of RV to reduce RF emission and reduce interference at RZ. An electrically rotatable valve was installed for the ventilation pipe of the central shaft, (b) shown from the outside (green) and (c) the inside (orange). (d) Resonator corner box of RZ in shaft 07 with two video cameras for beam walk monitoring and a photo diode for monobeam detection mounted on the optical table. (e) The weather stations inside each of ROMY's shafts (WROMY) consists of a data acquisition unit based on a Raspberry Pi and(f) a THP sensor.

Scripts running on the Raspberry Pi read, store and transmit data to the ROMY archive via network access. Malicious readings of the HTP sensors, occurring randomly, however,

infrequent, required an integrated relais circuit that interrupts the power supply and ends the error of the THP sensor. This causes irregular, minor data gaps. In 2024, DPS310 pressure sensors, called Pressure of ROMY (PROMY) were added to the sensor boxes located in the corner shafts to provide a better resolution for pressure and temperature readings. With a sampling rate of 1 Hz multiple values are averaged to reduce noise

This monitoring network allows to continuously monitor the atmospheric conditions inside ROMY starting in the summer of 2021. Current data are displayed on the ROMY monitor at the observatory. Complementary, the weather station BW.FURT (WXT530 by VAISALA) is at the surface about 30 m next to ROMY and provides observations of precipitation, wind direction and wind speed, air temperature, barometric pressure and air humidity.

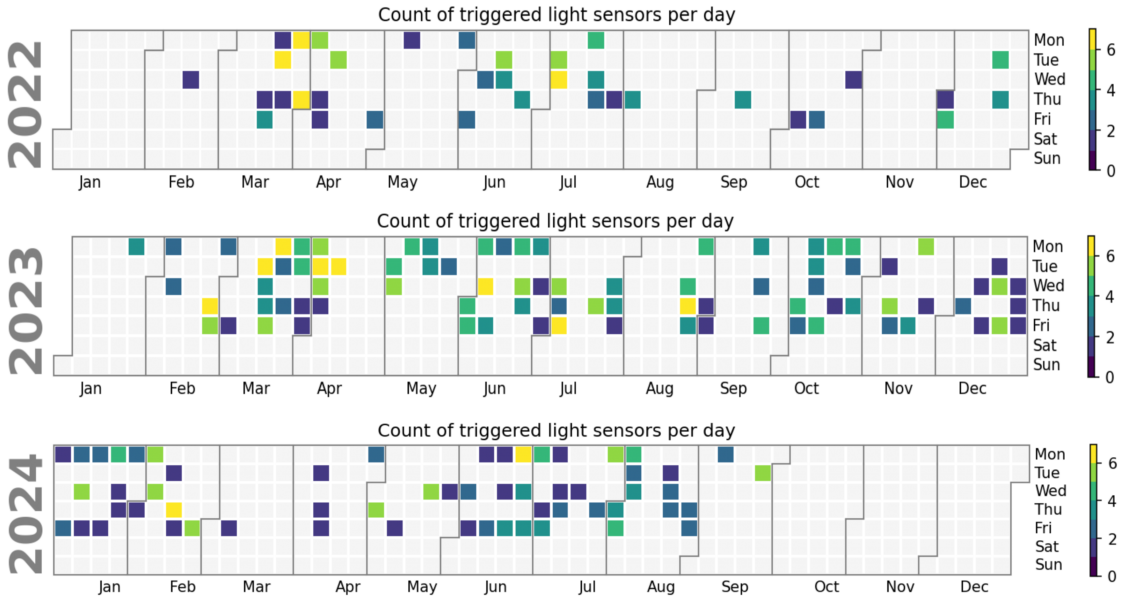

Figure 2.12: Maintenance log from 2022-01-01 to 2024-09-30 based on light sensing in ROMY's shafts. Color-scale indicates the amount of individual light sensors which detected light on that day.

Furthermore, a light sensor (BH1750) is used to detect two states: *dark* and *not dark*, in order to automatically log maintenance work, when at least one of the shafts was opened. This also provides the ability to issue warnings in case a lamp inside the shafts was not turned off after maintenance work. An overview of maintenance work from 2022-01-01 to 2024-09-30 is shown in Figure 2.12. The number of shafts opened that day is color-coded. More shafts being accessed usually indicates a major maintenance activity. Additional sensors have been installed in shaft 01 in order to monitor carbon monoxide (CO) and carbon dioxide (CO2) levels. For safety purposes, a radon sensor is also operated in shaft 01.

2.7 Passive Thermal Insulation

The exposure of ROMY to environmental changes at the surface is hardly reduced by the metallic covers on top of the access shafts. Heating up these covers could eventually lead to convection in the shafts. Since thermal effects on the optical resonator have to be minimized, a passive thermal insulation design has been developed and implemented.

The surface air temperature records for September 2022 based on the weather station FURT (Fig. 2.13a) shows strong daily variations of more than 10 °C, causing pronounced spectral peaks at one and two cycles per day (Fig. 2.13c). In the absence of thermal insulation, except for closed shaft covers, the temperature variations propagate down to ROMY's shafts recorded at all upper sensors (WS3 – WS9), especially at one cycle per day. WS4 and WS8 show elevated temperatures. Both sensors are located in shafts with at least one gain tube section. The increased temperature is explained by the excess heat of the RF-transmitters and other electronics.

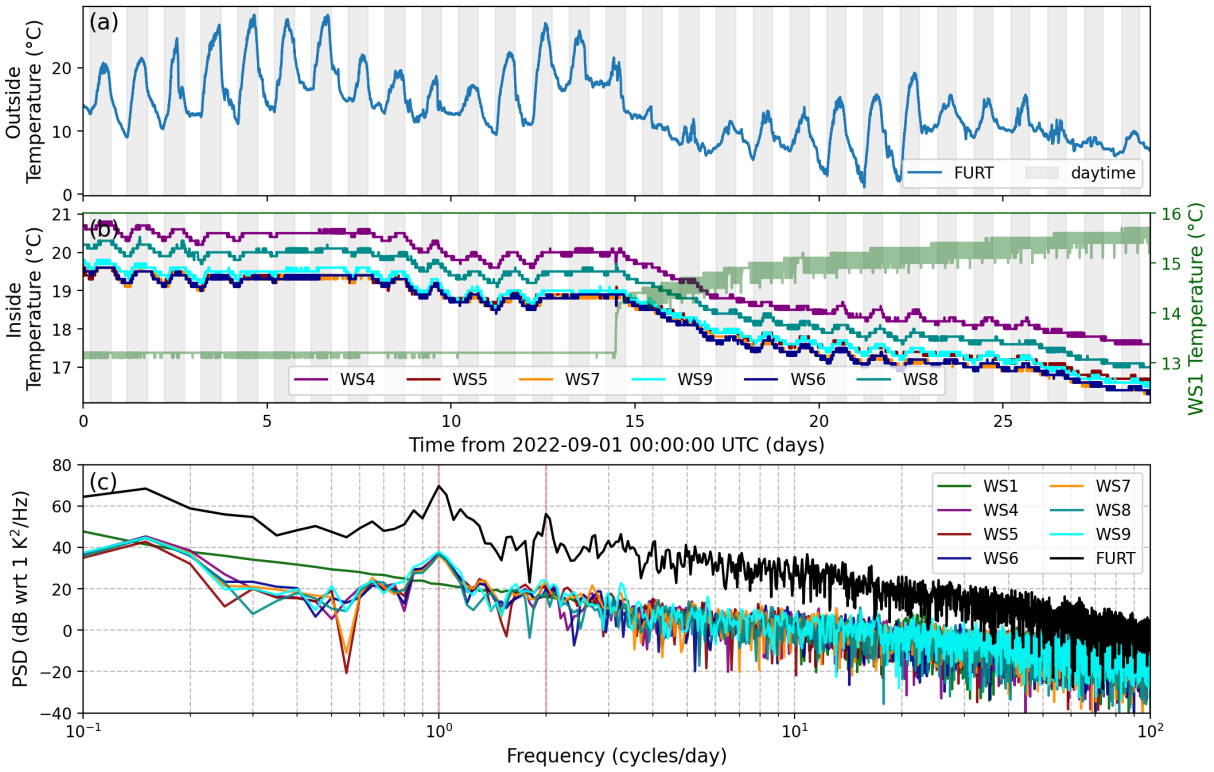

Figure 2.13: Temperature data is shown between 2022-09-01 and 2022-09-30. Gray bars indicate day time (sunrise to sunset). (a) shows the outside air temperature recorded at the weather station FURT. (b) shows air temperature records of THP sensors inside ROMY's shafts. In (c) power spectral density is shown for each THP and FURT records based on the time series in (a) and (b).

WS1 is located at the bottom of the central shaft (01), with the most stable temperature

conditions between 13 °C to 14 °C at a depth of about 15 m below the surface. The sudden increase in air temperature on day 14 is caused by the activation of a dehumidifier unit, which also distorts the corresponding PSD. The sensor resolution does not resolve any daily or sub-daily air temperature variations for WS1.

In order to reduce the observed temperature variations within the ROMY structure, and thus instrumental effects, a passive thermal insulation was designed and installed. The purpose is to provide a more stable temperature condition by 1) a suppression of the exchange of air masses between outside and inside and 2) a reduction of air convection at the resonator by a barrier to only allow the upper air volume to convect due to heat intake at the exposed metallic cover.

A 60 mm thick styrofoam plate, mounted on a sliding aluminum frame, separates the smaller entrance shaft off from the main shaft. The sliding system is installed on the ceiling of the access shafts and allows the sliding plate to be opened and closed from the inside and outside. An illustration of the schematic principle is presented in Figure 2.14a and 2.14b, while images of the realization are provided in Figure 2.14c and 2.14d.

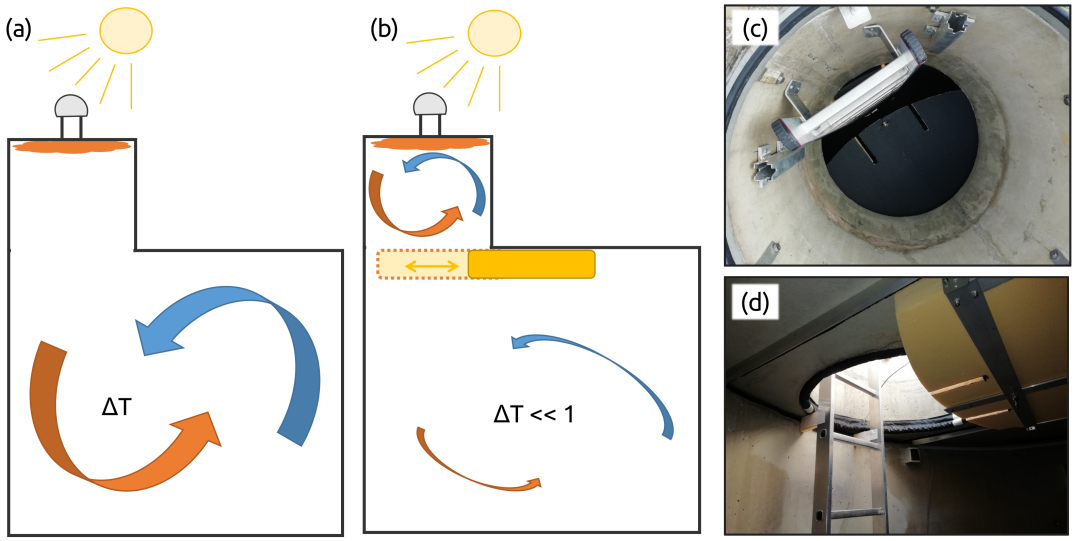

Figure 2.14: Schematic illustration of insulation plates installed in one of ROMY's access shafts. (a) Without passive insulation, the metallic cover heats up and temperature variations (ΔT) propagate via air convection and heat diffusion. (b) With insulation plates in a sliding system at the shaft ceiling (orange) two volumes are separated, stabilizing the main volume from air temperature fluctuations on a daily and sub-daily basis. An image of the insulation plate installed in one of ROMY's access shafts as (c) seen from the outside (top down) and (d) from the inside (bottom up).

A passive insulation system is fully operational in all small shafts (04 to 09) since 2024-03-09. In order to validate the system against the previous state (Fig. 2.13), a second period without maintenance work, between 2024-03-09 and 2024-04-09, is analyzed. The outside

air temperature for this period in spring shows variations comparable to the September data in Figure 2.13a.

Thus, this passive insulation system can be considered as a lowpass filter to reduce daily and sub-daily air temperature fluctuations. This system improves the temperature variation inside the shaft and successfully suppresses daily and sub-daily peaks. However, it is not capable to remove or suppress seasonal variations (see Fig. 3.19). More details can be found in Section 3.2.

The central access shaft has a ventilation system to provide fresh air during maintenance work and to reduce radon levels. The ventilation pipe in the central shaft provided a direct path for temperature equalization between outside and inside. A rotatable valve is now installed inside the ventilation pipe to close automatically, when no maintenance work is being conducted (see Fig. 2.11c).

2.8 Microbarometer Station

An MB2005 microbarometer sensor (by CEA) with a REFTEK data logger was installed inside ROMY's shaft 03 on 2023-08-28. The station, named BW.FFBI, provides high-quality observations of absolute barometric pressure (BDO) and infrasound (BDF), being able to sense pressure changes below 1 mPa. A comparison of the power spectral densities of the sensitivity-corrected and response-corrected infrasound data with the absolute pressure data yields a match between 20 mHz and 400 mHz (see Fig. 2.15). As expected for lower frequencies, the highpass infrasound channel is limited in dynamic range even when response-corrected, while for frequencies above 400 mHz the absolute pressure channel is limited in resolution.

Different inlet setups for the microbarometer have been briefly tested and evaluated. On this basis, a setup was selected that connects to inlets of the sensor via a porous hose placed inside shaft 03. The shaft cover is pressure permeable and reduces wind noise to some extent. There is a difference of about 30 dB between the PSD and the low noise model for barometric pressure by Marty et al. (2021) at 0.1 Hz (Fig. 2.15). The difference is smaller for lower frequencies. The peak of the micobarom around 0.2 Hz is resolved on generally quiet days (Fig. 2.16). The broader peak just below 2 Hz could be related to a resonance frequency of the central shaft, acting as a Helmholtz resonator.

The DPS310 digital pressure sensor is a low-cost, but high-precision barometer sensor based on micro-electro-mechanical system (MEMS) technology. Such a sensor is operated next to the MB2005 microbarometer station using a Raspberry Pi for data logging. A comparison of the DPS310 and MB2005 data for barometric pressure reveals identical PSDs and high coherence below 0.1 Hz (see Fig. S.4).

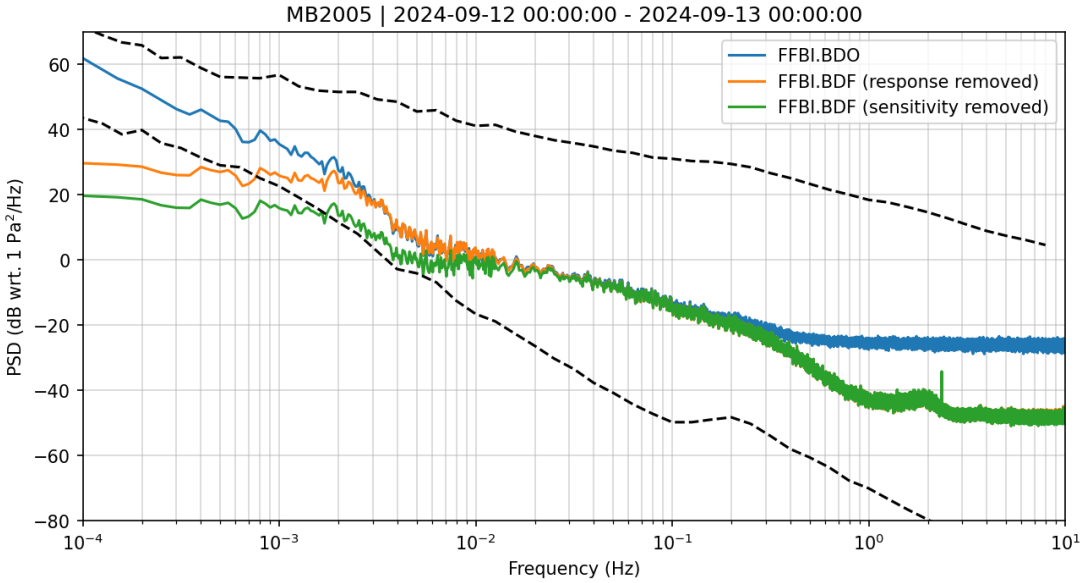

Figure 2.15: Power spectral density for absolute air pressure (FFBI.BDO) and high-pass filtered (infrasound) pressure (FFBI.BDF) with sensitivity or instrument response correction applied. Welch spectra are computed separately below and above 120 mHz. Low and high noise models for barometric pressure by Marty et al. (2021) are shown as reference (dashed black lines).

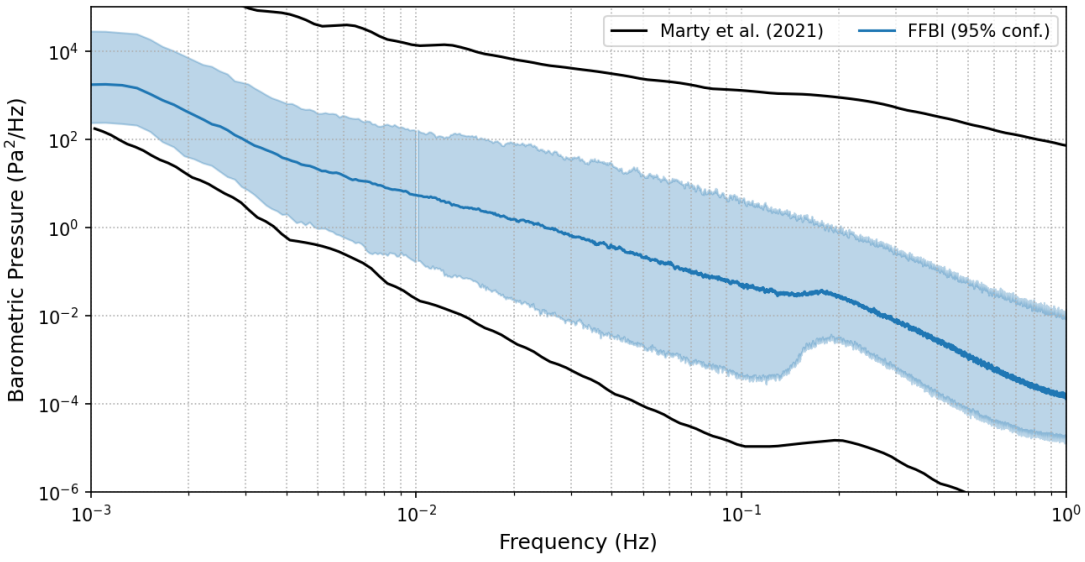

Figure 2.16: Median power spectral density (PSD) and an 95 % confidence interval for the microbarometer station FFBI is shown with regard to the low and high noise models for atmospheric pressure by Marty et al. (2021). Data of channel BDO and BDF are used to compute PSDs below and above 10 mHz, respectively.

2.9 Barometer Array

By 2024-03-09, all stations of the outer seismic array of ROMY (BW.TON, BW.ALFT, BW.BIB, BW.GELB, BW.GRMB) were equipped with a DPS310 barometer sensor and a Raspberry Pi as data acquisition unit. Together with either the DPS310 barometer or the MB2005 microbarometer at ROMY as a reference station, this forms a small barometer array of six stations with an aperture of approximately 4.2 km (Fig. 2.17).

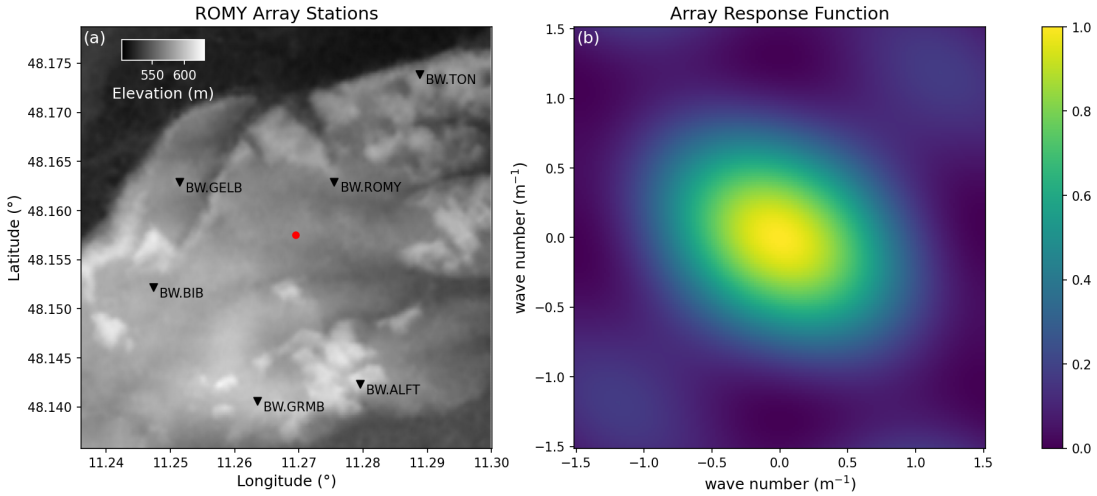

Figure 2.17: (a) Map of the local seismic and barometer array surrounding ROMY including topography. (b) Computed array response using the ObsPy package (Megies et al. 2011).

Figure S.5 compares two days of barometric pressure records of the array stations, bandpass filtered between 0.05 mHz to 100 mHz. A high coherence higher than 0.7 is obtained for all stations below 0.8 mHz, with respect to the central station (BW.PROMY). For frequencies above 0.1 Hz, the ability of the array to resolve an increasingly incoherent wavefield is limited due to its design. The array response function shown in Figure 2.17b deviates from an ideal impulse function by being slightly elliptical in a northwest-southeast direction. This is a result of the station distribution.

2.10 Tiltmeter

RLGs utilize the local Earth rotation rate to overcome the lock-in effect. This results in a sensitivity to the local orientation, especially in a north-south direction. Local tilts therefore affect the Sagnac frequency of RLGs (e.g., Schreiber & Wells 2023b). ROMY has temporarily been equipped with two tiltmeters:

- a two-component Lippmann borehole tiltmeter, named BoreholeROMY (BROMY), mounted at the foundation at the bottom of the central shaft 01 from 2021-02-10 until 2024-07-17 and

- a two-component Lippmann platform tiltmeter, named TiltmeterROMY (TROMY), with varying locations from 2021-01-25 until 2024-01-15.

A permanent platform tiltmeter for ROMY, called ROMYTiltmeter (ROMYT), was added in April 2022. The instrument recorsd north-south and east-west tilts as well as the temperature inside the sensor housing. All Lippmann tiltmeters are inertial accelerometers, equivalent to long-period optimized seismometers, and thus sensitive to inertial acceleration.

These tiltmeters show a high susceptibility to temperature and humiditiy variations, causing several microradians of tilt, which are not entirely linear, but contain certain non-linear hysteresis effects (Fig. 2.18). The instrumental effect of temperature could be observed in particular for the borehole tiltmeter being located in a stable environment (bottom of the central shaft). Temperature fluctuations introduced by operating a dehumidifier unit in the shaft during summer are recorded by the instrument.

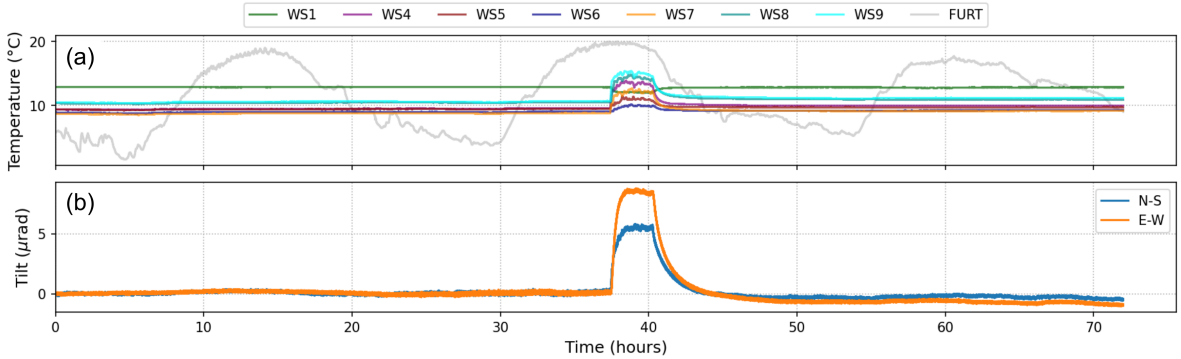

Figure 2.18: The effect of temperature variation on tiltmeter observations is demonstrated. (a) Absolute air temperature records inside ROMY (WS1-9) and outside (FURT) for 70 h with an anomaly starting at after about 37 h. (b) Tilt observations for north and east components showing the response to the strong temperature variation.

Efforts to insulate the instruments from temperature variations included absorbent cotton and boxes of styrofoam. The tiltmeter also benefits from more stable temperature conditions due to the passive insulation of the shafts themselves. For the current deployment of ROMYT in shaft 07 the sensor is mounted on a rigid, about 20 mm thick Gabbro baseplate, insulated with cotton, sealed with a stainless steel pot and eventually covered with a styrofoam box, as visually documented in Figure 2.19.

After insulation, an effect of long-term temperature variation remains, as shown in Figure 2.20. A time delay of 148.8 h for N-S tilts and 26.4 h for E-W tilts, enhances a linear relation (Fig. 2.20g and 2.20h). The time shifts are based on the maximum cross-correlation functions of about 0.9 for both components. Propagating long-term temperature changes appear to affect both components (N-S = 20 nrad/°C and E-W = 30 nrad/°C; Fig. 2.20), however, both components differntly.

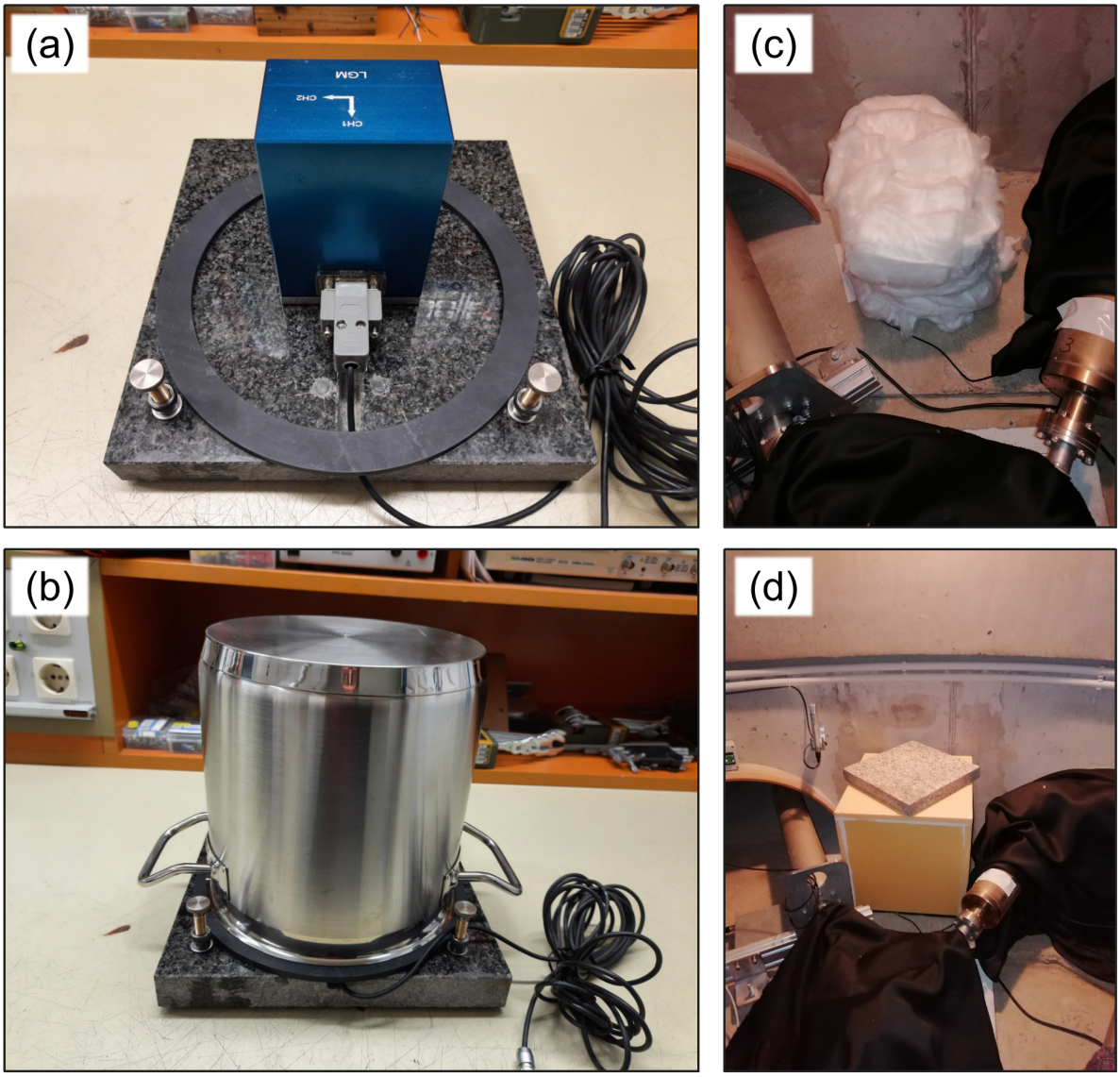

Figure 2.19: Images of the setup of an inertial, 2-K Lippmann tiltmeter. (a) The tiltmeter is mounted onto a 20 mm gabbro plate, (b) wrapped up in absorbent cotton and (c) sealed under a stainless-steel pot. (d) Then it is wrapped up in another layer of absorbent cotton for thermal isolation and covered by a box of styrofoam for more thermal shielding. It is deployed on ROMY's horizontal concrete foundation in the southern access shaft.

With regard to instrumental temperature effects, it is difficult to discriminate between thermal deformation of the local ground below the instrument introducing tilt deformation versus the temperature changes propagating through the insulation and then affecting the tiltmeter housing and electronics. An active stabilization of the shaft temperature to reduce slow, long-term temperature variations would benefit the tiltmeter observations.

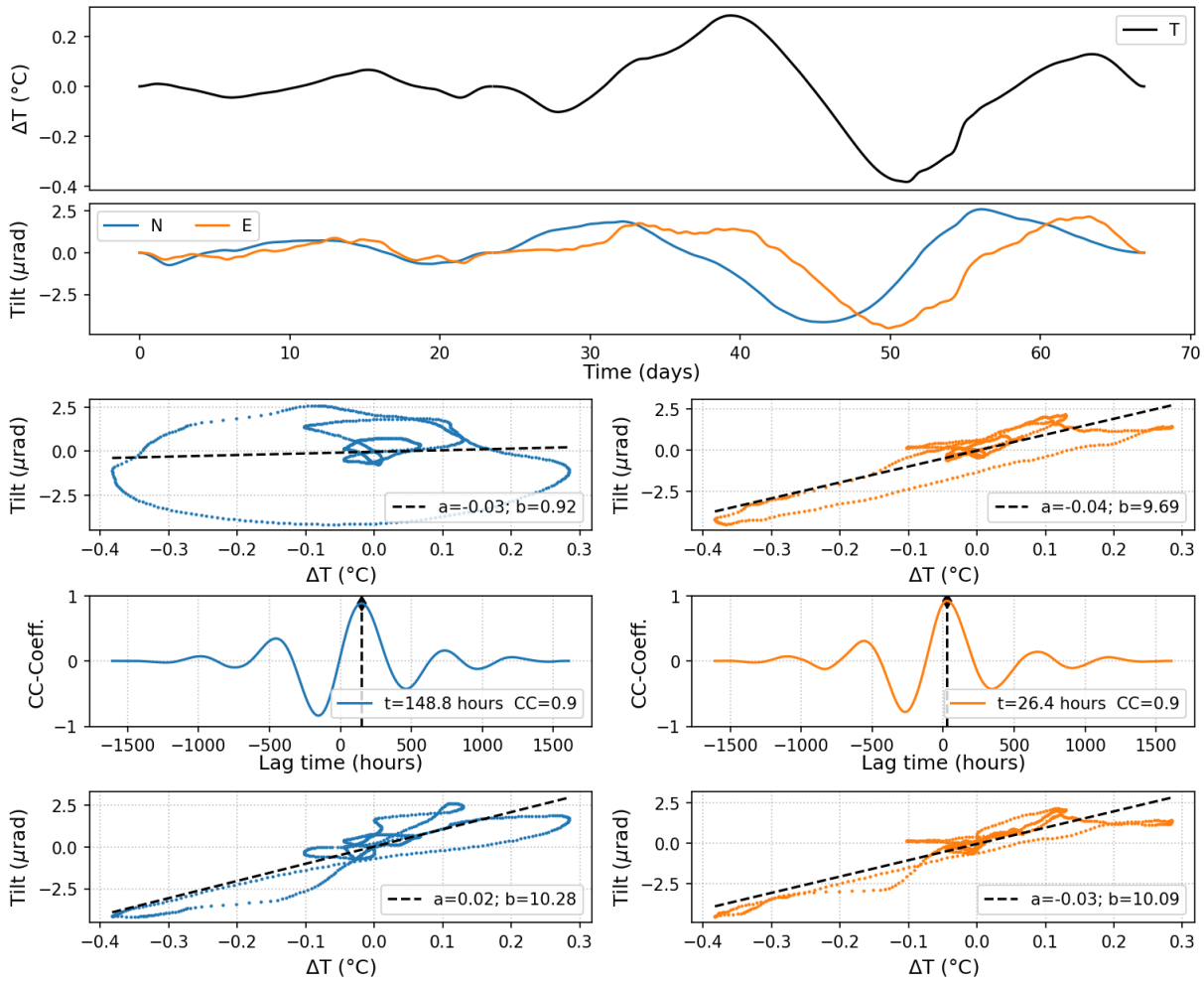

Figure 2.20: Temperature variation of an internal sensor (a) and N-S and E-W tilt (b) records of a Lippmann tiltmeter (BW.ROMYT) are shown for over two months since 2024-03-09. (c) and (d) show scatter plots for tilt versus temperature variation. Cross-correlation functions are computed and maximal cross-correlation coefficients of 0.9 obtained at 148.8 hours time lag for N-S tilt (e) and at 26.4 hours time lag for E-W tilt (f). Scatter plots of tilt versus temperature variation after shifting time series based on time lags are plotted in (g) and (h). Orthogonal distance regressions are shown in (c), (d), (g) and (h) as black, dashed lines with a=slope and b=intercept.

A comparison of tilt records from ROMYT and the nearby, permanent seismometer FUR helps to validate the operation of the tiltmeter (Fig. 2.21). The tilt observations are converted to acceleration by multiplying the gravitational acceleration ($= 9.81\,\mathrm{m\,s^{-2}}$). A high coherence value above 0.8 is obtained for the daily and sub-daily tidal signals sensed by both instruments. For frequencies above 20 mHz, where the tiltmeter is essentially an accelerometer, the coherence is close to 1 (Fig. 2.21d).

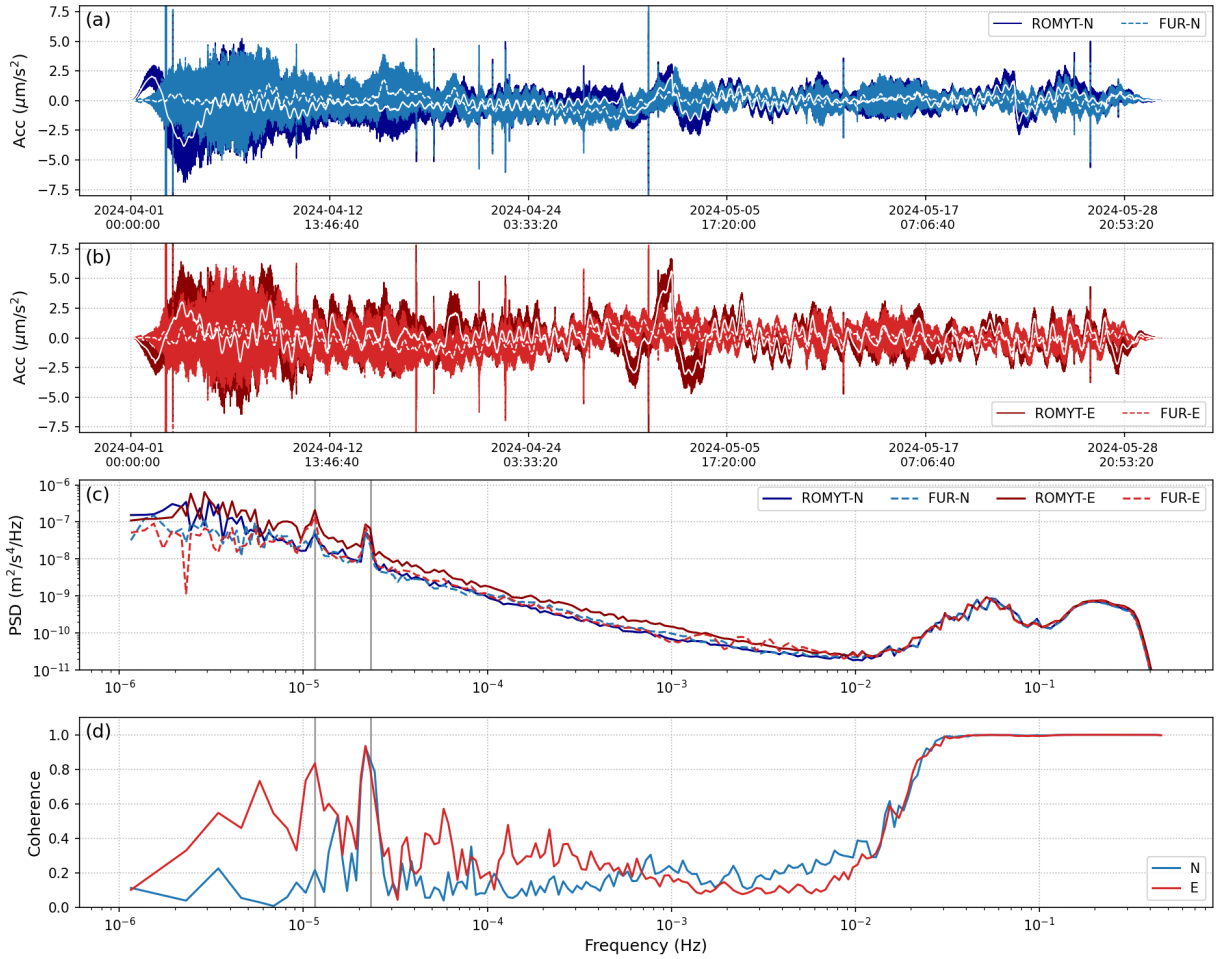

Figure 2.21: Data comparison for ROMYT tiltmeter and FUR seismometer. Tilts are converted to acceleration by multiplying $9.81\,\mathrm{m\,s^{-2}}$. (a) North component data with a moving average applied (white) and without (blue). (b) East component data with a moving average applied (white) and without (red). (c) Power spectral density of data in (a) and (b). (d) Coherence between FUR and ROMYT for north (blue) and east (red) component. Bandpass filter has been applied.

Chapter 3

Instrumental Characterization

For any scientific instrument, a profound understanding of instrumental effects is important in order to identify systematic errors and imposed limitations, which can then be mitigated or corrected. In case of active RLGs, one known source of error is backscatter coupling, which can be corrected for during post-processing when both monobeams are observed (Hurst et al. 2014). Monobeam observations are now included as part of the advanced setup of ROMY (see Sec. 2.1). Other systematic effects have been identified and discussed by (Hurst et al. 2017, Pritsch et al. 2007, Schreiber et al. 2008).

For the heterolithic RLGs of ROMY, the dominant drifts are related to environmental effects that cause scale factor changes by influencing the mechanical stability of the optical resonator. This in turn compromises the operational stability and the data quality. In the first article in this chapter, new methodology to better understand and assess the data quality is presented. A second article, discusses experimental approaches to study the interaction of ROMY's RLGs and its environment. Analyzes of the collected data allows to quantify these environmental influences and propose mitigation strategies in order to benefit a continuous observation of high-quality rotation data.

3.1 Automated Quality Assessment of Interferometric Ring Laser Data

by Andreas Brotzer, Felix Bernauer, Karl Ulrich Schreiber, Joachim Wassermann and Heiner Igel

Published in Sensors (2021), 21, 342
https://doi.org/10.3390/s21103425

Abstract

In seismology, an increased effort to observe all 12 degrees of freedom of seismic ground motion by complementing translational ground motion observations with measurements of strain and rotational motions could be witnessed in recent decades, aiming at an enhanced probing and understanding of Earth and other planetary bodies. The evolution of optical instrumentation, in particular large-scale ring laser installations, such as G-ring and ROMY (ROtational Motion in seismologY), and their geoscientific application have contributed significantly to the emergence of this scientific field.

The currently most advanced, large-scale ring laser array is ROMY, which is unprecedented in scale and design. As a heterolithic structure, ROMY's ring laser components are subject to optical frequency drifts. Such Sagnac interferometers require new considerations and approaches concerning data acquisition, processing and quality assessment, compared to conventional, mechanical instrumentation. We present an automated approach to assess the data quality and the performance of a ring laser, based on characteristics of the interferometric Sagnac signal. The developed scheme is applied to ROMY data to detect compromised operation states and assign quality flags. When ROMY's database becomes publicly accessible, this assessment will be employed to provide a quality control feature for data requests.

3.1.1 Introduction

In seismology, rotational motion observations supplement the conventional observation of translational motions and extend the scope of insight granted by seismic observations (e.g., (Igel et al. 2014, Schmelzbach et al. 2018, Li & van der Baan 2017, Sollberger et al. 2020)). Array derived rotations, based on classical translational seismometer array measurements (e.g., (Huang 2003, Suryanto et al. 2006, Donner et al. 2017)) and recent efforts to derive rotational motions using high-rate GNSS measurements (Xu et al. 2019), were complemented by rotational sensors in the course of the last decades (e.g., (Bernauer, Wassermann & Igel 2012, Bernauer et al. 2018)). Stationary ring laser installations, such as G-ring at the Geodetic Observatory in Wettzell, Germany (operating since 2002) and the four-component ring laser array ROMY at the geophysical observatory in Fürstenfeldbruck, Germany (operating since 2017), represent highly sensitive optical instruments in terms of absolute rotations. Ring lasers are optical interferometers (Schreiber & Wells 2013) and exploit the Sagnac effect (Sagnac 1913, Anderson et al. 1994).

For large ring laser installations with a cavity length exceeding four meters, we distinguish between monolithic and heterolithic structures. While the data quality of monolithic instruments greatly benefits from its inherently high mechanical stability, heterolithic devices are subject to a larger sensor drift, due to a lower mechanical stability. A monolithic design, commonly made of the class ceramic Zerodur, is technically limited in cavity length ($<$16 m). With each ring having a cavity length of about 36 m, ROMY represents a heterolithic structure made of stainless steel and concrete. Hence, in the absence of an active cavity stabilization system, we are dealing with a drift of the optical frequency in the interferometer. Since the free spectral range $FSR = c/P$, with c being the speed of light and P the perimeter, is around 8.6 MHz for ROMY's rings, the frequent changes of the longitudinal mode index of the oscillating laser modes result in two often observed scenarios:

1) a loss of contrast as the currently oscillating dominant laser mode is weakening, while it drifts away from the maximum of the laser gain curve and

2) a sudden change of laser modes, where the two counter-propagating laser beams are not operating on the same longitudinal mode index.

In the second scenario, we lose the interferogram entirely from our detector bandwidth, since the interferogram is biased away from the usually used audio frequency range by multiples of the FSR. In order to evaluate the ring laser output automatically, we need a reliable criterion to evaluate and flag the validity of the detected signal for all components of ROMY in near real-time. Such a data flag does not only exclude erroneous signals from the observation record, it also provides the necessary feedback signal to recover the proper operation state of each ring laser.

This paper is structured as follows. We first review the theoretical foundations of the Sagnac principle as used in ring laser technology. This is followed by a description of the data processing scheme developed for the quality assessment of the raw ring laser signal.

Finally, the scheme is applied to real multicomponent data recorded by the ROMY ring laser, followed by discussion and conclusions.

3.1.2 Fundamental Background on Ring Laser Instruments

3.1.2.1 Sagnac Interferometry

The Sagnac effect describes the effect of rotation on the propagation of light around a closed contour. In the case of an external light source, this effect shows up as a phase shift between the co- and the counter-rotating light beam (Sagnac 1913). If, however, we use laser excitation in a ring resonator, this effect causes a frequency shift, which allows us to observe a beat note δf, when interfering the counter-propagating laser beams (Macek & Davis 1963) (see Figure 3.1C–D). The beat note frequency depends on the scale factor of the Sagnac interferometer, more precisely the ratio of the enclosed area A and the perimeter P of the resonator. δf is strictly proportional to the rate of rotation experienced by the entire apparatus and can be expressed as:

$$\delta f = \frac{4A}{\lambda P}\, \vec{n}\, \vec{\Omega}\ , \tag{3.1}$$

where λ denotes the laser wavelength and $\vec{n}$ the normal vector on the area of the sensor. A ring laser, which is rigidly attached to the solid Earth, thus observes the Earth rotation vector $\vec{\Omega}$ as the primary signal. It is important to note that the Sagnac effect is an effect on the propagation of light, which allows for the observation of the motion of the encapsulating sensor housing (cavity) filled with a low pressure gas mix relative to the two counter-propagating light beams on a closed, reciprocal path (Schreiber & Wells 2013). Some properties of an optical Sagnac interferometer that come along with specific requirements are as follows:

- an entirely linear transfer function up to the Nyquist frequency as long as the sensor does not deform under external forces (e.g., centrifugal forces).
- a well-resolved study of Earth's rotation with merely one large-scale, ground-based sensor as long as the ring cavity is strapped down to the rigid Earth and shows stable long-term performance in terms of the optical frequency as well as the cavity geometry, which poses a great challenge.
- a high-sensitivity observation of seismically induced ground rotation commonly below 10^{-7} rad/s, which are contained in the measurement as perturbations of the rather uniform beat note of Earth rotation (Pancha et al. 2000, Igel et al. 2005). Detecting these signals requires a large and sensitive Sagnac interferometer and the ROMY ring laser array represents such a sensitive device.

Rotational rates are obtained by sophisticated processing with an instantaneous frequency estimation at its core, as outlined by Igel et al. (2021). Rather than evaluating the quality of the rotation rate time series, we present an approach to classify the quality based on the

raw beat note signal and thus infer important information on the instrument's operation state at the same time.

3.1.2.2 Characteristics of a Large-Scale Ring Laser Array

ROMY abbreviates **RO**tational **M**otions in seismolog**Y** and represents the only existing four component large-scale ring laser array, unprecedented in its design and scale (Igel et al. 2021, Gebauer et al. 2020). It was constructed in 2016 at the site of the Geophysical Observatory in Fürstenfeldbruck, Germany. The setup and working principle is schematically shown in Figure 3.1. Each component is realized as an equilateral, triangular ring laser with approximately 12 m side length and arranged to form a downward pointing tetrahedron. The evacuated resonant cavity of each ring is filled with a helium-neon gas mix. Laser functions are established with radio frequency excitation of a plasma at the gain tube (see Figure 3.1B). Three low-loss super mirrors form a closed optical beam path. In order to make the instrument highly sensitive (Schreiber & Wells 2013), the cavity is designed for minimal loss. The fundamental limit of an optical gyroscope is the shot noise of the photon flux on the detector. Since this has the characteristics of white noise, it averages down according to: $1/\sqrt{t}$, with t being the observation time. Practically more important is the Q-factor of the ring laser cavity, which determines the linewidth of the laser radiation and can be quantified by measuring the ringdown time. The ringdown time of a cavity depends on its losses, which vary considerably across ROMY's rings at this point in time. We observe that the horizontal ring is about 1.5 orders of magnitude more sensitive than the worst of the slanted rings (Igel et al. 2021). A possible cause is dust contamination of the bottom mirrors in the slanted cavities, which can thus be remedied in principle.

ROMY has a large heterolithic optical cavity made from stainless steel, referenced to a solid concrete foundation. Temperature variations, mechanical vibrations and ongoing settling of the newly built monument cause a substantial drift of the optical frequency in the cavity. While most of these perturbations are a common mode effect and cancel out in the interference, some of it does not cancel, since the laser process is not entirely reciprocal. Backscatter coupling and a nullshift offset are responsible for variable drift effects in the interferogram, which affect the long-term stability of the sensor. As a result, ROMY does not yet resolve variations of Earth rotation.

In the short-term, however, ROMY performs very well given that the two counter-propagating laser modes are lasing on the same longitudinal mode index. If that is the case, we can typically observe a slow variation of the nominal beat note at the level of 10 ppm over several hours, which is an effect caused by gain medium dispersion and backscatter coupling (Schreiber & Wells 2013, Aronowitz 1971).

A nominal Sagnac frequency characterizes each of ROMY's equilateral triangles being defined by the projection of Earth rotation onto its respective normal vector. A difference of observed and expected nominal Sagnac frequency is caused by a small misalignment towards north and a small inclination to the horizontal (Gebauer et al. 2020). At the

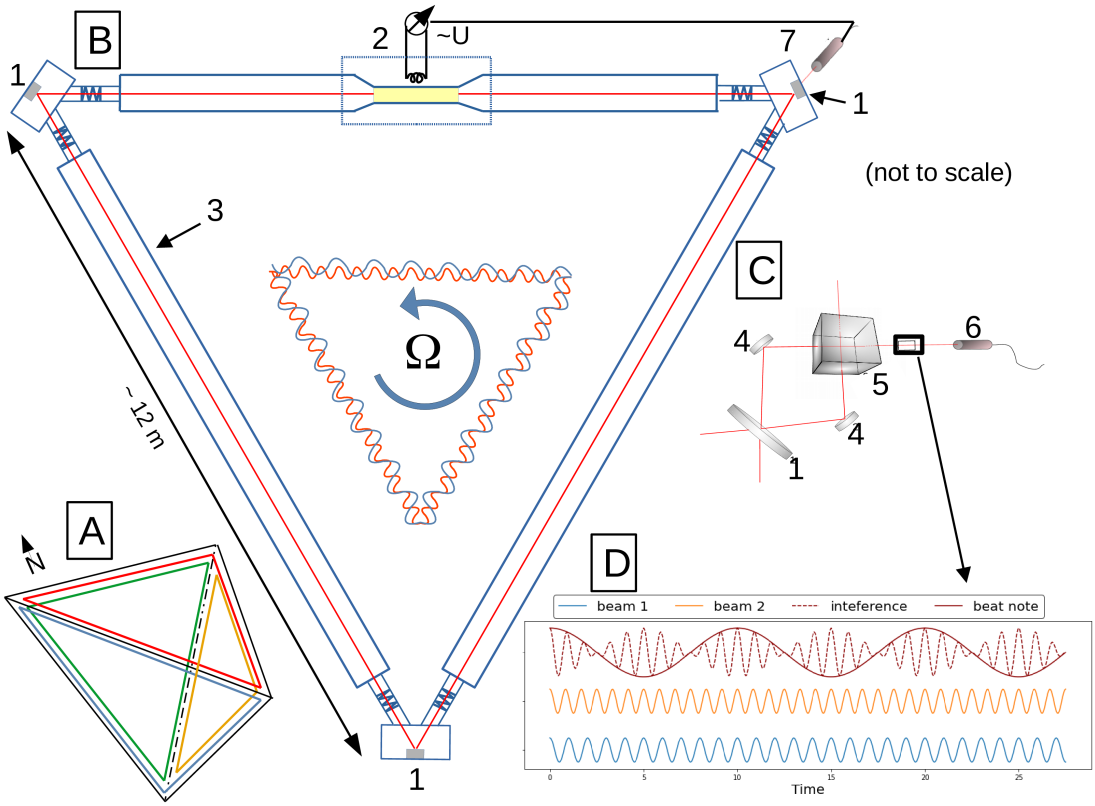

Figure 3.1: (**A**) all four components of ROMY form a downward pointing tetrahedron. (**B**) a schematic cutaway drawing of the design of one of ROMY's components, each realized as an equilateral, triangular ring laser. (1) The triangular lasing path is closed using highly reflective mirrors. (2) gas discharge is sustained inductively with a radio antenna at the narrowed gain tube. (3) evacuated resonant cavity filled with a Helium-Neon mix. An illustration at the center shows the frequency shift between counter-propagating laser beams introduced by rotation Ω according to the Sagnac effect. (**C**) combination of the two beams using two deflection mirrors (4) and a beam combiner (5) is installed at the lower corner of the ring. A photo multiplier (7) records the monobeam intensity used to stabilize the laser intensity via a control loop.(**D**) illustration of the interference (dashed red) of counter-propagating laser beams (blue and orange) with shifted frequencies which create the beat note (solid red) that is recorded by a photo multiplier (6).

moment, all four components achieve a sensor resolution of the order of 10^{-11} rad/s, as shown by the Allan deviation for integration times between 60 and 200 seconds (Igel et al. 2021). A large-scale ring laser as ROMY has the potential to reach a resolution below 10^{-13} rad/s, if the laser cavity was fully stabilized, thus enabling one to routinely observe not only solid Earth tides, but also the Chandler Wobble. Moreover, an array of ring laser is capable to resolve the complete Earth rotation vector due to its four components, as demonstrated for ROMY (Gebauer et al. 2020).

3.1.2.3 Ring Laser Operation in the Presence of Optical Frequency Drift

The laser transition of the helium-neon ring laser is about 1.6 GHz wide and we use an equal mix of ^{20}Ne and ^{22}Ne isotopes to decouple the two beams from each other. Lasing is achieved near the line center, where the gain is at a maximum. We employ gain starvation in order to reduce the number of excited laser modes in the cavity, thereby running the system at very low gain. Intra-cavity mode selection devices are prohibitive, since they would reduce the Q-factor and hence the resolution.

Due to the massive size of the cavity of 36 m, it only takes a cavity variation by one wavelength to cause a frequency drift of about 8.6 MHz, thus a higher mode activation. In the presence of thermal expansion, this would cause rapid transitions of longitudinal modes. This effect is reduced by overpressuring the cavity, causing a suppression of neighboring laser modes over a range of about $\pm$100 MHz by homogeneous line broadening. Longitudinal mode changes nonetheless occur frequently and given the narrow FSR we have the difficulty that both laser beams match in longitudinal mode index after such a mode transition. Although this does not remove the Sagnac effect from the measurement, it pushes the interferogram outside the sampling window of the digitizer and therefore becomes undetectable.

Furthermore, the set of laser modes becomes unstable when it faces such a mode transition, due to mode competition effects. During such a transition phase, the mode contrast is dramatically reduced and as a consequence the interferogram is not stable. In the absence of a perimeter stabilization mechanism, we have to detect and exclude the periods of compromised operation states and the corresponding observations from the data analysis procedure. Moreover, a detection of the presence of different mode indices allows one to recover proper operation by automatically triggering a restart of the lasing process.

3.1.3 Methodology

3.1.3.1 Evaluation Scheme: Quality Measures

The developed evaluation scheme is designed to detect operation states compromised by mode competition effects or the loss of an interferogram due to the presence modes with different longitudinal mode index. On the basis of this scheme, a quality flag is assigned to the individual data sections. In order to judge not only the quality of the seismological important rotation rate but also why and how the signal is distorted, the introduced scheme is based on analysis of the raw sinusoidal signal obtained by Sagnac interferometry. Due to nominal frequencies of up to about 553 Hz (z-component), the beat note signal is sampled at a rate of 5 kHz with 24 bit resolution, which results in a large data volume.

In order to automatically calculate quality measures, 15 min chunks of raw data ($= 4.5 \times 10^6$ samples) are queried and the quality measures, as defined below, are calculated for 2 secs sliding windows with a 50 % overlap. No significant improvement was found for windows below 2 sec. The obtained values on these 2 sec windows are either averaged or

the corresponding extreme values are extracted for 20 secs intervals, which correspond to the sampling rate of the quality measures (= quality samples).

For the assessment of individual data sections, the following signal characteristics or quality measures are determined:

- **Mean value:** calculated mean values ($\mathbf{M}$) of 2 sec windows are averaged for 20 sec intervals. The resulting function relates to an averaged laser intensity level, which is amplified by the photodetector. It is used to monitor automatic restarts of the lasing process and ensure lasing is initiated. Additionally, $\mathbf{d_t M}$ is computed as the absolute of a first-order finite difference of the mean value (M) to enhance the identification of jumps in laser intensity.

- **Frequency estimate:** represents a simple count of zero-crossings over 2 sec windows. The median of the frequency ($\mathbf{f_{sagnac}}$) over 20 secs serves as a quality measure. A deviation of the specific, single-mode nominal frequency of each ring indicates the presence of multiple longitudinal mode indices.

- **Maximal amplitude $\mathbf{A_{max}}$** and **minimal amplitude $\mathbf{A_{min}}$** for each 2 sec window are computed and the median over 20 secs is used to monitor the stability of the maximal peak-to-peak amplitude (A_{pp}) of the Sagnac signal.

- **Signal contrast $\mathbf{\Gamma}$**: is computed according to: $\Gamma = (A_{max} - A_{min})/(A_{max} + A_{min})$ and $\partial_\mathbf{t}\mathbf{\Gamma}$ represents its derivative based on a first-order difference. The contrast ranges from 0 to 1, where a high contrast reflects a high-quality interferogram at low laser intensity, while a low-contrast signal indicates a potential mode transition due to optical frequency drift.

- **$\mathbf{\Delta A_{ext}}$** is computed as the maximal variation of peak-to-peak amplitudes in a sub-window. A_{pp} is calculated for each 2 sec window of data. Across each 20 sec interval, which corresponds to the sampling rate of the quality measures, the maximum and minimum of the set of A_{pp} values is determined. The difference of these maximal and minimal values is stored as ΔA_{ext}. This serves as a measure of the maximal variability of the peak-to-peak amplitude over an interval of 20 secs. This provides a measure to detect variations of the interference signal caused by mode competition effects due to a developing frequency drift.

Figure 3.2 shows three signal cases: 1) desired single-mode, high-contrast signal, 2) intensity increase causing a low contrast and 3) distorted signal due to an appearing second longitudinal mode. For each 2 second bin, the signal characteristics are indicated, excluding the frequency estimate. For illustration purposes, the shown amplitude variations are exaggerated and the nominal frequency is reduced.

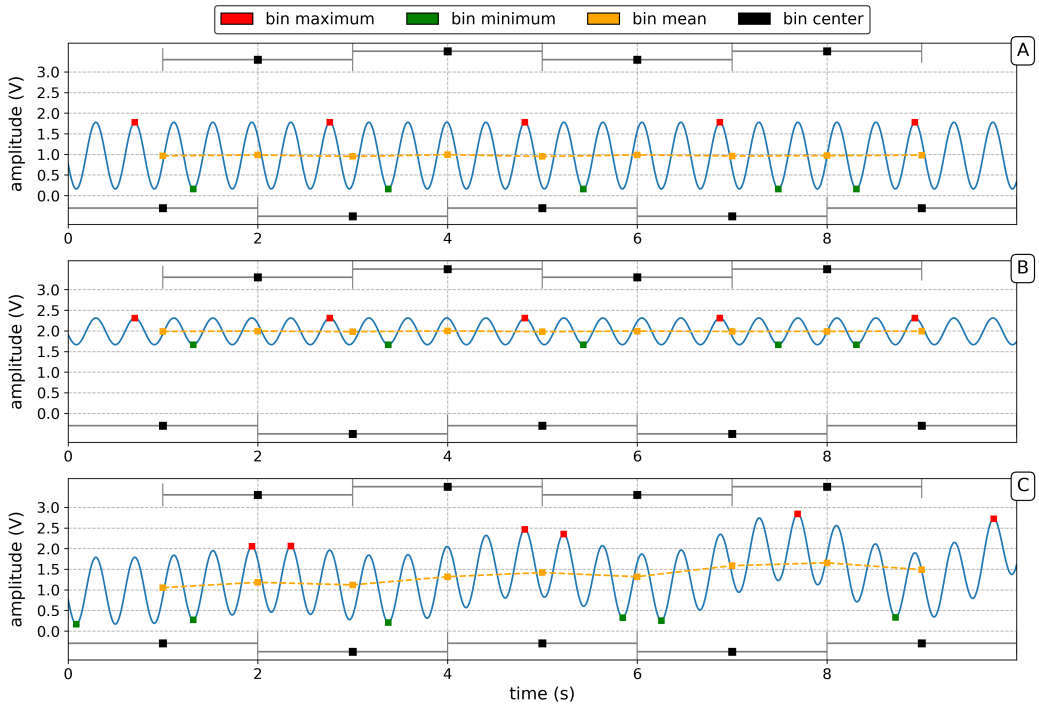

Figure 3.2: Schematic example of the quality measure computation for: (**A**) Single-mode, high-contrast signal; (**B**) A single-mode, low-contrast signal due to mode competition effects; (**C**) An appearing multimode operation state. Shown are synthetic signals for 2 sec windows with exaggerated amplitude variations and reduced frequency for demonstration purposes. Mean (orange), maximal value (red) and minimal value (green) is calculated for each bin as well as an estimate of the frequency based on zero-crossings (not shown). Bins with 50 % overlap are indicated (black).

3.1.3.2 Evaluation Scheme: Thresholds

In order to classify detections of compromised operation states and assign a quality flag for each 20 sec interval, three quality levels are defined:

- **Q0:** good quality data with high contrast (= green).
- **Q1:** medium quality data, allowing fluctuations in the signal contrast (= yellow).
- **Q2:** bad quality data, not suitable to be used for processing and analysis (= red).

The thresholds needed for the assignment of the corresponding quality levels are inferred from an empirical analysis of existing data of ROMY. The most relevant signal characteristic is the nominal frequency of the corresponding ring, which is the projected Earth rotation in single-mode operation. An interval of ± 1.5 Hz (approx. 1.5×10^{-7} rads/s)

centered around the respective nominal frequency ($f_Z = 553.4\,\mathrm{Hz}$, $f_U = 303.0\,\mathrm{Hz}$, $f_V = 447.5\,\mathrm{Hz}$, $f_W = 451.7\,\mathrm{Hz}$) is defined as a quality criterion for the frequency estimate. Compromised operation states cause the nominal frequency to exceed this frequency interval and are not suitable for the calculation of rotation rates, thus assigned Q2 quality. In order to act more robust, an additional criterion is used to also classify single quality samples of Q0 or Q1 surrounded by samples of Q2 as Q2 quality data. This helps one to avoid false assessment due to frequency estimates during operating phases of unstable frequency (Figure 3.3C).

The feedback controlled beam intensity is kept at a low level to facilitate gain starvation of higher lasing modes and corresponds to a voltage between 0.5 V and 1.5 V. For the mean values (M), a minimal threshold of 0.1 V is set to avoid false positives for unpowered rings due to electronic noise randomly meeting Q0 or Q1 criteria. Exceeding an upper threshold of 2 V results in an assignment of Q1, since it significantly reduces the contrast and indicates mode competition effects. Sudden intensity changes are detected by $d_t M$ with a threshold set to 0.02 V/s and often coincide with an automatically triggered reset of the lasing process.

The calculated contrast Γ monitors the sinusoidal amplitude of the beat note signal with respect to the overall intensity. A high and stable contrast is linked to a good interference at single-mode operation. As part of manual maintenance, the contrast is commonly optimized by varying the gain of the photodetectors and therefore no nominal contrast is applicable as a threshold. However, a minimal contrast of 0.08 is inferred, and lower levels are classified as Q2.

Exceeding the threshold defined for ΔA_{ext} by 0.3 V is another criteria that results in an assignment of Q1 quality. This threshold aims at the detection of periods with fluctuations of the peak-to-peak signal, which is related to mode competition effects.

3.1.4 Results and Discussion

For validation purposes, a data selection of November 14, 2019, is shown in panel A and B of Figure 3.3, comprising the raw beat note signal and the obtained rotation rate with distorted sections of high amplitude, respectively. Several examples show the effects of optical frequency drift and their detection. Panels C to H of Figure 3.3 display the corresponding quality measures and the applied thresholds.

Between minute 566 and minute 583 of Figure 3.3, the intensity increases to a level of 3 V to 4 V, decreasing the contrast and causing several quality measures to pass their thresholds. Accordingly, the samples are classified as Q1 and Q2, as shown color-coded in Figure 3.3.

Two examples of an operation on different longitudinal modes, starting at minute 613 and minute 625 (Figure 3.3), respectively, are indicated by a disappearing interference signal (panel A and F) and detected by f_{sagnac}, ΔA_{ext}, Γ and $\partial_t \Gamma$. An interferogram could be restored after a mode competition had been triggered.

When the presence of different longitudinal modes is detected, a control software automatically triggers a restart of the lasing process involving a brief boost of the power ($M \approx 5$ V) at the gain tube of the cavity, resulting in the excitation of several lasing modes. The natural mode selections controlled by the characteristic gain curve of the resonator eliminates higher modes, thus ideally achieving a single-mode operation. Several successful, automatically triggered restarts can be seen in Figure 3.3 ($t = 616\,\text{min}, 625\,\text{min}, 656\,\text{min}$). If re-establishing a single-mode operation is not successful, a manual maintenance is necessary. Depending on the situation, this can result in a longer downtime for the acquisition of good quality data.

This sort of maintenance often includes a realignment of the lasing path and realignment of the radio frequency excitation, which varies the laser intensity. A detection of lost Sagnac interference is shown in Figure 3.3 at around $t = 616$ min. If the difference ΔA_{ext} exceeds a value of 0.3 V, Q1 quality is assigned. An example is provided in Figure 3.3 at t = 597 min, where fluctuations of the interferometric signal are detected based on this criterion. Figure 3.3 also shows that several measures are required to work together to avoid wrong classification or false positives.

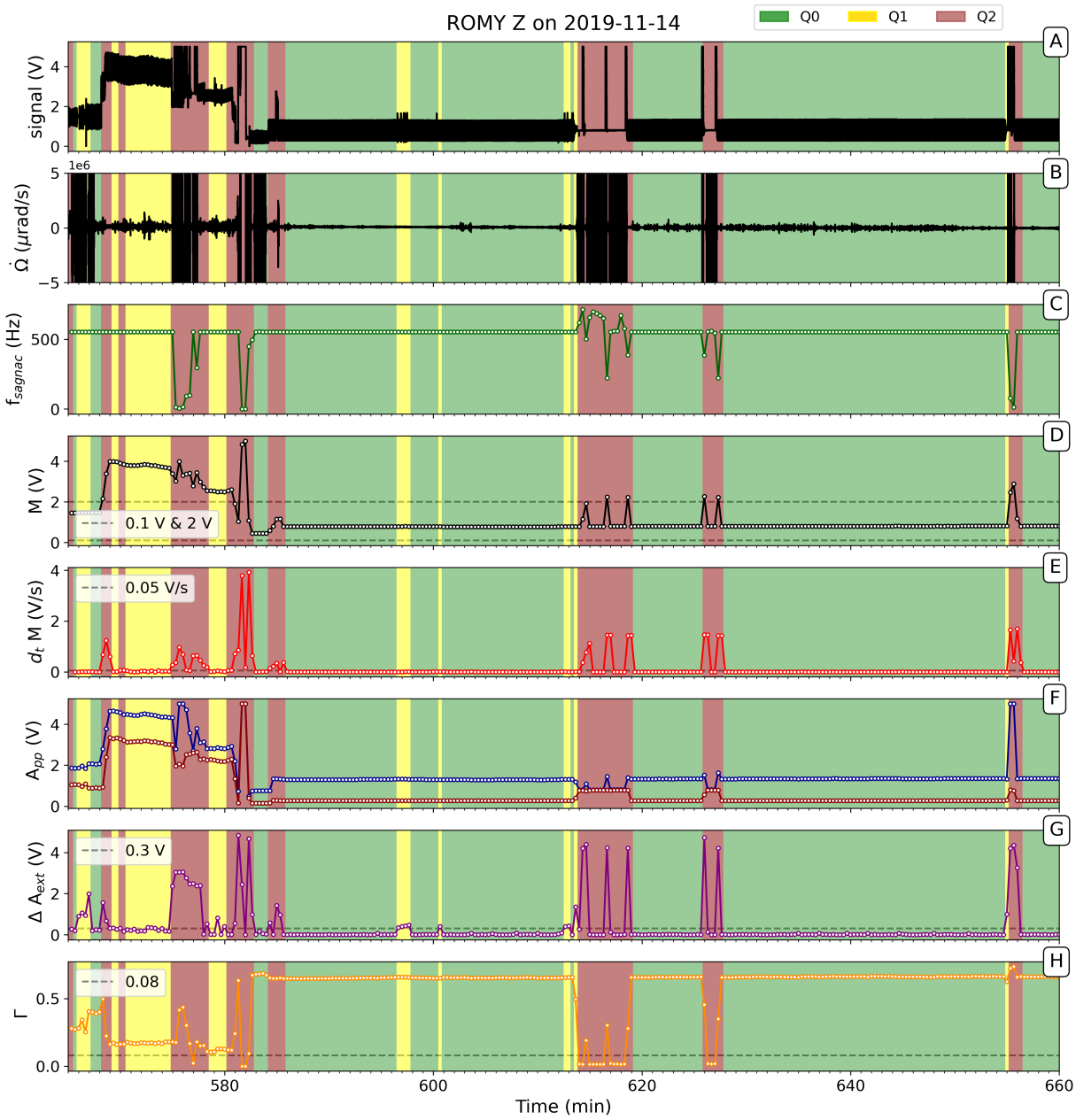

Figure 3.3: Selected data section of ROMY's z-component on 2019-11-14. (**A**) Raw beat note signal; (**B**) Obtained rotation rate $\dot{\Omega}$ (clipped at $\pm 5\,\mu$rad/s); (**C**) Estimated Sagnac frequency; (**D**) Mean values M; (**E**) first-order finite-difference of M; (**F**) Median of maximal and minimal amplitudes A_{pp}; (**G**) Maximal variance of peak-to-peak amplitudes ΔA_{ext}; (**H**) Calculated contrast value Γ. Quality evaluation thresholds are indicated as gray, dashed lines. The background colors correspond to the classified quality level.

Furthermore, the scheme was applied to data of all four components of ROMY for November 2019. During this period an active field experiment was conducted at the site of the observatory, for which ROMY served as a reference station and all four rings were operating. Panels A–D of Figure 3.4 display the daily share of all quality levels across November 2019 for each of ROMY's four components Z, U, V and W, respectively. Apart from a data gap on November 27 and maintenance work between November 11 and November 14, the z-component demonstrates the best performance in terms of percentage and continuity of Q0 data. Here, the slanted rings confirm an increased vulnerability to optical frequency drift effects and underline a currently missing long-term stability. Overall, Q1 quality accounts for only a small share.

The median frequency estimates shown in Figure 3.4, based on Q0 and Q1 data only, remains stable within a tolerance of 0.25 Hz, while the frequency offset for the z-component is related to maintenance work. The corresponding contrast for the z-component included in Figure 3.6A, being on an overall low level ($\approx$ 0.2), shows a further decrease before maintenance was required due to drift effects that could not be automatically recovered.

Figure 3.6 shows the evaluated data of ROMY's z-component for the entire month of November 2019 not only by daily shares but also resolved temporarily across daily hours. Such a temporal visualization demonstrates the distribution of data sections with compromised operation states and subsequently the potential of a selection of a time series with good quality only. While several failures interrupt a stable performance of the instrument at the beginning of November, a continuous record of Q0 data is significantly improved for the second half of November.

An application of the scheme for six hours of ROMY's w-component are shown in Figure 3.5, where rotation rates are shown with the quality levels as the background. Four occurrences of mode competition effects are detected (Q1), with the last resulting in an operation state where multiple longitudinal modes with different mode index are present (Q2). Additionally, rotation rates of a regional event in Albania on November 28, 2019, at 10:52:43 UTC with a magnitude of 4.7 are shown in the record.

The presented scheme will help to provide quality measures for ring laser data of ROMY and possible other instruments, when the database becomes publicly available. It is planned to run a service similar to the FDSN web service "waveform catalog" (Trani et al. 2017), which consists of a database with corresponding quality measures entries. The remote user will then be able to select only those data which meet predefined quality criteria. This could either be data without any gaps or data with Q0 quality only.

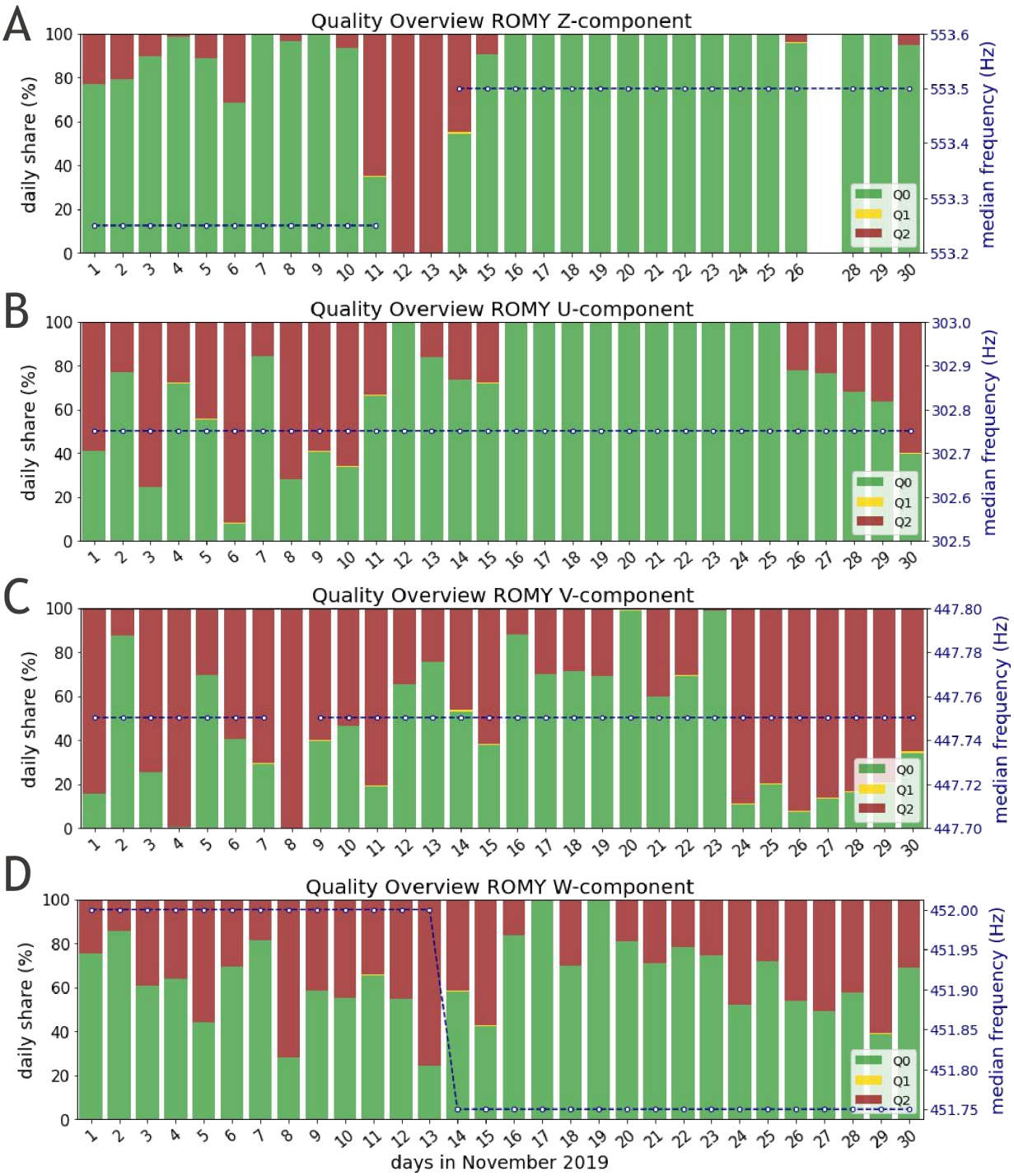

Figure 3.4: Quality assessment applied to all four components of ROMY (A-D) for November 2019. Quality measures are computed for 20 second intervals. Daily shares shown in green, yellow and red resemble the qualities Q0, Q1 and Q2, respectively. The daily median of frequency estimates, based on Q0 and Q1 data only, is plotted on a second y-axis (blue) for each component (A-D), respectively. No data is available for the z-component on November 27, 2019.

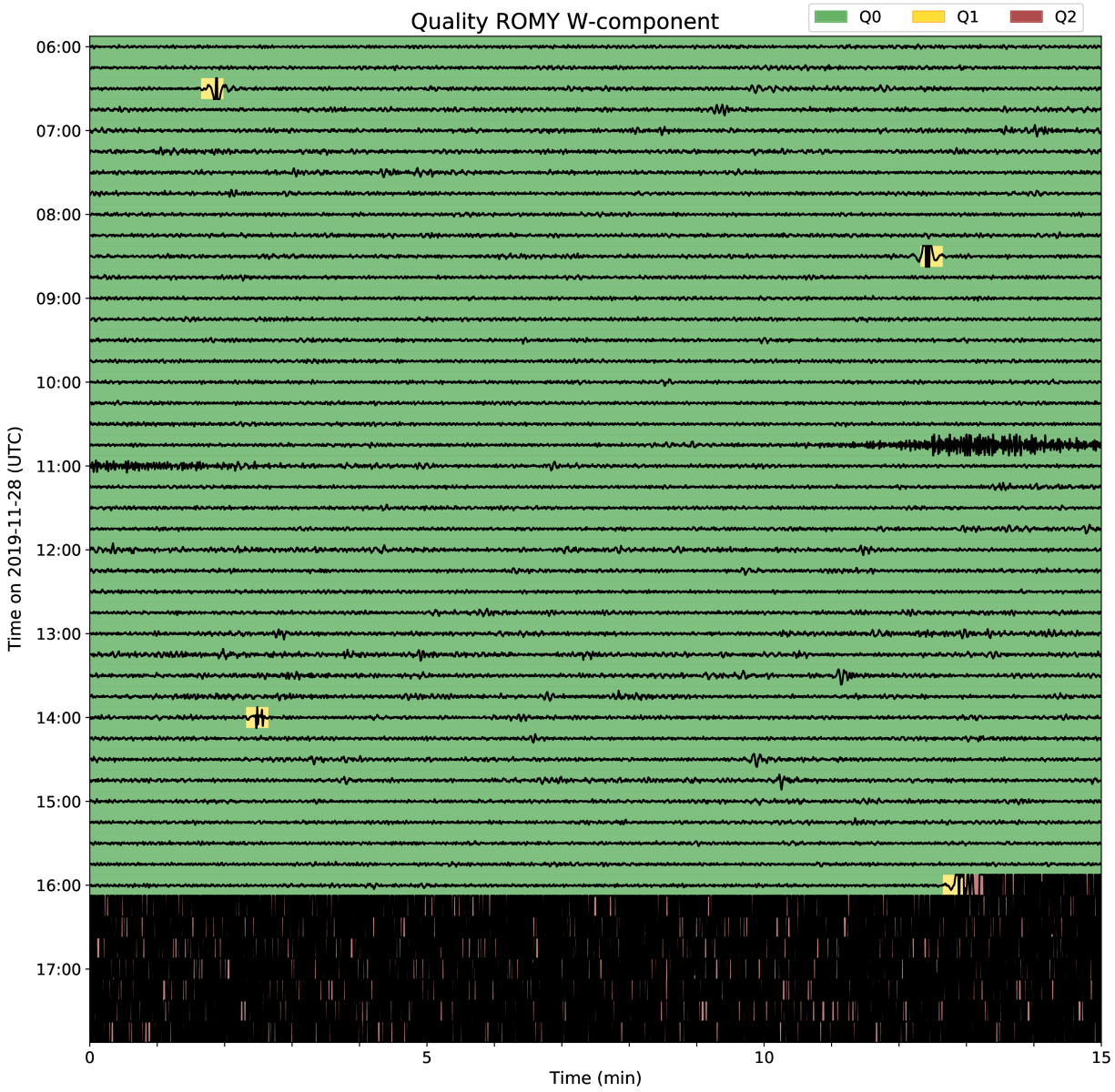

Figure 3.5: Six hours of data of ROMY's w-component on November 28, 2019, are shown, including a regional event in Albania ($M_w = 4.7$) at 10:52:43 UTC. The rotation rate record is mean corrected, bandpass filtered (0.1 Hz to 1.0 Hz) and clipped. Background colors indicate assigned quality levels for 20 sec intervals.

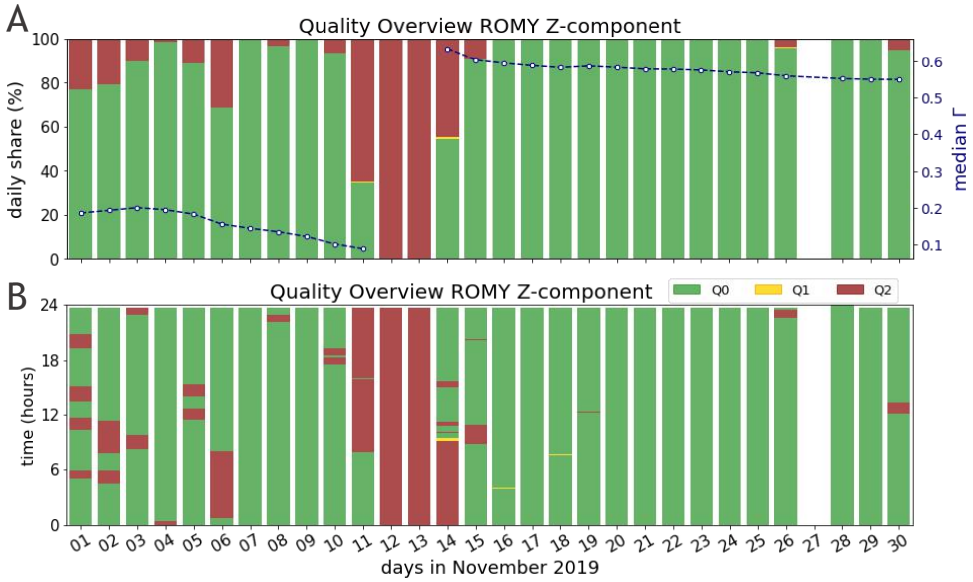

Figure 3.6: Data of ROMY's z-component for November 2019 is shown in (**A**) as daily shares and in (**B**) across daily hours, in order to visualize the temporal quality distribution. No data is available for the z-component on November 27, 2019. The data is evaluated for 20 second based on 2 second windows and color code according to three quality levels Q0 (good), Q1 (medium) and Q2 (bad). (**A**) additionally shows the daily median of the contrast Γ computed by using Q0 and Q1 data only.

3.1.5 Conclusions

Realized as a heterolithic structure, ROMY's four ring lasers experience an optical frequency drift as a consequence of mechanical instability of the resonant cavities. The large scale factor provides ROMY with unprecedented sensitivity to absolute rotations, however, at the same time reduces the free spectral range and facilitate longitudinal mode transitions and an operation of counter-propagating beams with different longitudinal mode index, both compromising a stable Sagnac beat note.

An automated quality evaluation scheme for ring laser data has been developed, using the recorded raw Sagnac beat note signal to infer quality measures and classify the record into three quality levels. Using the raw interferometric signal allows to gain important information on the sensor's current performance and health state. For this purpose, several quality measures, which jointly characterize the interferometric Sagnac signal, are computed. Empirically defined thresholds for these quality measures are applied to assign quality levels. The automated evaluation scheme is applied for data of November 2019 for all four components of the large-scale ring laser ROMY. This reveals multiple detection of mode transitions and amplitude fluctuations due to mode competition effects, as well as compromised operation states due to counter-propagating beams with different longitudinal mode index, in an automated way. The scheme will be employed to provide the remote

user with an opportunity to request data according to quality levels as soon as the ROMY database becomes publicly available.

Data and Resources

Second level data presented in this study are openly available in a publicly accessible repository: https://syncandshare.lrz.de/getlink/fi72mpaCFH1XbPnMwoDYarzY/.
Raw data of ROMY are not yet publicly accessible due to the large amount of data, but available on request from the corresponding author.

Acknowledgements

We thank Jens Oeser and his team for the support of the IT infrastructure and Sven Egdorf and Jürgen Loos for their technical support.

3.2 On environment-related instrumental effects of a multi-component, heterolithic ring laser array

by Andreas Brotzer, Heiner Igel, Felix Bernauer, Joachim Wassermann, Jannik Zenner, Simon Stellmer, Jan Kodet and Karl Ulrich Schreiber

Submitted to Review of Scientific Instruments (2024)

Abstract

Large-scale ring laser gyroscopes (RLGs) are essential scientific instruments to study a variety of geophysical and geodetic phenomena. The first and so far only large-scale RLG array ROMY (ROtational Motions in seismologY) comprises four triangular, heterolithic, active RLGs and can provide high-quality, three-component rotational ground motion observations. Compared to other RLGs, often being located in underground laboratories, ROMY is a near-surface sensor that is more exposed to environmental influences. Understanding and quantifying the instrumental effects caused by its environment is essential to enhance a continuous operation of ROMY. External forces are known to deform a heterolithic optical ring resonator, which resembles an instrumental drift due to an alteration of the scale factor. A new sensor network inside ROMY monitors key environmental parameters such as barometric pressure and temperature. In order to quantify deformation of the resonator, we use camera-based beam tracking and free spectral range measurements. Applying a correction for backscatter-induced errors, we achieve a reduction of Sagnac frequency fluctuations of several millihertz. We discuss the current operational stability of ROMY, recent upgrades, such as a passive thermal insulation and correlate observed instrumental drifts with environmental drivers. Using a linear, multi-variant modelling approach, we can identify dominant drivers and reduce long-term drift of the Sagnac frequency. A deeper understanding of environment-induced instrumental effects allows to develop strategies for a further improvement in operational stability.

3.2.1 Introduction

Large-scale ring laser gyros (RLGs) with perimeters of several meters were originally developed to observe Earth's rotation and its variations with high precision at our planet's surface, potentially complementing the tremendously more involved measurements using VLBI (Very Long Baseline Interferometry). The sensitivity of RLGs rests predominantly on the dimension of the encircled area and in particular on its stability during operation. Therefore, a monolithic realization with thermally stable material supporting the RLG structure was chosen for the single-component, so-called G-ring, installed at the Geodetic Observatory Wettzell, Germany, in 2002 (Schreiber et al. 2009, Schreiber & Wells 2023b). The G-ring observes rotational motions around a locally vertical axis, thus the latitude-dependent contribution of Earth's rotation and any local perturbation thereof. This concept has led to the successful observation of polar motion (Schreiber et al. 2004) and length-of-day variations (Schreiber et al. 2023a).

However, to observe the full vector of rotation, an array of at least three RLGs is required. Such an RLG array was realized at the Geophysical Observatory Fürstenfeldbruck, Germany, with the so-called ROMY (ROtational Motions in seismologY) ring laser array in 2016 (Gebauer et al. 2020, Igel et al. 2021) combining four triangular ring lasers in an overall tetrahedral shape with side lengths of 12 m. Given the dimensions, the location and financial constraints, ROMY is based on a heterolithic design, embedding the optical ring resonators within a near-surface, concrete structure. As a potential design of highly-sensitive, multi-component RLGs for geoscientific applications, the design-related susceptibilities to environmental influences were explicitly intended to be the subject of detailed scientific investigation.

These applications not only include the monitoring of the complete vector of Earth's rotation, polar motion, and length-of-day variations, but also local perturbations as generated by the omnipresent seismic wavefield, that - in addition to the classic three translational components - also has three components of ground rotations. RLG observations of such rotational ground motions have contributed substantially to the emergence of the new field of rotational seismology (e.g., Schmelzbach et al. 2018, Sollberger et al. 2020). It is important to note that the sensitivity of portable rotation sensors for seismic field deployments, currently, are orders of magnitude above that of RLGs (e.g., Bernauer et al. 2018, Jaroszewicz et al. 2016, Brotzer et al. 2023).

The heterolithic realization of ROMY (Igel et al. 2021) naturally poses challenges with regard to the mechanical stability of the resonators. In addition to internal processes, such as backscatter errors (Hurst et al. 2014), there are external drivers, such as ambient temperature or barometric pressure, that cause instrumental effects on the RLG by altering the scale factor (e.g., Schreiber & Wells 2023b, Belfi et al. 2012, Hurst et al. 2009). Since ROMY is built close to the surface, it is particularly exposed to environmental influences. Harnessing ROMY's potential for observations of geodetic processes, the requirements for mechanical stability to reduce the changes in the scale factor are even higher.

In order to enhance the operation stability for continuous data acquisition, to benefit further geophysical studies, these effects have to be understood. Identifying key drivers requires multi-parameter observations of environmental phenomena. This allows us to develop further strategies to reduce such instrumental effects by stabilizing each optical ring resonator and/or develop models to correct for them during post-processing to enhance the data quality.

To further illustrate the problems related to ring laser operations, we will briefly introduce their basic properties as well as the potential for instrumental errors, followed by an introduction to special features and the environment of the ROMY ring laser array.

3.2.1.1 Sagnac Interferometry and Instrumental Effects

Active (commonly filled with a helium-neon gas medium) or passive, large-scale resonators are optical interferometers in a Sagnac configuration, providing access to Earth's spin and variations therein (e.g. Schreiber et al. 2023a), as well as local rotational ground motions as caused for instance by passing seismic waves of earthquakes (e.g. McLeod et al. 1998, Igel et al. 2005). The Sagnac beat frequency δf (hereafter only Sagnac frequency) for an RLG is given by:

$$\delta f \;=\; \frac{4\,A}{\lambda\,P}\,\vec{n}\,\vec{\Omega}\;, \tag{3.2}$$

P being the perimeter, A the encircled area and λ the optical wavelength (=632.8 nm). The rotation rate Ω is a superposition of the Earth's spin rate Ω_E and a local rotation rate Ω_L.

$$\delta f \;=\; \frac{4\,A}{\lambda\,P}\,(|\vec{\Omega}_E| + |\vec{\Omega}_L|)\;sin(\varphi+\theta) \;=\; S\;(|\vec{\Omega}_E| + |\vec{\Omega}_L|)\;, \tag{3.3}$$

with φ as the local latitude, S the scale factor and θ as local tilt in N-S direction. In case of an equilateral triangular-shaped resonator, the scale factor can be expressed as:

$$S \;=\; \frac{\sqrt{3}\,L}{3\,\lambda}\;sin(\varphi+\theta)\;, \tag{3.4}$$

with L as the side length ($P = 3L$). The sensitivity of a ring laser gyroscope (also referred to as ring laser or merely ring) is controlled by the scale factor S (Eq. (3.4)). The dominant wavelength for active helium-neon lasers at λ= 632.8 nm is exposed to variations due to internal lasing dynamics (e.g., Hurst et al. 2017, Schreiber & Wells 2023b) and is utilized, where applicable, in this study.

Other defining quantities of the scale factor are geometrical variations of the optical ring resonator affecting the side length (or perimeter) and/or the areal vector's orientation. A more rigid ring resonator therefore reduces instrumental effects caused by geometrical deformation. A monolithic design, as realized for the square 4×4 meter G-ring (Schreiber et al. 2009), is not feasible for larger RLGs, which rely on a heterolithic design at the cost of less mechanical rigidity. Hurst et al. (2017) investigated subtle instrumental effects on the scale factor for the ultra stable monolithic G-ring. In particular, the internal effects

discussed by Hurst et al. (2017) are certainly present in ROMY's rings, but are of minor importance in this study, since external forces on the resonator's geometry are dominant on the scale factor.

3.2.1.2 Structural and Environmental Aspects of ROMY

ROMY is a multi-component large-scale ring laser array, intended to provide high-sensitivity observations of rotational ground motions for geophysics and geodesy (Gebauer et al. 2020, Igel et al. 2021), located at the Geophysical Observatory in Fürstenfeldbruck, Germany. The four individual, triangular-shaped RLGs are arranged in a downward pointing tetrahedral concrete structure (Fig. 3.7c). This includes one horizontally oriented RLG (RZ; Fig. 3.7a) and three slanted RLGs (RU, RV, RW). Operating at least three RLGs simultaneously allows reconstructing all three components of rotational ground motion (Igel et al. 2021, Gebauer et al. 2020). While the horizontal RLG is located at a depth of about 2.5 m below the surface, the tetrahedral tip is at a depth of about 14 m below the surface. Maintenance access is provided by seven individual access shafts from the surface (Fig. 3.7c). The three corner mirrors of the optical ring resonators are housed in stainless steel corner boxes, which are mechanically decoupled from the connecting pipes of the triangular ring resonator via stainless steel bellows (Fig. 3.7b). At each corner of the tetrahedron, three corner boxes are mounted on a common solid concrete foundation (Igel et al. 2021), as illustrated in Figure 3.7b.

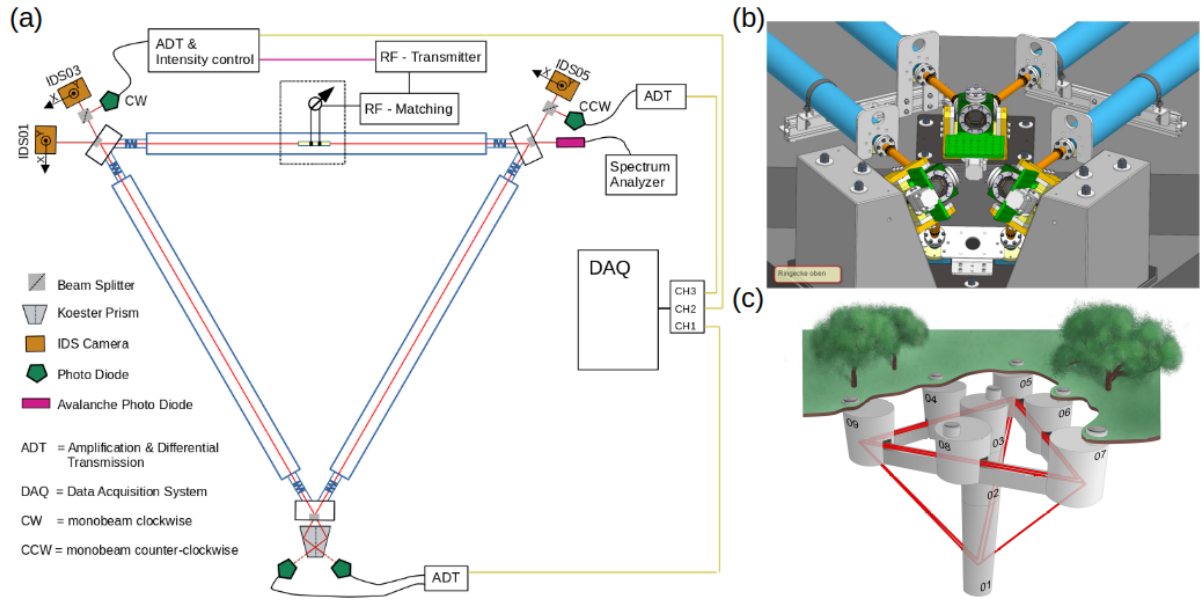

Figure 3.7: a) Schematic experimental setup for FSR measurement at RZ. (b) 3D model of a corners with three mirror boxes as found in shafts 05, 07 and 09. (c) Near-surface ROMY structure with access shafts. All sketches are not to scale.

Every scientific instrument is influenced by ambient environmental factors, which have to be understood and quantified. These perturbations must be mitigated by either shielding or applying appropriate corrections. Generally, the effects of ambient temperature and barometric pressure on optical resonators have been observed for other RLGs, particularly those of heterolithic design (e.g., Schreiber & Wells 2023b, Basti et al. 2021). In contrast to other RLGs located underground in the Cashmere caves (e.g., Schreiber & Wells 2023b), Gran Sasso Laboratory (Belfi et al. 2017) or a vault at the observatory Wettzell (Schreiber et al. 2009), ROMY is located near the surface (Igel et al. 2021).

A sensor network to monitor environmental factors was installed at ROMY in 2021. This network comprises sensors for air temperature, air pressure and humidity inside each of ROMY's seven access shafts (one central shaft and six upper shafts; see Fig. 3.7c). A weather station (BW.FURT) next to ROMY provides observations for precipitation, surface air temperature and barometric pressure and serves as an external reference. A two-component inertial tiltmeter (BW.ROMYT) is installed inside ROMY's southern shaft on the concrete monument, providing observations of local tilt deformation. A barometer station (BW.FFBI) provides infrasound and absolute air pressure observations. A groundwater gauge on the site of the Geophysical Observatory (approx. 400 m from ROMY) provides a reference for variations in near-surface hydrology. A set of video cameras monitors the beam walk at individual corners, which serves as proxy for deformation at the resonator corners, influencing the RLG's scale factor. We use these data to quantify and relate variations in the Sagnac frequency as well as beam walk to environmental changes, such as temperature and pressure. Here, we have to separate two effects that have an impact on the change in the scale factor. On the one hand, the common foundation of the corners in the shafts experiences deformation and, on the other hand, the stainless-steel corner boxes and their alignment controls are deformed directly. Deformation of the controls acts via a lever and is expected to be the dominant source of deformation. However, it is extremely difficult to observe these effects separately. Geometric deformation, such as displacement or tilting, at the corners alters the perimeter of the optical resonator, thus the scale factor (Eq. (3.4)). But also orientation changes are induced by forcing the beam plane, defined by reflection points on the three corner mirrors, to re-align to form a closed path.

In the following sections, we will first present insights to the current operational performance and stability of ROMY. Observations of long-term drifts are intended to introduce the existing dynamics with regard to the Sagnac frequency. This is followed by results of the backscatter correction applied to the Sagnac frequency of the large heterolithic rings of ROMY. We then present observations of deformation using a beam walk monitoring system and free spectral range measurements. Instrumental effects caused by deformation are discussed and related to the observations of the environmental factors (e.g. temperature or pressure) for case studies. In a last step, we attempt to bring these correlations together using a linear multi-variant modelling approach.

3.2.2 Operational Performance Analysis

For an active RLG, a mode jump is defined as a transition to another longitudinal lasing mode for both directions of propagation. A mode jump can be triggered by changes in the length of the ring resonator's perimeter or by changes in the refractive index of the gas medium (e.g. by increasing the plasma excitation power). When this occurs for both counter-propagating beams simultaneously, a mode jump causes a shift of the Sagnac frequency. However, it does not cause a break-down of the interferogram within the passband of the detector, usually referred to as split-mode operation, and therefore does not require recovery. The absence of the interferogram is detected by an automatic control software, which launches a recovery procedure, referred to as MLTI (MuLtimode TrIgger), by interrupting the intensity stabilization to enable a mode competition regime before returning to the intensity controlled operation state. MLTI launches can occur every 30 sec. When successful, this restores a single-mode or a stable multimode (phase-locked) operation state.

Triggered MLTI launches are logged and used to compute MLTI sequences by merging MLTI launches which are separated by less than 60 sec. After an MLTI sequence, the split-mode operation state is considered successfully resolved. A cumulative percentage count of MLTI sequences in the observational period between 2024-03-09 and 2024-07-31 is shown in Figure 3.8a. Times of conducted maintenance work are automatically logged using light sensors inside the access shafts and generally indicated hereafter by yellow, vertical bars (e.g., Fig. 3.8a).

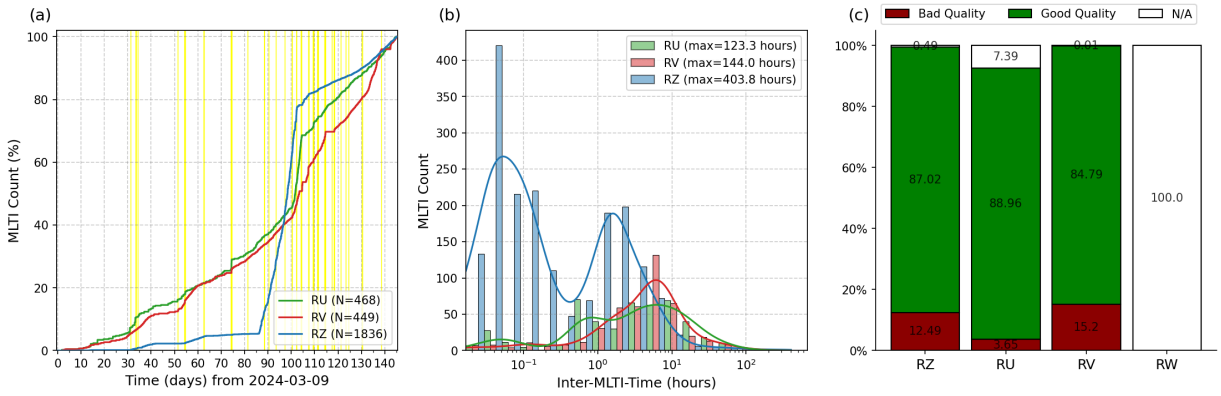

Figure 3.8: Each MLTI launch required to resolve a detected split-mode operation state is logged. Statistics for rings RZ (blue), RU (green) and RV (red) between 2024-03-09 and 2024-07-31 are shown. (a) Cumulative percentage count of MLTI sequences. Yellow bars indicate time periods of maintenance work. (b) Histogram and distribution of Inter-MLTI-Time (= elapsed time between MLTI sequences). (c) Uptime classified by good (green) and bad (red) quality and downtime (white) in percentage.

A sudden increase in MLTI occurrences is often visible after performed maintenance work related to thermal perturbations. We use the elapsed time between MLTI sequences, called

Inter-MLTI-Time, to describe and quantify the operational stability of the individual rings.

The absolute count of MLTI sequences for RZ amounts to 1821 for this observational period caused by a poorly configured, thus unstable multimode operation state between day 86 and day 102 (see Fig. 3.8a). RU and RV reveal a similar count of 464 and 443, respectively. A distribution of Inter-MLTI-Times for RZ shows two pronounced peaks, the first peak at below one hour is attributed to the mentioned period between day 86 and day 102. The second specifies the characteristic time between 1 and 2 hours. Based on the Inter-MLTI-Time distribution for RU and RV, their average characteristic time between split-mode operation states is around 6 hours (Fig. 3.8b).

The uptime statistic in Figure 3.8, being classified as good and bad quality data and non-operation (downtime), is based on a modified approach presented in Brotzer et al. (2021) and yields comparable uptimes of around 85% for all three operated RLGs (Fig. 3.8c) between 2024-03-09 and 2024-07-31. Continuous, good quality data on three RLGs is essential to obtain three component rotational ground motions. For the presented example, this comes down to merely 66.2 % simultaneously good data quality. Vertical rotation is observed independently by the horizontal ring RZ. However, for a continuous and stable operation with good quality data, the MLTI count generally has to be minimized and the Inter-MLTI-Time maximized.

The following section examines the variation in the Sagnac frequency of multiple rings over several months, revealing that this operational instability is reflected in drifts on various scales, data gaps, and frequency shifts.

3.2.3 Long-term Sagnac Frequency Drift

Three of ROMY's RLGs have been successfully operated for an extended period from October 2023 up to July 2024. The observed frequency drift of the Sagnac beat frequency, as well as frequently occurring mode jumps, is mostly a result of a non-stabilized heterolithic ring resonator. Within this observational period, intervals of varying duration of non-operation for one or multiple RLGs are identifiable, caused by different instrumental effects. A crucial condition for operating an RLG is a closed optical beam path inside the ring resonator. Geometric misalignment of a ring resonator prevents lasing and requires manual re-alignment efforts. A mechanically more rigid RLG, such as the monolithic G-ring (Schreiber et al. 2009), is less susceptible to deformation and frequent misalignment.

Figure 3.9 shows time series of the estimated Sagnac frequency of ROMY's horizontal (RZ), western (RV) and northern (RU) RLG from January to July 2024, where intervals of non-operation and MLTI sequences are excluded. Data gaps in the time series generally follow misalignment or maintenance work. The subsequent offsets in Sagnac frequency are explained by a modified geometry of the ring resonator, hence an altered scale factor and areal vector orientation, as a result of the manual re-alignment (see Fig. S.6). We attribute the significantly greater dynamic in short-term frequency drift of RU to a lower quality,

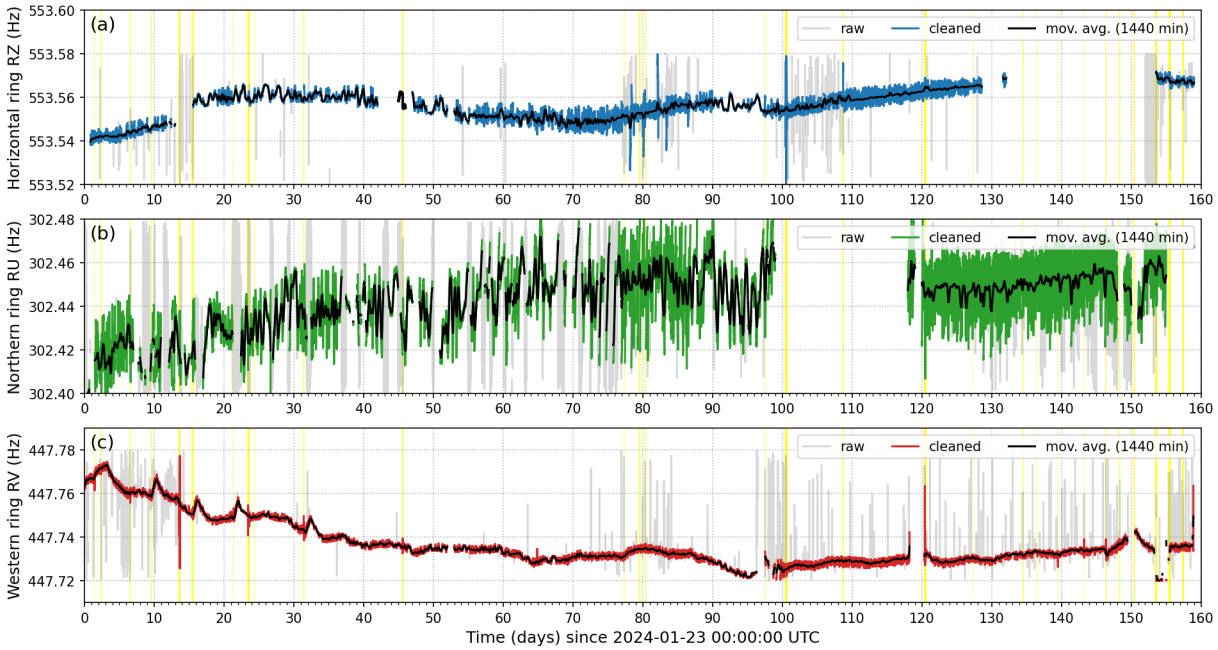

Figure 3.9: Long-term drifts of Sagnac frequency over several months of (a) RZ, (b) RU and (c) RV are shown. Colored traces are cleaned by removing times of logged MLTI launches (gray). The low-frequency drift is represented by applying a moving average (black) of 12 hours (720 min). Yellow bars indicate time intervals of maintenance work.

natural neon gas mix, while RZ and RV are operated with a 50:50 mix of Ne^{20} and Ne^{22} isotopes.

A moving average is computed for 12 h windows to better capture the long-term drift. For this observational period, the maximum drift range for RZ, RU and RV is about 30 mHz, 40 mHz and 50 mHz, respectively. Attributing a Sagnac frequency change of 10 mHz to pure length change ΔL (Eq. (3.4)), would correspond to an elongation of about 202 μm. An orientation change of the beam plane in north-south direction θ (Eq. (3.4)) of 0.1 mrad, would cause a frequency drift of 49.4 mHz.

These long-term drifts integrate all instrumental effects and emphasize the existing dynamic range. For seismological observations, long-term drifts are negligible, but disrupt continuous observations due to data gaps or mode jumps. For geodetic signals, these drifts are still orders of magnitude above the required stability.

3.2.4 Backscatter Correction

Backscattered light at each of the resonator mirrors from the propagation direction results in a frequency pulling and pushing, impacting the Sagnac beat frequency of the interfered laser beams. A correction procedure for this systematic errors was presented by Hurst et al. (2014), which is based on observations of relative monobeam amplitude ratios as well

as their phase relation.

We monitor monobeams for each of the operational rings RZ, RU and RV in successive experiments in order to quantify the contribution of the backscatter effect to the observed Sagnac frequency drifts. The signal of the photo diodes is amplified and then transmitted differentially in order to provide a sufficient signal quality (Fig. 3.7a). For RV, a 50:50 isotope gas mix is suspected to contribute to less variance in the Sagnac frequency (Fig. 3.9), when compared to the also slanted ring RU.

An example for the Sagnac signal (FJV) and the monobeam signals (F1V, F2V) for RV are shown for the time and frequency domain in the appendix (Fig. S.7). The Sagnac frequency peak on the monobeams due to backscattered light is modulated and dominated by electric hum signals of 50 Hz and their harmonics. The 450 Hz harmonic peak is visible in the spectra of the monobeams in Figure S.7 and happens to be close to the Sagnac frequency peak of 447.5 Hz.

An example of the Sagnac frequency time series of RV before and after an applied backscatter correction is presented in Figure 3.10. The long-term drift for this example across 22 days is about 7 mHz, while the short-term variation is within 3 mHz. This is about one order less than observed for RU (approx. 10 mHz; Fig. S.8). The backscatter correction reduces the variation of the Sagnac frequency by about 1 mHz or 2 mHz (Fig. 3.10b). This can be expressed as a variance reduction R between signal variance σ^2_{sig} and residual variance σ^2_{res}:

$$R = \frac{\sigma^2_{sig} - \sigma^2_{res}}{\sigma^2_{sig}} \times 100 \ , \tag{3.5}$$

which amounts to 94.5 % for the example in Figure 3.10. The long-term drift is still present after the backscatter correction has been applied, which strongly indicates that mechanical scale factor variations and drifts are the dominant error source for ROMY. A focus on two shorter time intervals emphasizes the achieved reduction related to backscatter errors. A response of the Sagnac frequency to a dominantly thermal perturbation after maintenance work is presented in Figure 3.10d. A sudden drop after a split-mode operation state of approximately 3 mHz is recovered after about 6 hours.

Figure S.8a shows an example of a backscatter correction applied to the Sagnac frequency time series of RU over 3 days, characterized by several mode jumps and split-mode occurrences with subsequent MLTI launches. The non-ideal gas mix of this ring promotes frequent mode jumps. The Sagnac frequency for RU in this example ranges between 302.42 Hz to 302.48 Hz, thus a maximal drift range of about 60 mHz is observed (Fig. S.8a). The backscatter correction partially achieves reductions of up to 15 mHz, but does not compensate everything. This indicates other causes for the remaining drift. The maintenance period in this example, during which a convection-driven equalization of inside and outside temperature occurs, causes thermal forcing on the instrument. The reaction is a subsequent periodic oscillation dominating the drift behavior (from about 14:00-00:00 UTC).

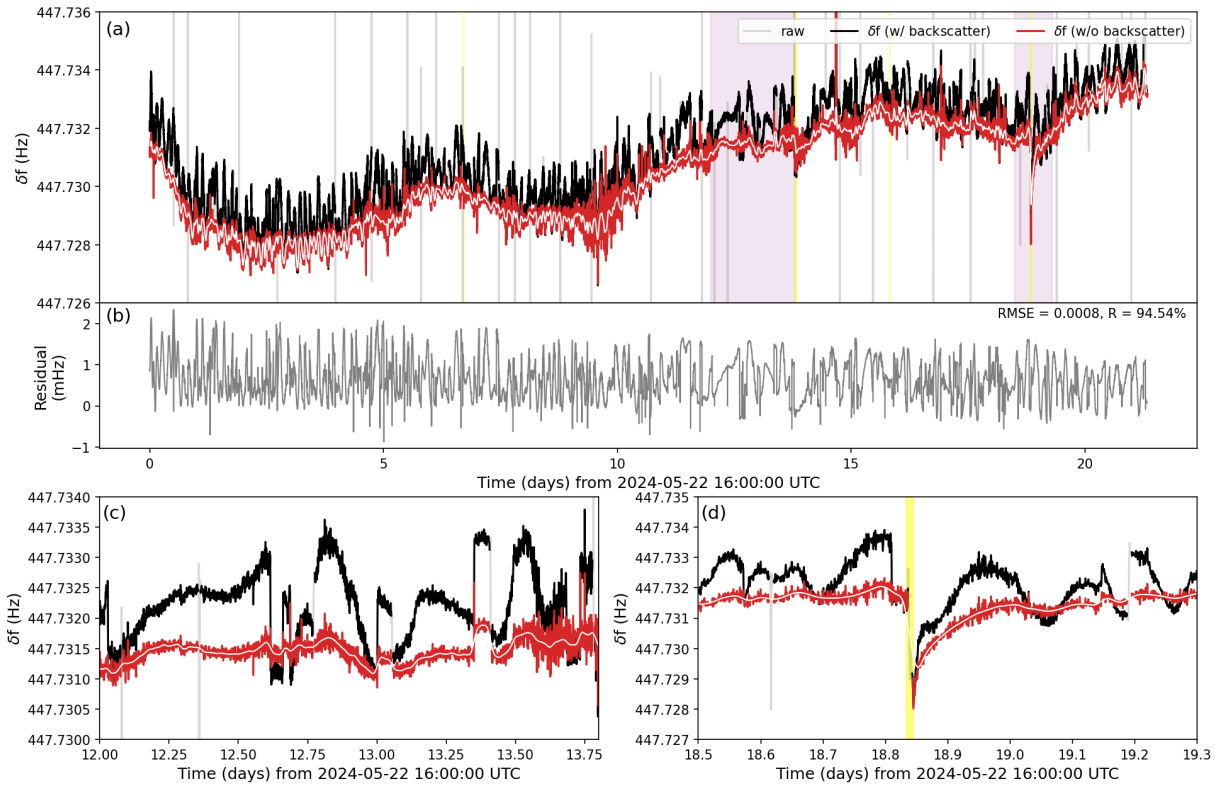

Figure 3.10: (a) The time series for RV of the raw Sagnac frequency (gray), the processed Sagnac frequency by removing MLTI launches (black) and with a backscatter correction applied (red). (b) Residual of δf before and after backscatter correction is applied. In (c) and (d) a data zoom-in on the left and right purple shaded time intervals in (a) are shown, respectively. Yellow, vertical lines indicate maintenance periods.

3.2.5 Resonator Deformation at ROMY

3.2.5.1 Beam Walk

In order to qualitatively capture the deformation of the optical resonator, we use a method that has been applied at other large heterolithic RLGs, such as UG-2 (Hurst et al. 2009, Pritsch et al. 2007). The two-dimensional displacement of the transmitted beam can be tracked using video cameras mounted behind the corner mirrors. Monitoring of beam positions at all corners enables to constrain the beam plane and quantify the experienced deformation at the corners in two dimensions. This has also been used to apply a correction based on ray tracing techniques (Pritsch et al. 2007, Hurst et al. 2009).

We use a set of monochromatic cameras by IDS Imaging (Tab. 1) for the beam wander monitoring. In contrast to a rectangular ring laser, a triangular one has the advantage that the lasing area remains plane and well-defined at all times. With a triangular-shaped ring, however, a simultaneous observation of the combined and both uncombined beams limits the amount of deployable cameras for beam tracking.

An initial camera (IDS00) was installed at the northwestern corner of RU, monitoring the counter-clockwise beam displacements. The camera is mounted onto the optical bench behind the corner and aligned manually with approximately orthogonal orientation of the sensor with respect to the transmitted beam. The x-direction and y-direction of the camera sensor, as indicated in Figure 3.7a), can be converted to displacement (in micrometers) using the camera sensor's pixel size (see Tab. 1). The x-direction hereby resembles the in-plane degree-of-freedom of the mirror corner, while the y-direction relates to the out-of-plane motion. A monochromatic image of the beam is taken and stored every minute automatically. Assuming a Gaussian beam kernel, a fit for a 2D Gaussian distribution is performed on an image and the maximum of the distribution is picked (see Figure S.10). Tracking of the fitted Gaussian beam maximum over time allows conclusions on corner deformation.

Long-term beam tracking of RU for 74 days (2024-03-09 to 2024-05-21) reveals some dynamic in beam walk, corresponding to beam plane adjustments due to corner deformation. A sudden offset on day 54 is attributed to minor resonator re-alignment during maintenance work.

A relative beam displacement in x-direction, of about 340 µm, is accumulated over the entire observation period (Fig. 3.11). This in-plane deformation is well correlated with the increasing combined temperature at all resonator corners. The deformation in-plane seems to be dominantly controlled by thermal expansion, since at times of temperature decrease, the deformation is significantly reduced (Fig. 3.11b).

The relative beam displacement in y-direction reveals more short-term dynamics in an overall range of about −40 µm to 60 µm. Most of the variations correlate well with inverted changes in barometric pressure (Fig. 3.11c). For the heterolithic RLG UG-2, Pritsch et al. (2007) reported a maximal beam walk of about 30 µm in vertical and about 50 µm in horizontal direction across 2.5 days. UG-2, however, was located in an underground cave with rather stable environmental conditions.

Between 2024-07-06 and 2024-07-29, two cameras (IDS01 and IDS03) were installed at the southern corner of RZ, in order to observe both monobeam directions (Fig. 3.7a). The beam tracking over 23 days reveals a more prominent displacement in y-direction (up to 80 µm) compared to x-direction (up to 40 µm). The x-position shows a linearly increasing trend, while the y-position also increases, however, with more short-term modulation (see Fig. 3.12c and 3.12d).

A diverging trend is evident for both directions, which is also reflected in the relative peak intensity derived from the fitted Gaussian peak. After 23 days, the offset amounts to 15 µm and 75 µm, for x- and y-position, respectively. Nevertheless, the time series for the displacement in both directions correlate well when comparing cameras IDS01 and IDS03. Small contributions to the difference might result from slightly different distances of the camera sensor behind the mirror, which is also the pivot point of the corner, thus amplifying displacements due to an increased lever.

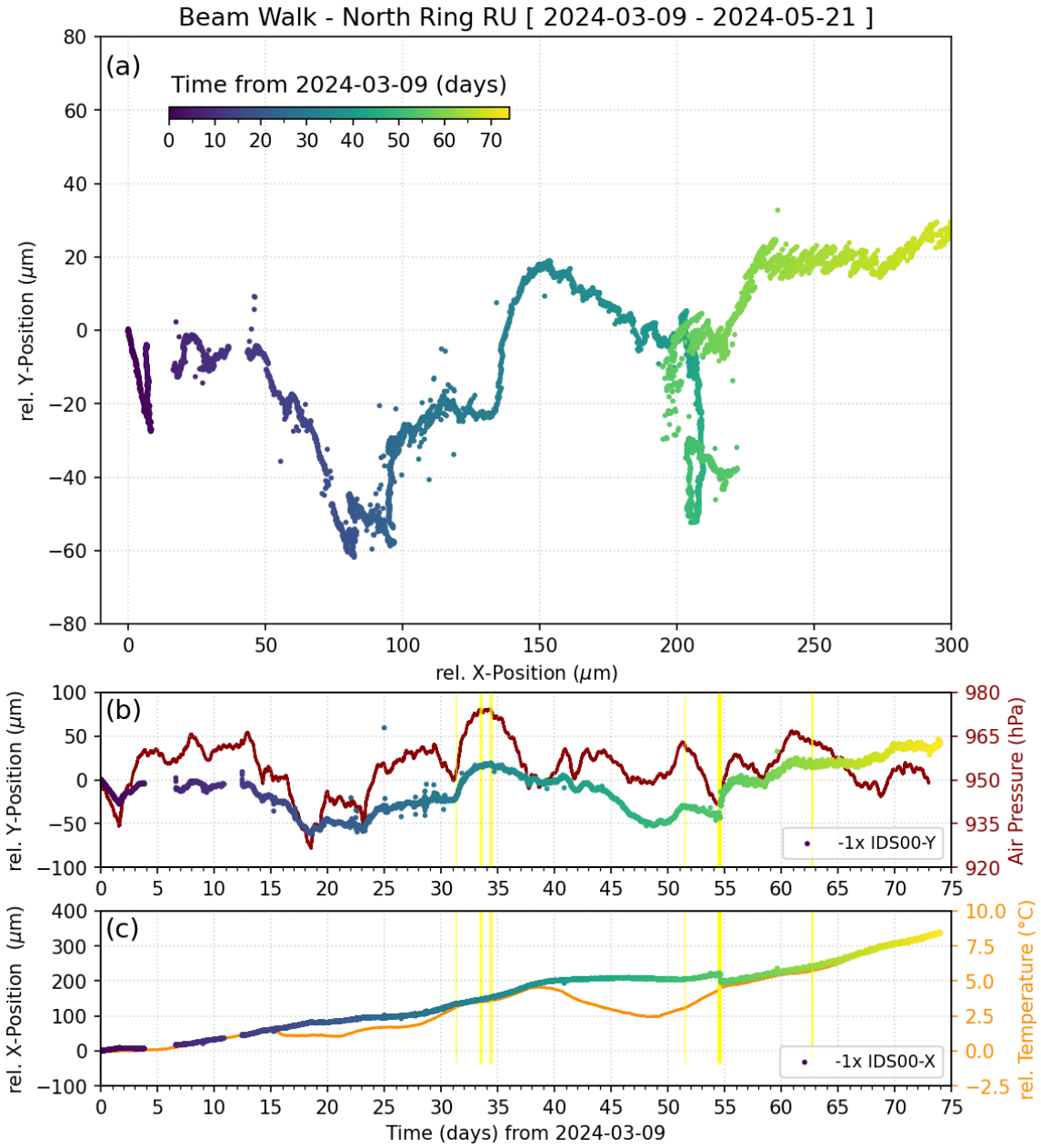

Figure 3.11: (a) The beam peak position tracking as relative displacement in x-direction (in-plane) and y-direction (out-of-plane) for the counter-clockwise monobeam of ROMY's northern ring RU at its northwestern corner over 74 days. (b) The out-of-plane displacement over time with barometric pressure. (c) The in-plane displacement and combined air temperature change at the resonator corners. The y- and x-displacements are reversed in all panels. The sampling rate for beam tracking is 10 min and outliers are removed. Yellow, vertical lines indicate maintenance periods.

We infer the beam intensity using the peak of the 2D-Gaussian fitted on the images. The relative intensity decreases by up to 40% for IDS01 and only by about 15% for IDS03 (Fig. 3.12b). The peak-to-peak amplitude of the Sagnac signal is related to the interferogram contrast and serves as a quality measure of the interferogram. A decreasing trend of overall about 0.7 V matches with the declining beam intensity. Sudden shifts of beam intensity and Sagnac signal peak-to-peak amplitude align well.

This demonstrates the influence of deformation at the corners causing beam walk on the beam combination at the Koester prism (see Fig. 3.7a) and consequently the interferogram contrast. Several causes are possible: 1) a decrease in overlapping area and alignment for the beam combination, 2) a reduction of the resonator finesse, thus beam intensity, by moving the reflection point on the mirrors and 3) a shift in the beam plane causing misalignment with the constricted gain tube, hence reducing beam intensity.

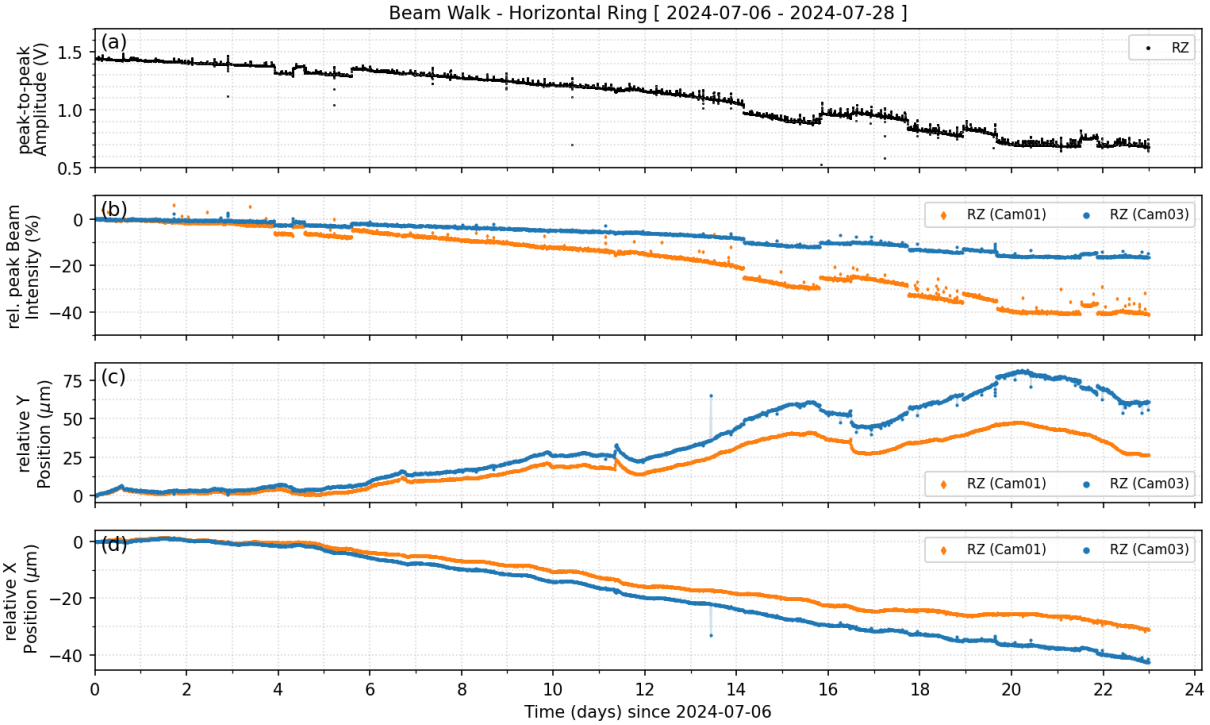

Figure 3.12: The observed peak-to-peak amplitude of the Sagnac signal, acting as a proxy for the interferogram quality. Two cameras (IDS01 and IDS03) are installed at the southern corner of the horizontal ring (RZ), observing (b) the relative maximal beam intensity (0-255) and the beam displacement (c) in y-direction (= out-of-plane) and (d) in x-direction (= in-plane) for both monobeams. The sampling rate is 10 minutes. Outliers have been removed.

3.2.5.2 Perimeter Variation

A commonly employed method to monitor deformations of an optical ring resonator is based on the free spectral range (FSR):

$$n\ FSR\ =\ \frac{c}{P}\ , \tag{3.6}$$

where c is the speed of light ($\approx\ 3\ \times\ 10^8\,\mathrm{m\,s^{-1}}$), n the integer mode index and P the perimeter of the optical ring resonator (e.g., Schreiber & Wells 2023b). For large RLGs, such as RZ with a perimeter of about 33.55 m, the FSR is 8.94 MHz. Considering a gain curve with a width of about 1.8 GHz, an operation on a stable phase-locked multimode regime is challenging, but feasible. Monitoring the relative FSR variation over time using an adequate fast avalanche photo diode and spectrum analyzer, stabilized by a 10 MHz GPS reference, enables to track the changing perimeter (Eq. (3.6)).

We track the 12^{th} FSR (= 107.2994 MHz) of RZ and compare the derived relative perimeter changes to beam walks and environmental observations. A schematic setup of this experiment is illustrated in Figure 3.7a.

The pressure of the gas mix causing a homogeneous broadening, which suppresses the closest neighboring modes. Of the excited FSR peaks, the 12^{th} FSR peak was found to be the most stable. Peak tracking reveals a frequency drift of about $20\,\mathrm{Hz\,d^{-1}}$, which corresponds to a perimeter variation of about $7\,\mu\mathrm{m\,d^{-1}}$ or $0.115\,\mathrm{mHz\,d^{-1}}$ in Sagnac frequency variation (Fig. 3.13a). The dominantly linear increase seems to be controlled by temperature changes, where the increasing combined temperature (at all corners of RZ), scaled by $30\,\mu\mathrm{m\,^{\circ}C^{-1}}$ (for presentation reasons), matches this trend.

Three cameras (IDS01, IDS03 and IDS05) provide beam displacements during this experiment (see Fig. 3.7a). Here, a dominant contribution of temperature increase is observed in shaft 07, explaining a stronger effect on beam displacement observed by IDS01 and IDS03, which are also located in shaft 07, whereas IDS05 is not. The absolute beam walk displacement (IDS*-A = $\sqrt{X^2 + Y^2}$) requires only half of the linear thermal coefficient compared to the perimeter change, indicating that there is a portion of homogenous thermal expansion of the resonator not contributing to beam walk.

In order to remove the dominant linear trend, a highpass filter with corner period of 36 hours is applied to the data. Hereby, the small scale perturbations of beam displacement in the order of $<5\,\mu\mathrm{m}$ in y-directions and tens of micrometer in x-direction become visible (Fig. 3.13b and 3.13c). The beam displacement of several micrometers in y-direction shows a high correlation with barometric pressure changes (Fig. 3.13b). This is also evident in the perimeter variation record, although with a minor correlation, and has to be scaled by a factor of four (Fig. 3.13b).

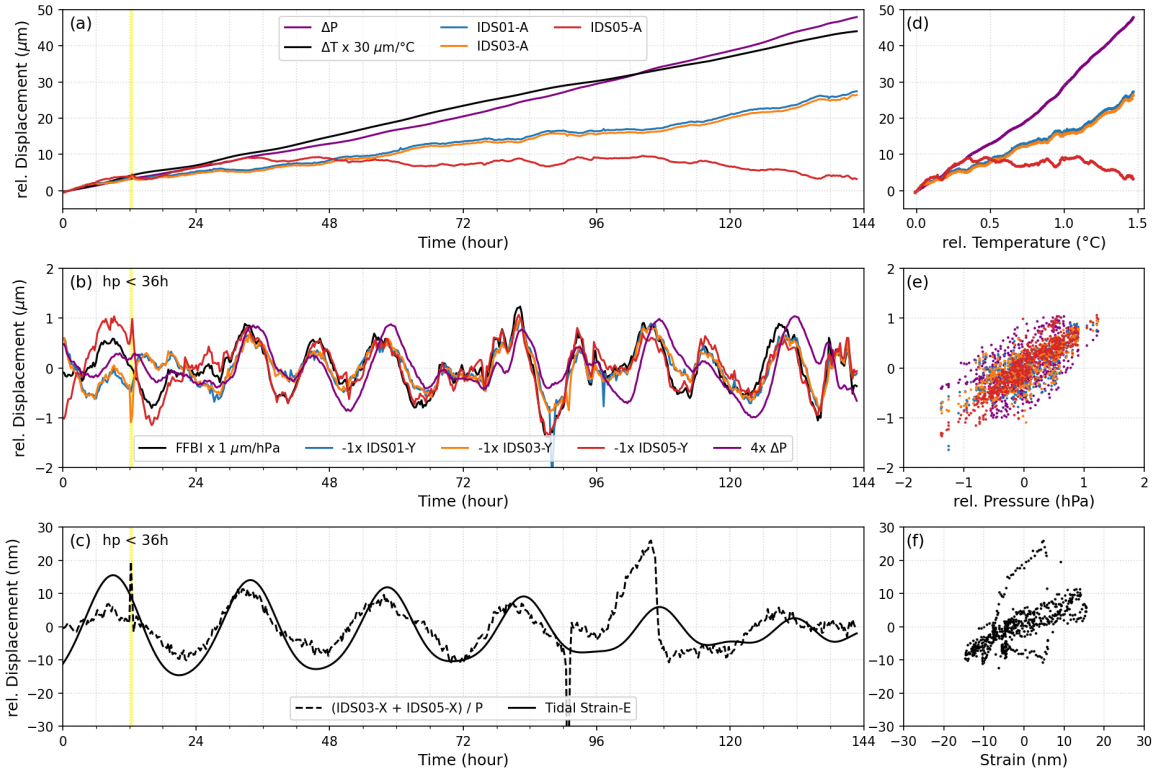

Figure 3.13: Separation of external effects on perimeter changes and beam walk at RZ. (a) Relative integrated displacement of the resonator's perimeter (ΔP) based on FSR measurements and absolute beam walk displacement ($\sqrt{X^2 + Y^2}$) for cameras IDS01, IDS03 and IDS05 are compared with combined temperature (black) at all corners (05, 07, 09) scaled by $30\,\mu\mathrm{m}\,^{\circ}\mathrm{C}^{-1}$. (b) Highpass filtered displacements in y-direction (out-of-plane) with changes in barometric pressure scaled by $1\,\mu\mathrm{m}\,\mathrm{hPa}^{-1}$. (c) A summation of IDS03-X and IDS05-X, thus highpass filtered displacements in x-direction (in-plane), divided by the perimeter (P = 33.5 m), is shown as a dashed, black line. Theoretical horizontal tidal strain in eastern direction (solid, black), computed using PyGTide (Rau et al. 2022), is shown. A highpass with corner period of 36 hours is applied to displacements in (b) and (c). Corresponding scatter plots of displacement against temperature change, pressure change and tidal strain are shown in (d), (e) and (f), respectively.

When removing the linear trend for the beam displacement in x-direction, a periodic signature of approximately one cycle per day (1 cpd) and a peak-to-peak amplitude of about 10 nm is found (Fig. 3.13c). This agrees in magnitude and phase with theoretical horizontal tidal strain in eastern direction, which is computed using the PyGTide package (Rau et al. 2022). A summation of IDS03-X and IDS05-X, which are oriented towards the same corner mirror (see Fig. 3.7a), divided by the perimeter (P = 33.5 m), aligns well with the theoretical predicted tidal strain.

3.2.6 Environmental Effects

3.2.6.1 Thermal Response

The optical resonator includes stainless steel bellows, decoupling the beam pipe enclosures from the three corner boxes (Fig. 3.7a). Therefore, we subsequently assume, that deformations mainly occur at the corner boxes and their foundation. We further assume, that the air temperature in the corners shafts is representative for the mirror corner itself without any lag time.

Thermally Induced Drift in Sagnac Frequency

A variation in temperature in the corner shafts of the resonator introduces thermal deformation. Two sources contribute dominantly to thermal deformation. Firstly, the concrete foundation expands or contracts due to thermal forcing, therefore increasing or decreasing the resonator side length, and hence the scale factor (Eq. (3.4)). Secondly, the stainless steel corner boxes, which are designed to minimize thermal deformation with regard to the mirror position, nevertheless, contribute to deformation via the alignment lever assembly used to manually align the resonator. However, these two sources of deformation are difficult to separate. Any change in the scale factor is considered an instrumental effect or error, in this case introduced thermally.

A response of the Sagnac frequency of RV to a temperature perturbation as a result of an extended interval of air ventilation is shown in Figure 3.14. The maintenance work causes a sudden increase in temperature of up to 2.5 °C in the central shaft 01. The temperature at the other two corners of the resonator (07 and 09) is only slightly perturbed. The seasonal temperature trend over 80 hours here is about 250 m°C and more pronounced on temperature records of PS7 and PS9.

The time series of the relative Sagnac frequency without backscatter errors shows a pronounced response to the temperature perturbation, including a fast increase of about 6 mHz followed by a slower decay. A thermal expansion of the resonator causes an increase of the scale factor, thus the Sagnac frequency (see Eq. (3.4)). Here, 6 mHz variation would correspond to a pure length change of about 160 µm. This assumes no change in orientation of the beam plane in connection with thermal deformation at the corner. The response of the Sagnac frequency of RU (scaled by -0.5) without backscatter correction, is less comparable (see Fig. 3.14). The drift signatures in the Sagnac frequency as a response to temperature changes are observed for all rings, in particular during or after maintenance periods (Fig. 3.9). Several upward drifts due to thermal expansion of the resonator followed by relaxing contraction are clearly visible for RV in Figure 3.9c.

Thermal Signature of Beam Walk

Between 2024-05-24 and 2024-06-24, beam displacement for one corner of RZ (IDS01, southern shaft), RU (IDS00, northwestern shaft) and RV (IDS07, southern shaft) was monitored simultaneously (Fig 3.15). Until day 24, the displacement of the monitored beams, in particular for x-directions, follows an increasing trend that is reflected in the temperature records of the upper shafts (PS5, PS7, PS9). The long-term temperature increase of about 2 °C across 24 days corresponds to beam displacements in the x-direction of 60 µm (RZ), 110 µm (RU) and 220 µm (RV). The temperature in the central shaft remains rather undisturbed, except of temperature spikes of short duration during maintenance work (Fig. 3.15). The strong displacement observed between day 24 and day 28 is forced dominantly by the activation of the internal air ventilation system of ROMY, introducing strong temperature perturbations. In the upper shafts, the introduced thermal perturbation amount to 1 °C to 2 °C and in the central shaft up to 0.3 °C (Fig. 3.15d).

Linear coefficients between the combined displacement of x- and y-direction and temperature changes are estimated before and after the thermal perturbation on 2024-05-24, as shown in Figure 3.16a and 3.16b, respectively. For the regression, a summed temperature

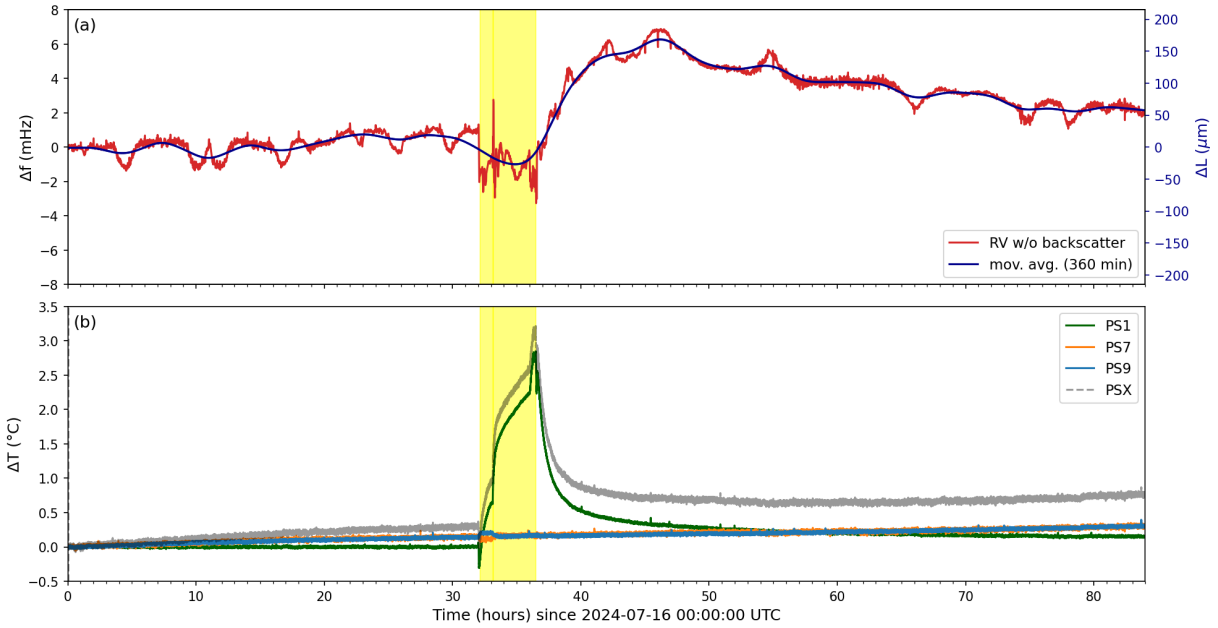

Figure 3.14: (a) Relative Sagnac frequency (Δf) for RV without backscatter errors during a drift, which is controlled by strong temperature variation. The strong temperature change (ΔT) is introduced due to running air ventilation in the central shaft starting prior to the maintenance work (yellow area). The Sagnac frequency of RU is multiplied by a factor of -0.5 to fit and a moving average is applied. A second axis shows the corresponding resonator side length variation (ΔL). (b) Relative temperature change in central shaft (PS1) as well as corner shafts of RV (PS7 and PS9). PSX represents a stacked temperature variation.

is used, which is composed of the individual measurements at the corners of reach ring resonator. A linear trend is evident, but overlain by more complex interactions. The coefficients for RZ, $4.2\,\mu m\,°C^{-1}$ and $6.7\,\mu m\,°C^{-1}$, vary only insignificantly for both examples (Fig. 3.16) and are small compared to the RU and RV.

For RU, thermal coefficients between the two selected periods of $17.3\,\mu m\,°C^{-1}$ and $31.5\,\mu m\,°C^{-1}$ are obtained and for RV $52.9\,\mu m\,°C^{-1}$ and $90.9\,\mu m\,°C^{-1}$ are estimated. Higher thermal coefficients are obtained for the period with a strong, short-term temperature perturbation. The strongest thermal response is observable at the resonator of RV.

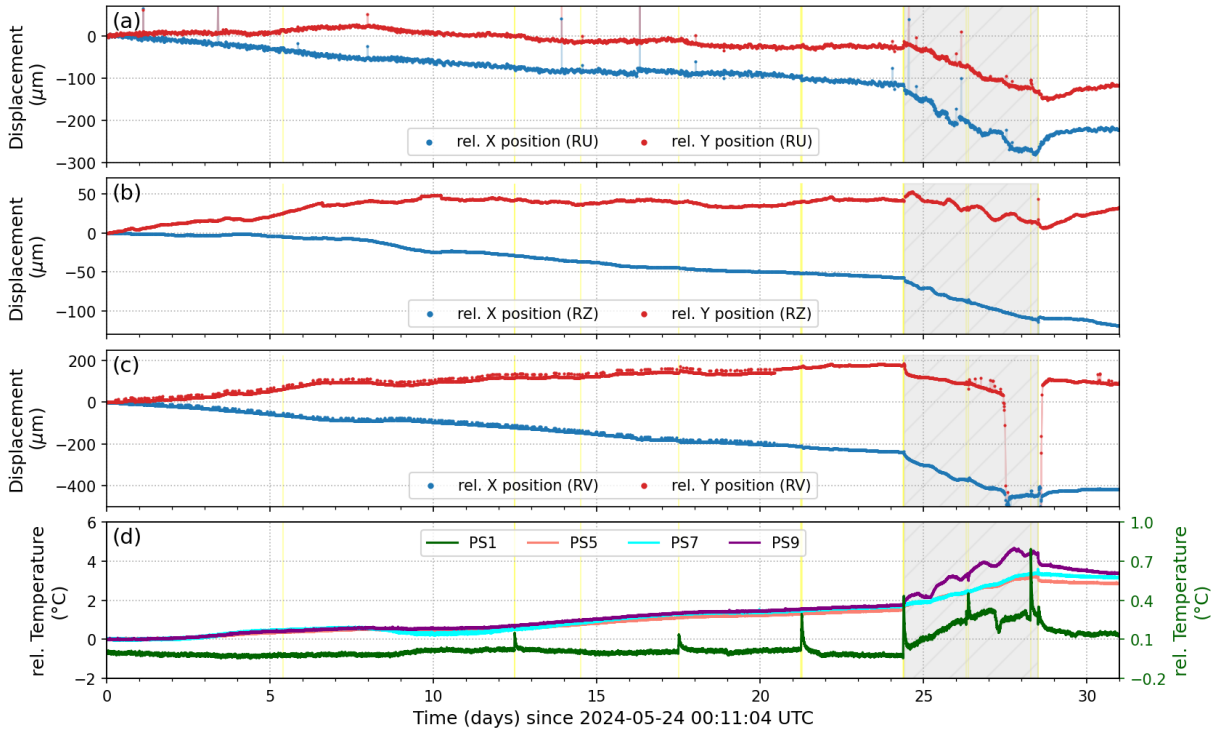

Figure 3.15: Relative beam displacement of (a) RU, (b) RZ and (c) RV across 31 days since 2024-05-24. (d) Temperature observations at all corners are shown. The hatched, gray area marks a time period with activated air ventilation. Yellow, vertical lines indicate maintenance periods. The beam displacement has a sampling time of 10 min and outliers have been excluded.

A long-term thermal coefficient of $40\,\mu m\,°C^{-1}$ or $0.6\,\mu m\,°C^{-1}\,d^{-1}$ is obtained for RU, based on 300 µm displacement in x-direction for 7.5 °C over 70 days (Fig. 3.11c).

A thermal effect on the ring resonator is expected and observed for multiple rings of ROMY. Temperature variations have shown to deform the stainless-steel corners, in particular by affecting the adjustment levers, and hence cause scale factor changes reflected in beam walk. This can be detected by observing beam wander at the corners. The thermal deformation coefficients for individual rings vary and range in the tens of micrometer displacement per degree Celsius.

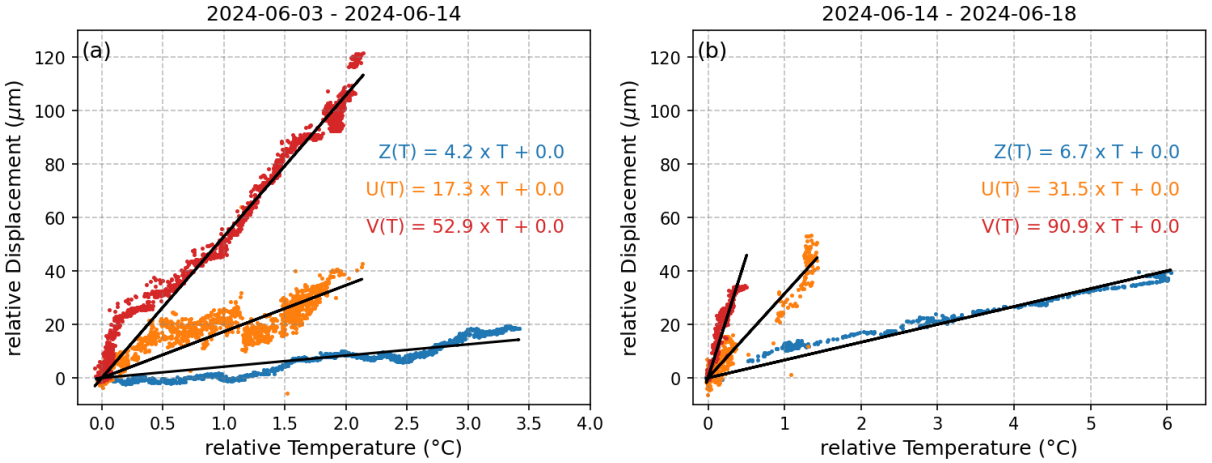

Figure 3.16: Linear regression of beam displacement and temperature for RZ, RU and RV. Absolute beam displacement ($d = \sqrt{x^2 + y^2}$) and combined temperatures at all corners of RU (orange), RZ (blue) and RV (red) for two time periods (a) 2024-06-03 to 2024-06-14 and (b) 2024-06-14 to 2024-06-18 are used. Hereby, data (a) before and (b) during a strong temperature perturbation, as indicated in Figure 3.15, is analyzed.

Temperature Variation and Mode Jumps

Within the Sagnac frequency time series, we observe frequent mode jumps not causing split-mode states, however, shifting the Sagnac frequency. An exemplary mode jump is shown in Figure 3.17a, occurring after about 14 hours, shifting the Sagnac frequency of RV by about 2 mHz.

When assuming that a mode-jump occurs as soon as the perimeter of the ring resonator is expanded or contracted by at least one wavelength ($\simeq$633 nm), we can estimate linear thermal expansion coefficients. In order to study the temperature variation only, we have to assume, that no other environmental effects act on the Sagnac frequency at this time. Most thermal deformation is assumed to accumulate at the corners of the triangular ring resonator, since the resonator edges and corners are decoupled by stainless steel bellows. The air temperature measurements inside the corner three shafts (01, 07 and 09) of the RV ring resonator as well as a summed, overall temperature trace are shown in Figure 3.18.

In order to accumulate a linear strain along the resonator perimeter of about 633 nm, a linear thermal expansion coefficient of $\alpha = 15\,\mu\epsilon/°\mathrm{C}$ has to be used. In this example, most temperature variation, hence strain, is attributed to the corner in shaft 07. An expansion of the ring resonator as a result of an increase in temperature causes an increase of the enclosed area and perimeter, and thus the in Sagnac frequency (Eq. (3.2)), as seen in Figure 3.18a.

A second example with a sequence of five mode jumps, with a rather constant repetition time of approximately 2 hours, is shown in Figure 3.17a for RV. Before and after this

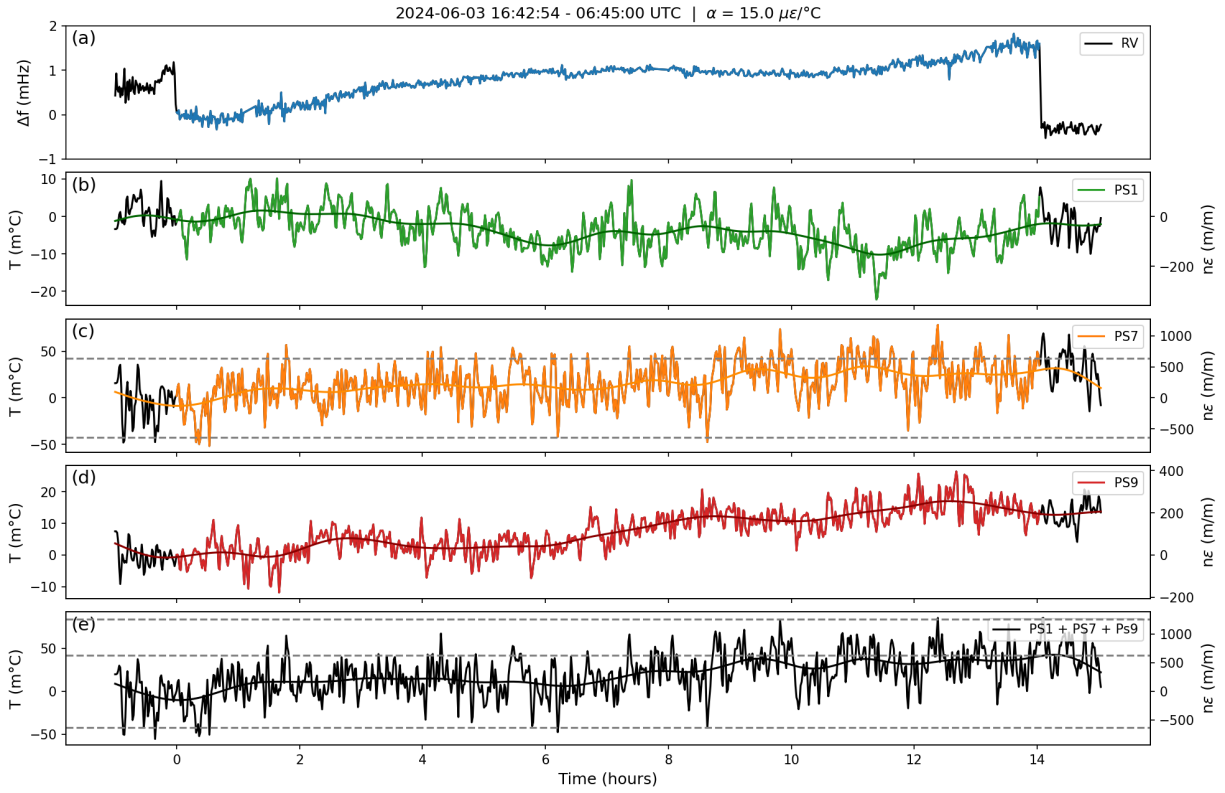

Figure 3.17: An example for observed mode jumps at RV related to temperature variations and thermal expansion of the ring resonator. (a) A mode jump is observed after approx. 14 hours for the relative Sagnac frequency of RV. (b) - (d) Air temperature measurements in the corner shafts 01, 07 and 09 of ROMY. (e) A superposition of the individual temperatures. Each temperature has a strain axis showing converted temperature to linear strain using a thermal expansion coefficient of $\alpha = 10\,\mu\epsilon/°\mathrm{C}$.

sequence, a split-mode operation state occurs. Between the mode jumps, the Sagnac frequency shows an increasing trend which does not meet the expectations for an overall decreasing temperature trend, namely a contraction of the resonator. From the start of the sequence to the end, however, we find an overall decrease in Sagnac frequency, in accordance with expectations. For an α of $10\,\mu\epsilon/°\mathrm{C}$, an integrated strain of 633 nm is obtained between the split-mode states with regard to the overall temperature (Fig. 3.18). We can not explain the intermediate mode jumps comprehensively.

The estimated thermal coefficients of $10\,\mu\epsilon/°\mathrm{C}$ to $15\,\mu\epsilon/°\mathrm{C}$ are similar to commonly used values for concrete ($8\,\mu\epsilon/°\mathrm{C}$ to $13\,\mu\epsilon/°\mathrm{C}$; Eurocode 2; Bamforth et al. (2008)), which can vary strongly depending on the used concrete aggregate. Structural steel is based on similar values ($10\,\mu\epsilon/°\mathrm{C}$ to $12\,\mu\epsilon/°\mathrm{C}$; Eurocode 3, (ECCS 2015)).

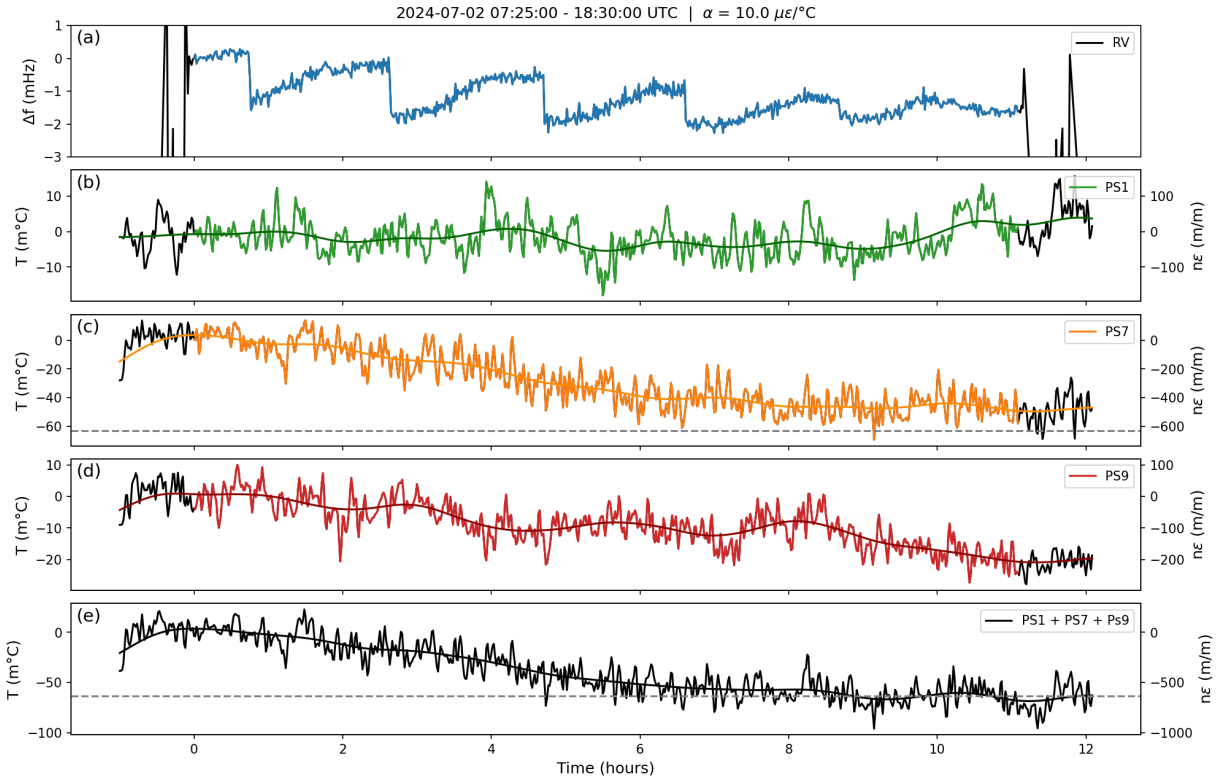

Figure 3.18: An example for observed mode jumps at RV related to temperature variations and thermal expansion of the ring resonator. (a) Over 12 hours five mode jumps are observed for the relative Sagnac frequency of ROMY's western ring (RV). (b) - (d) Air temperature measurements in the corner shafts 01, 07 and 09 of ROMY. (e) A superposition of the individual temperatures. Each temperature has a strain axis showing converted temperature to linear strain using a thermal expansion coefficient of $\alpha = 15\,\mu\epsilon/°\mathrm{C}$. Dashed, gray lines represent multiples of 633 nm. Moving averages are shown for the temperature measurements in order to better visualize the trend.

Thermal Insulation

Thermal stability is essential to improve the operational stability of the heterolithic RLGs of ROMY, as described in the sections above. The observed temperature variations (°C down to m°C) have a significant effect on the scale factor (see Figs. 3.14 or 3.17). In order to reduce observed temperature variations inside ROMY's shafts, a passive thermal insulation was designed and installed.

The passive thermal insulation intends to provide more stable temperature conditions by 1) suppressing air mass exchange between outside and inside by introducing a low conductive barrier and 2) limiting strong air convection to the upper volume near the exposed metallic cover, experiencing strong heat intake.

A 60 mm thick styrofoam plate is mounted on a sliding aluminum frame to separate the

smaller, upper volume from the main volume containing the resonator corners. The sliding system is installed at the ceiling of the shaft. This design can be considered as a lowpass filter to reduce daily and sub-daily air temperature fluctuations. Additionally, an electrically rotatable valve was installed for the ventilation pipe of the central shaft to automatically close this direct link, avoiding ambient temperature fluctuations to enter, unless maintenance work is being conducted.

To verify the enhancement, observations before and after the installation of the insulation are provided in Figures 2.13 and 3.19, respectively. Outside air temperature observations in September 2022 (Fig. 2.13a) contain many days with strong daily variations of more than 10 °C, also reflected as pronounced spectral peaks in Figure 2.13c at one and two cycles per day. With no thermal insulation, except of closed metallic top covers, the temperature variations propagate inside the shafts, visible in the time and the frequency domain, especially by a broad spectral peak at one cycle per day. Temperature sensors WS4 and WS8 are located in access shaft that host electronics for plasma discharge, and elevated absolute temperature levels in these shafts are most likely related to electronic excess heat. Sensor WS1 is located at the bottom of the central shaft at a depth of about 14 m below surface, with the most stable temperature conditions at about 12 °C to 16 °C throughout the year. If present, any daily or sub-daily air temperature variations for WS1 are below the sensor resolution threshold. The sudden increase in air temperature on day 14 (Fig. 2.13b) is linked to automatic activation of a dehumidifier unit, which is also reflected in the corresponding power spectral density.

The insulation is fully operational since 2024-03-09. The impact of the passive, thermal insulation is tested by comparing the period before the insulation (Fig. 2.13) and a period without disturbance due to maintenance work between 2024-03-09 and 2024-04-09 after all insulation plates were installed. Outside air temperature for this period in spring shows comparable variations as before in September (Fig. 3.19a).

Inside temperature is based on records of upgraded sensors located in five access shafts (01, 04, 05, 07 and 09). Being at the bottom of the central shaft, PS1 represents again the most stable air temperature between 15.4 °C to 15.6 °C. Daily or sub-daily air temperature variations are, however, not visible in the time series nor the power spectra. At the daily and sub-daily spectral peaks, the difference between outside and inside is approximately 50 dB.

We find that the passive thermal insulation successfully acts as a low-pass filter, suppressing short-term variations. In turn, this reduces thermal forcing on the ring resonators, hence instrumental effects and drifts and improves the short-term operational stability. The upper shafts still show a slow long-term temperature increase. The passive insulation, however, cannot mitigate seasonal variations (Fig. 3.19).

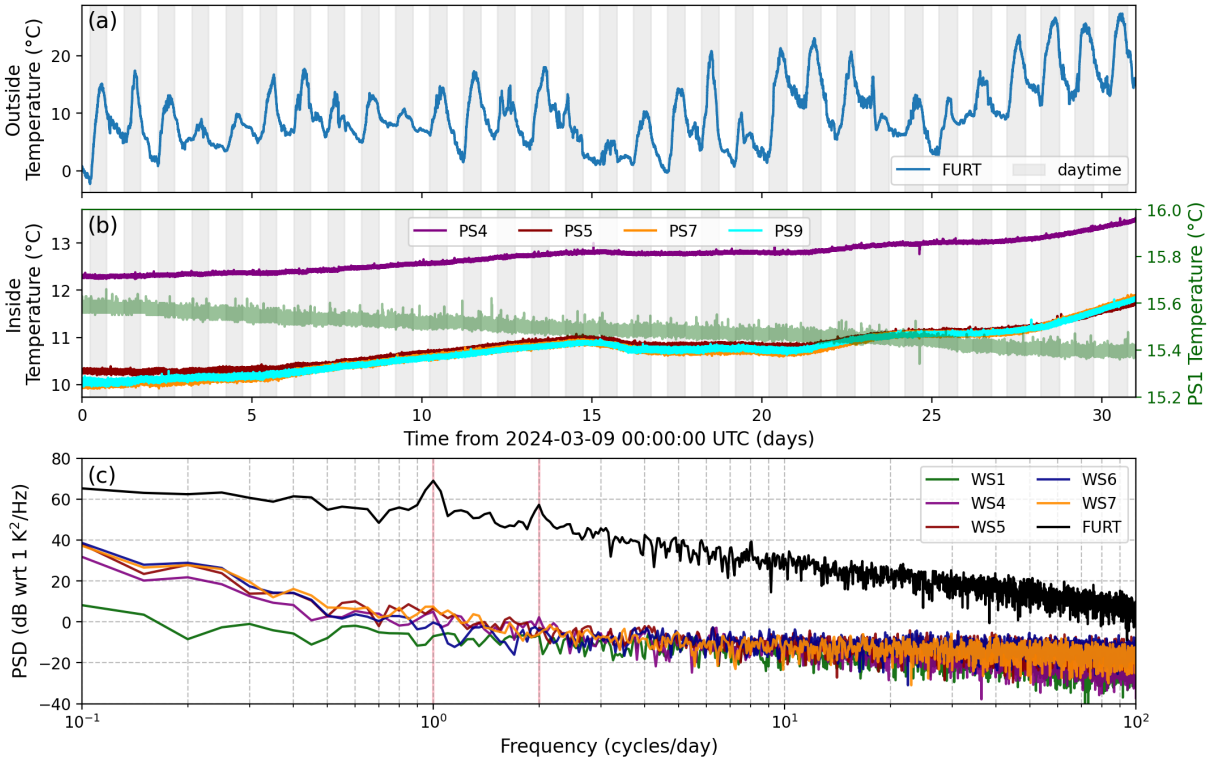

Figure 3.19: Temperature data is shown between 2024-03-09 and 2024-04-09. Gray areas indicate day time (sunrise to sunset). (a) The outside temperature recorded at the weather station FURT. (b) Temperature records of five DPS310 sensors inside ROMY's shafts. (c) Power spectral densities are shown for DPS310 and FURT records based on the time series in (a) and (b).

3.2.6.2 Barometric Response

An example of a distinct, passing low-pressure system around midday of 2024-05-06 and the response in terms of beam displacement at RZ is shown in Figure 3.20. The peak beam displacement in reversed y-direction ($\approx -6\,\mu$m) is about ten times more pronounced compared to the x-direction ($\approx 0.6\,\mu$m) of this example. The displacement in x-direction represents a twist of the corner (= in-plane motion), which is less correlated since excited due to local pressure changes.

There is a clear correlation (CC=0.8) between the local barometric pressure and the reversed y-direction of the beam displacement (Fig. 3.20a). This, in turn, causes deformation, such as tilting, at the corners of the resonator, which is reflected in beam walk. Observations of a co-located inertial Lippmann tiltmeter ROMYT confirm E-W tilt deformation at the corner basement exceeding the tidal deformation at the time during minimum air pressure. Tilt deformation in N-S direction is less pronounced (Fig. 3.20).

The Hilbert transform of the barometric pressure can be used to approximate the surface

deformation in the surrounding area by a travelling pressure wave (Zürn et al. 2007). No obvious correlation is found for the Hilbert transform, thus most deformation is rather caused locally due to deformation of additional barometric loading deforming the shafts (= cavities) of ROMY.

A negative tilt deformation of about 550 nrad appears on the absolute tilt of ROMYT and BROMY (= borehole tiltmeter deployed at the tip of ROMY), for the low pressure period (Fig. 3.20c). This agrees well with the reversed beam displacement of almost −3 µm. The low-frequent, backscatter corrected Sagnac frequency of RV correlates well with the barometric pressure and a relative change of approximately −1.6 mHz is observed (Fig. 3.20c).

A second example for pressure loading induced deformation at the resonator corner is provided in Figure S.11, confirming the presented observations.

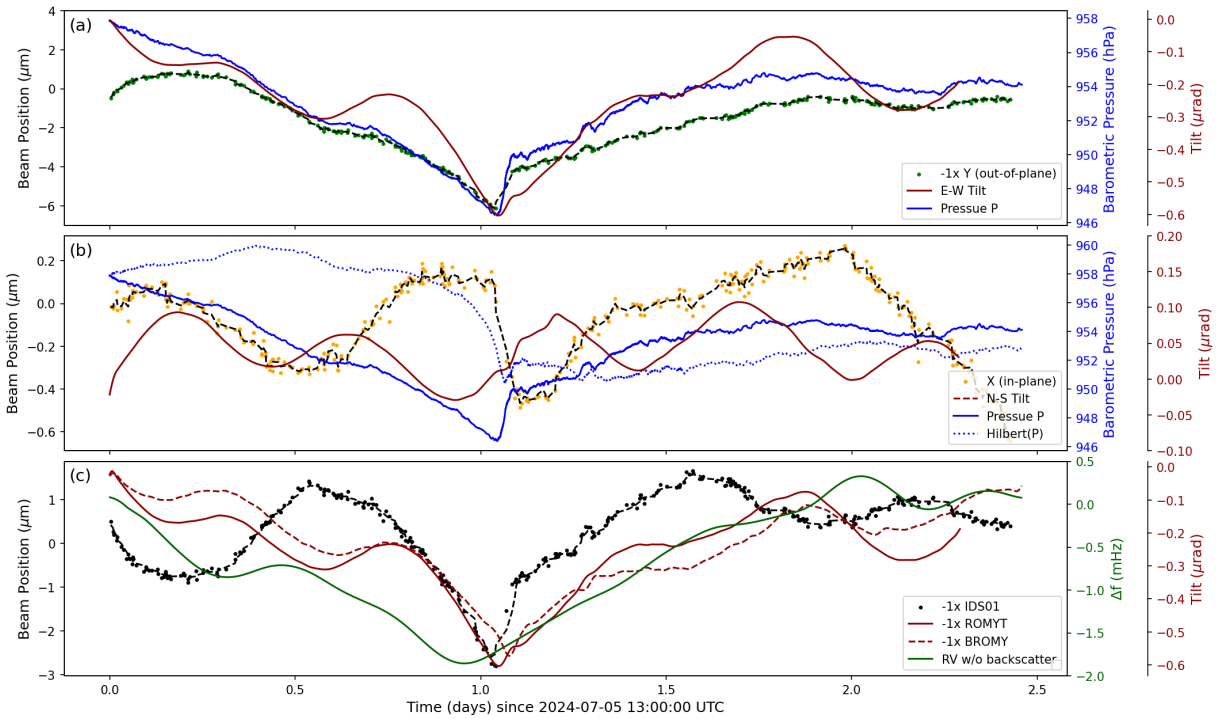

Figure 3.20: Beam position of RZ is shown (a) in reversed y-direction (= out-of-plane) and (b) in x-direction (= in-plane) between 2024-07-05 to 2024-07-08. Outliers for beam wander were removed. The absolute barometric pressure (solid blue) and the Hilbert transform of the barometric pressure (dotted blue) are shown. Tilt observations of the ROMYT tiltmeter located about 50 cm next to the corner are plotted as N-S (dashed red) and E-W (solid red) tilt. (c) Comparison of the absolute beam displacement ($\sqrt{X^2 + Y^2}$) of IDS01, the absolute tilt ($\sqrt{N^2 + E^2}$) for ROMYT (solid) and BROMY (dashed) as well as the 6 hour moving average of the Sagnac frequency of RV without backscatter.

3.2.6.3 Hydrological Response

The near-surface, concrete ROMY structure is exposed to a near-surface groundwater layer. Variations of the groundwater table, in particular after heavy rain, are expected to exert asymmetric hydrostatic pressure on the ROMY structure. Increasing pore pressure in the refilled material of the ROMY structure also contributes to its deformation. Both contribute to deformation of the entire ROMY structure and alter the scale factor due to orientation and geometric changes of the ring resonator. For a large one-sided hydrostatic pressure change, a response of the Sagnac frequency due to an orientation changes of the areal vector, in particular for N-S directed tilts, is expected. Assuming the entire structure behaves monolithic (no internal deformation) the overall change in orientation should be resembled complementary in Sagnac frequency observations of multiple rings. Without backscatter corrections for all RLGs simultaneously, however, small variations in orientation due to hydrological forcing are not easily discernible from other long-term effects (e.g. temperature variation). Moreover, a substantial short-term hydrological event (e.g. heavy rain) would be required in order to distinguish and quantify this effect reliably.

3.2.6.4 Modelling Instrumental Drifts

Beam Walk Model

The observed instrumental drifts in beam positions, caused by resonator deformation, are strongly related to environmental factors, as described above. A simple, multi-variant linear model is used to link environmental observations and beam wander (bw) comprehensively, assuming a dominantly linear relation:

$$bw \;=\; \sum_{n} c_n \, Q_n \;, \tag{3.7}$$

with c_n as linear coefficients and Q_n as corresponding observed quantities.

The Kendall rank correlation serves as a measure of dependence between pairs of observables (Figs. 3.21b and 3.21d). Different Kendall rank correlations are found for pairs of observables for beam displacement in x- (bwx) and y-direction (bwy), while both show high correlation with air temperature observations (Fig. 3.21b and 3.21d).

An example model for bwy and bwx at RV is presented in Figure 3.21a and 3.21c, respectively. The first two-thirds of the dataset (gray shaded area) is used to determine linear coefficients for each model with a subset of observables based on their Kendall rank correlation:

$$\begin{aligned} bwy &= c_0 \cdot bdo + c_1 \cdot ps1 + c_2 \cdot ps7 + c_3 \cdot ps9 + c_4 \cdot mae + c_5 \cdot man, \\ bwx &= c_0 \cdot ps1 + c_1 \cdot ps7 + c_2 \cdot ps9 + c_3 \cdot mae + c_4 \cdot man \end{aligned}$$

with abbreviations of observables listed and described in Table 3.1. The linear regression is based on a RANSAC (RANdom SAmple Consensus) algorithm, which is a robust regression approach that automatically rejects outliers.

The modelled beam wander (light red) captures the trend and major modulations well (Fig. 3.21) with overall R^2 values about 0.99 The observable quantities are smoothed using a moving average of 30 min and reduced by the start value. Obtained coefficients are listed in Table 3.1.

Beam wander for the last one-third of the dataset is predicted using the obtained linear coefficients. The predicted beam displacement (purple) deviates significantly from the observation (black), which indicates an oversimplified model and/or missing observables of driving forces (Fig. 3.21). Also, hysteresis effects or insufficient sampling of the observables, like temperature along the resonator or concrete foundation, might contribute. Furthermore, the observables are not entirely independent, which is reflected by higher Kendall correlation between the observables, not merely with respect to *bwy* and *bwx* (Fig. 3.21a and 3.21b).

Spikes in the predicted data are related to temperature spikes during maintenance, which are not captured during coefficient modelling. Generally, the linear model reproduces the observed, underlying drifts, which supports that the included observables are main drivers, as outlined for case studies in Section 3.2.6.

Table 3.1: The code used for quantities, the unit, and a quantity description are provided. C_n are linear coefficients obtained using a multi-variant model based on a RANSAC regression.

Code	Unit	C_n(bwx)	C_n(bwy)	C_n(fs)	Description
fsbs	mHz	–	–	–	Sagnac frequency w/o backscatter error
bwx	µm	–	–	0.06	x-displacement on ids07
bwy	µm	–	–	0.001	y-displacement on ids07
peg	m	–	–	-0.1	groundwater level
man	µrad	-3.1	4.6	1.1	N-S tilt of ROMYT
mae	µrad	9.9	24.9	0.4	E-W tilt of ROMYT
ps1	°C	319.6	223.1	-0.8	air temperature in shaft 01
ps7	°C	-14.2	-39.4	2.7	air temperature in shaft 07
ps9	°C	115.7	82.6	-4.8	air temperature in shaft 09
bdo	hPa	–	-2.6	0.1	absolute barometric pressure of FFBI
hp	hPa	–	–	–	Hilbert transform of barometric pressure

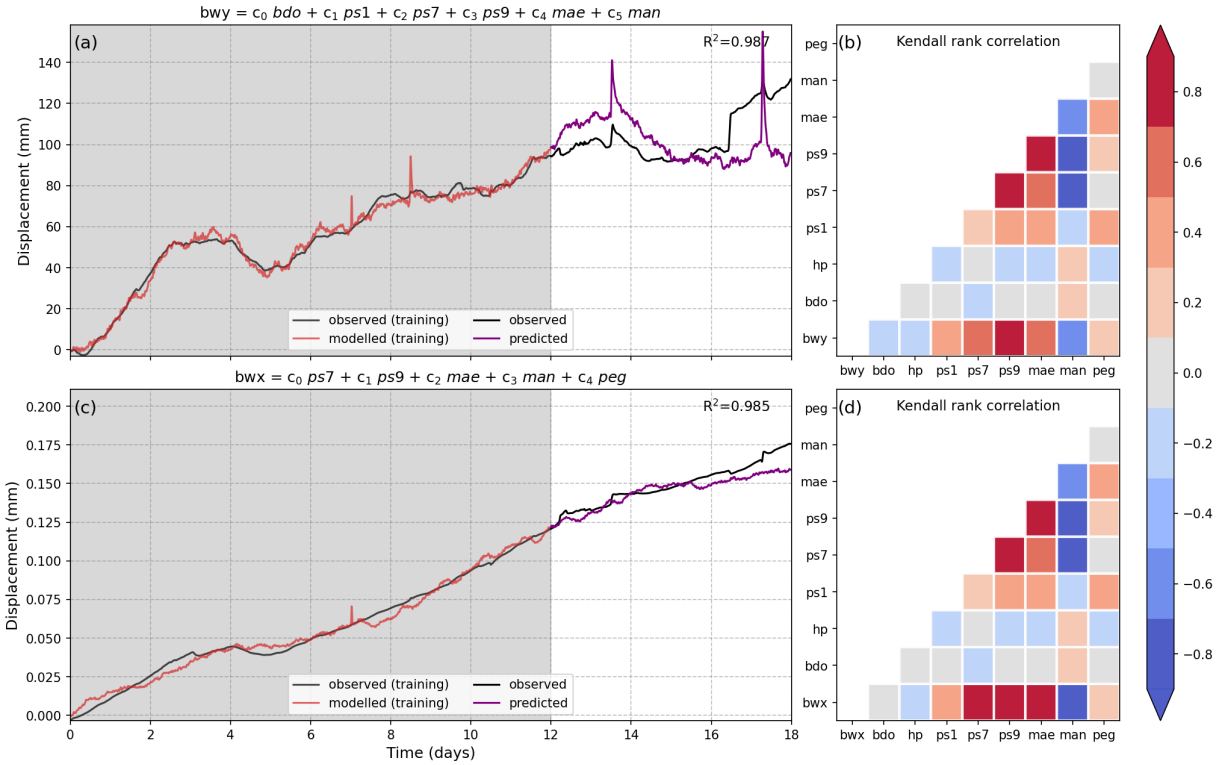

Figure 3.21: Time series of the relative beam displacement for RV are shown (a) in x-direction (bmx, in-plane) and (c) in y-direction (bwy, out-of-plane) as observed (black) and modelled (red). Data in the gray shaded area are used to fit a linear, multi-variant model as defined on top. The prediction (purple) is based on the obtained model coefficients. Kendall rank correlation coefficient matrices are shown in (b) and (d) for bwy and bwx, respectively. Observables are: peg = water level, man = N-S tilt, mae = E-W tilt, $ps1|ps5|ps9$ = air temperature inside shaft 1|5|9, bdo = absolute air pressure, hp = Hilbert transform of air pressure.

Sagnac Frequency Model

As a next step, we use the same approach to model drifts of the Sagnac frequency directly, taking into account a set of observables, including beam walk (bwx and bwy), temperatures ($ps7$ and $ps9$) and barometric pressure (bdo), as well as the Hilbert transform of the barometric pressure (hp). The observable quantities are smoothed using a moving average of 60 min and reduced by the start value of the time series. Two prominent downward spikes in the Sagnac frequency are attributed to maintenance work, thus temperature spikes, in shaft 01 (Fig. 3.22a).

Hereby, the assumption of simple, linear dependencies is even stronger, since the underlying relationships are more complex. Nevertheless, the model, with an R^2 of 0.974 , is able to capture long-term drifts of the time series (Fig. 3.22a). The prediction accuracy of the model seems good, although we believe the model is rather simplistic.

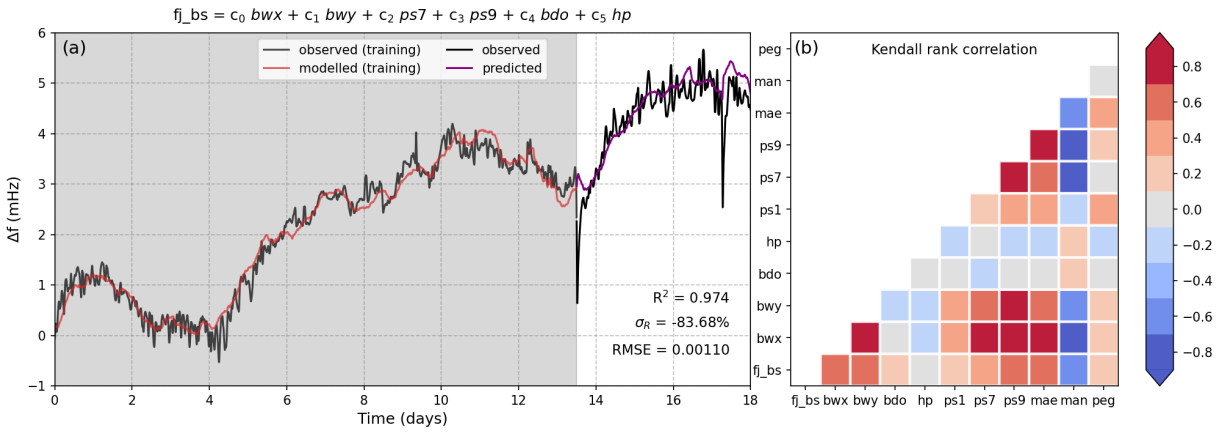

Figure 3.22: (a) A time series of the smoothed Sagnac frequency at RV as observed (black) and modelled (red). Data in the gray shaded area are used to fit a linear, multi-variant model as defined on top. The prediction (purple) is based on the obtained model coefficients. Kendall rank correlation coefficient matrices are shown in (b) for the smoothed Sagnac frequency without backscatter (fj_bs) with other observables: bwy = beam displacement in y-direction, bwx = beam displacement in x-direction, peg = water level, man = N-S tilt, mae = E-W tilt, $ps1|ps7|ps9$ = air temperature inside shaft 1|7|9, bdo = absolute barometric pressure, hp = Hilbert transform of barometric pressure.

Drift Correction

The estimated model can be used to correct for instrumental long-term drifts, yielding a strong variance reduction of the Sagnac frequency across 18 days compared to the backscatter corrected time series and reduces drifts to below 1 mHz (Fig. 3.23a).

An Allan deviation for the uncorrected Sagnac frequency shows a minimum for integration times around 120 s, and an increase towards larger integration times that is related to instrumental drifts. A backscatter corrected Sagnac frequency shifts the Allan deviation minimum towards 400 s. When additionally reducing the drift model, a reduction for integration times of above 10^5 sec is visible (Fig. 3.23b).

3.2.7 Discussion

Currently, only few large ring laser gyroscopes are operated for geophysical or geodetic observations of rotational motions. With its four individual RLGs, ROMY is the only existing instrument that can provide all three components of ground rotation at high sensitivity. The heterolithic realization of the ROMY structure naturally poses challenges with regard to the mechanical stability of the optical resonators. External drivers causing instrumental effects by altering the scale factor have to be understood, correlations quantified, and potentially avoided or corrected for in the future in order to enhance the operational stability for continuous high-quality data acquisition.

We report on observations of multiple RLGs operated across several months with simultaneous monitoring of the external environment. Uncorrected Sagnac beat frequency time series exhibit long-term drifts in a range of several tens of mHz over 5 months. For this period, the uptime with good quality data is around 85 % for all three operated RLGs (Fig. 3.8). An increase in maintenance frequency towards the end of this observational period is notable, introducing additional thermal variation. In terms of times between split-mode operation states, RU and RV appear to have a higher operational stability at around 6 hours (Fig. 3.8b). These parameters, however, are influenced by the configuration of the intensity control of the respective ring, which had to be adjusted individually over the observation period, and are therefore only of limited use for comparison purposes.

We present first results of a backscatter correction applied to an active, triangular-shaped, heterolithic RLG with 12 m side length. The detection of weak monobeam signals – relevant for backscatter corrections – is challenging in the presence of relatively strong electronic hum noise. As expected for larger RLGs, the contribution of backscatter-induced errors/drifts is reduced (Hurst et al. 2009), but the achieved reduction in frequency drift still ranges within 1 mHz to 2 mHz (see Fig. 3.10, S.8, and S.9). By correcting backscatter-induced frequency errors, a variance reduction of above 90 % can be achieved. For the 6.25 m^2 square, heterolithic ring ER-1, the backscatter introduced error is larger, reach-

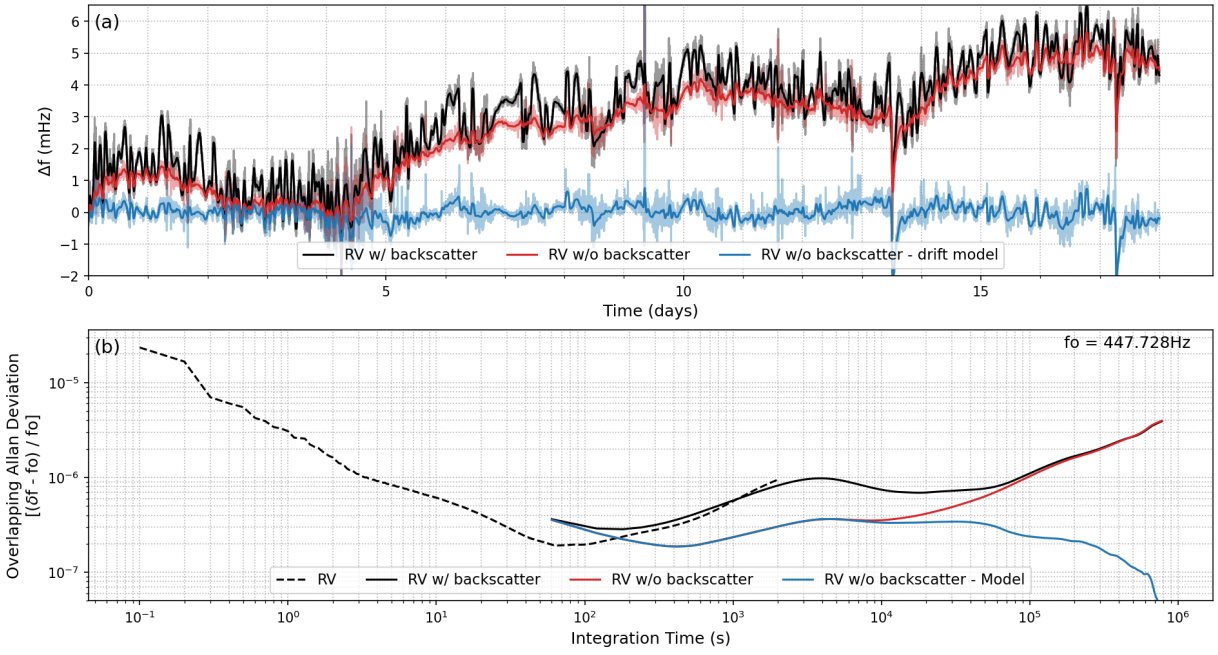

Figure 3.23: (a) Sagnac frequency variation of RV for 18 days (black) and without backscatter errors (red). The backscatter correct data is reduced by the drift model (blue). Solid lines represent a moving average of 60 min. (b) Overlapping Allan deviations of the scaled relative Sagnac frequency time series ($\Delta f/f_0$) with f_0=447.728 Hz. The dashed, black line is based on 5 hours of 10 Hz data to extend towards smaller integration times.

ing 50 mHz to 90 mHz (Zou 2021). For the square, heterolithic GINGERino with a side length of 3.6 m, the backscatter correction reduces Sagnac frequency fluctuations between −25 mHz to 30 mHz to below 2 mHz (Belfi et al. 2017).

In the backscatter corrected signal, long-term and short-term drifts remain, which we relate to atmospheric pressure and temperature induced deformations of the optical ring resonator. As these effects overlap, it is difficult to analyze them separately. We therefore focus on examples with a dominant influence of individual environmental drivers.

Short-term frequency drifts of several mHz in the backscatter corrected time series are observed and related to thermal perturbations. Across several hours, we relate temperature variations at the corners to integrated thermal strain along the resonator, causing expected mode jumps after one wavelength of deformation. The inferred linear thermal expansion coefficients are comparable to common values for concrete (Bamforth et al. 2008) or structural steel (ECCS 2015). These mode transitions often result in split-mode operation states, thus compromising the operational stability.

We present a passive thermal insulation design for ROMY's access shafts that successfully suppresses significant daily and sub-daily temperature variations previously observed in the near-surface shafts. This improves the short-term operational stability due to a more thermally stable condition at the corners of the ring resonator. Seasonal temperature trends, however, still propagate and compromise the long-term stability due to thermal deformation. Further passive shielding or active temperature stabilization might provide additional enhancement.

A beam wander monitoring setup has been successfully realized to quantify deformation at individual resonator corners, which reveals beam displacements of up to 200 µm over 3 weeks in a relatively undisturbed setup, while in the presence of strong temperature forcing similar displacements are observed within a few days.

Beam displacements over 74 days for RU vary in a range of 100 µm and 340 µm for the out-of-plane and in-plane direction, respectively (Fig. 3.11). Pritsch et al. (2007) reported beam displacements of 50 µm for the rectangle, heterolithic RLG UG-2 with a perimeter of 121.435 m, located in an underground cave near Christchurch, New Zealand. While a rotational deformation in-plane seems to be dominated by thermal expansion, the out-of-plane deformation reveals contributions of cavity deformation due to barometric pressure loading.

We find maximal coefficients for beam displacements at RV of up to 90.9 µm °C^{-1} over 4 days with dominantly temperature driven deformation. Strong temperature perturbations might promote non-linear behavior. For slower, more linear temperature variations, the coefficients are about half as large ($<$53 µm °C^{-1}).

Linear coefficients for the beam displacement caused by temperature variations are estimated for RZ, RV and RU. Absolute beam displacements for RZ show a low response to slow temperature variations 4.2 µm °C^{-1}, whereas RV seems to have a stronger thermal

response $52.9\,\mu m\,°C^{-1}$. For RU, we estimate a long-term thermal coefficient of $40\,\mu m\,°C^{-1}$ over 70 days (apporx. $0.57\,m\,°C^{-1}\,d^{-1}$) for in-plane beam displacement, driven by a seasonal temperature increase.

The in-plane direction of beam wander seems to dominantly result from inhomogeneous thermal deformation at the corners and foundation. This influences the Sagnac beat signal by varying the combination of the beams for the interferogram, as illustrated in Figure 3.24b and observed in Figure 3.12. When compared with FSR inferred perimeter changes, about half of the thermal expansion contributes to deformation at the corner and foundation that results in absolute beam walk, whereas the other half seems to be homogenous expansion, contributing only to perimeter change.

A periodic signature in the highpass filtered in-plane beam displacements, divided by the perimeter, with an amplitude of about 10 nm implies a correlation with theoretical tidal strain towards east.

Highpass signatures well correlated with pressure are present at the perimeter change record, although about four times smaller. Consequently, pressure induced deformation has a reduced effect on the perimeter change. We find a high correlation between the out-of-plane direction of the beam displacement with changes in barometric pressure for long-term observations (Fig. 3.11) and individual passing low pressure events (Fig. 3.20). For approx. 10 hPa change in barometric pressure, a displacement of about 6 µm is observed. Displacement in x-direction is roughly one order of magnitude smaller and does not reveal a clear correlation.

A response is also observed on the inertial tiltmeter, which is why we attribute this deformation to a local cavity effect, as discussed by Zürn et al. (e.g., 2007). The local barometric loading/unloading at the surface deforms the cylindrical corner shaft, being an underground cavity, in a way that the resonator corner deforms dominantly along the out-of-plane degree of freedom as illustrated in Figure 3.24a. A low twisting, i.e. in-plane displacement, deformation is expected for the vertically acting loading due to barometric pressure.

Variations of the near-surface hydrology causing asymmetric hydrostatic pressure changes are expected to have an effect on the orientation and possibly also internal deformation of the ROMY structure. At this stage, however, these effects are obscured by more pronounced effects, such as ambient temperature and air pressure.

A simple, linear multi-variant model reproduces dominant trends in beam displacements and supports a dominant effect of temperature on the in-plane and stronger effects of barometric pressure in the out-of-plane direction. While supporting the discussed correlations, the linear coefficients derived from the comprehensive modelling approach differ from those inferred from individual examples. Concerning thermal coefficients, comparable values for PS7 and PS9 as above between $-39.4\,\mu m\,°C^{-1}$ to $115.7\,\mu m\,°C^{-1}$ are obtained comprising both beam walk directions (see Table 3.1). In the comprehensive model, a coefficient of $-2.6\,\mu m\,hPa^{-1}$ is obtained, whereas a comparison with high frequency signatures of dis-

placement and pressure indicates a coupling coefficient of $1\,\mu m\,hPa^{-1}$. The discrepancy might be attributed to low-frequency pressure content involved in the modelling.

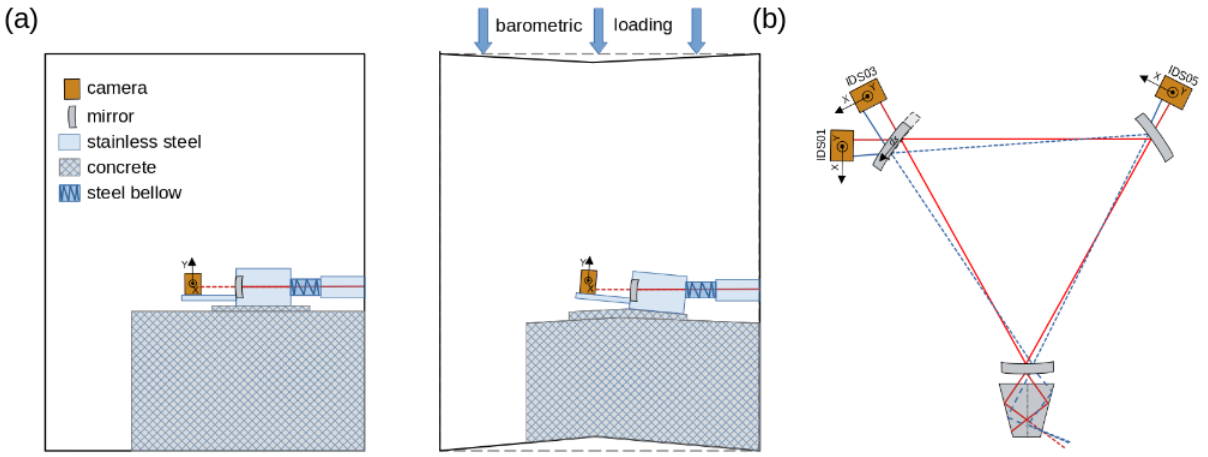

Figure 3.24: (a) Schematic deformation processes of a shaft due to barometric loading, reflected in out-of-plane beam displacement. (b) Schematic in-plane beam displacement due to mirror corner deformation. The upper left mirror is displaced, causing the formerly red beam plane to adjust to the blue dashed beam plane. Sketches are exaggerated and not to scale.

Predictions based on the model-derived coupling coefficients for beam walk based on the currently available short dataset show a decreased fit with actual observations. A linear approach might therefore be too simplistic to capture all involved processes appropriately. Observables, such as temperature, might also be sampled too coarsely along the optical resonator. A dominant contribution of the included observables, however, supports findings from case studies presented in Section 3.2.6.

In a next step, a linear, multi-variant drift model is derived for a Sagnac frequency times series of RV, incorporating a selected subset of six observables, that captures underlying drifts well.

When computing an Allan deviation for uncorrected data, the minimum is encountered at about 100 s to 200 s. After removing the backscatter errors, the minimum is shifted towards 400 s. A correction, based on the drift model, applied to the Sagnac frequency time series without backscatter errors, results in an improved Allan deviation, for integration times above 10^4 s (Fig. 3.23). For integration times of hours to days, the stability is improved.

An improved model might offer a removal of dominant long-term trends caused by environmental factors during post-processing, however, not improving short-term effects and the operational stability. The latter requires a sophisticated geometric stabilization system for all resonators. This is planned for the ROMY RLG in the near future.

3.2.8 Conclusions

We present observational data for the multi-component ring laser array ROMY with respect to environmental observations in order to relate external forcing to instrumental drifts. Operation of multiple RLGs of ROMY with an uptime more than 80% is feasible, providing observations for three components of rotational ground motion for geophysical (and eventually geodetic) applications. We acknowledge, however, that at this stage manual supervision and frequent maintenance is required. Backscatter correction, applied to the 12 m, triangular RLGs of ROMY, reduces the Sagnac frequency variations by about 2 mHz to 3 mHz and is compatible with the expectations.

Camera-based monitoring of beam walk at the mirror corners provides access to deformation of the optical resonator. We find beam displacements of tens to hundreds of μm over several days up to weeks, leading to significant variations of the RLG scale factor. This decreases the overall operational stability. Monitoring the 12^{th} FSR, we obtain perimeter changes of the order of $7\,\mu\mathrm{m\,d^{-1}}$, which is about twice the rate of beam walk, indicating a portion of a homogeneous corner expansion as well.

A dominant, long-term driver for deformation is thermal expansion, in particular for the in-plane beam displacement. We can attribute this to an undesired temperature sensitivity of the alignment lever assembly, in particular for the in-plane alignment. The in-plane displacement also reveals a periodic signature, likely related to horizontal tidal strain deformation. For the out-of-plane beam displacement, we observe a clear correlation with barometric pressure, likely related to tilt deformation of the corner's foundation induced by varying pressure loading on top.

A linear, multi-variant modelling approach enables to reproduce trends in beam displacement as well as the Sagnac frequency variations. Improvements in short-term thermal insulation are achieved by a newly installed passive insulation system. A seasonal temperature variation, however, is still present. Barometric pressure shielding with the current structural design is not realizable.

To exploit ROMY's full potential as the only multi-component, high-sensitive ring laser array for geodetic signals (e.g., polar motion or length of day variations) more effort has to be invested to increase long-term stability. The presented contribution to a better understanding of instrumental effects of ROMY caused by its environment, based on a new monitoring sensor network, serves as a basis to develop further strategies to stabilize the RLGs. Model based corrections of drifts caused by environmental factors during post-processing seem feasible. In order to achieve an enhanced operational stability and uptime by reducing short-term effects, a well-designed, active control system stabilizing the resonator geometry is essential.

Data and Resources

Ring laser data of ROMY were provided by the Geophysical Observatory in Fürstenfeldbruck (BayernNetz 2001). Extensive parts of data processing were done using modules of the ObsPy python package (Megies et al. 2011). All other data used in this paper came from published sources listed in the references. Processed data, data processing scripts and Jupyter notebooks to create the figures are accessible at the following repositories. For more details, please contact the corresponding author.

1. https://syncandshare.lrz.de/getlink/fiN8s26Zjy4bSoQBA9hSyF/RSI-ROMY-2024
2. https://github.com/andbrocode/InstrumentalEffectsROMY.git

Acknowledgements

We gratefully acknowledge support from the European Research Council for funding the ERC-Advanced ROMY Project (Grant number 339991). We appreciate the research funding and support of the faculty of geosciences of the Ludwig-Maximilians Universität München, Germany We are grateful for technical equipment for experimental setups provided by the Quantum Metrology Group of the University of Bonn, Germany. We are grateful to K. Maetschke for contributing the ROMY illustration in Fig. 3.7c. Continuous technical support from the staff at the Geophysical observatory in Fürstenfeldbruck, namely, J. Loos, M. Teerporten and S. Egdorf, is highly acknowledged.

Chapter 4

Rotational Seismology

Rotational seismology is a field that emerged after advances in ring laser technology made direct observations of weak ground rotations possible. Combining translational and rotational ground motion observations of the seismic wavefield provides an information gain of the particle motion with a single station. By following the linear elastic waveform theory for plane waves, information, for instance, about the local subsurface velocity structure or the backazimuth of plane waves can be obtained (e.g. Cochard et al. 2006, Keil et al. 2021).

The first article in this chapter (4.1) presents the first rotational low noise model on Earth. This model is derived from the constrained NLNM for vertical ground accelerations by Peterson (1993). Using global, model-based Rayleigh wave phase velocities, a RLNM for transverse rotations is constrained and validated with available observations. Knowledge of the background noise level is essential for experimental design, for a deeper understanding of our planet, and for instrument development as a benchmark.

The second article (4.2) was inspired by a research stay at PFO in 2022 within the scope of a Paros Scholarship awarded by the American Geophysical Union for projects related to geophysical instrumentation. During the research project, the former one-component ring laser gyroscope, named GEOsensor (Schreiber et al. 2006a), installed at the underground vault of the Piñon Flat Observatory was recovered. Instead, a three-component rotation rate sensor was installed, which, together with a seismometer, functions as a six degrees-of-freedom (6-DoF) station. This provides the opportunity to continuously study the local and regional seismicity using the 6-DoF methodology.

4.1 Characterizing the Background Noise Level of Rotational Ground Motions on Earth

by Andreas Brotzer, Heiner Igel, Eléonore Stutzmann, Jean-Paul Montagner, Felix Bernauer, Joachim Wassermann, Rudolf-Widmer Schnidrig, Chin-Jen Lin, Sergey Kiselev, Frank Vernon and Karl Ulrich Schreiber

Published in Seismological Research Letters (2024), 95 (3), 1858–1869
https://doi.org/10.1785/0220230202

Abstract

The development of high-sensitive ground motion instrumentation for Earth and planetary exploration is governed by so-called low-noise models, which characterize the minimum level of physical ground motions, observed across a very broad frequency range (0.1 mHz-100 Hz). For decades, broad-band instruments for seismic translational ground motion sensing allowed for observations down to the Earth's low noise model. Knowing the lowermost noise level distribution across frequencies enabled not only to infer characteristics of Earth such as the ocean microseismic noise (microseisms) and seismic hum, but also to develop highly successful ambient seismic noise analysis techniques in seismology. Such a low noise model currently does not exist for rotational ground motions. In the absence of a substantial observational database, we propose a preliminary rotational low noise model (RLNM) for transverse rotations based on two main wave field assumptions: the frequency range under investigation is dominated by surface wave energy and the employed phase velocity models for surface waves are representative. These assumptions hold in particular for a period range of about 2 s to 50 s and lose validity towards long periods when constituents produced by atmospheric pressure dominate. Since noise levels of vertical and horizontal accelerations differ, we expect also different noise levels for transverse and vertical rotations. However, at this moment, we propose a common model for both types of rotations based on the transverse RLNM. We test our RLNM against available direct observations provided by two large-scale ring lasers (G-ring and ROMY) and array-derived rotations (Piñon Flat Observatory PFO array, Gräfenberg array and ROMY array). We propose this RLNM to be useful as guidance for the development of high-performance rotation instrumentation for seismic applications in a range of 2 s to 50 s. Achieving broadband sensitivity below such a RLNM remains a challenging task, but one that has to be achieved.

4.1.1 Introduction

The concept of low noise models is known in many scientific fields and characterizes a minimum background noise level for a certain measurement in a given environment. Non-coherent noise levels, thus non-transient signals, are commonly described by computing a power spectral density (PSD) across the relevant frequency bandwidth. Applied on seismic, or more general, physical ground motions, this reflects the minimal power of seismic or physical background motions expected on a planet per frequency band under best observational circumstances. Therefore, a low noise model sets a minimum threshold for observations of signals of interest. For translational seismic ground motions, more precisely acceleration, a new low and high noise model (NLNM/NHNM) has been presented by Peterson (1993) replacing previous models by Brune & Oliver (1959). These models were based on the envelope of averaged PSDs computed for recordings of ground acceleration for a set of 75 global stations (Peterson 1993). The NLNM still serves as a benchmark for instrumental self-noise level of translational seismic sensors in order to resolve observations of the lowermost expected signals. With the emergence of rotational observations in seismology due to new instrumentation developments, such as large-scale Sagnac interferometers, also referred to as ring lasers (Stedman et al. 1995, McLeod et al. 1998, Schreiber & Wells 2023b), and optical fibre gyroscopes (Bernauer, Wassermann & Igel 2012, Bernauer et al. 2018), at the beginning of this century, a constant drive for improved instrumentation and application in seismology could be observed (e.g Pancha et al. 2000, Igel et al. 2005, Wassermann et al. 2009, Schmelzbach et al. 2018, Kislov & Gravirov 2021). Observations of three components of rotational ground motions complement classic observations of three components of translational ground motions. In general, a deformable elastic medium has 12 independent degrees of freedom (3 translations, 3 rotations and 6 strains; Aki & Richards (e.g. 2002)). Co-located seismometers and rotational sensors, with three components each (6C station), enable the application of new processing techniques (e.g. Igel et al. 2007, Sollberger et al. 2020), in particular for field deployment (Yuan et al. 2020), to better understand seismic wave fields and the subsurface. Resulting benefits comprise, for instance, general wave field decomposition (Sollberger et al. 2020), ambient noise analysis (Hadziioannou et al. 2012, Tanimoto et al. 2015), site characterization (Keil et al. 2021, Singh et al. 2020), local measurement of anisotropy (Noe et al. (2022), Tang et al., (in prep.)), improved structural health monitoring (Zembaty et al. 2021, Liao et al. 2022), teleseismic and eigenmode observations (e.g. Igel et al. 2011, Nader et al. 2015, Lin et al. 2011), enhanced moment tensor inversion (Donner et al. 2016), dynamic tilt correction of horizontal components of seismometers (e.g. Bernauer et al. 2020b), especially for ocean-bottom seismometers (Lindner et al. 2017), as well as structural health monitoring (Guéguen & Astorga 2021). Currently, a variety of rotational sensors are operated and developed, such as large-scale ring lasers (e.g. Igel et al. 2021, Schreiber et al. 2006b, Ortolan et al. 2016), fibre optic gyroscopes (e.g. Bernauer et al. 2018), mechanical beam balances (e.g. Venkateswara et al. 2021, McCann et al. 2021) or liquid-based sensors (Leugoud & Kharlamov 2012). However, to fully exploit the above-mentioned variety of benefits for seismological applications, portable rotational sensors with improved sensitivity across a wide

frequency range are required. To benchmark this instrumentation development, knowing the rotational low noise model (RLNM) for Earth (and eventually other extraterrestrial bodies) is crucial.
We describe the employed methodology in Section 4.1.2, all data used for comparison to the theoretical low noise model for rotations in Section 4.1.3 and our results in Section 4.1.4. Supporting materials are appended.

4.1.2 Methodology

The NLNM by Peterson (1993) for vertical acceleration is inferred from global observations. Due to a current shortage of permanently operated rotational sensors with high sensitivity, we chose a theoretical approach to convert the NLNM for vertical accelerations to obtain a theoretical rotational low noise model (RLNM) for transverse rotations on Earth.

4.1.2.1 Translation to Rotation

In order to convert translations to rotations, we use known relations for plane waves in linear elasticity, introducing rotations at the free surface (e.g. Cochard et al. 2006). The rotation rate $\dot{\vec{\Omega}}$ is generally defined as:

$$\dot{\vec{\Omega}}(\vec{r},t) = \frac{1}{2}\frac{\partial}{\partial t}\left(\vec{\nabla} \times \vec{u}(\vec{r},t)\right). \tag{4.1}$$

where $\vec{u}(\vec{r},t)$ is the seismic displacement, at the location $\vec{r}$ and time t.
For SH-polarized waves (Love waves), the vertical rotation rate $\dot{\Omega}_Z$ is related via the horizontal Love phase velocity c_L with the transverse acceleration $\ddot{u}_T$:

$$\dot{\Omega}_Z = -\frac{1}{2}\frac{\ddot{u}_T}{c_L}. \tag{4.2}$$

For SV-polarized waves (Rayleigh waves), the transverse rotation rate $\dot{\Omega}_T$ is related via the horizontal Rayleigh phase velocity c_R with the vertical acceleration $\ddot{u}_Z$:

$$\dot{\Omega}_T = \frac{\ddot{u}_Z}{c_R}. \tag{4.3}$$

The equations (4.2) and (4.3) have been described in previous literature (e.g. McLeod et al. 1998, Igel et al. 2005, Pancha et al. 2000, Belfi et al. 2012, Lin et al. 2011). A more detailed derivation is provided in the supplementary materials of this article (Appendix 6).
The existing NLNM for vertical translations as power spectral density (PSD) (Peterson 1993), commonly encountered as relative decibel units, enables an estimate of a low noise model for (transverse) rotations using equation (4.3) according to:

$$PSD_\Omega(T) = \left(\sqrt{10^{PSD_a^{dB}(T)/10}}/c_{ph,R}(T)\right)^2 \quad \text{with} \quad [PSD_\Omega(T)] = \frac{rad^2}{s^2 Hz}, \tag{4.4}$$

where T denotes the period and $c_{ph,R}(T)$ is the dispersive Rayleigh phase velocity. See appendix 6 for more details. This approach, however, relies on two essential assumptions:

1. The power of the vertical acceleration in the NLNM is attributed dominantly to fundamental mode Rayleigh waves, at least for a range of 2 s to 200 s where this assumption approximately holds.

2. The global, dispersive Rayleigh phase velocity structure (for the fundamental mode) is known or modelled as a distribution or maximum likelihood curve.

These assumptions and their consequences are discussed in detail in Section 4.1.5. In this article, figures are consistently discussed in terms of power or rather power density ($\frac{rad^2}{s^2 Hz}$) of rotational rate ($\frac{rad}{s}$) observations and across periods instead of frequencies.

4.1.2.2 Global Phase Velocities

We used the global S-wave velocity model obtained by Haned et al. (2016), hereafter called HUM2. This model was derived from the inversion of path average Rayleigh wave group velocities measured on empirical Green functions in the period range from 32 s to 246 s. The crustal part of the model is based on Crust1.0 (Laske et al. 2013) laterally smoothed with a correlation length of 800 km, which corresponds to the resolution of the mantle part of the model. The lateral resolution of this model is sufficient for investigating the rotational low noise model. Phase velocities were then computed on a grid of 1x1 degrees, following Saito (1988) and using the model HUM2. To infer the global phase velocities for fundamental mode, dispersive Rayleigh waves, two processing steps were applied:

1. The sampling density at the pole regions has been reduced by introducing a minimum distance (4 degrees $\approx$ 444 km) between sampling locations along each latitude, to avoid a regional bias. The re-sampled locations are shown in Figure S.17b.

2. Sampling locations in the oceans are neglected by using a geographic continent/ocean mask (Todd 2020) in order to satisfy the assumption of observing dominantly fundamental mode Rayleigh wave energy and use comparable velocity profiles for continental crust only.

The sampled locations to extract phase velocities, based on the HUM2 model (Haned et al. 2016), are shown in Figure S.17a. A probability density distribution of all 1542 extracted phase velocities within 2 s to 200 s are shown in Figure 4.1b as a probability density distribution. As expected, high variance of Rayleigh phase velocities is observed for shorter periods (below 10 s), which are mostly sensitive to the large lateral variations of the crust and lithosphere. Towards longer periods, phase velocities display less lateral variations.

4.1.3 Observational Data

In order to validate the proposed theoretical RLNM, we compare it to available direct observations of large-scale ring lasers as well as array-derived rotational ground motions based on three seismic arrays with different apertures, thus period ranges. All data cover

the entire year of 2019 and are described in detail hereafter. An explicit exclusion of seismic events has been neglected and dominating seismic noise is assumed across the long observation period justifying PSD computation.

4.1.3.1 Statistical Single Station Validation

To evaluate the model in a first step, we chose a statistical approach to infer many local rotational models using vertical acceleration recordings and the local Rayleigh wave phase velocities computed for the HUM2 model (Haned et al. 2016). Data of the entire year of 2019 of 120 globally distributed seismic stations (Figure S.17a) are used to infer mean and median PSDs for each station. An estimate of the local PSD for rotational ground motions is obtained using the local Rayleigh wave phase velocities, which are interpolated at each station location (Figure 4.3e).

4.1.3.2 Array Derived Rotations

Rotational ground motions can be inferred from well-designed seismic arrays (Huang 2003, Spudich & Fletcher 2008, Suryanto et al. 2006). Three-component array derived rotations (ADR) are computed for 2019 for three different seismic arrays: 1) the ROMY array (RMY) surrounding the site of the Geophysical Observatory in Fürstenfeldbruck, Germany, 2) a subset of the Piñon Flat Observatory array (PFO array) in California, USA, and 3) a subset of the Gräfenberg array (GRF) located in southeastern Germany.
For RMY, an inner array comprising four stations (FUR, FFB1, FBB2, FFB3) and an outer array with six stations, using FUR as a central station, is deployed (see Figure S.12b). The station distribution of the selected seismic arrays is shown in Figure S.12 with the arrays' aperture indicated. The frequency range for array derived rotations is limited:

$$\frac{0.03\ c}{a} < f < \frac{0.25\ c}{a}\ , \tag{4.5}$$

where the lower limit depends on the array's aperture a and the local apparent horizontal seismic phase velocity c (Spudich & Fletcher 2008, Poppeliers & Evans 2015). Poppeliers & Evans (2015) set the value of 0.03 for the lower frequency limitation based on amplitude measurement uncertainty and inter-station distances, both being crucial for gradient calculation. For the PFO array, Donner et al. (2017) adjusted the lower frequency limit:

$$\frac{0.00238\ c}{a} < f < \frac{0.25\ c}{a}\ , \tag{4.6}$$

based on a re-evaluation of the amplitude uncertainty of the arrays' sensors. Table 4.1 lists the applied limits for the three arrays. Hourly power spectral densities are computed for each of the three components (Figures S.13, S.14, S.15 and S.16). As a statistical representation, a median PSD is generally compared with the proposed RLNM.

Table 4.1: *Frequency limits (f_{min} and f_{max}) according to equations (4.6) and (4.5) and required quantities (a = aperture; c = apparent phase velocity) for the seismic arrays PFO, GRF and RMY (see. Figure S.12 are listed. The RMY array is divided into an inner (RMY_i) and outer (RMY_o) sub-array.*

	a (m)	c (km/s)	f_{min} (Hz)	f_{max} (Hz)	$1/f_{min}$ (s)	$1/f_{max}$ (s)
PFO	730	3.8	0.01	1.3	80.7	0.8
GRF	17851	3.8	0.006	0.05	156.6	18.8
RMY_o	2628	3.4	0.04	0.3	3.1	25.8
RMY_i	230	3.4	0.4	3.7	0.3	2.3

4.1.3.3 Ring Laser Observations

Direct measurements of vertical ground rotations are provided by permanent, large-scale ring lasers (= optical Sagnac interferometers). For this study, data of 2019 of the G-ring, located at the Geodetic Observatory in Wettzell (Germany) (e.g. Schreiber et al. 2006b) and the vertical component of ROMY (ROtational Motions in seismologY) ring laser array (Igel et al. 2021), located at the Geophysical Observatory in Fürstenfeldbruck (Germany), are incorporated. Lasing in a horizontal plane, both the G-ring as well as the horizontal ring of ROMY are sensitive to rotations around a vertical axis. Hence, these rotational motions are induced by SH-polarized seismic waves (Love waves). The computed hourly PSDs for ROMY and G-ring of 2019 are shown in Figure 4.2. Gaps result from non-operational periods and maintenance work. The secondary microseism is the dominating signal (2 s to 10 s), with expected seasonal variation, yielding more energy in the winter months compared to the summer months (e.g. Tanimoto et al. 2015).

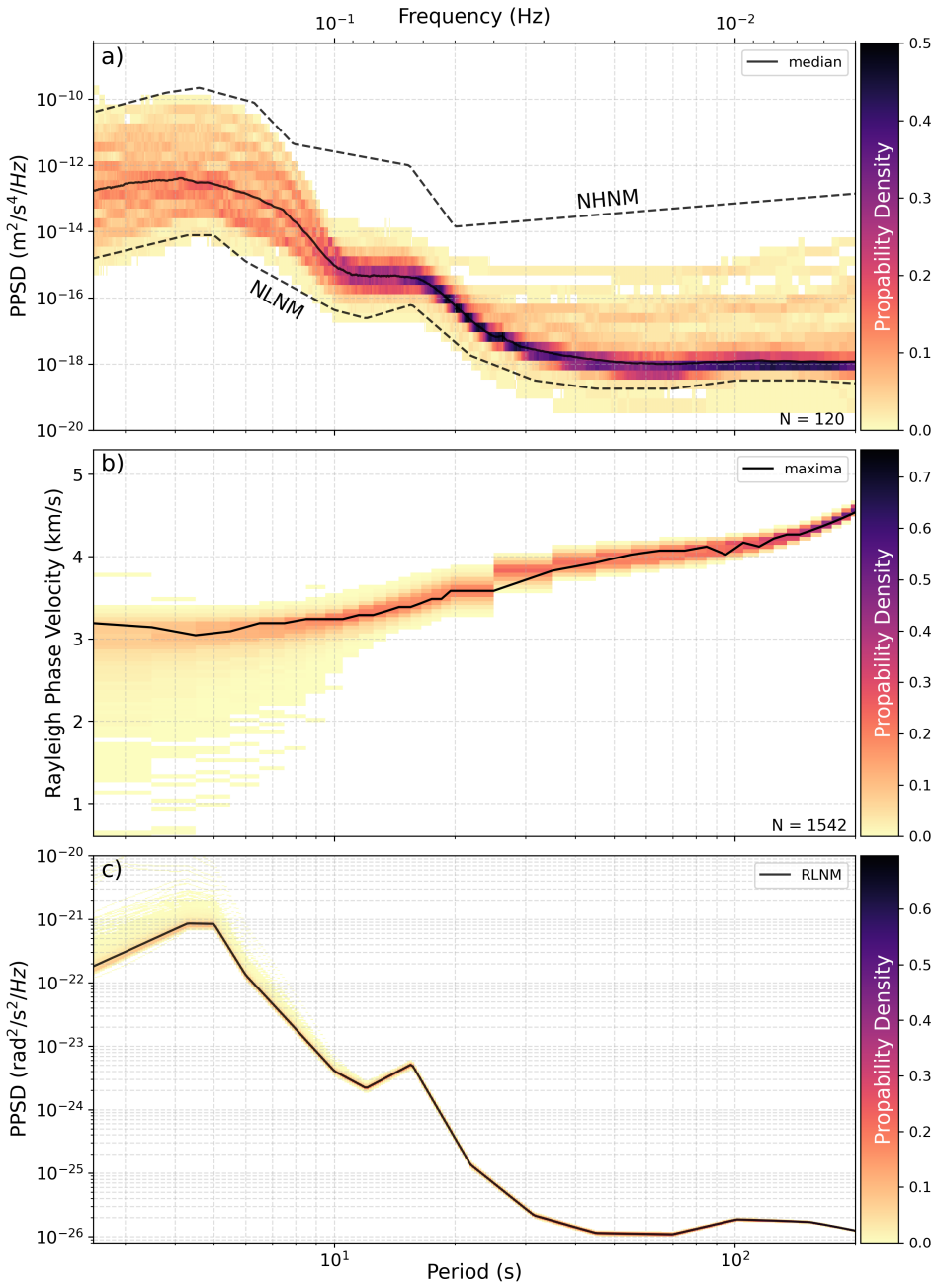

Figure 4.1: **a)** shows the distribution of yearly median PSDs for all stations shown in Fig. S.17A color-coded as a probability density with a computed median PSD and the NLNM and NHNM (, black lines) by Peterson (1993). **b)** shows the probability density of Rayleigh phase velocity curves extracted and smoothed from CRUST1.0 (Laske et al. 2013) at sampling locations shown in Fig. S.17b. The black line indicates the maximum of the distribution. **c)** shows the estimated rotational low noise models based on the NLNM in panel A and the phase velocity curves in panel b). The black, solid line indicates the median rotational low noise model (RLNM).

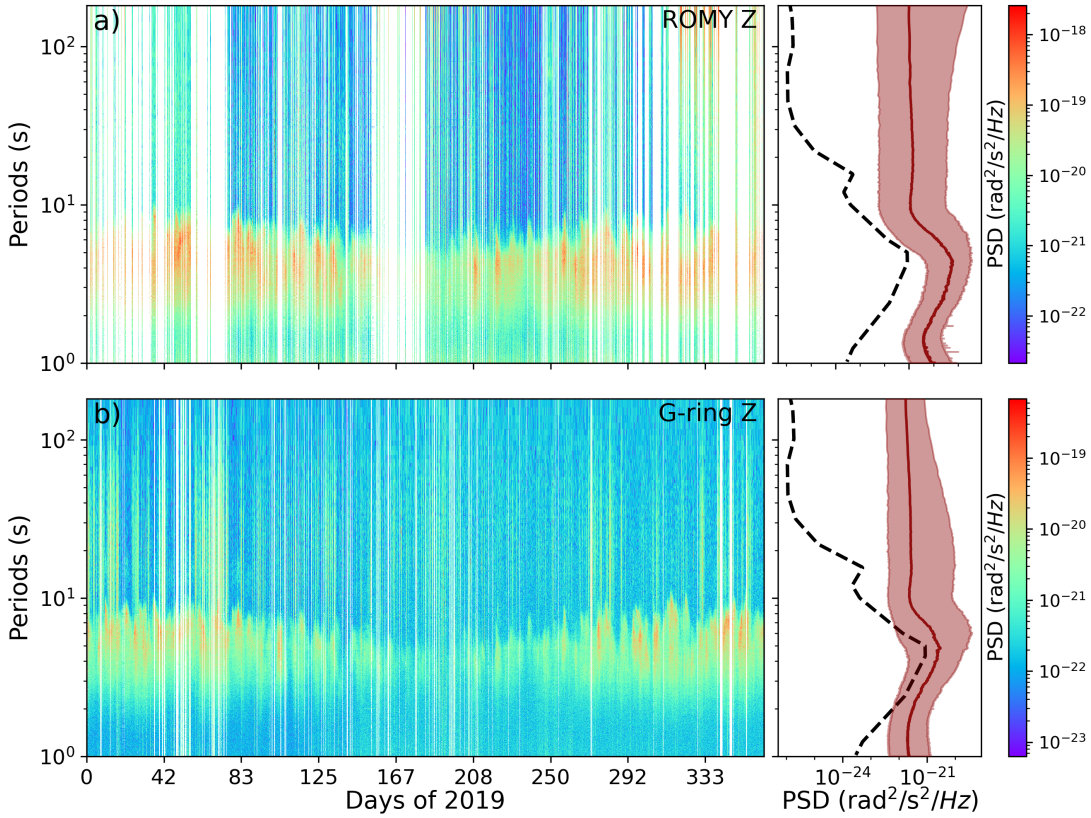

Figure 4.2: The left panels show hourly power spectral densities for 2019 for the vertical component of **a)** the ROMY ring laser in Fürstenfeldbruck, Germany and **b)** G-ring in Wettzell, Germany. The right panel represents the median of all PSDs (red, solid) with a 95% confidence interval (red shade). The black, dashed line represents the Rotational Low Noise Model (RLNM).

4.1.4 Results

We convert the NLNM for vertical acceleration to a low noise model for transverse rotations using equation (4.3). Figure 4.1c shows the obtained rotational low noise models as a probability density distribution for a selected bandwidth of 2 s to 200 s. The median of the distribution is selected and referred to hereafter as a theoretical rotational low noise model (RLNM). For the secondary microseism peak at approx. 4 s to 5 s, the RLNM yields a level of about $10^{-21}\,\mathrm{rad^2\,s^{-2}\,Hz^{-1}}$ and for the primary microseism peak (approx. 14 s) a level of about $5 \times 10^{-24}\,\mathrm{rad^2\,s^{-2}\,Hz^{-1}}$. A minimum rotational noise level is defined at 50 s to 70 s with $10^{-26}\,\mathrm{rad^2\,s^{-2}\,Hz^{-1}}$. For the secondary microseism, all three components of ADR of the PFO array show a smooth increase in power towards the peak with a steep drop towards 10 s (Figure 4.3a).

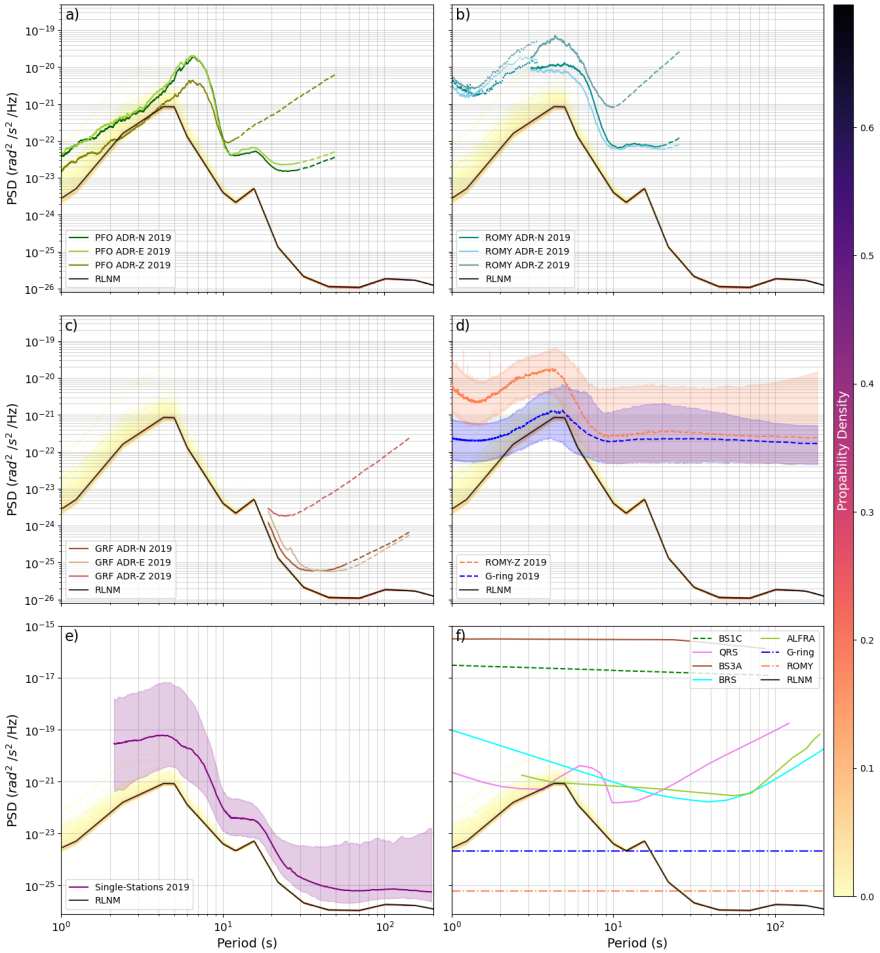

Figure 4.3: Inferred Rotational Low Noise Models (RLNM) are shown as a probability density distribution while the minimal RLNM is plotted as a black, solid line. Compared are median PSDs of 2019 for three components of array derived rotations (ADR) for **a)** the Piñon Flat Observatory (PFO) array in California, USA (UCSD 2014), **b)** the outer (solid) and inner (dotted) ROMY (RMY) array in Fürstenfeldbruck, Germany as well as **c)** a sub-array of the German Gräfenberg array (GRF) (GRSN 1976), where fainted colors are outside the estimated usable frequency range of this array. Dotted lines towards longer periods for ADR indicate contamination by tilt predominantly by horizontal components, thus affecting vertical rotations the most. **d)** shows the median PSDs of 2019 (dotted) and medians of selected days (solid) for vertical rotations of the large ring laser ROMY and G-Ring both located in Germany. The 90%-confidence interval is shown as colored area, respectively. A single-station model in **e)** is based on median PSDs of 2019 of global seismic stations converted to rotations using local phase velocity profiles extracted from CRUST1.0 (Laske et al. 2013). **f)** compares self-noise levels of existing portable sensors BS3A (Bernauer et al. 2018), QRS (Venkateswara et al. 2021), BRS (Venkateswara et al. 2017), ALFRA (McCann et al. 2021) (solid lines), a theoretical limit based on geometrical design only for large-scale ring lasers (ROMY and G-ring; dash-dotted lines) and planned BS1C (Guattari (pers. comm.); dashed line).

The peak for the secondary microseism shows an offset of about 2 s towards longer periods compared to the RLNM (Figure 4.3a and 4.3b). Detailed investigations of this shift, observed at the PFO, is not within the scope of this article. For the horizontal components, the peak of primary microseism is present with about one order of magnitude in power above the model (Figure 4.3a). The ADR power spectra of the inner and outer RMY array show a broad peak for the secondary microseism band with approximately one order of magnitude in power higher (Figure 4.3b). For the horizontal components, a signature of the primary microseism is present. The horizontal components of ADR for the GRF array follow the RLNM for periods within 18 s to 70 s (Figure 4.3c), supporting the estimated low noise level for these periods. A continuation of the PSD outside the sensitive period band of the array (see Table 4.1) is indicated with dotted and dashed lines in Figure 4.3c. Median PSDs and a 95 % confidence interval based on all PSDs of 2019 is shown in Figure 4.3d. For periods longer than 10 s, the optical Sagnac interferometers G-ring and ROMY approach a power level at approximately $2 \times 10^{-22}\,\mathrm{rad^2\,s^{-2}\,Hz^{-1}}$ and $3 \times 10^{-22}\,\mathrm{rad^2\,s^{-2}\,Hz^{-1}}$, respectively. This limit is mainly controlled by optical losses of the optical resonator at the coated mirrors. Generally more energy in the period band for secondary microseisms for ROMY compared to G-ring is most likely attributed to the geological setting of ROMY inside the pre-Alpine Molasse basin and its amplification characteristics.

4.1.5 Discussion

4.1.6 Validation of the Rotational Low Noise Model

The new low and high noise models by Peterson (1993) have been influencing seismology in terms of better understanding Earth by quantifying its continuously excited noise levels across frequencies, as well as a benchmark for instrument developers to provide instruments able to observe the smallest signals. If taken at face value, the RLNM is 3 to 4 orders of magnitude (see Figure 4.3f) in power below the self-noise level of currently operating (portable) ground rotation sensors, while at the same time self-noise level of today's broad band seismometers are below the NLNM in the studied period band. In order to close this gap and observe rotational ground motions at the level of the RLNM, major technical developments are still required. We provide a first estimate of the transverse rotational low noise model for Earth based on a conversion of the new low noise model for vertical accelerations using globally distributed phase velocities of Rayleigh waves. The underlying assumptions are 1) that Rayleigh waves are the most energetic waves contributing to the seismic noise for periods between 2 s to 200 s and 2) the model-based phase velocities are representative. Concerning the latter assumption, the largest variations are at short period and related to the crust and lithospheric lateral heterogeneities. We are using phase velocities derived from recent global models. In order to convert vertical acceleration into transverse rotation with equation (4.3), it is assumed that most of the seismic energy corresponds to the Rayleigh waves as stated at the end of Section 4.1.2.1 as assumption 1. Ambient seismic noise in the 3 s to 300 s period range is generated by ocean wave interactions with specific mechanisms depending on the period range (Hasselmann 1963,

Ardhuin et al. 2015). Secondary microseisms (period band: 3 s to 10 s) are generated by ocean gravity wave-wave interactions and have been successfully modeled by considering the propagation of Rayleigh waves from the source regions to the stations (Stutzmann et al. 2012). Primary microseisms (period band: 10 s to 20 s) are generated by ocean gravity waves interacting with the shallow ocean floor at the coast and can also be effectively modeled by considering only Rayleigh wave propagation (Gualtieri et al. 2019). Finally, the seismic hum with periods between 50 s to 300 s was successfully modeled by considering ocean infragravity waves hitting continental shelves as source mechanisms and the propagation of Rayleigh waves (Deen et al. 2018). Most sources of seismic noise in the period range of 3 s to 300 s originate from the ocean. Based on excitation by pressure loading at the ocean floor, Rayleigh waves are excited predominantly and polarized in the plane of propagation. However, Love waves, which have transverse polarization, have also been observed (e.g. Friedrich et al. 1998). Recently, Le Pape et al. (2021) and Gualtieri et al. (2021) showed that Love wave constituents of secondary microseisms can be generated by Rayleigh-to-Love wave conversion on a 3D interface close to the source region. An analysis of the average energy ratio of Rayleigh-to-Love waves for the secondary microseism including rotational measurements for the G-ring site in Wettzell yields a range of 0.9 to 1.0 (Tanimoto et al. 2015). For the site of PFO using seismic array data, energy ratios of 2.0 to 2.5 were obtained (Tanimoto et al. 2016). For Japan, a ratio estimate of approximately 2 was reported by Nishida et al. (2008). Although the Rayleigh-to-Love ratio is highly variable (Juretzek & Hadziioannou 2016), it seems that considering only Rayleigh waves propagation serves a valid first-order approximation to support assumption 1 in Section 4.1.2.1. To account for assumption 2, stated in Section 4.1.2.1, on dispersive, global phase velocities for Love and Rayleigh waves, we relied on up-to-date crustal and upper mantle models and employed median velocities to suppress local effects of the globally sampled velocities.

The median and confidence interval of the single station estimate based on local rotational models is compared to the RLNM in Figure 4.3e. The overall characteristics of the model are reflected, however with an overall higher power level, that we attribute mostly to station quality.

ADR data of three arrays support the RLNM for their respective frequency range. An increase in power towards longer periods is observed for all array-derived rotation data, which can be attributed to a dominating influence of amplitude noise for longer periods affecting derived gradients. For all arrays, the vertical ADR spectra show higher noise levels compared to the horizontal ones. Generally, horizontal components of translational records are more noisy.

Large-scale ring lasers currently provide the best direct, high-sensitive measurement of rotational round motions. A non-portable ring laser, however, is not directly comparable to portable sensors neither in design nor operation effort operation costs. A theoretical sensitivity limit, for the large-scale ring lasers G-ring and ROMY, respectively, is shown in Figure 4.3f. This resolution or sensitivity limit is merely taking into account the geometrical design of the ring, therefore defining a pure theoretical limit. We neglect limitations due to noise sources (e.g. lasing process, electronic self-noise or cavity losses at the mir-

rors). The dominant limitation, defining the current observation levels (see Figure 4.3d), is dominated by the scattering, transmission and absorption losses at the coated mirrors of the resonator cavity.
Fiber optic rotational rate sensors, such as the blueSeis-3A sensor (BS3A; Bernauer et al. (2018)) or the planned blueSeis-1C sensor (BS1C; pers. comm.), already offer many field applications based on rotational sensing, however, their instrumental self-noise levels are still $2-4$ orders of magnitude in power above the presented RLNM. Self-noise characteristics of three mechanical beam balances under development for horizontal components, namely ALFRA (McCann et al. 2021), QRS (Venkateswara et al. 2021) and BRS (Venkateswara et al. 2017), are shown in Figure 4.3f. With regard to the QRS sensor, the presented self-noise level is inferred from observations in a vault (Venkateswara et al. 2021), which seemed to reveal some power in the secondary microseism band. For the secondary microseisms range (2 s to 10 s), a reduction of the self-noise level for BRS, QRS and ALFRA of about 1 to 2 orders of magnitude in power would be sufficient to resolve signals at the RLNM. For periods above about 20 s, still 2 to 3 orders of magnitude in power of reduction is required.
In order to gain access to the full dynamic range of rotational signals, the self-noise levels of these sensors have to be further reduced below the RLNM for the seismically active frequency range between 2 s to 100 s (10 mHz to 0.5 Hz).

4.1.6.1 Comparison of NLNM and GSN Low Noise Models

We decided to focus on the NLNM by Peterson (1993) as a well-cited benchmark for vertical seismic acceleration observations. Other low noise models, based on data of the Global Seismic Network (GSN) for vertical (GSN-Z) and also horizontal (GSN-H) accelerations, introduced by Berger et al. (2004), are converted to rotational models in Figure 4.4 for comparison purposes. The GSN-Z model only shows minor deviations from the NLNM, thus the converted transverse rotational low noise models RLNM-T$_{NLNM}$ and RLNM-T$_{GSN-Z}$, respectively, match well.
For the conversion, an assumption of dominantly first-order Rayleigh wave energy for vertical component for the investigated frequency bandwidth has been made and discussed. In order to convert the GSN-H noise model to rotational rates, an assumption of dominantly Love wave energy would be required. This would be a very strong assumption, when assuming equipartitioning of Love wave and horizontal Rayleigh wave energy. We nevertheless include the conversion of the GSN-H model for horizontal accelerations using Love phase velocities (see Fig. 4.4b) according to equation (4.2). The resulting model (RLNM-V$_{GSN-H}$) shows a noise level for vertical rotations of about one order of magnitude in power lower compared to transverse rotations, while converging towards longer periods (Fig. 4.4c). This resembles the characteristics for horizontal acceleration noise levels, being lower for the microseisms bands and higher towards longer periods, in comparison with vertical acceleration noise models (Fig. 4.4a). For the range of 2 s to 20 s, the GSN-H model suggests a lower noise floor for horizontal accelerations with respect to vertical accelerations. As vertical rotations are induced by horizontal motions, we assume the noise floor

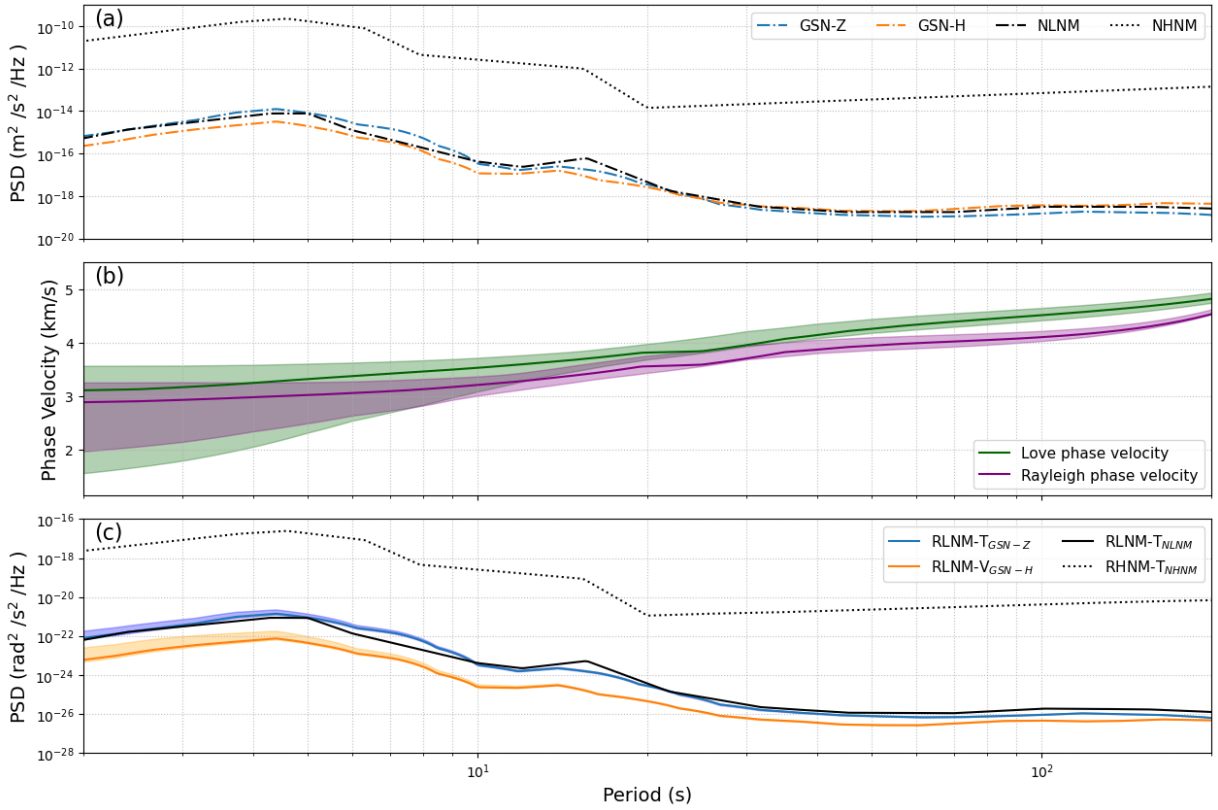

Figure 4.4: **a)** shows a translational low noise models for ground acceleration: the new low/high noise models (NLNM/NHNM) by Peterson (1993) as well as the horizontal (GSN-H) and the vertical (GSN-Z) low noise model based on data of the Global Seismic Network (GSN)) by Berger et al. (2004)). In **b)** the phase velocities for Rayleigh and Love waves are shown, including a 95% confidence interval. **c)** shows the corresponding low noise models for transverse (-T) and vertical (-V) rotational motions according to equations (4.2) and (4.3). Here we assume that the GSN-Z noise is predominantly composed of Rayleigh waves while the GSN-H noise is predominantly made up of Love waves, being aware that the latter assumption of equipartitioning is a very strong assumption.

of a vertical RLNM to be rather lower than higher with regard to the transverse RLNM for the respective period band.

While we consider the assumptions for the derivation of the transverse RLNM to be on solid ground, we acknowledge that the assumptions that went into the construction of the vertical RLNM are not. Therefore, we simply propose that the former model should be taken as a benchmark for both types of rotations until better constrained vertical RLNM models become available.

4.1.6.2 Towards Long Periods

The proposed low noise model for rotational ground motions is restricted by the discussed assumptions, in particular concerning the period range. Towards long periods above 200 seconds to 300 seconds, locally generated noise resulting from atmospheric movement above the station starts to dominate seismic far-field signals, such as spheroidal and toroidal hum introduced rotations. Those influences are likely pronounced differently for vertical and transversal rotational components. For vertical and horizontal rotational observations at long periods, we expect a different level in analogy to translational observations since local processes, such as atmospheric pressure induced ground tilts, influence vertical and horizontal components differently.

4.1.7 Conclusions

We propose a (transverse) rotational low noise model (RLNM) based on the NLNM by (Peterson 1993) for vertical accelerations, assuming dominantly Rayleigh wave type energy across a period range of 2 s to 200 s. The conversion is based on surface wave velocities extracted from state of the art lithospheric seismic velocity models. A comparison with GSN low noise models for accelerations by Berger et al. (2004) reveals a lower noise level for vertical rotations of about one magnitude in power, however, requiring a strong assumption of equipartitioning for the conversion. We expect different levels for transverse and vertical rotation noise floors, but we propose that the transverse RLNM be taken as a benchmark for both types of rotations until better constrained vertical RLNM models become available.

In order to validate the RLNM with currently available observations, we used array-derived rotations from three differently sized seismic arrays and direct rotational measurements of the large-scale ring lasers, G-ring and ROMY, over the entire year of 2019. All observational data are compatible with the inferred background noise level for rotations of the RLNM for their representative period bands.

Self noise of state of the art rotational sensors, either already operational or still under development, are compared against the RLNM. Large-scale, high-sensitive ring lasers, such as G-ring and ROMY, approach the RLNM, in particular at the secondary microseism peak. Lowering the currently limiting self-noise levels for these ring lasers requires technical improvements, especially for the coated corner mirrors, to reduce losses of the optical cavity.

Available portable rotational sensors (e.g. blueSeis-3A, ALFRA, QRS) already provide a sensitivity level sufficient for a wide range of geophysical applications or seismic isolation (e.g. gravitational wave detectors). None of these sensors, however, has currently a self-noise level below the proposed RLNM. Although lowering self-noise levels of rotational sensors below the RLNM remains technically challenging, it is nevertheless essential to achieve this goal to extend the domain of applications to that currently possible with classic seismometers.

Data and Resources

Data of the Ring laser ROMY and its seismic array were provided by the Geophysical observatory in Fürstenfeldbruck (BayernNetz 2001). Data of the G-ring were provided by the Geodetic observatory in Wettzell. Data of the Piñon Flats Observatory array (UCSD 2014) and the Gräfenberg array (GRSN 1976) are openly accessible via IRIS and BGR FDSN services, respectively. Data of the Global Seismograph Network II (GSN 1986), Global Seismograph Network IU (GSN 2014) and GEOSCOPE network G (GEOSCOPE 1982) went into the analysis and the free availability is acknowledged. Extensive parts of data processing were done using modules of the ObsPy python package (Megies et al. 2011). Phase velocities are computed using the model from Haned et al. (2016). GSN noise model data are based on Berger et al. (2004). All other data used in this paper came from published sources listed in the references.

The supplementary materials of this article (see Sec. 6) include a more detailed background for the equations presented in Section 4.1.2 and additional figures related to the observational data used for comparison to the rotational low noise model.

Data files of the transverse rotational low noise model (RLNM) as well as Jupyter notebooks to re-create the figures of this article are provided online:

- https://github.com/andbrocode/RotationalLowNoiseModel.git
- https://zenodo.org/doi/10.5281/zenodo.10027880
- https://syncandshare.lrz.de/getlink/fiGtpiKTn9cmUtHixKqP1A/SRL-RLNM-2023

For more information, please contact the first author.

Acknowledgements

We gratefully acknowledge support from the European Research Council for funding the ERC-Advanced ROMY Project (Grant number 339991) and additional support from the Ludwig-Maximilians University (LMU) Munich. Heiner Igel is grateful for support from the Cecil and Ida Green Foundation supporting his visit to the Institute of Physics and Planetary Physics, University of Southern California, in 2022 and 2023. Special thanks to Céline Hadziioannou for fruitful discussions on the ocean microseism generation and energy partitioning. Finally, we acknowledge the suggestions made by the reviewers and the editor to enhance our manuscript.

4.2 On single-station, six degree-of-freedom observations of local to regional seismicity at the Piñon Flat Observatory in Southern California

by Andreas Brotzer, Heiner Igel, Felix Bernauer, Joachim Wassermann, Robert Mellors and Frank Vernon

Submitted to Seismica (2024)

Abstract

In September 2022, a portable, three-component rotational rate sensor, namely a blueSeis-3A gyroscope, has been deployed at the underground vault of the Piñon Flat Observatory (PFO) in southern California. A three-component, broadband seismometer is co-located, jointly forming a six degree-of-freedom (DoF) station for long-term observations of local and regional seismicity and multi-component wavefield studies. The seismic recordings are available online via IRIS FDSN services as PY.BSPF (BlueSeis at Piñon Flat).

The instrumentation at PFO additionally provides high-quality strain observations, allowing now to study translation, rotations and strain of the seismic wavefield in a low noise and high seismicity area (e.g. San Andreas fault zone). The seismic array at PFO is used to compute array derived rotations and validate the direct observations of rotational ground motions. We show results of 6 DoF processing applied to a local M_w=4.1 and a regional M_w=6.2 event to obtain backazimuth estimates, which we validate with array beamforming, and estimates of local seismic phase velocities.

For observed events between October 2022 and October 2023, we detect more than 400 events of which 118 are triggered on all six components. Peak rotation rate amplitudes are used to derive empirical peak amplitude relations for vertical and horizontal rotation rates to provide valuable insights towards resolvability for comparable 6 DoF campaigns. We find the dominating limitations for rotational motion observations currently to be set by the self-noise level of the blueSeis-3A rotation sensor and encourage further instrumental development.

4.2.1 Introduction

With the emergence of rotational ground motion observations in seismology based on new instrumentation development (e.g. optical fiber or vacuum Sagnac interferometer) at the beginning of this century, a constant drive for improved instrumentation and application in seismology could be observed (e.g., Pancha et al. 2000, Igel et al. 2005, Schreiber et al. 2009). Observations of three-components of rotational ground motions supplement classic observations of three-components of translational ground motions, thus provide a more complete observation of particle motions considering a full linear elastic seismic wavefield, which is characterized by a total of 12 degrees-of-freedom (3 translation, 3 rotation and 6 independent strain). A co-located broad-band seismometer and rotation sensor, with three-components each, are referred to as a six degree-of-freedom (6 DoF) station. 6 DoF observations at a single station enable the application of new processing techniques (e.g., Cochard et al. 2006, Sollberger et al. 2020) to obtain similar information as a seismic array. Beneficial applications comprise, for instance, general wavefield decomposition by polarization analysis (Sollberger et al. 2018, 2020), near-surface site characterization (Keil et al. 2021, Singh et al. 2020), improved structural health monitoring (e.g., Zembaty et al. 2016, Trifunac 2009, Bońkowski et al. 2023, Guéguen et al. 2020, Guéguen & Astorga 2021), enhanced moment tensor inversion (Donner et al. 2016, 2018, 2020, Donner 2021, Ichinose et al. 2021) and dynamic tilt correction of horizontal components of seismometers (Bernauer et al. 2020b, Lin et al. 2022), especially for ocean-bottom seismometers (e.g., Lindner et al. 2017), source tracking (Yuan et al. 2020, Chen et al. 2023), teleseismic observations (e.g., Igel et al. 2005, Schmelzbach et al. 2018, Abreu et al. 2023) or for applied exploration data analysis (e.g., Schmelzbach et al. 2018). An increased information gain for single-station observations holds potential for studies on extraterrestrial bodies (Bernauer et al. 2020a). Currently, a variety of rotational sensors are operated and developed, such as large-scale ring lasers (Igel et al. 2021, Belfi et al. 2017), fiber-optical gyroscopes (e.g., Bernauer et al. 2018), mechanical beam balances (e.g., Venkateswara et al. 2017, McCann et al. 2021, Ross, Venkateswara, Hagedorn, Gundlach, Kissel, Warner, Radkins, Shaffer, Coughlin & Bodin 2017, Ross et al. 2023) or fluid based sensors (e.g., Bernauer, Wassermann & Igel 2012). However, to fully exploit the above-mentioned variety of benefits for seismological applications, portable rotational sensors with improved sensitivity across a wide frequency range are required. Brotzer et al. (2023) characterized the rotational background noise level to set a benchmark for instrumentation development.

Before recent, wavefield gradients, in particular rotations, were commonly neglected in seismological analysis and modelling due to their small amplitudes (Aki & Richards 2002) and a lack of instrumentation to observe the rotational motion of the seismic wavefield. While direct observations of local surface strain are observed for decades (e.g., Agnew & Wyatt 2003), it was a challenge to observe weak rotational ground motions (e.g., Schreiber et al. 2014). Technical advances in recent years, in particular optical sensing and read-out technologies, resulted in new instrumentation (Bernauer, Wassermann & Igel 2012, Bernauer et al. 2021) to directly access rotational ground motions (e.g. fiber-optical gyroscopes,

beam balance rotation sensors) and dynamic ground strain (e.g. distributed acoustic sensing (DAS)). This also called for the ongoing development of open-source packages for 6 DoF signal analysis, such as TwistPy (Sollberger 2023, Sollberger et al. 2023). Most experiments employing portable rotational sensors for 6 DoF observations and processing were short-term field deployments for specific case studies (e.g Wassermann et al. 2020, Yuan et al. 2020, Sbaa et al. 2017, Perron et al. 2018, Takeo 2009). A one-component, horizontal ring laser gyroscope, called GEOsensor, was installed at Piñon Flat Observatory (PFO) in 2005 (Schreiber et al. 2009) and dismantled in 2022. We report on a long-term deployment of a three-component blueSeis-3A rotation sensor (Bernauer et al. 2018) next to a three-component, broadband seismometer forming a 6 DoF station at PFO in southern California as replacement for the GEOsensor. The PFO is located between the San Andreas (25 km NE) and the San Jacinto fault zone (14 km SW) systems (Agnew & Wyatt 2003), which are seismically active fault zones on the Southern California segment of the Pacific and North-American plate boundary. The 6 DoF data is openly accessible online and provides an opportunity to apply 6 DoF analysis to local and regional seismicity.

4.2.2 Deployment

Currently, most 6 degree-of-freedom (DoF) stations are deployed for short-term field measurements (e.g Wassermann et al. 2020, Sbaa et al. 2017, Yuan et al. 2020). In late September 2022, a first permanent (= open-end) 6 DoF station was installed on an isolated granite pillar inside the underground vault at the Piñon Flat Observatory (PFO) in Southern California (see Fig. 4.5). Hence, the installation benefits from good coupling to the sub-surface while being decoupled from the vault, as well as stable ambient temperature conditions. The station consists of a portable, fibre-optic gyroscope blueSeis-3A sensor (by Exail, formerly iXblue), measuring three-components of rotational ground velocity (rad/s). This rotational sensor is provided by the Incorporated Research Institutions for Seismology (IRIS), now EarthScope Consortium. A full characterization of the blueSeis-3A was conducted by Bernauer et al. (2018). The data are openly accessible via IRIS FDSN service (UCSD 2014) with seed code: PY.BSPF..HJ* (with 200 Hz). All metadata is specified in a stationXML. A Trillium T120 broad-band seismometer (by Nanometrics) provides three-components of translational ground motion observations (II.PFO.10.BH* with 40 Hz). Since April 02, 2023, a STS-2 seismometer (by Streckeisen), named PY.PFOIX..HH*, was installed next to the blueSeis-3A, in order to provide translation and rotation observations up to about 50 Hz (based on a sampling rate of 200 Hz and the transfer function of the STS-2). The complete 6 DoF station (= six components) is hereafter referred to as BSPF.

4.2.3 Dataset

Generally, a basic, yet rapid event analysis is provided to the scientific community by an integration of the BSPF station into the rotational event database (Salvermoser et al. 2017). In this study, we analyze one year of data from October 01, 2022 until September 30, 2023. Figure 4.6a and 4.6b show all events listed by the USGS catalog (gray circles)

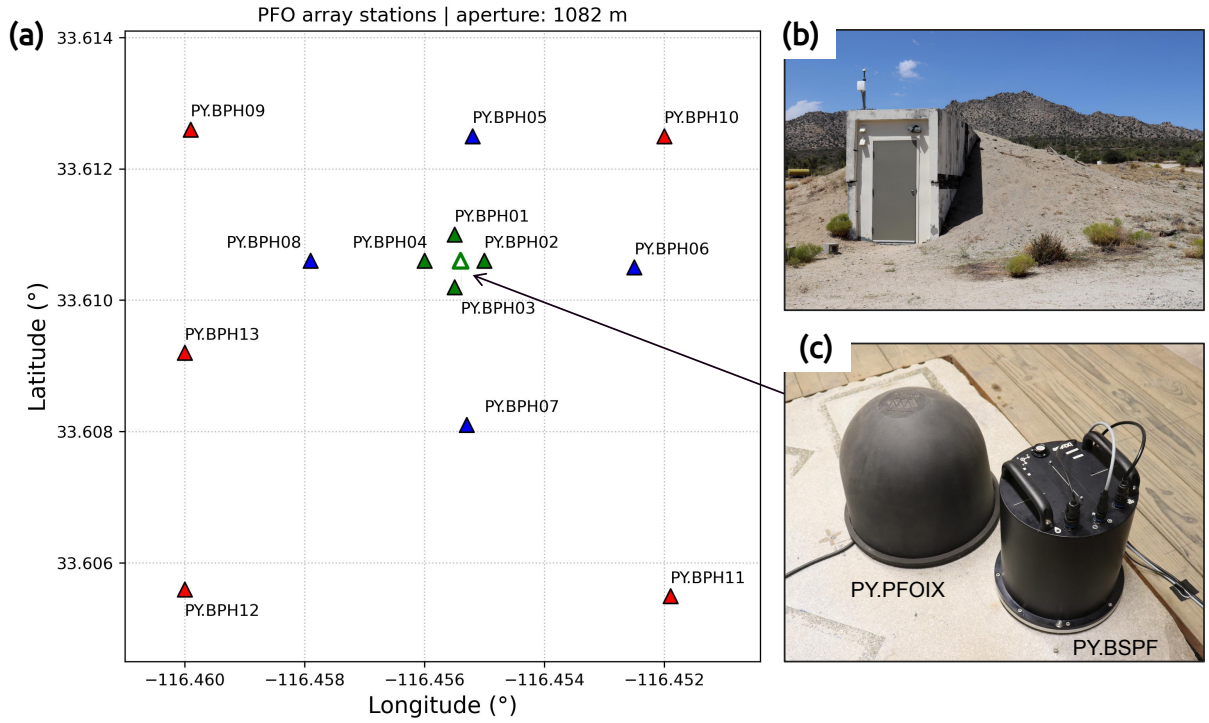

Figure 4.5: (a) shows the station map of the seismic array at the Piñon Flat Observatory in southern California. The array is subdivided in an inner array (green stations) and middle array (green and blue stations) and all stations (green, blue and red stations). (b) pictures the entrance of the underground vault, shielding environmental influences, that hosts the (c) 6 degree-of-freedom station (PY.BSPF and PY.PFOIX), including a co-located blueSeis-3A rotational rate sensor and broad-band seismometer placed on an isolated granite pillar.

scaled by magnitude across time and geographic distribution, respectively. Most of the local seismicity is occurring along the nearby northwest-southeast oriented fault systems, including the San Jacinto fault and the San Andreas fault (Fig. 4.6d, red lines represent known fault lines). A prominent cluster of local seismicity is located to the south of PFO, referred to as the Trifucation seismicity cluster (Ross, Hauksson & Ben-Zion 2017).

4.2.3.1 BSPF: Direct Rotations

We use a recursive LTA-STA coincidence trigger of the ObsPy package (Beyreuther et al. 2010) to detect seismic events recorded on at least four of the six channels of BSPF. This allows a distinction between events with coincidence of 4, 5 and 6 depending on the amount of triggered channels. This generally includes three translational channels, due to the enhanced signal-to-noise characteristics of the broad-band seismometer, plus N channels of the rotation sensor. The event count by magnitude shown in Figure 4.6b reveals that only 118 events are detected with a coincidence of 6 out of 406 events with a

coincidence of at least 4. Triggered events are color-coded by magnitude in Figure 4.6a, and by depth in 4.6c and 4.6d. The seismicity detected by the 6 DoF station is limited to local seismicity within a radius of about 150 km around PFO (Fig. 4.6a and 4.6d). An exception is the M_w=6.2 regional event on 2022-11-22, with an epicentral distance of about 312 km (Fig. 4.9). Triggered event times are matched to events in the USGS catalog via a nearest-time criteria.

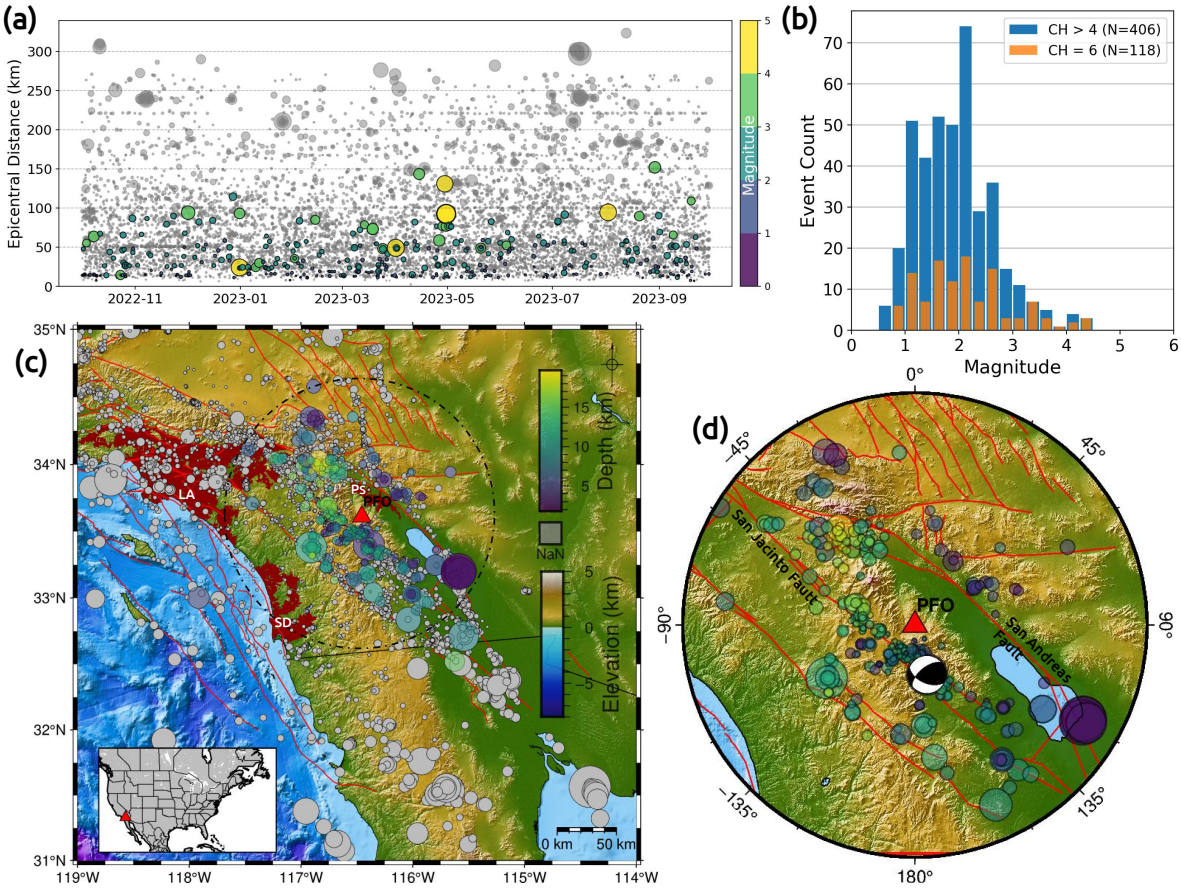

Figure 4.6: The regional seismicity around the Piñon Flat Observatory (PFO) in southern California based on the USGS catalog from October 2022 to October 2023 is shown over time (a) and as geographic distribution (c), including known fault lines (SCEDC 2013) as red lines and urban centers: San Diego (SD), Los Angeles (LA) and Palm Springs (PS), as dark red areas (Patterson 2012). Events are scaled by magnitude and triggered events on the 6 degree-of-freedom station are color-coded by magnitude (a) and depth (c). A histogram by magnitude of the total count of 406 triggered events (b) on at least 4 of 6 channels (blue) are compared to 118 events triggered on all 6 channels (orange). A focus on the local area around PFO (d) displays triggered, local events and a centroid moment tensor of the M_w 4.1 event (2022-12-31 12:12:26 UTC) at an epicentral distance of 24.3 km from PFO.

Figure 4.7 displays a selection of detected events with a coincidence of 6. The magnitudes range from 1.1 to 3.6, while epicentral distances range from 11 km to 115 km. Peak ground rotation velocities (PGRV) range from 0.6 μrad/s to 16.4 μrad/s. A strong variation of signal-to-noise ratio (SNR) can not only be observed across events, but also across different components. For the entire dataset, the SNR for PY.BSPF does not exceed 10, while for most events a SNR of about 2 is found. This is a result of the still relatively high instrumental self-noise level of the blueSeis-3A sensor (Bernauer et al. 2018).

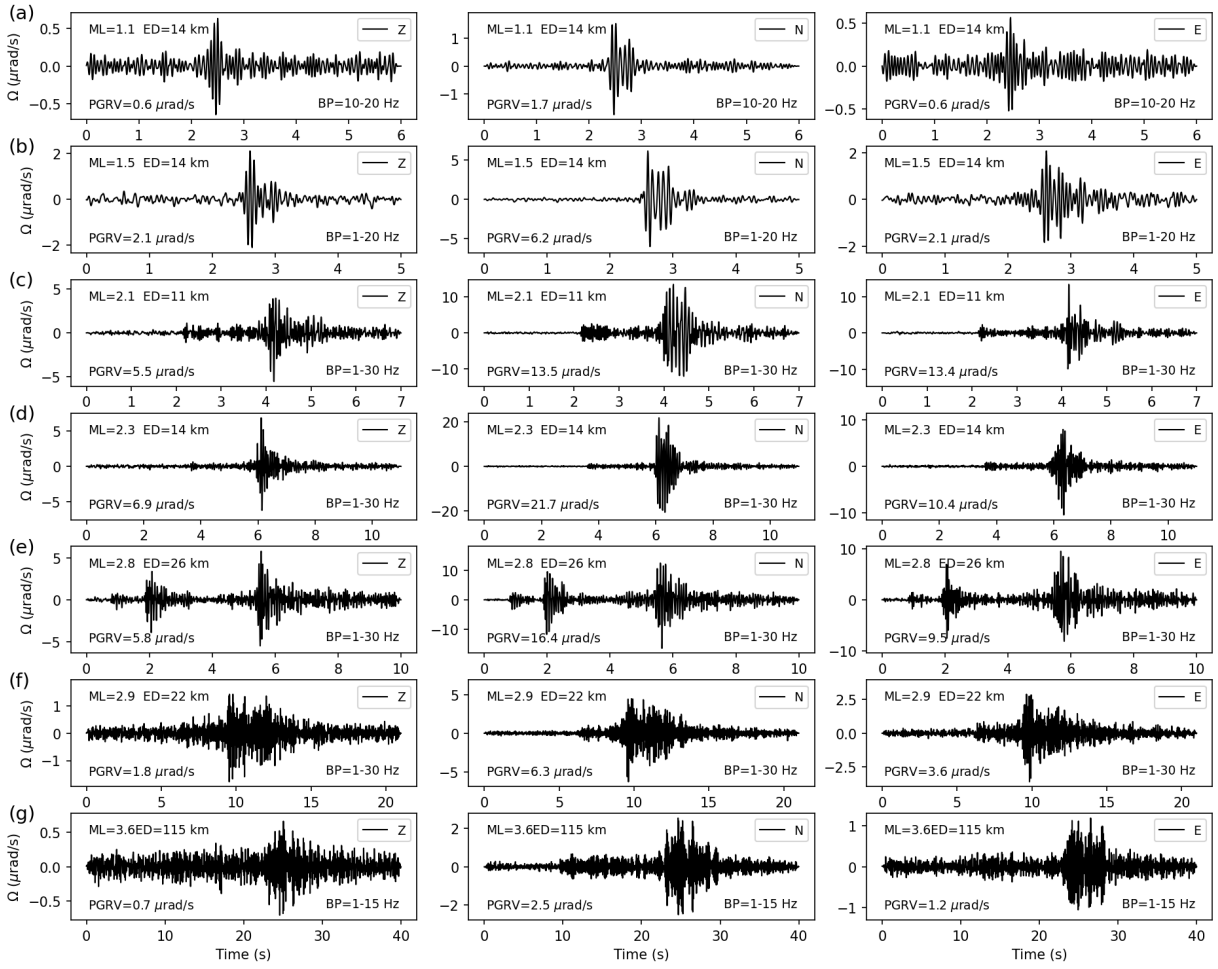

Figure 4.7: (a) to (g) show a selection of events detected by BSPF across magnitudes (1.1 $<$ M $<$ 3.6) and epicentral distances (11 km $<$ ED $<$ 115 km). Each column displays one component of rotational rate observation (Z, N, E from left to right). Peak ground rotation velocity (PGRV) and the applied bandpass filter is shown for each record. The origin times are found in Table 4.3. The recording in (e) comprises two events.

4.2.3.2 Array-Derived Rotations

We use the seismic array at PFO to derive rotational ground motions, serving as a reference for our single-point, direct measurements. Commonly, three-component ground velocities observations are used in a finite-difference approach to estimate three-components of ground rotation across the area of the array (e.g Spudich & Fletcher 2008, Poppeliers & Evans 2015). We employ an implementation for ADR computations in the ObsPy package (Beyreuther et al. 2010). Although these derived-rotations are a good estimate (Suryanto et al. 2006) for frequency bands imposed by the geometry of the seismic array (e.g., Poppeliers & Evans 2015, Donner et al. 2017), assumptions, such as a rigid plate across the seismic array, result in uncertainties with regard to true ground rotations. Nevertheless, ADR can still be used for validation as it represents an independent measurement within the given assumptions.

The seismic stations at PFO are shown in Figure 4.5a. We subdivide the seismic array into three subarrays, thus frequency ranges, to compute ADR. The frequency limits for ADR computation as described by Donner et al. (2017) requires an apparent velocity and the aperture of the array (Tab. 4.2). For the analysis, the frequency bands were conservatively adjusted to a narrower range (f_{min}-f_{max} in Tab. 4.2) for the comparison. The inner array (green stations) comprises five seismic stations and provides the highest frequency band from 1 Hz to 5 Hz (iADR). By extending the *inner* array by four more seismic stations (blue stations in Fig. 4.5), we define a *mid* array to compute ADR for a frequency band from 0.5 Hz to 1 Hz (mADR). Finally, by including all 14 seismic stations for *all* array provides ADR between 0.1 Hz and 0.5 Hz (aADR).

Table 4.2: Parameters used to subdivide the seismic array at Piñon Flat Observatory (PY.BHP) to three subarrays (see Fig. 4.5) to compute array-derived rotations for different frequency bands (f1-f2), based on Donner et al. (2017), imposed by the subarray aperture a and apparent velocity of 3 km/s. For the analysis, the frequency bands were conservatively adjusted to a narrower range (f_{min} - f_{max}).

subarray	code	# stations	a (m)	f_{min} (Hz)	f_{max} (Hz)	f1 (Hz)	f2 (Hz)
all stations	aADR	14	1082	0.1	0.5	0.01	0.7
mid stations	mADR	9	501	0.5	1.0	0.01	1.5
inner stations	iADR	5	93	1.0	5.0	0.08	8.1

Some stations of the seismic array at PFO had to undergo maintenance for certain time periods, hence could not be used for ADR computations for events within these periods. The station PY.BPH05 was down for the whole year of interest, unfortunately.

Table 4.3: Detailed information on earthquake events shown in Figure 4.7. ED = epicentral distance; D = Depth; M = Magnitude; BAz = backazimuth; T = Magnitude Type; CA = California

Panel	Starttime (UTC)	M	MT	D (km)	ED (km)	BAz (°)	Region
(a)	2022-10-01T05:36:14	1.1	ML	9	14.3	199.7	Anza, CA
(b)	2022-10-02T03:25:19	1.5	ML	8	14.9	199.4	Anza, CA
(c)	2023-09-11T09:20:16	2.1	ML	9	11.6	188.1	Anza, CA
(d)	2023-03-01T22:49:03	2.3	ML	11	14.0	188.7	Anza, CA
(e)	2022-10-26T08:14:38	2.8	ML	14	26.8	276.5	Anza, CA
(f)	2024-02-27T22:50:48	2.9	ML	13	22.9	161.8	Borrego Springs, CA
(g)	2024-02-16T07:38:50	3.6	ML	13	115.7	294.5	Ontario, CA

4.2.3.3 Signal-to-Noise Ratio

The signal-to-noise ratio (SNR) is a good measure for signal quality. We computed SNRs automatically for each triggered event for direct rotation rate, array-derived rotation rate and acceleration and each frequency band (see Tab 4.2). The SNR is defined as the maximum of absolute amplitudes in a 15 second window following the trigger time. The noise level is computed as the maximum of absolute amplitudes of a 15 second window of data before the trigger time, being shifted 2 seconds back in time in order to avoid event signals.

Figure 4.8 provides a statistical analysis of the signal-to-noise ratios and shows histograms for signal-to-noise estimates for all three components of ADR, direct rotation observations of BSPF and translation motion for all three frequency bands (a = 0.1-0.5 Hz, m = 0.5-1.0 Hz, i = 1.0-6.0 Hz), corresponding to the subarrays used for ADR computation. For local seismicity, commonly a higher signal content for higher frequencies is expected and observed. Therefore, an increase in signal-to-noise ratio is observed for seismometer data (PFO) for the frequency band m (SNR ≈ 2-3) and i (SNR ≈ 80-100) compared to band a, where noise dominates (SNR ≈ 1). This tendency can be seen across all components. Since ADR benefits from the low-self noise of the seismometer, the behavior is equivalent. For BSPF, thus direct rotation rate observations, for most events centers around a SNR of 1, while it improves for band i with higher frequencies. However, most signal energy for rotational ground motion is found beyond 5 Hz and is not reflected in this analysis focusing on frequency bands comparable with ADR.

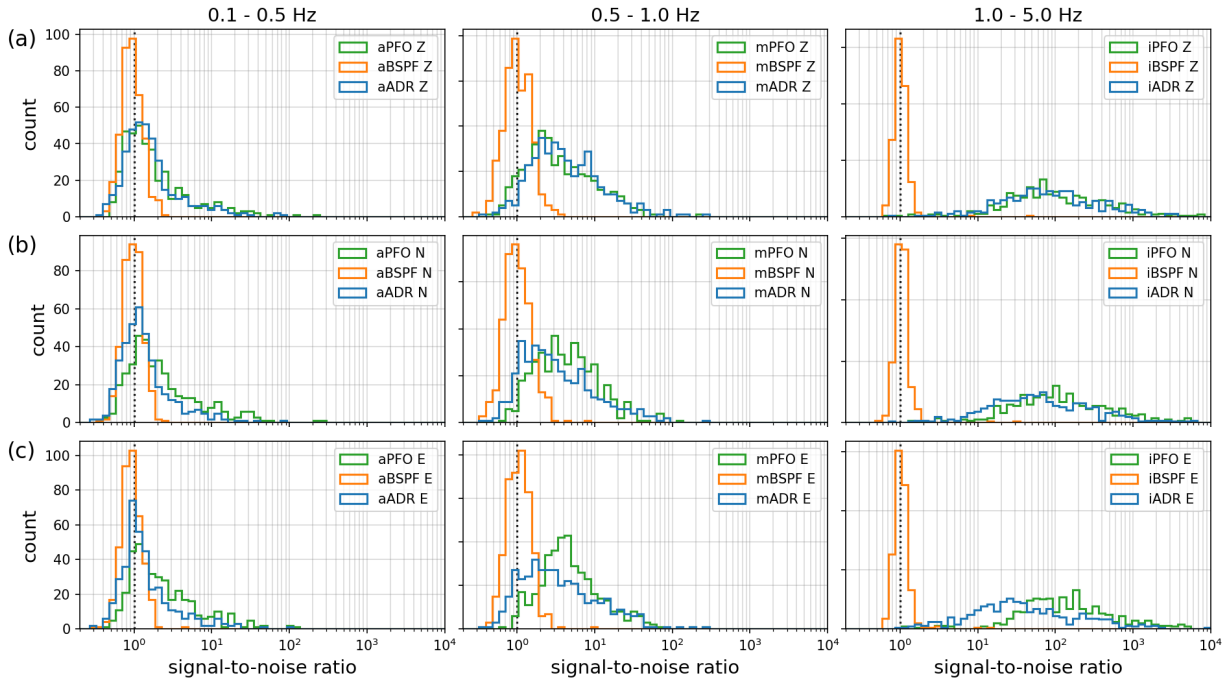

Figure 4.8: The panels show histograms of signal-to-noise ratios computed for all events for acceleration (PY.PFO), array-derived rotation rate (ADR) and direct rotation rate (PY.BSPF) by component Z, N and E from top to bottom and by frequency band a (0.1-0.5 Hz), m (0.5-1.0 Hz) and i (1.0-6.0 Hz) from left to right.

4.2.4 6 DoF Analysis

Hereafter, we show results of an exemplary 6 DoF analysis for two selected events, a regional M_w 6.2 and a local M_w 4.1.

4.2.4.1 Event M6.2

The M_w 6.2 event occurred on 2022-11-22 (16:39:05 UTC) in Baja California about 312 km south of PFO and was recorded with the 6 DoF station. This event represents the largest magnitude recorded up to now and provides energy in the lower frequency *a*-band (0.1-0.5 Hz), thus enabling a comparison with ADR for lower frequencies. However, at this time, there is no data available for station BPH02, BPH03 and BPH05, in turn affecting the array-derived rotation rate estimates, in particular the north-south component.

Waveforms of array-derived rotation rate observations and direct rotation rate observations for this event are compared in Figure 4.9 across all three frequency bands defined in Table 4.2. Zero-lag cross-correlation values are as high as 0.97 for the east component (0.5-1.0 Hz). The correlation of the north component is reduced to 0.85, most likely due to missing station data for ADR computations.

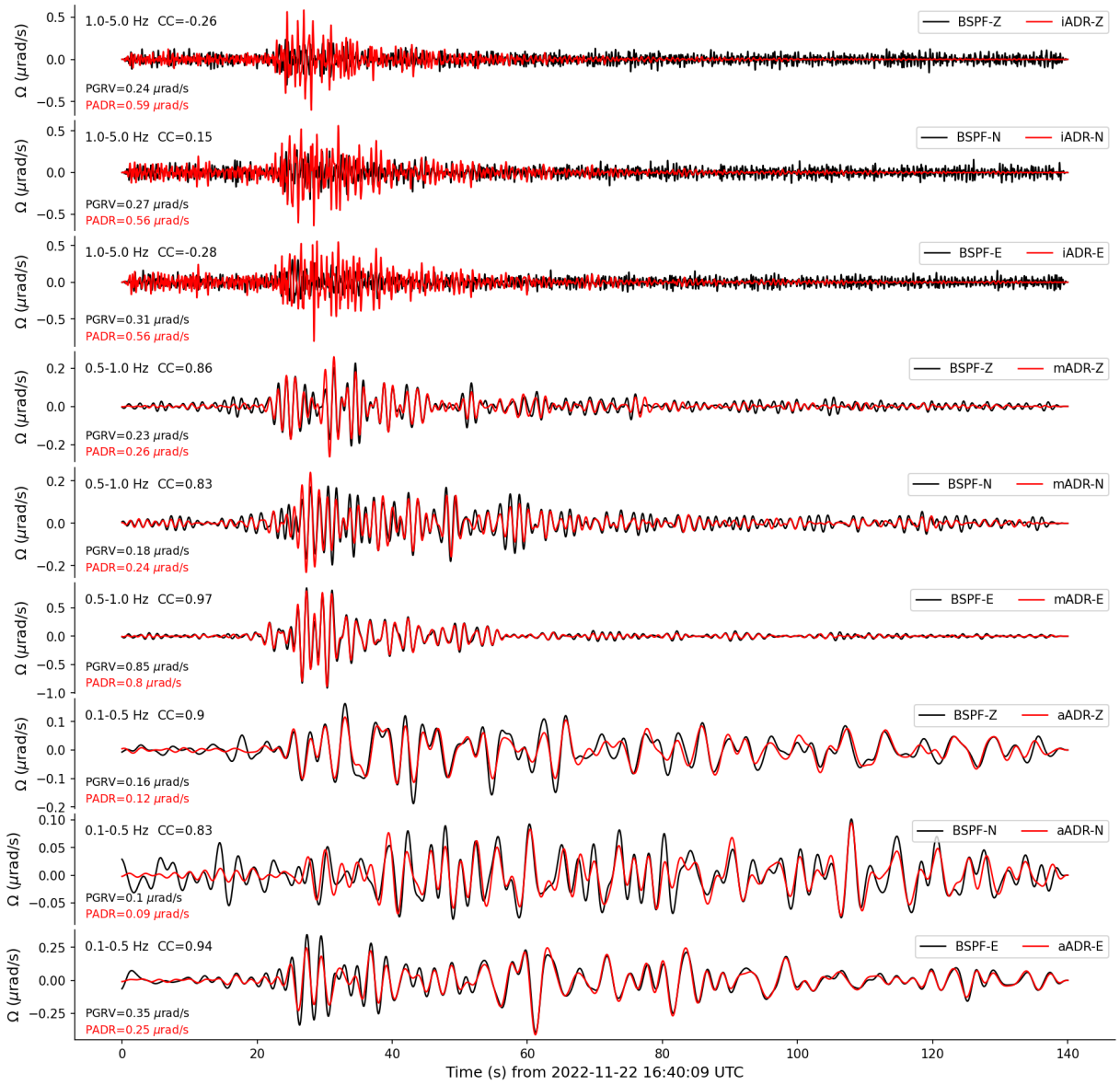

Figure 4.9: Direct (black) and array-derived rotational rate (ADR) waveforms of the M_w 6.2 event (2022-11-22 16:39:05 UTC) at an epicentral distance of 312 km are shown. Top to bottom all three components (Z, N, E) are compared in three different frequency bands (1.0-6.0 Hz, 0.5-1.0 Hz, 0.1-0.5 Hz) according to the PFO inner subarray (iADR), mid subarray (mADR) and the entire array (aADR). An almost perfect phase and amplitude fit of array-derived and direct rotation rate is observable for the east component in the mid-frequency array with a cross-correlation coefficient of 0.98. (Self-) noise dominates the PY.BSPF recording for the low frequencies (0.1-0.5 Hz). Especially for the north component of the high frequency range (1.0-6.0 Hz), the effect of missing station data for ADR computation is recognizable.

4.2.4.2 Event M4.1

On December 31, 2022, a M_w 4.1 event occurred southeast of PFO at an epicentral distance of 24.3 km. Waveforms of this event were recorded with the 6 DoF station and compared to ADR estimates in Figure 4.10. For ADR computations at this time, station PY.BPH05 (Fig. 4.5a) is missing, having an influence on the north-south south geometry of ADR visible in the waveform comparison in Figure 4.10. This is quantified by lower ADR amplitudes of the north-component and smaller cross-correlation coefficients in Figure 4.10. Zero-lag cross-correlation coefficients (CCC) between ADR and direct rotation rates are above 0.87 and as high as 0.96 for the east component of the m-band. For this frequency band, signal amplitudes are in good agreement, although ADR seems to slightly underestimate peak amplitudes. This is likely a result of spatial smoothing across the array stations as part of the ADR estimation procedure. For frequencies within 1 Hz to 5 Hz, the phase match between iADR and BSPF results in CCC values of up to 0.9 (east component), while peak amplitudes differ significantly. iADR underestimates peak rotations by 47% (Z), 73% (N), 42% (E). ADR generally reveals smaller amplitudes than direct measurements, hence underestimating single-point rotational ground motions, likely as a result of spatial averaging. The main frequency content for the local M_w 4.1 is above 5 Hz for the rotation rates observed by PY.BSPF (Figure 4.11). For the a-band, the SNR is poor and the waveforms are dominated by instrumental self-noise, thus not suitable for interpretation (see Fig. 4.10).

4.2.4.3 Backazimuth Estimation

With a single 6 DoF station, observing co-located acceleration and rotation rate, the backazimuth of a plane wave can be estimated by exploiting the polarization information of particle motion (e.g., Igel et al. 2007, Sollberger et al. 2020, Igel et al. 2014). The following approaches are compared:

1. *Love polarization*: A grid search across backazimuth range used to rotate horizontal acceleration to transverse acceleration, which is correlated with vertical rotation rate. This is a Love wave polarization filter and is applied for overlapping windows along the event. The maximum zero-lag, cross-correlation value then provides a backazimuth estimate.

2. *Rayleigh polarization*: A grid search across backazimuth range used to rotate horizontal rotation rate to obtain transverse rotation rate, which is correlated with vertical acceleration. This is a Rayleigh wave polarization filter and is applied for overlapping windows along the event. The maximum zero-lag, cross-correlation value then provides a backazimuth estimate.

3. *Covariance (CoVar) approach*: Based on a classic three component single-station approach using both horizontal components, hence dominantly Rayleigh waves. An estimate of the backazimuth angle is obtained by determining the first eigenvector of the covariance matrix based on the north and east component of rotation rate. The

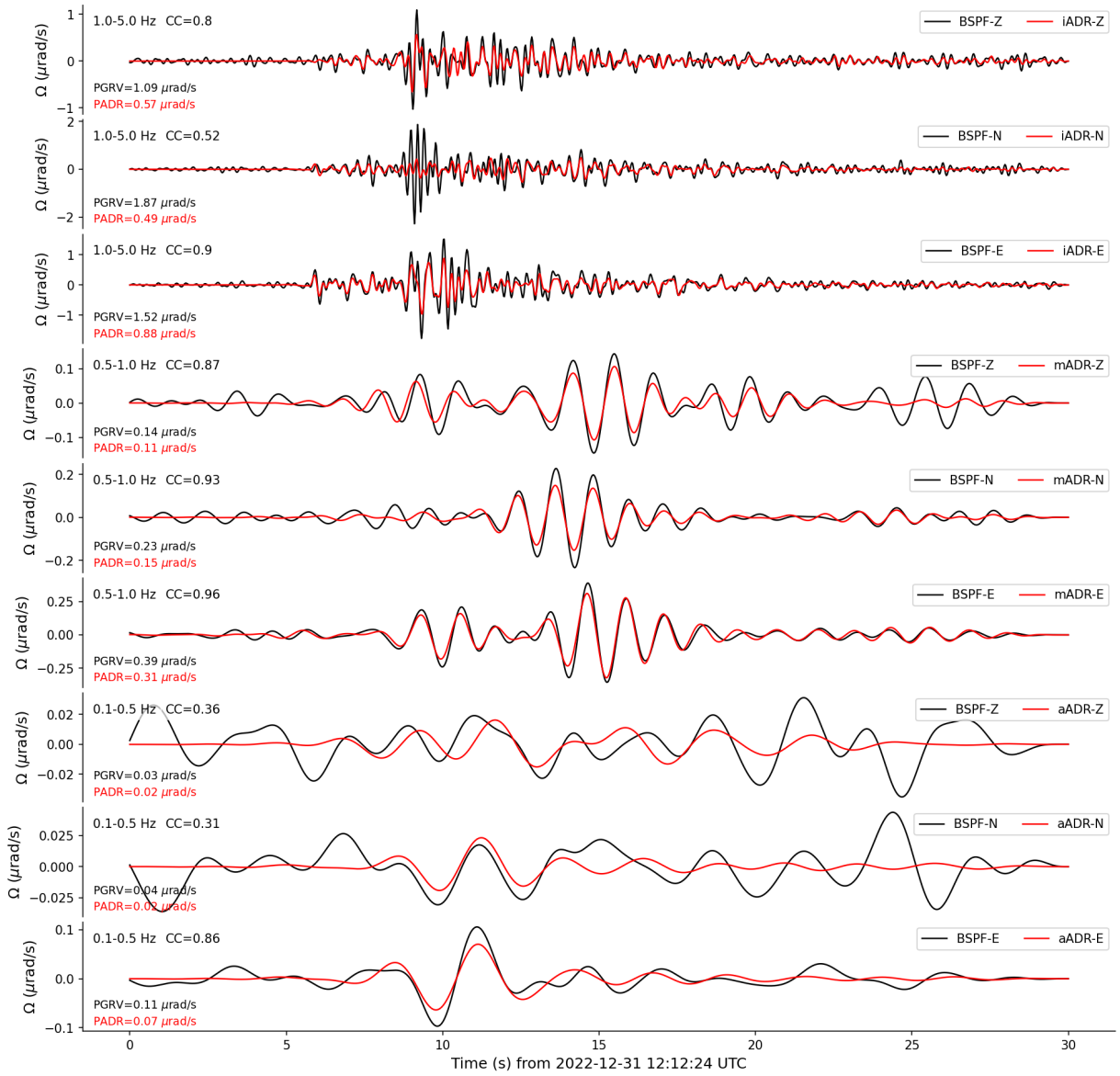

Figure 4.10: Direct (black) and array-derived rotational rate (ADR) waveforms of the M_w 4.1 event (2022-12-31 12:12:26 UTC) at an epicentral distance of 24.3 km are shown. Top to bottom all three components (Z, N, E) are compared in three different frequency bands (1.0-6.0 Hz, 0.5-1.0 Hz, 0.1-0.5 Hz) according to the PFO inner subarray (iADR), mid subarray (mADR) and the entire array (aADR). An almost perfect phase and amplitude fit of ADR and direct rotation rate is observable for the mid-frequency band with a cross-correlation (CC) coefficient up to 0.97 (east component). Instrumental self-noise dominates the PY.BSPF recording for frequencies between 0.1-0.5 Hz. In particular, for the north component of the high frequency range (1.0-5.0 Hz), the effect of missing station data for ADR computation is recognizable.

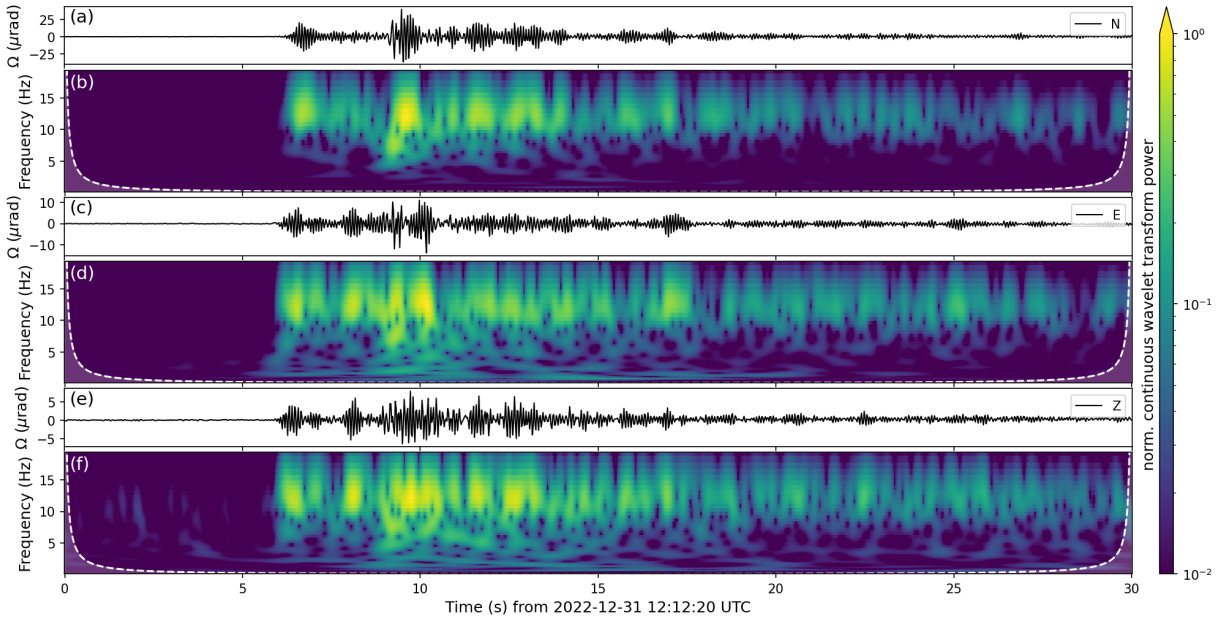

Figure 4.11: (a), (c) and (e) show rotation rate records of the M_w 4.1 event (2022-12-31 12:12:26 UTC) for north, east and vertical component, respectively, while (b), (d) and (f) show corresponding spectrograms based on the continuous wavelet transform.

angle is obtained computing the tangent of north over east. A remaining 180 degree ambiguity can be resolved by evaluating the sign of the cross-correlation between vertical acceleration and transverse rotation rate, which should be in phase.

The window length is 2 seconds with 90% overlap. Each backazimuth estimate is color-coded by the respective zero-lag, cross-correlation (CC) value. An overall backazimuth estimate is obtained by using the peak of a kernel-density estimate using Gaussian kernels of the correlation-weighted distribution (e.g., Fig. 4.12). A minimum CC value of 0.2 is required for a backazimuth estimate to be considered for the kernel-density estimate. With an expected backazimuth of 166 degrees and 170 degrees, the seismic wavefield for both analyzed events arrives from the south and most horizontal rotation caused by Rayleigh waves will be present on the east component, while hardly any rotational motion around the north component is expected. Figure 4.12 and Figure 4.13 show backazimuth estimates for all three approaches listed above, each compared to the expected backazimuth based on the catalog event location for the M_w 4.1 event and M_w 6.2 event, respectively. Waveforms band pass filtered between 0.5 Hz to 1.0 Hz are shown for different combinations of acceleration and rotation rate using the expected backazimuth for matrix rotation (Fig 4.12a-c and Fig. 4.13a-c). Due to the proximity of the source location for the M_w 4.1 event, there is no clear phase separation, nonetheless, a decent waveform fit is observed (Fig. 4.12). The backazimuth estimates for Rayleigh waves and the CoVar approach yield directions close to the expected backazimuth with CC values above 0.9, while for Love wave estimates the CC values are reduced and the directions differ significantly from the expected backazimuth.

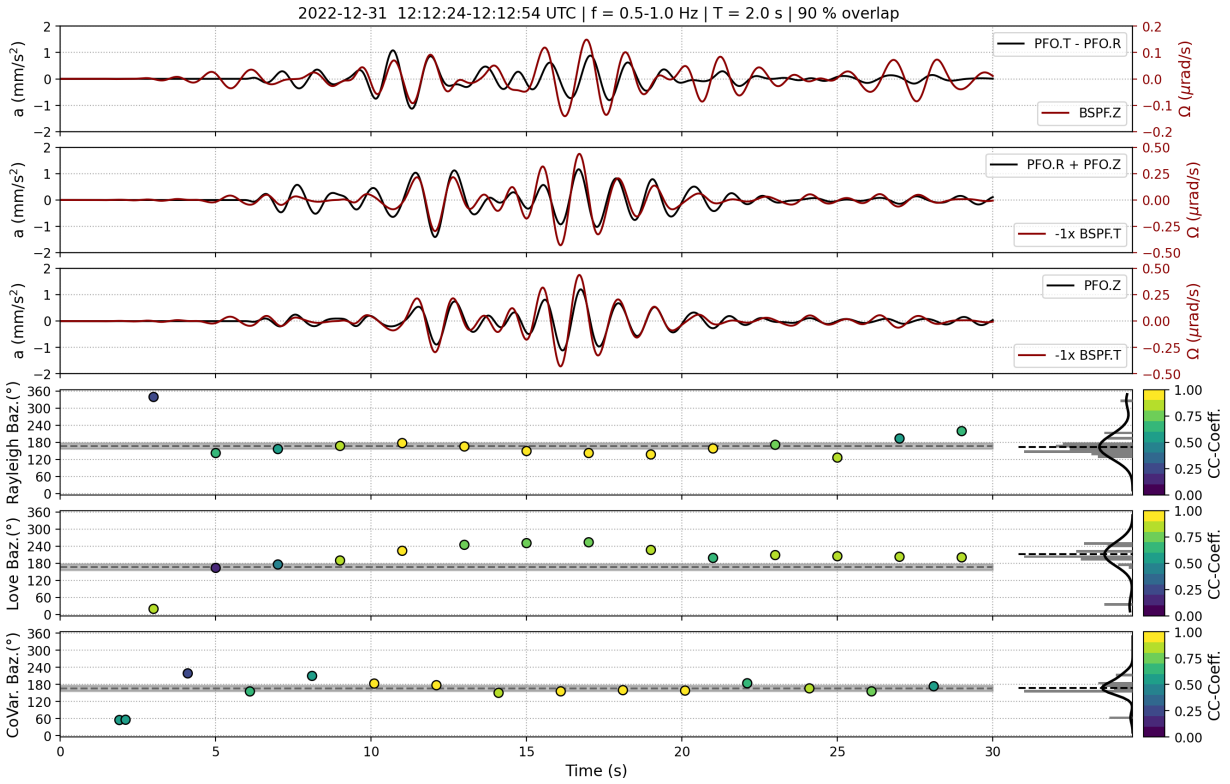

Figure 4.12: Comparison of backazimuth estimates for the M_w 4.1 event (2022-12-31 12:12:24 UTC) event. Top to bottom: difference of transverse and radial acceleration (black) and vertical rotation rate (red), sum of vertical and radial acceleration (black) and reversed transverse rotation rate (red), vertical acceleration (black) and reversed transverse rotation rate (red), grid search based backazimuth estimates using Rayleigh polarization, grid search based backazimuth estimates using Love polarization, covariance optimization of horizontal rotation rate with polarization filter using vertical acceleration. For all backazimuth estimates, a histogram, weighted cross-correlation coefficient, and a probability density function with its maximum is shown on the right y-axis. The backazimuth, based on the catalog epicenter location, at 179 ° is shown as a black, dashed line with a ±5 ° interval in gray.

For the M_w 6.2 event, all approaches yield directions in agreement with the expected backazimuth of 179 degrees for the dominant part of the surface waves (see. Fig 4.13). The CoVar approach yields the most stable estimates (CC $>$ 0.9), whereas backazimuth estimates for Love and Rayleigh polarization reveal more variance around the expected backazimuth for equally high CC values. For the coda, CC values decrease and directions scatter significantly around the expected backazimuth. For each frequency band imposed by ADR a backazimuth estimation for different approaches is presented in Figures 4.14a and 4.14b for the M_w 4.1 event and M_w 6.2 event, respectively. The three 6 DoF approaches are applied using direct rotational observation and ADR. Established seismic array f-k

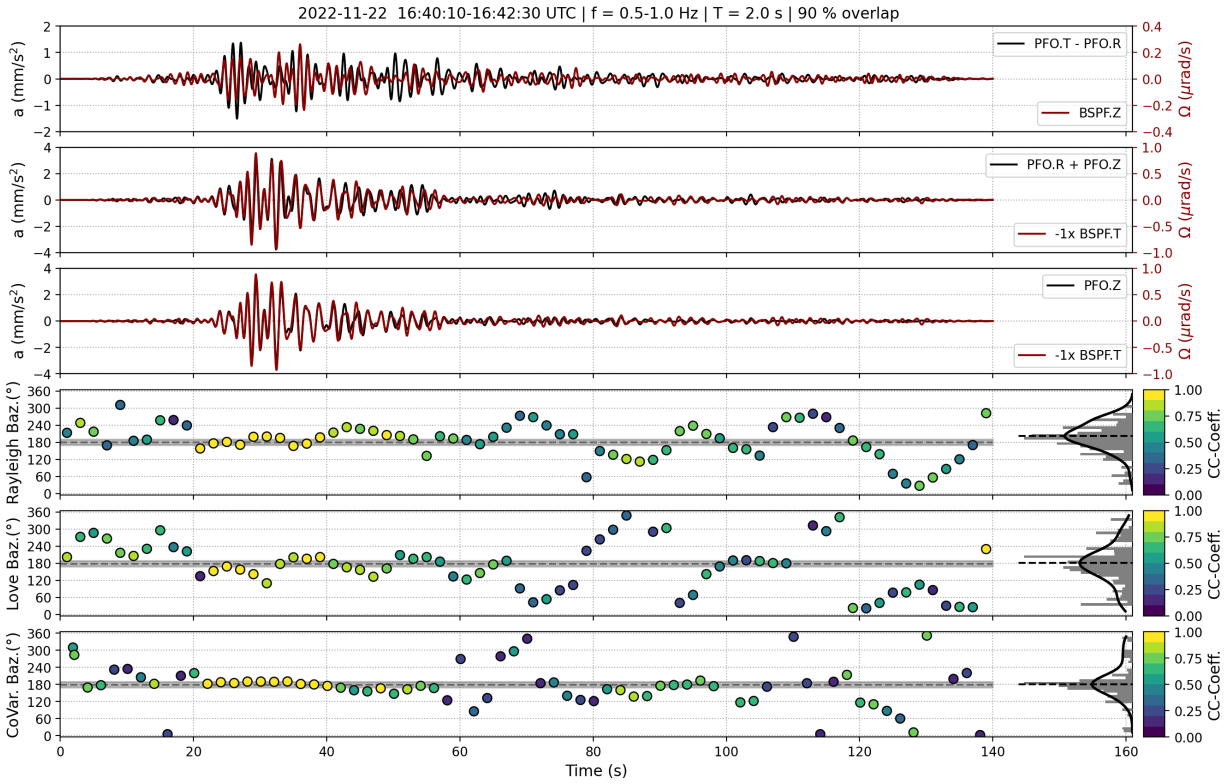

Figure 4.13: Comparison of backazimuth estimates for the M_w 6.2 event (2022-11-22 16:39:05 UTC) event. Top to bottom: difference of transverse and radial acceleration (black) and vertical rotation rate (red), sum of vertical and radial acceleration (black) and reversed transverse rotation rate (red), vertical acceleration (black) and reversed transverse rotation rate (red), grid search based backazimuth estimates using Rayleigh polarization, grid search based backazimuth estimates using Love polarization, covariance optimization of horizontal rotation rate with polarization filter using vertical acceleration. For all backazimuth estimates, a histogram, weighted cross-correlation coefficient, and a probability density function with its maximum is shown on the right y-axis. The backazimuth, based on the catalog epicenter location, at 179 ° is shown as a black, dashed line with a ±5 ° interval in gray.

beamforming for vertical components serves as a reference for backazimuth estimation. Mean backazimuth estimates and standard deviations are obtained from the peaks and variances of the kernel-density estimates, as shown in Figures 4.12 and 4.13.

4.2.4.4 Seismic Phase Velocities

Observing 6 DoF of the seismic wavefield provides direct access to local seismic phase velocities of plane-waves utilizing amplitude ratios for

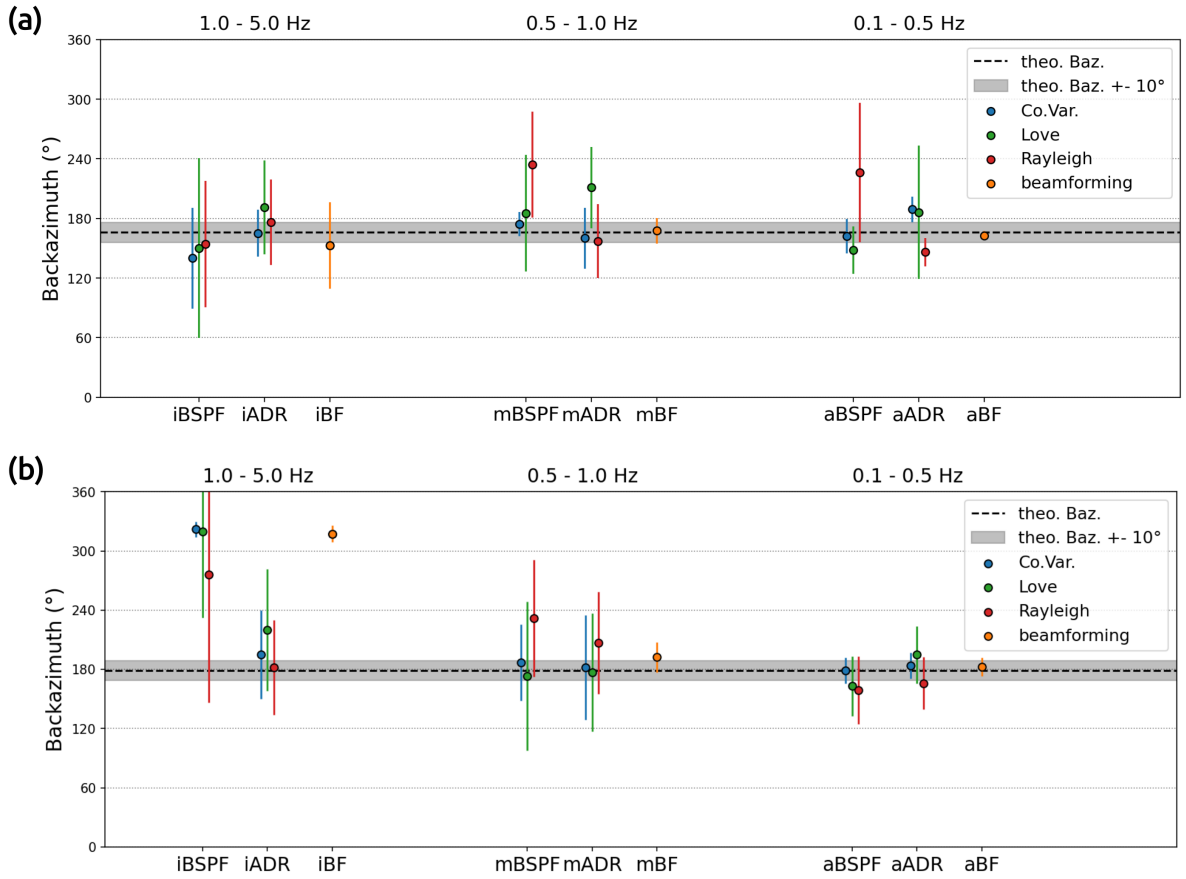

Figure 4.14: Comparison of backazimuth estimates for (a) the M_w 4.1 event and (b) the M_w 6.2 event. Shown mean estimates and their standard deviation are based on Gaussian kernel-density fits to correlation weighted distributions with a minimum correlation value of 0.5. The respective expected backazimuth is indicated as a black, dashed line with a ± 10 ° interval in gray. For each frequency band i=1.0-5.0 Hz, m=0.5-1.0 Hz, a=0.1-0.5 Hz and 0.8-1.0 Hz and each method Love (grid search based on Love wave polarization), Rayleigh (grid search based on Rayleigh wave polarization), Co.Var. (co-variance optimization using horizontal rotation rates and seismic array beamforming (using vertical velocities). Standard deviations are displayed as vertical error bars.

1. Love waves:

$$c_{Love,phase} = -\frac{1}{2}\frac{a_T}{\Omega_z}, \tag{4.7}$$

2. Rayleigh waves:

$$c_{Rayleigh,phase} = \frac{a_z}{\Omega_T}, \tag{4.8}$$

with a denoting translation acceleration, Ω rotation rate and T and z transverse and vertical

components, respectively (e.g., Pancha et al. 2000, Igel et al. 2007, 2014). As for many detected events the entire waveform is compromised by self-noise and phase identification difficult, we focus on peak amplitudes. Average apparent phase velocities are estimated for SH-polarized and SV-polarized waves using peak ground rotation velocity (PGRV) and peak ground translation acceleration (PGTA) amplitudes according to equations (4.7) and (4.8), respectively.

Components are rotated to a ZRT system based on the expected backazimuth from catalog locations before peak amplitudes are determined. The velocity is estimated as the slope of an orthogonal distance regression with an enforced the intercept to equal zero. This approach yields an apparent phase velocity of about 2882 m/s for SH-polarized waves and about 2565 m/s for SV-polarized waves, using all 118 events (with a coincidence equal to 6). When only events with a magnitude above 2 are considered, apparent phase velocities of 2876 m/s and 2581 m/s for SH- and SV-polarized wave phase velocities are obtained, respectively.

Since no direct seismic phases are analyzed, the velocities are not linked to Rayleigh or Love waves directly and an uncertainty arising by using peak amplitudes and merely 118 events has to be taken into account. In order to obtain estimates for Rayleigh and Love phase velocity, we analyze our two selected events.

For moving time windows of 2 seconds and 50% overlap (before and after), we compute orthogonal distance regressions amplitude ratios according to equations (4.7) and (4.8) to estimate Love and Rayleigh phase velocities. Figure 4.15 shows waveforms and phase velocity estimates for the M_w 4.1 and M_w 6.2 event, color-coded by zero-lag cross-correlation values. Components are rotated to a ZRT system using the expected backazimuth. Phase mismatches in waveforms that are projected into velocity estimates might result from differences in actual backazimuth due to scattering and the expected backazimuth of plane waves along a great circle path.

An interpretation towards associated phase velocities has to assume distinct phases of plane Rayleigh and Love waves, which is challenging for local events of short duration, in particular for higher frequencies. We focus on a frequency band between 0.5 Hz to 1.0 Hz. Velocity estimates for the M_w 4.1 event in this frequency band with high cross-correlation coefficients ($>$0.8) range within 1.7-2.1 km/s and 2.5-3.5 km/s for Love and Rayleigh wave phase velocities, respectively.

For the M_w 6.2 event, Rayleigh waves seem to dominate with high cross-correlation values ($>$0.8) and a phase velocity between 3.2-4.2 km/s. Love wave phase velocities for this event are in a wide range of 2.0-4.0 km/s with generally lower cross-correlation values compared to Rayleigh type waves.

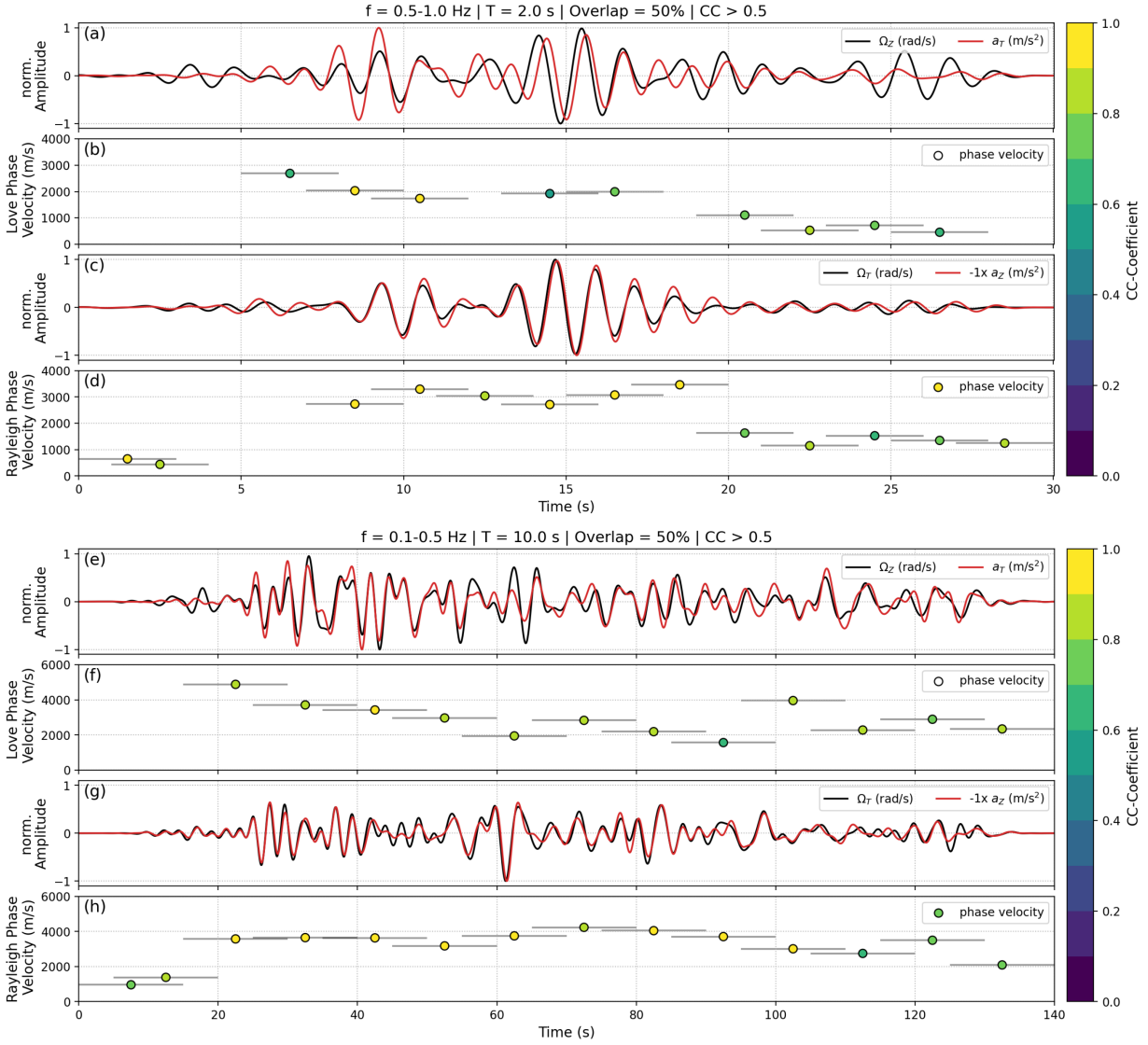

Figure 4.15: Band-pass filtered (0.1-0.5 Hz) observations of normalized vertical rotation rate Ω_Z and transverse acceleration a_T (a) and transverse rotation rate Ω_T and vertical acceleration a_Z (c) are shown for the M_w 4.1 event. (e) and (g) show the same combinations for the M_w 6.2 event. (b) and (d) show windowed phase velocity estimates based on amplitude ratios for Love (b) and Rayleigh (d) waves. Each estimate is color-coded by the corresponding maximal, zero-lag cross-correlation coefficient. (f) and (h) show the phase velocity estimates accordingly for the M_w 6.2 event. Time windows with 50% overlap are indicated by horizontal error bars.

4.2.5 Empirical Scaling Relation for Rotation Rates

In order to quantify the potential observations of a 6 DoF station with a blueSeis-3A sensor for studying the local and regional seismicity, we require a relation of magnitude

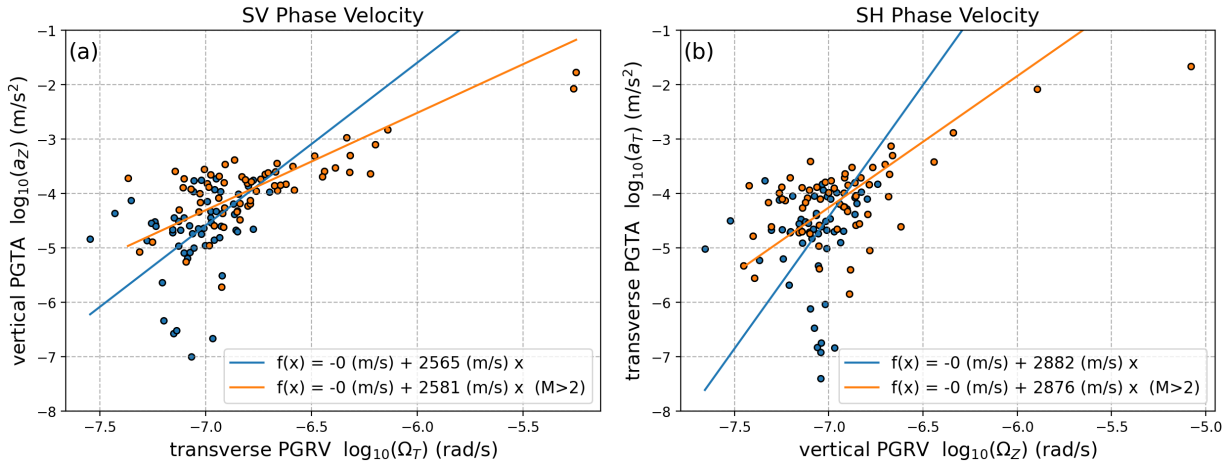

Figure 4.16: Estimates of (a) SV-wave and (b) SH-wave phase velocities based on equations (4.7) and (4.8) using peak ground translation acceleration (PGTA) and peak ground rotation velocity (PGRV) amplitudes (instead of windows phase) for the subset with a coincidence trigger of six (118 events). An orthogonal distance regression is used to determine the phase velocity (=slope) using for all events (blue and orange circles) and events with magnitude above two only (orange circles). Components are rotated to a ZRT system based on the theoretical backazimuth from catalog locations before peak amplitudes are picked.

and hypocentral distance with rotation rate amplitudes. Chow et al. (2019) used teleseismic observations to infer a logarithmic relation for vertical rotation rates (Love waves). We follow a similar approach to infer an empirical scaling relation based on a local magnitude scale for horizontal and vertical peak ground rotation rates individually:

$$M_L = log_{10}(A_{max}) + a\ log_{10}(R) + b\ R + c \tag{4.9}$$

with R being the hypocentral distance in km and A_{max} the peak ground rotation rate for horizontal PGRV:

$$A_{max} = \sqrt{A_N^2 + A_E^2}\ ,$$

and vertical PGRV

$$A_{max} = \sqrt{A_Z^2}\ .$$

For this purpose, we use a reduced dateset of 118 events triggered on all six component to pick peak ground rotation rates in a frequency band of 1 Hz to 20 Hz (a sampling rate of 40 Hz imposes a limit for the first half year of data). This results in a linear system of

equations of the form:

$$\begin{bmatrix} M_0 - log_{10}(A_{max,0}) \\ \vdots \\ M_i - log_{10}(A_{max,i}) \end{bmatrix} = \begin{pmatrix} log_{10}(R_0) & R_0 & 1 \\ \vdots & \vdots & \vdots \\ log_{10}(R_i) & R_i & 1 \end{pmatrix} \times \begin{bmatrix} a \\ b \\ c \end{bmatrix} \tag{4.10}$$

that allows to solve for the coefficients a, b and c using a least-squares misfit criterion.

Peak amplitudes for the detected regional M_w 6.2 event were added manually to add a constraint for larger distances and higher magnitudes. Peak amplitudes of small-magnitude events with a poor signal-to-noise ratio are more compromised by sensor self-noise. Therefore, events below M 1 are down-weighted for the curve fit by assigning a higher variance of 5. High-magnitude events (> M 2.5) are up-weighted instead using a lower variance value of 0.5, while all others are assigned a default variance value of 1.

The coefficients for vertical and horizontal rotation rates of equation (4.9) and variance values are obtained using a least-square optimization and listed in Table 4.4. Deviations between the final coefficients of vertical and horizontal rotation rates are as low as 0.3% for c and maximal for b with 6.6%. Variances listed in Table 4.4 are provided by the employed method *curve_fit* of the SciPy python package. Figure 4.17 visualizes the empirical scaling

Table 4.4: Coefficients a, b and c for an empirical scaling relation for vertical and horizontal rotation velocities as defined in equation (4.9) and their variances (σ^2) as obtained by a least-squares minimization.

	a	b	c	σ_a^2	σ_b^2	σ_c^2
M_L (vertical)	1.42	0.00652	6.42	0.114	$1.88e^{-6}$	0.177
M_L (horizontal)	1.37	0.00695	6.40	0.0690	$1.14e^{-6}$	0.107
deviation	3.5%	6.6%	0.3%			

relations for a regional range of hypocentral distance up to 350 km and magnitudes up to M_w 6.5. For a hypothetical M 3.0 event at 50 km hypocentral distance, we would consequently expect vertical rotation rates of 0.69 μrad/s and horizontal rotation rates of 0.84 μrad/s. The shown self-noise limits for the blueSeis-3A sensor are extracted from operational range diagrams by Bernauer et al. (2018) and represent a minimum detection threshold at 10 nrad/s and 30 nrad/s for 1 Hz and 10 Hz, respectively (Fig. 4.17). A limit based on the rotational low noise model for transverse rotations by Brotzer et al. (2023) based on rms amplitudes of the model at 1 Hz provides a lowermost resolvable level (see Fig. 4.17). The shaded area for Figure 4.17 indicates a poor model resolution, thus no reliability in this magnitude-distance range due to missing observational constraints.

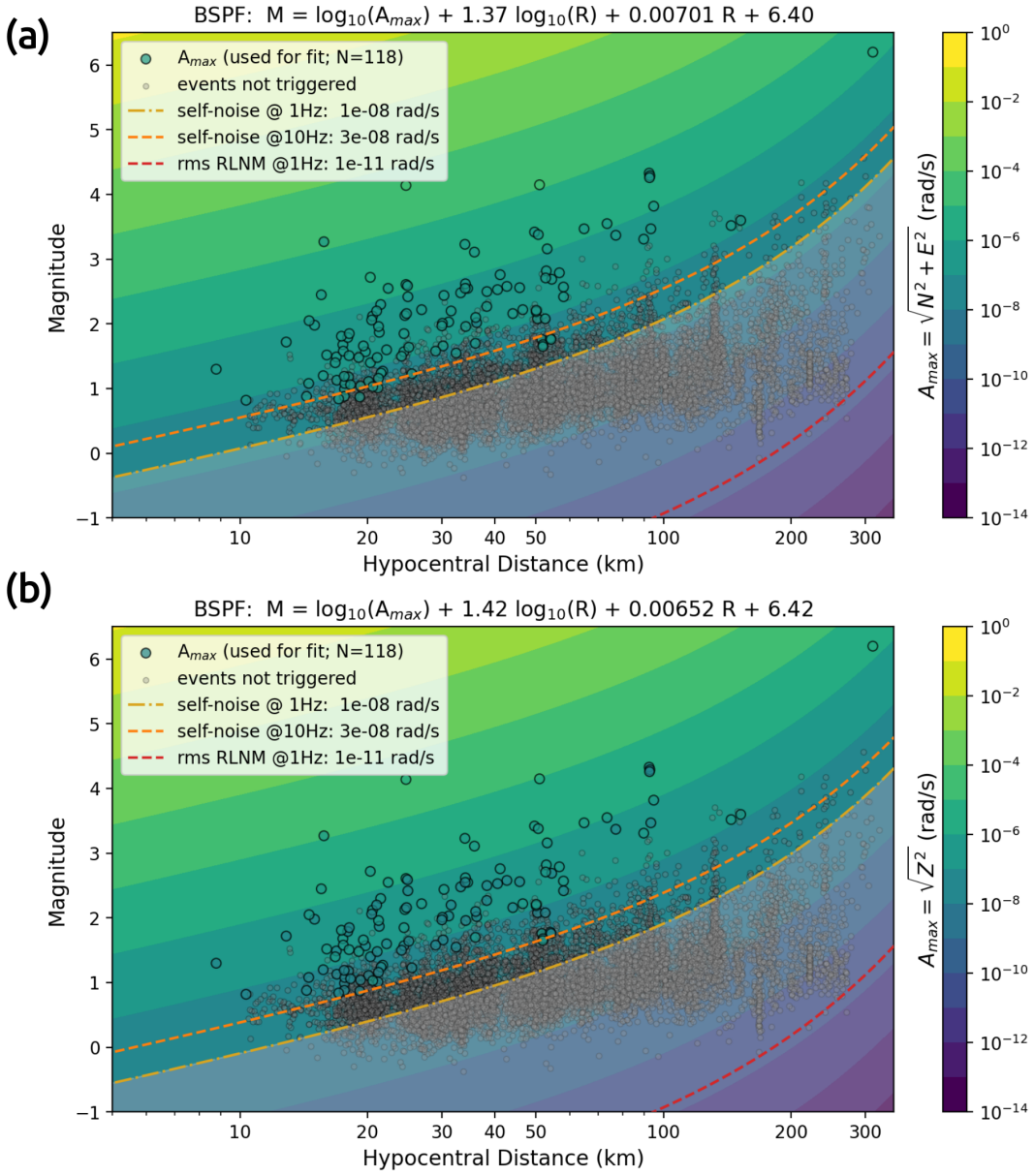

Figure 4.17: This map shows the expected maximal (a) horizontal and (b) vertical rotation rates based on observations with a blueSeis-3A sensor at Piñon Flat Observatory. Color-coded circle represent observations of peak ground rotation velocities on all six channels (N=118) used for the determination of coefficients. Grey circles represent catalog events that are not triggered at the 6 DoF station. The self-noise level of the blueSeis-3A sensor is shown at 1 Hz (≈ 10 nrad/s) and 10 Hz (≈ 30 nrad/s), based on operational range diagrams by Bernauer et al. (2018). The rms amplitude value at 1 Hz of the rotational low noise model (Brotzer et al. 2023) is plotted as a lowermost value (≈ 10 prad/s). The gray shaded area is poorly constrained, thus the model is not representative here.

4.2.6 Discussion

4.2.6.1 Comparison of single-station and array-derived rotations

In the absence of portable rotational sensors, array-derived rotations served as a mean to access rotational ground motions for 6 DoF waveform analysis (Spudich & Fletcher 2008, 2009). ADR also served as a benchmark for observations of large-scale ring laser gyroscopes (e.g., Suryanto et al. 2006, Donner et al. 2017). ADR, however, is based on assumptions such as plane-wave propagation and a rigid baseplate below the array stations, which hold best for low-frequency teleseismic events (Suryanto et al. 2006). When targeting regional or local seismicity, the higher frequencies dominate and a plane wave assumption will eventually not hold, for instance due to small-scale scattering effects.

The inner PFO array allowed a comparison of direct observations and ADR estimates for frequencies up to 5 Hz, revealing strong variations in peak rotation rate amplitudes, while for lower frequencies, rotation rate amplitudes of direct observations and ADR are comparable, if the signal-to-noise ratio allows a comparison. Since ADR amplitudes are affected by averaging across the array stations, this approach might not capture full peak rotation rate amplitudes, especially towards higher frequencies (see Fig. 4.10).

These findings are important in particular when comparing direct measurements of rotation (or strain) with array-derived rotations (or strain) in areas with expected local lateral heterogeneities. A fraction of the amplitude differences between ADR and direct observations might be attributed to strain-induced rotations (e.g., van Driel et al. 2012) caused by a local site effect at the single-point 6 DoF station.

4.2.6.2 Six Degree-of-Freedom Analysis

Applications of 6 DoF analysis for teleseismic events, which provide clear phase separation, low frequencies signal content and ensure that a plane wave can be assumed, produce accurate results (Sollberger et al. 2020). Challenges arise for local seismicity since most seismic energy is contained in higher frequencies (> 10 Hz). Higher frequencies are known to be affected by scattering of local heterogeneities, thus plane-wave assumptions might not be justified. Due to small epicentral distances of local events, a clear separation of seismic phases is not to be expected. 6 DoF observations still allow separation by particle motion polarization to some degree and attribute apparent phase velocities.

We apply basic 6 DoF processing techniques, such as backazimuth estimation and local phase velocity estimation, for a local M_w 4.1 event and a regional M_w 6.2 event. First, we focus on a frequency range of 0.5 Hz - 1.0 Hz, which shows a good signal-to-noise ratio. Hereby, three different approaches to estimate the backazimuth are compared, while for both events a ratio of horizontal rotation rate amplitudes (CoVar) yields the closest estimates to the expected backazimuth based on the catalog event location. Approaches based on Love and Rayleigh polarization require separated phases to exit adequate particle motion.

For the local M_w 4.1 event, array f-k beamforming is in good agreement with the expected backazimuth although the variance increases towards higher frequencies. The backazimuth estimation for ADR and direct rotation observations show poor results with high variance for the *i*-band (2.0 Hz - 5.0 Hz). For the *m*-band (0.5 Hz - 1.0 Hz), the CoVar approach yield the best estimates for both events. The signal-to-noise ratio is poor for the *a*-band, thus any interpretation not suitable. With regard to the *i*-band estimates for the M_w 6.2 event, low accuracies and high variance is observed and also the beamforming reveals a strong offset compared to the expected backazimuth. Good signal-to-noise ratios in the *a*-band and *m*-band result in backazimuth estimates close to the expected backazimuth, except of the Rayleigh approach being far off the expected backazimuth.

4.2.6.3 Empirical Scaling Relation for Rotation Rates

A first empirical amplitude relation map for vertical and horizontal rotation rates for local to regional scale seismicity is presented in Figures 4.17a and 4.17b and may serve as an orientation towards resolvability of seismic events for future campaigns with a comparable station setup. These empirical relations are derived using 118 events with a coincidence of 6. The applicability is likely restricted to the incorporated cluster of observed magnitudes and hypocentral distances and merely extrapolated outside. Apart from the M_w 6.2 event, further constraints for regional distances and larger magnitudes are missing.

We are aware that the transferability is not universal, and the relation is primarily valid for this station setup and location geology. In particular, settings with soft sediments likely amplifies amplitudes, thus decrease the resolution limit, despite the fixed self-noise level. Nevertheless, this serves well as a first orientation enabled by the long dataset of a permanent installation.

4.2.7 Conclusions

We report on a first permanent 6 DoF station, comprising a rotation rate sensor (blueSeis-3A gyroscope) and a broad-band seismometer, at the Piñon Flat Observatory in southern California. Compared to the former one-component GEOsensor gyroscope (Schreiber et al. 2009), this station runs continuously with low maintenance effort. The data is openly accessible to the scientific community via IRIS FDSN services.

Being located in a tectonic active area embedded in the well-instrumented Piñon Flat Observatory infrastructure and scientifically interesting area, we are sure it can contribute to further valuable observations and studies. We evaluate a first dataset of the local to regional seismicity using one year of data from October 2022 to October 2023. Most triggered events are originated within an epicentral distance of 150 km from the station and cover a magnitude range from below 1.0 to 4.1. An exception is a regional magnitude 6.2 event.

The signal-to-noise ratio is essential to obtain good results for the 6 DoF analysis techniques, however, varies strongly for the events of this dataset depending on their epcientral

distance, magnitude and presumably the radiation pattern (see examples in Fig. 4.7). A comparison of ADR and PY.BSPF in terms of signal-to-noise ratio yields better results for ADR, profiting from low self-noise levels of seismometers. This comparison is, however, limited by the imposed frequency bands of the subarray geometry. Most signal energy for direct observations of PY.BSPF is generally found between 10 Hz and 30 Hz.

We find that the current limitation for observations is set by the self-noise limit of the blueSeis-3A sensor. In order to complete observations at lower-magnitudes for local seismicity or mid-magnitudes for regional seismicity, the self-noise limit has to be decreased by about 3 to 4 orders of magnitude (see Fig. 4.17; Brotzer et al. (2023)). This is especially required for studies based on ambient seismic noise sources, such as seismic microseism, which are deeply hidden in the self-noise at the moment. In order to compare direct rotational motion observations with array-derived rotations, we divide the seismic PFO array into three subarrays with different frequency bands. Cross-correlation values of above 0.9 indicate a good match in waveforms for lower frequency bands with sufficient signal-to-noise ratio for a local M_w=4.1 and a regional M_w=6.2 event. For higher frequencies (>1 Hz), amplitudes for rotation rates differ significantly, which is partially attributed to an incomplete set of stations at the time of the event. Instead of an averaged rotational motion across an array of stations, a rotational sensor provides direct point observations of the curl of the seismic wavefield. A contribution to the discrepancy might be a result of strain-rotation coupling, which was not investigated further in this study.

The results of 6 DoF processing to the aforementioned events to obtain backazimuth and local seismic phase velocities estimates demonstrates a possible application for local and regional scale seismicity given a good signal-to-noise ratio.

Furthermore, we used peak rotation rate observations of 118 events to infer an empirical amplitude relation for peak vertical and horizontal rotation rates based on a local magnitude scale equation. Determined coefficients for this empirical amplitude relation for vertical and horizontal rotation rates are very similar (0.3% - 6.6% deviation). A validity of the empirical relations below the self-noise level is not guaranteed, therefore shaded. The presented relations might serve as orientation for further installations of 6 DoF, especially for this type of sensor, in order to study local and regional seismicity.

Data and Resources

Processed data, metadata not available online as well as Jupyter notebooks and python scripts to create the shown figures are provided at these repositories:

- https://github.com/andbrocode/BlueSeisPinonFlat
- https://doi.org/10.5281/zenodo.11582084
- https://syncandshare.lrz.de/getlink/fiXq8RsYcpwAzLa7hZ4YbT/Seismica-PFO-BlueSeis-2024

Acknowledgments

Andreas Brotzer is grateful for being awarded the Jerome M. Paros Scholarship by the American Geophysical Union in 2021 enabling his research stay at the Scripps Institution of Oceanography in San Diego in 2022 under supervision of Mark Zumberge. This stay included the deployment of the blueSeis-3A at the Piñon Flat Observatory. Our gratitude goes to the staff at Scripps, namely Sonya Wilson, William Hatfield and Daniel Auerbach, who helped with the logistics and set-up of the sensor at PFO. We would also like to thank the EarthScope Consortium, formerly Incorporated Research Institutions for Seismology (IRIS), for providing the blueSeis-3A sensor for this deployment. We also want to thank Tobias Megies for incorporating the BSPF station into the rotational database.

Chapter 5

Observations and Preliminary Analyses

This chapter presents and discusses specific observations related to ROMY and other instrumentation therein. This includes preliminary results of initiated, but not yet completed, projects deemed worthy of elaboration and documentation in this chapter.

First, recent observations of ROMY's ring laser gyroscopes and the complementary instruments in and around ROMY are presented and further examined. This includes the seismic array surrounding ROMY, which is used to compute array derived rotations, and the environmental network within the ROMY structure. Observations from the tiltmeter and the infrasound station are discussed. Furthermore, the experiment and preliminary results on the natural frequencies of the ROMY structure are briefly outlined and explained.

Second, results of a comparative study of earthquake-based amplitude levels for rotation rates around a vertical axis between the horizontal ring of ROMY and the G-ring at Wettzell are presented and examined.

Third, an extended analysis of the interaction between the atmosphere and the solid Earth as a result of elastic deformation due to barometric loading is discussed. Direct observations of pure rotations promise an enhanced understanding of these processes. The availability of longer time series of ROMY allows to estimate compliance functions and to constrain a barometric tilt model at the ROMY site.

Finally, the potential for seismic source tracking employing 6 DoF methods based on observations of a single station are demonstrated and discussed. Applications to a local source and distant sources of secondary microseisms are presented.

All of these projects address several scientific questions that remain open, such as the specific site characterization or the atmospheric contribution to the ground deformation, thus the low noise model towards long periods. The high-quality, 6 DoF observations that ROMY can provide have the potential to address these open scientific questions, and the preliminary results presented provide a starting point for further projects.

5.1 ROMY's Observational Framework

5.1.1 Sagnac Frequency Observations

Three of ROMY's rings have been operated almost continuously from October 2023 until now (October 2024) to collect three-component geophysical rotation data. The Sagnac frequency, which is different for each ring due to the orientation of its areal vector in space, shown in Figure 5.1 contains sudden offsets, long-term (weeks to months) drifts and also short-term variations due to instrumental effects, such as backscatter and mode jumps (see Sec. 3.2 for more details). The sudden offsets are caused by geometric changes of the ring resonator during manual re-alignment, which is necessary to keep the lasing path closed and thus the ring operational. Frequent maintenance work was required throughout the observation period in order to keep all the rings operational and to optimize the data quality (Fig. 5.1).

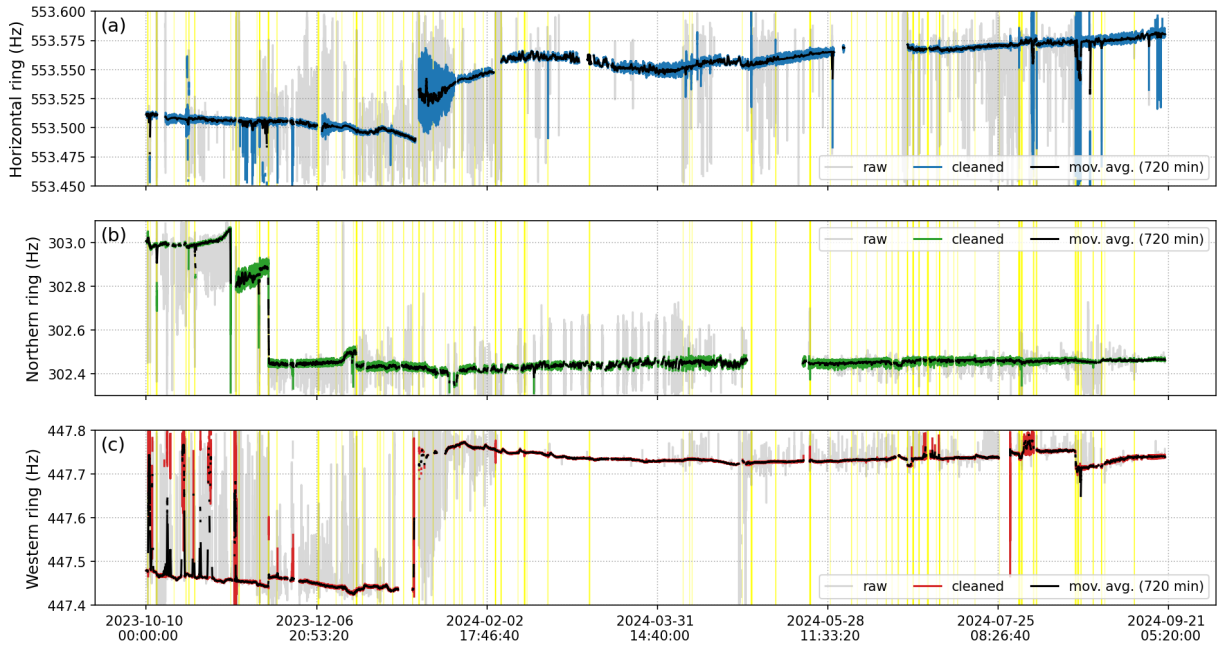

Figure 5.1: Sagnac frequency over one year for (a) RZ, (b) RU and (c) RV. Grey traces include distorted data (e.g. MLTI launches). Color-coded data are cleaned by removing MLTI launches and downtimes. A moving average of 720 min windows is shown in black. Yellow bars indicate time periods of maintenance work.

5.1.2 Direct Observations and Array Derived Rotation

When fully operational, ROMY provides four observations of rotational ground motions in a non-orthogonal component system (Z, U, V, W). The M_w 7.5 earthquake in the New Britain Region (P.N.G.) on 2019-05-14 (12:58:28 UTC) was recorded on all of ROMY's

rings. A spectral comparison of the direct Z-component of RZ and the combined Z'-component by rotating the U-V-W system demonstrates, that the combined signal (dark blue) below 0.01 Hz and above 0.07 Hz is elevated with respect to the recording of RZ (pale blue), mainly driven by the worst performing component, here RW. In the frequency band dominated by the event (0.01 Hz to 0.1 Hz), the vertical components are more comparable. A rotation to an orthogonal Z-N-E system therefore relies on comparable, ideally low, noise floor, thus performance of the individual rings.

In general, the north and east components can be reconstructed using only the contributions of the U-V-W system, but still suffer from the highest self-noise contribution. A comparison of a reconstruction using the full U-V-W- system and a reduced U-V system is shown in Figure S.19 Data used in this section and following analyses (Sec. 5.3 and 5.4) are based on direct observations for the vertical component and combined signals for the north and east component based on rotation of RU and RV.

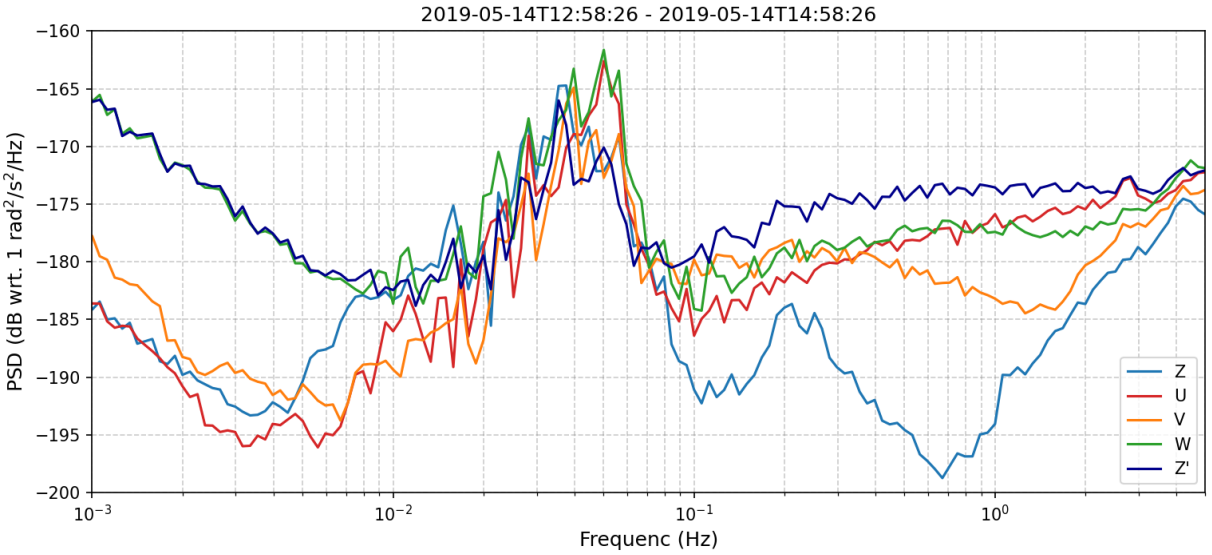

Figure 5.2: Power spectral densities for components Z, U, V and W based on a multitaper approach and averaged in 12^{th} octave bands for the M_w 7.5 earthquake on 2019-05-14. The Z' component is reconstructed using the U-V-W non-orthogonal system.

Having longer rotation time series for three rings of ROMY in 2024 allows a better statistical characterization of the resolution. A median for hourly PSDs for RZ, RU and RV are computed between 2024-01-01 and 2024-03-31 and shown with a 95 % confidence interval with respect to the RLNM (Brotzer et al. 2023) in Figure 5.3. Missing data from a fourth ring, allowed to include G-ring data instead. Compared to the G-ring, ROMY's rings yield an overall wider confidence interval. A signature of the secondary microseism peak (7 s to 10 s) is evident for the median PSD of all rings. The increase in energy above 1 Hz appears to be related to the location of ROMY, as it is less pronounced for the G-ring. The elevated levels of the 97.5 quantile of the RU and RV between 4 mHz and 400 mHz are related to

the atmospheric coupling, as further explained in Section 5.3.

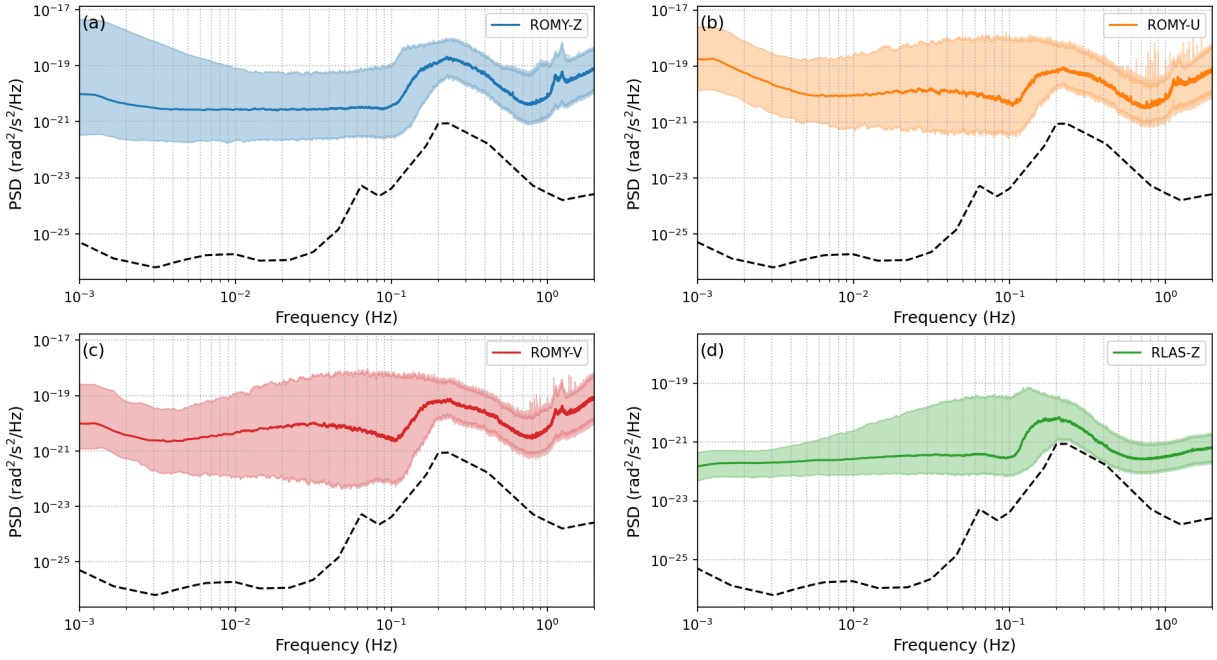

Figure 5.3: Median PSD with 95% confidence interval for the (a) horizontal, (b) northern and (c) western ring of ROMY as well as (d) G-ring (RLAS). The PSDs are based on hourly data between 2024-01-01 to 2024-03-31. The rotational low noise model (dashed black line) by Brotzer et al. (2023) is shown as a reference.

A seismic array of nine stations is used to compare array-derived rotations (ADR) with direct measurements from ROMY. An inner array consists of three borehole sensors (BW.FFB1, BW.FFB2, BW.FFB3) and the permanent station GR.FUR. In 2021, all five seismometers of the outer array (BW.BIB, BW.TON, BW.GRMB, BW.GELB, BW.ALFT) were replaced by STS-2 (Streckeisen) seismometers (Fig. 2.17a). For these stations, Gabbro baseplates were designed, prepared and deployed in order to provide the best possible pressure and thermal shielding in the field. To derive ADR from a seismic array, a rigid baseplate beneath the array and plane wave propagation are assumed (Spudich et al. 1995, Spudich & Fletcher 2008, 2009). These assumptions are generally valid for low-frequency teleseismic events, while they become strong assumptions for local and regional events with higher dominant frequency content (see Sec. 4.2). Based on the frequency band assessment of (Poppeliers & Evans 2015), ADRs for the inner and outer ROMY array are limited to the ranges listed as RMY in Table 4.1.

Waveforms of ADR and ROMY for the M_w 6.9 Al Haouz earthquake on 2023-09-08 for frequencies between 0.02 Hz to 0.1 Hz are shown in Figure. 5.4. The waveforms for ADR are shifted by 0.75 s to optimize the variance reduction, but the origin of the shift is not clear and needs to be investigated with respect to the ADR processing chain. This is one of several three-component teleseismic events recently observed with ROMY. There is

good visual agreement between the waveforms for the north and east components, which are inferred from the vertical displacement. The vertical rotation (= torsion or twist) is derived from the horizontal displacements. An overall underestimation of peak rotation rates of around 2 nrad s^{-1} for the horizontal components and 5.6 nrad s^{-1} for the vertical component can be partially attributed to spatial averaging across the array. Another contribution may be the absence of data for station ALFT for the ADR computation. The best match in the waveforms is observed for the north component, which is accompanied by an achieved variance reduction of more than 97 % and a CC coefficient of 0.99(Fig. 5.4a). The worst agreement in peak amplitude is obtained for the vertical component, with is consistent with a variance reduction of only 87.74 %.

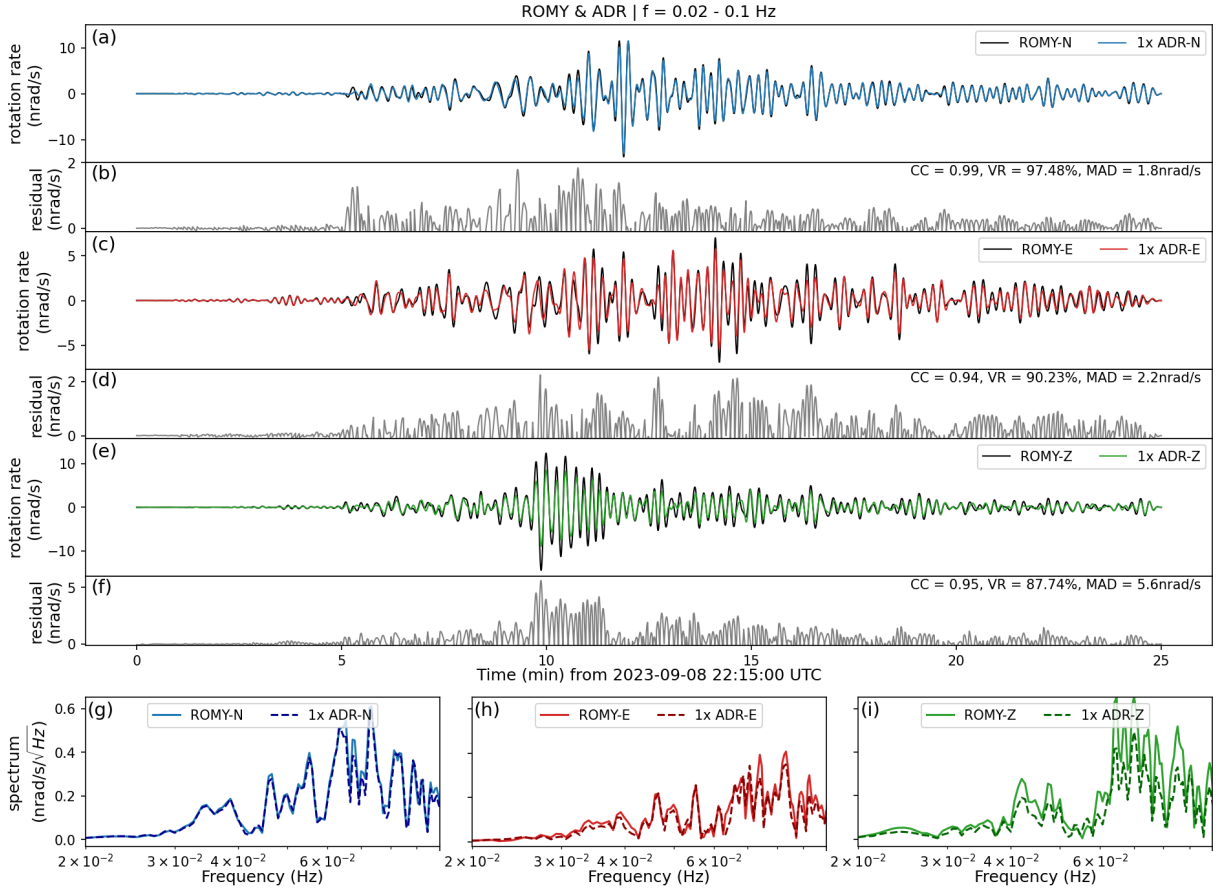

Figure 5.4: Array-derived rotation and direct ROMY observations of the M_w 6.9 Al Haouz earthquake (2023-09-08 22:11 UTC) for north (a), east (c) and vertical (e) ground rotation rate are compared. (b), (d) and (f) show residuals between ADR and ROMY. (g), (h) and (i) show amplitude spectra for the north, east and vertical components, respectively. A bandpass between 0.02 Hz and 0.1 Hz is applied to the data. ADR is based on stations: GR.FUR, BW.BIB, BW.GELB, BW.GRMB, BW.TON and shifted by 0.75 s. CC=cross-correlation value; VR=variance reduction; MAD= maximal amplitude difference

5.1.3 Environmental Observations

Environmental data between 2022-01-01 and 2023-05-31 (before the passive insulation system was installed) are shown in Figure 5.5, which contains an extended data gap at the beginning of 2023 due to errors in the archiving code.

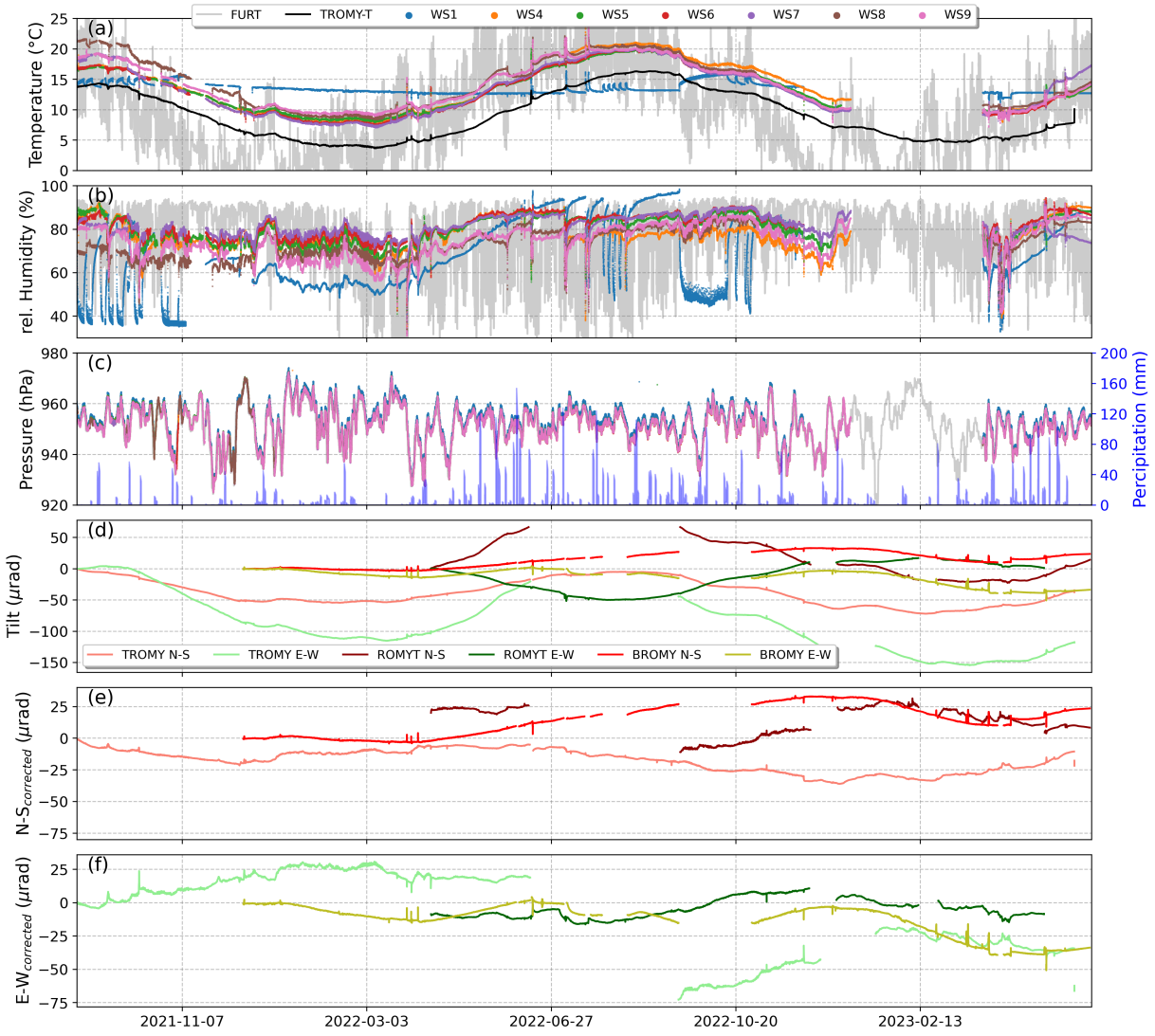

Figure 5.5: An overview of environmental monitoring data and local tilts inside the ROMY structure. (a) Air temperature, (b) air humidity and (c) barometric pressure of the sensor network WS1-WS9 and the outside weather station FURT. Precipitation of FURT is added. (d) Two component tiltmeter data for ROMYT, TROMY and BROMY. Corrupt and distorted data are removed, and data after gaps referenced to last valid values. (e) East tilts and (f) north tilts with removed linear temperature trend.

Differences in absolute temperature within ROMY's shafts are explained by additional excess heat from electrical devices in some shafts. Temperature records inside ROMY

show a seasonal trend ranging from about 7 °C to 22 °C. There is a seasonal lag compared to the outside temperature (FURT) due to the depth of several meters. The strong diurnal and sub-diurnal variation in surface temperature and humidity that are damped inside ROMY, but not entirely suppressed (see Sec. 3.2.6.1).

At the bottom of ROMY's central shaft (WS1), the temperature variations are small between 14 °C to 16 °C throughout the year. Signatures for WS1 with a sudden increase in temperature followed by a slow decrease are related to activation and operation of a dehumidifier unit and therefore show up in the corresponding humidity and temperature record. The apparent linear decrease for WS1 is incomprehensible and should be verified with longer multi-year time series in the future.

Humidity correlates with the temperature inside the shafts, ranging from 70 % in winter to 90 % in summer. For the central shaft, values of 100 % have also been recorded since.

5.1.4 Local Tilt Observations

Long-term tilt observations for different tiltmeter located at different locations within ROMY are shown in Figure 5.5d-c. A strong dependence on temperature and temperature changes has been observed for the instruments, however, only a linear correction does not capture all influences (see seasonal trends in Fig. 5.5e and 5.5f). Linear coefficients vary for the different sensors, the respective observation period and the individual components. An experiment was conducted with one platform tiltmeter to investigate the temperature dependence. The sensor was placed under an insulated box and exposed to a controlled thermal influx. The results are inconclusive and suggest non-linear effects in the presence of strong temperature variation (increase and decrease) and with an exponential decay during readjustment after removal of the heat source. Generally, independent tilt observations at ROMY are important to monitor the deformation of the ROMY structure and corner boxes and will benefit from further improvements in passive thermal insulation or an active temperature stabilization.

More than two months of data since 2024-03-09 of N-S and E-W ground tilt at ROMYT are shown in Figure 5.6 as bandpass filtered waveforms and continuous wavelet transforms. The spectrogram reveals dominant sub-daily tides for the N-S and the E-W tilt motions. Weak daily tides are present only on the E-W component. This is consistent with theoretical expectations for latitudes around 48 °N, with vanishing diurnal tidal rms tilt amplitudes for the north component of about 0 nrad to 4 nrad and strong tilts in east direction of about 18 nrad to 20 nrad (Agnew 2010). For semi-diurnal tides, both north and east, are expected to be pronounced with rms tilt amplitudes of 20 nrad and 30 nrad, respectively (Agnew 2010).

Several energetic events with periods longer than 24 h are additionally causing tilt signals (Fig. 5.6). This is more prominent on the E-W component. For very long periods, the dominant source of ground motion is elastic deformation caused by atmospheric pressure

loading (Zürn et al. 2007). This would agree with more signal energy on E-W components for a dominant eastward wind direction at ROMY's location.

Predicted solid Earth tidal tilts are computed using the python package PyGTide (Rau et al. 2022) to compare it to observations. A good agreement for semi-diurnal tilts is found. When comparing several months of mixed diurnal and semi-diurnal signals between 11 h to 26 h period, the residuals are minimized by scaling predicted eastern tilts by 1.09 and northern tilts by 0.82 (Fig. 5.7). Transient signals in the residual time series often coincide with times of maintenance (see Fig. 5.7) when opening and closing shaft covers causes artificial pressure signals. Partially discrepancies in predicted and observed signals might also origin in strain to rotation coupling, attributable to local heterogeneities, not least the ROMY structure itself.

Barometric loading of the Earth's surface causes deformations and introduces tilt motion coupling to the seismometer components (see Sec. 5.3). The signal content in the residuals in Figure 5.7, left after expected solid Earth tides have been removed, is largely the result of local atmospheric pressure effects. Modelling tilts based on a linear model with local barometric pressure ($P(t)$) and its Hilbert transform ($H[P(t)]$) can reduce the residuals in terms of variance reduction (Eq.(3.5)) by 44 % for the east component and 13 % for the north component (Fig. 5.8). The coefficients, derived by multi-variate RANSAC regression,

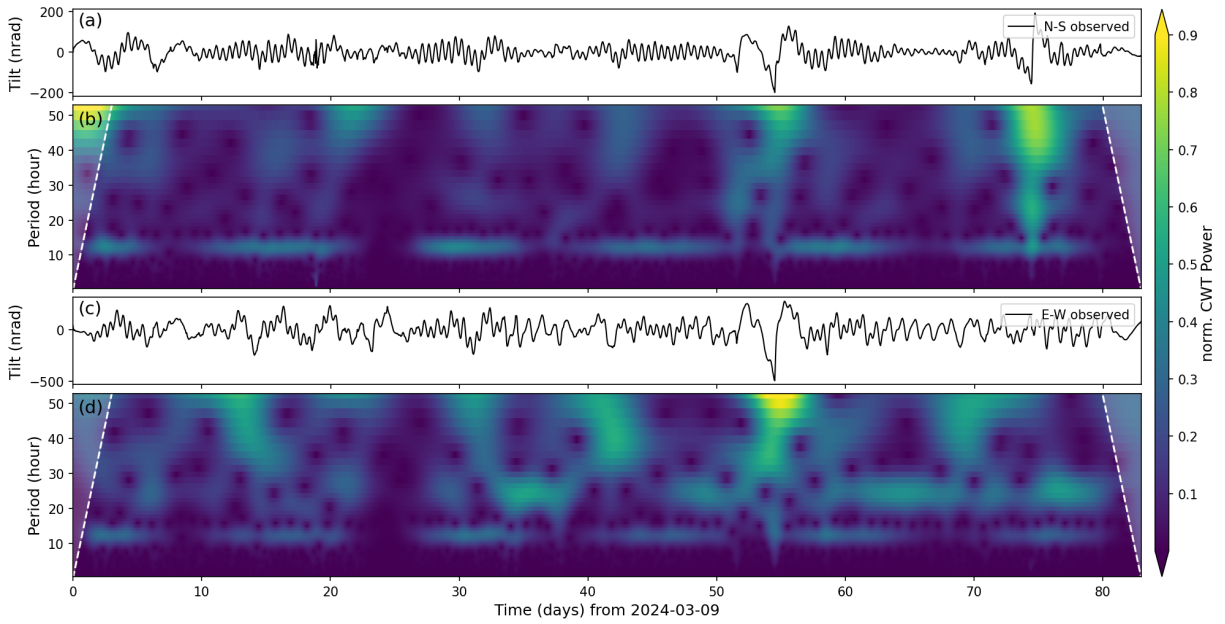

Figure 5.6: Observed N-S (a) and E-W (c) tilt of BW.ROMYT is shown with corresponding continuous-wavelet transform (CWT) in (b) and (d), color-coded by the normalized CWT power. White shaded areas are unresolved. A bandpass (1 h to 100 h) has been applied.

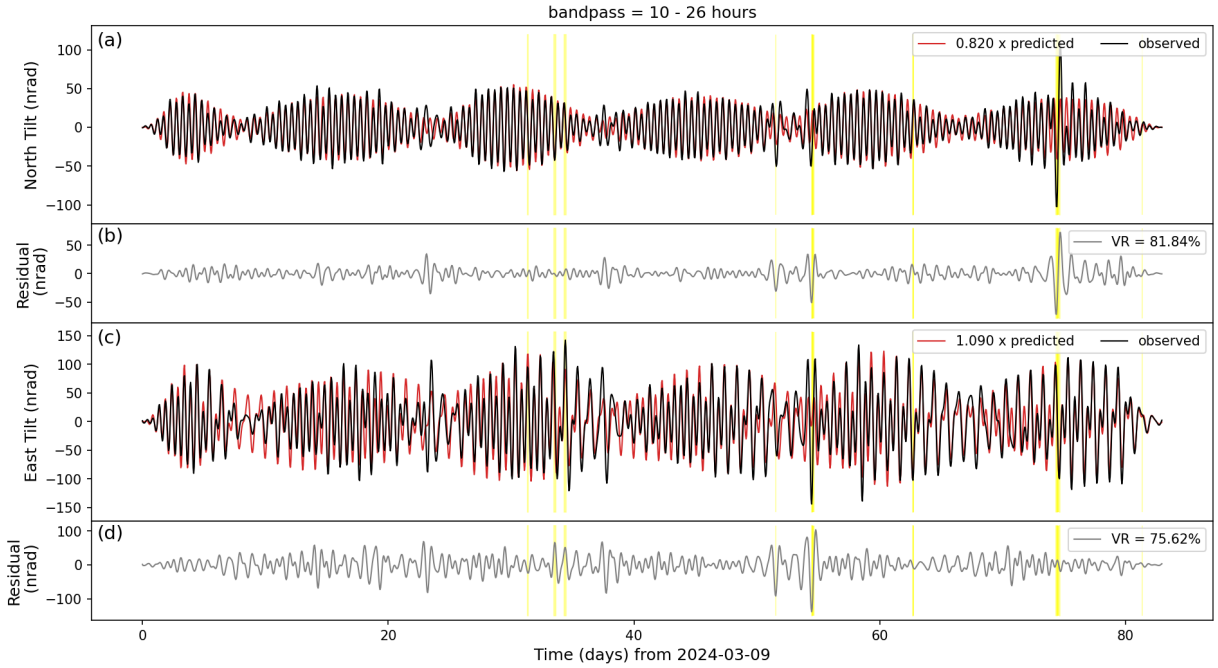

Figure 5.7: Predicted (red) and observed (black) solid Earth tidal tilts for (a) north-south and (c) east-west components. Observed data is based on ROMYT tiltmeter and prediction computed using PyGTide (Rau et al. 2022). The data are bandpass filtered between 11 h to 26 h period to cover daily and sub-daily tidal signals. The residuals of predicted and observed signals are shown in (b) and (d). Predicted signals are scaled by 0.82 for north and 1.09 for east components in order to reduce the residuals. Yellow bars indicate maintenance periods.

are:

$$N'(t) = -5.3\ nrad/hPa \cdot P(t) + 8.4\ nrad/hPa \cdot H[P(t)] \quad (5.1)$$

$$E'(t) = 28.0\ nrad/hPa \cdot P(t) + 10.1\ nrad/hPa \cdot H[P(t)] \quad (5.2)$$

The north component yields a larger contribution from the spatial pressure gradient, while the east component is dominated by local deformation or 'cavity effect' (Zürn et al. 2007, 2022). Therefore, the differences between the coefficients for the two components may be due to the geometry of the shaft or cavity and the concrete foundation on which the tiltmeter rests. The 'cavity effect' also includes a contribution from strain-rotation coupling due to a heterogeneous subsurface features that a cavity represents (Zürn et al. 2007, 2022).

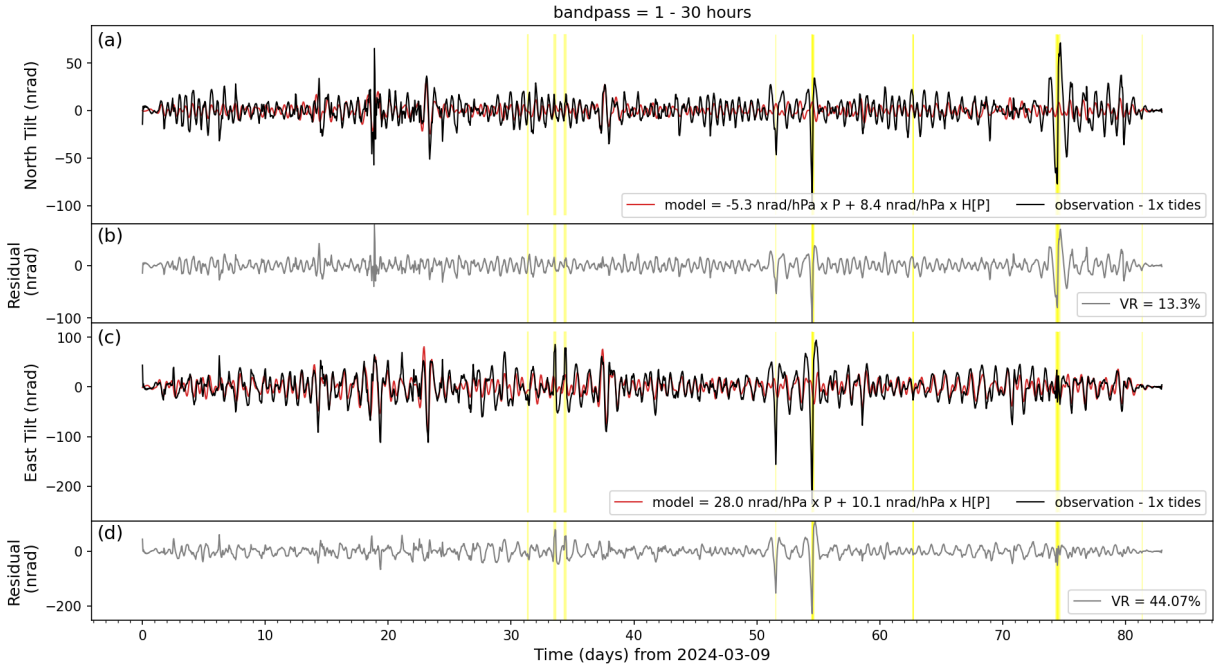

Figure 5.8: Observed tilts (black) for (a) north and (c) east component are corrected using predicted solid Earth tides based on PyGTide (Rau et al. 2022) with scaling factors of 0.82 and 1.09, respectively. A linear model for barometric pressure and the Hilbert transform thereof is fitted (red). Residuals of the model and observations are shown in (b) and (d). Yellow bars indicate maintenance periods.

5.1.5 Infrasound Observations

Infrasound signals recorded at FFBI seem to be affected during maintenance work when access shafts are opened, thus allow air circulation inside ROMY and especially whenever active air ventilation is activated in the central shaft (Fig. 5.9a). As expected, dominant contributions of infrasound are can be attributed to wind, independent of the direction. An increase in wind speed causes a stronger signal for the infrasound channel of FFBI (Fig. 5.9).

The BDO channel of FFBI, which records absolute barometric pressure, shows a constant offset of 7 hPa compared to PS3 next to FFBI. This is attributed to a missing recent calibration of the sensor, adjusting its reference to the respective altitude, before its installation at ROMY. The weather station FURT is about 3 m elevated at the surface level, which explains the slightly lower pressure readings.

On calm days, the microbarom around 0.2 Hz, representing infragravity waves caused by oceanic-atmospheric interaction (e.g., Waxler & Gilbert 2006), is clearly resolved (Fig. 5.10). Better infrasound observations could potentially be achieved by adding a spatial filter to suppress wind noise.

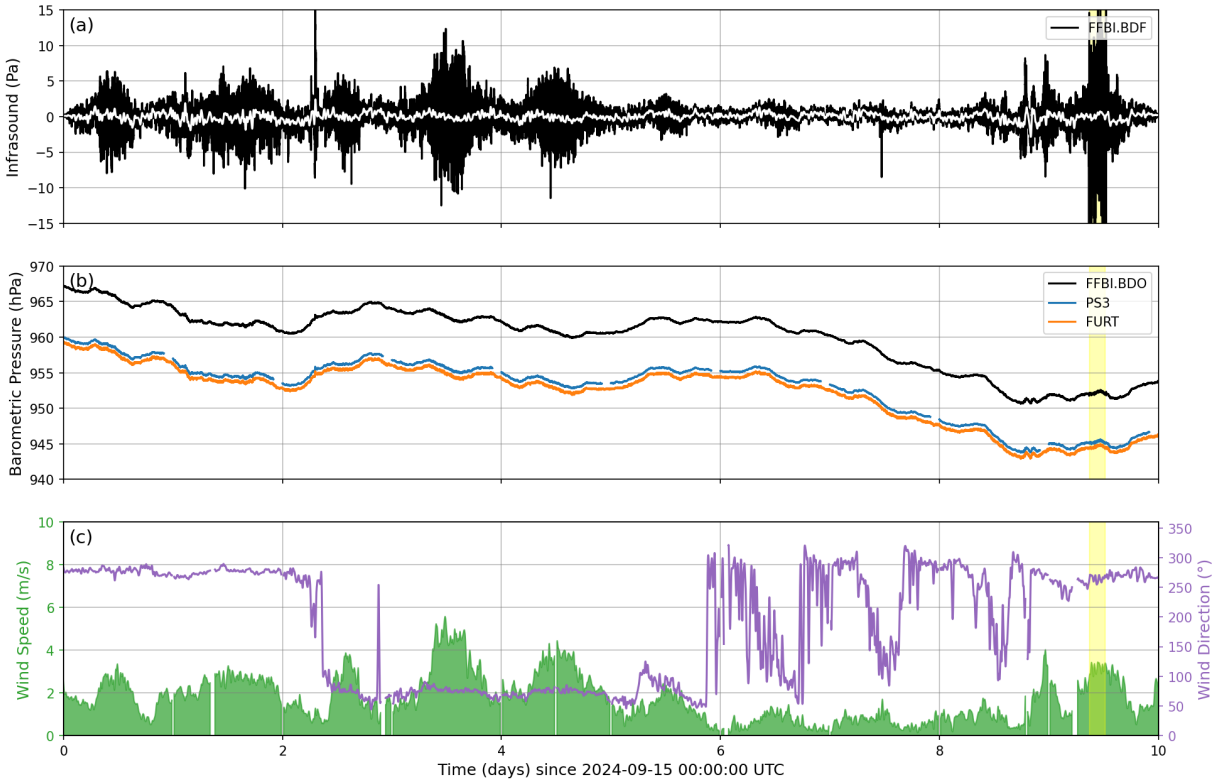

Figure 5.9: (a) Raw infrasound observations of FFBI at ROMY (black) and with a moving average (3600 s) applied (white). (b) Absolute barometric pressure of FFBI, FURT and PROMY. (c) Smoothed wind speed and direction recorded at FURT. Yellow vertical bars indicate maintenance work.

5.1.6 Natural Mode Observations of the ROMY Structure

It is expected, that the glass fiber reinforced concrete structure (or building) of ROMY, embedded in the shallow subsurface, as indicated in Figure 3.7, has an impact on the recorded signals based on its natural frequencies (or eigenmodes). The eigenmodes of a structure are commonly estimated using an experimental modal analysis (EMA) or operational model analysis (OMA). For the EMA, the structure must be excited with a known source signal, which is not possible for ROMY. An OMA relies on the excitation of the eigenmodes by ambient signals during operation.

In the spring of 2023, an experiment was conducted in which nine Trillium Compact broadband seismometers were installed in ROMY's access shafts to record ambient seismic noise and infer the eigenmodes of the structure. The median power spectral density for one week (2023-03-10 and 2023-03-17) is computed for all components and each station inside ROMY, as well as the borehole stations FFB1, FFB2 and FFB3 surrounding ROMY (Fig. 5.11). The borehole stations provide an external reference outside the ROMY structure. FFB1 is located at a depth of about 90 m, while FFB2 and FFB3 are at depths of

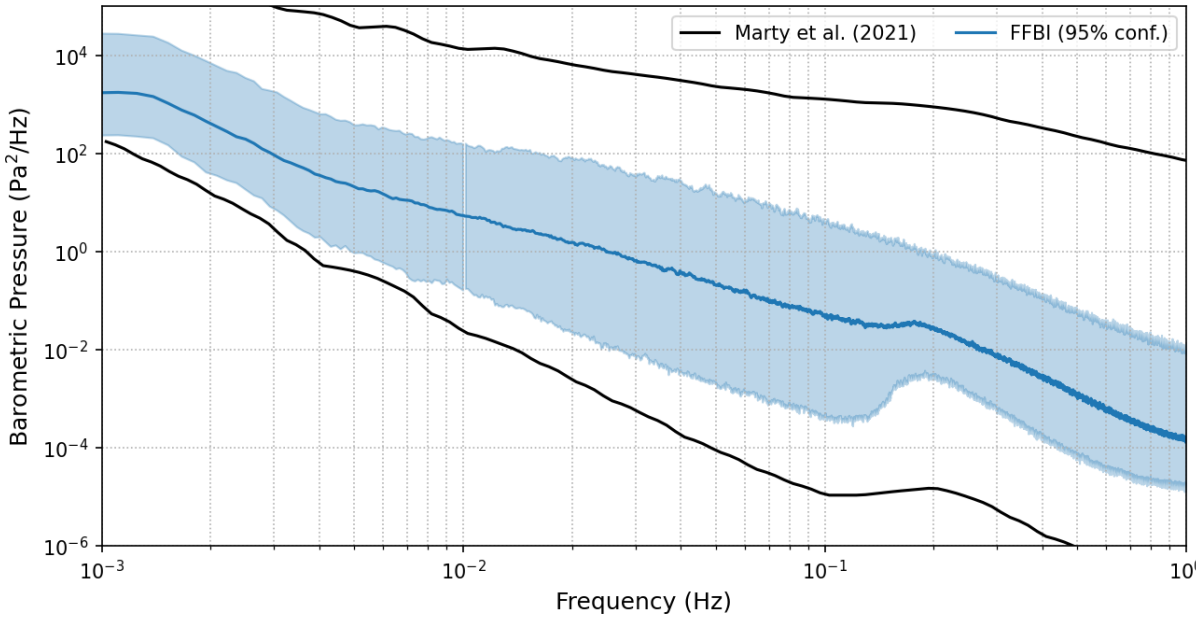

Figure 5.10: A median PSD with a 95 % confidence interval is shown for barometric pressure recorded at FFBI using data of channel BDO below 10 mHz and BDF above. Noise models by Marty et al. (2021) are shown as reference.

about 15 m, hence comparable to the deepest point of the ROMY structure. Stations RY03 and RY04 had to be excluded due to data distortions. High frequency distortions and a pronounced 50 Hz peak are evident for RY09, limiting its reliability above 10 Hz.

In general, less seismic energy is present for the deep borehole station FFB1 above 1 Hz for the horizontal components and above 2 Hz for the vertical component. The shallower borehole stations are, as expected, more comparable to the stations within the ROMY structure. Distinct frequency peaks are present, such as the adjacent peaks at 1.13 Hz and 1.24 Hz. The peak at 1.13 Hz is larger for the east component, while the 1.14 Hz peak is dominant for the north component. All prominent peaks are consistent across all stations, as expected for eigenmodes. However, since the same peaks also occur at the external stations, their cause is more likely to be found in the subsurface structure than in the ROMY building. Most likely, the excitation by ambient seismic vibrations is not sufficient to excite the eigenmodes of the ROMY building and allow for an OMA.

The median PSDs of horizontal (H) and vertical (V) components are used to compute H/V curves:

$$H/V \;=\; \frac{\sqrt{PSD_N^2 + PSD_E^2}}{PSD_Z}\,, \tag{5.3}$$

for all stations, which are presented in Figure 5.12.

Distinct peaks are identified for all stations at the following frequencies: 0.228 Hz, 1.13 Hz, 1.24 Hz, 2.085 Hz, 2.775 Hz, 3.125 Hz , and indicated by yellow bars in Figure 5.12. A peak

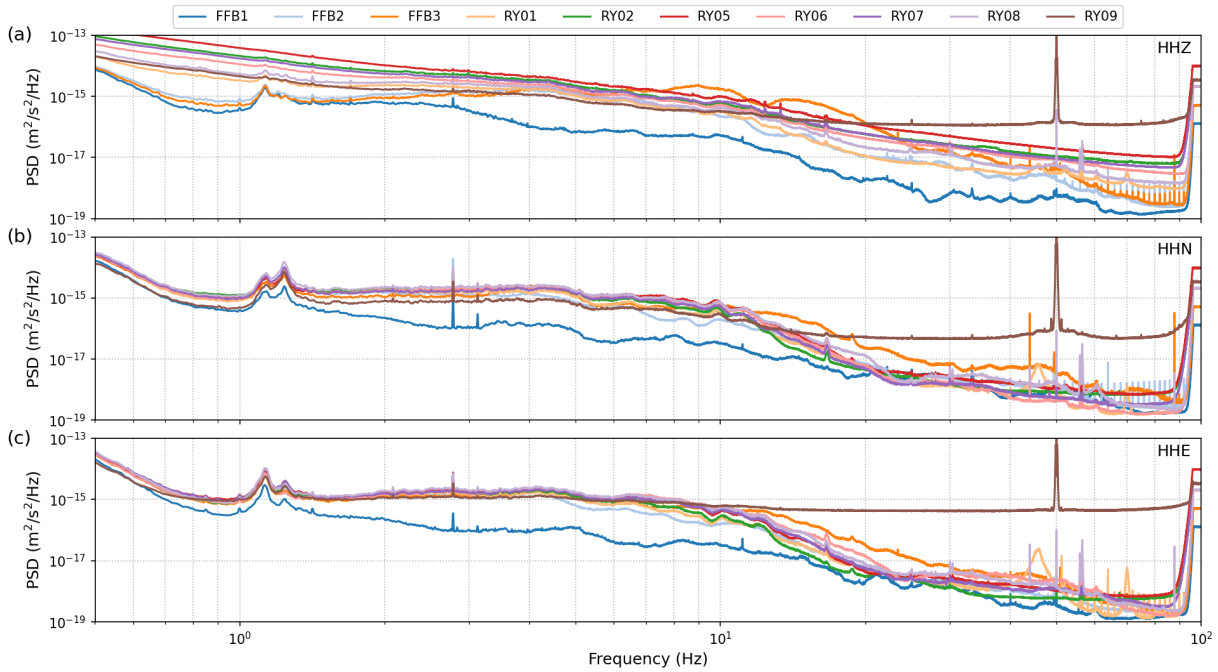

Figure 5.11: Median PSDs for the vertical (a), north (b) and east (c) component of seismometers inside ROMY (RY01 – RY09) and the inner ROMY array (FFB1, FFB2, FFB3) between 2023-03-10 and 2023-03-17 are shown. A moving average has been applied for visualization purposes.

at 16.66 Hz is present only for the stations inside the ROMY building and might be linked to electrical crosstalk via grounding, originated from the nearby electrified tram system, which typically operates at high-voltage at 16.7 Hz.

Preliminary Conclusions and Outlook

The presented preliminary results presented may indicate a negligible effect on the observations due to the natural frequency amplification of the embedded structure of ROMY. Virtual modelling of the complex ROMY structure to obtain theoretical eigenmodes and eigenvectors could improve the understanding of potential influences on the observations, but would require a sophisticated software and engineering insight. The H/V curves could be used in combination with more data to characterize the local subsurface and potentially correct local site effects in observations of teleseismic events (see Sec. 5.2).

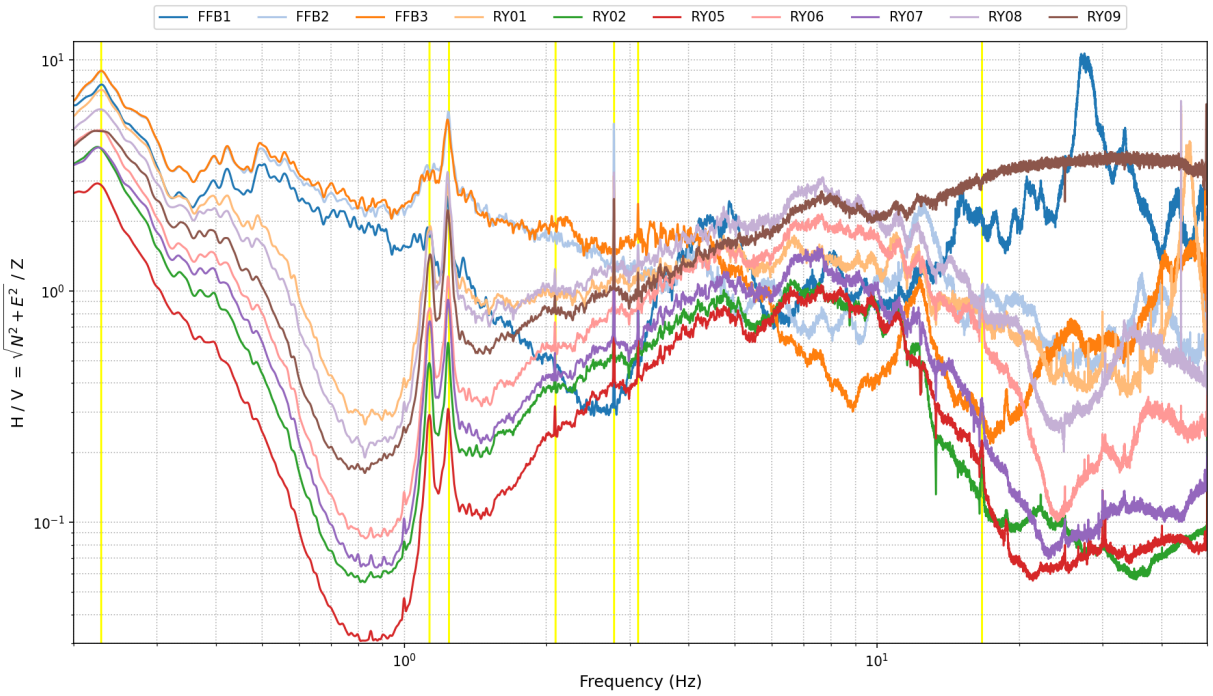

Figure 5.12: Median PSDs for the vertical (a), north (b) and east (c) component of seismometers inside ROMY (RY01 – RY09) and the inner ROMY array (FFB1, FFB2, FFB3) between 2023-03-10 and 2023-03-17 are shown. A moving average has been applied for visualization purposes.

5.2 Amplitude Amplification: ROMY and G-ring

For many teleseismic earthquake records, a difference in amplitude for rotation rate between ROMY and the G-ring is reported. The different geological setting, hard crystalline rock for the G-ring in Wettzell and softer sediments for ROMY in Fürstenfeldbruck is a likely candidate for the different amplitudes. The quantitative explanation for this discrepancy between locations is still not fully understood. Since the G-ring is a single, horizontal RLG, only a comparison of rotational motions around a vertical component is possible.

In order to systematically and statistically evaluate the amplitude ratio between ROMY and G-ring, a dataset of global earthquake detections is required. Based on the ISC (International Seismological Center) catalog, all events with magnitude of 6 and above between 2019-01-01 and 2024-04-30, were analyzed, which amounts to 428. Data for the vertical components of ROMY (BW.ROMY) and G-ring (BW.RLAS) and the co-located broadband seismometers FUR (GR.FUR) and WET (GR.WET), respectively, are used for the analysis.

A manual quality assessment and selection of observations was required due to frequent instrumental distortions of ROMY records. This leaves 48 usable events, or about 11 %. Reasons for the small number of useable events are maintenance work for the RLGs, espe-

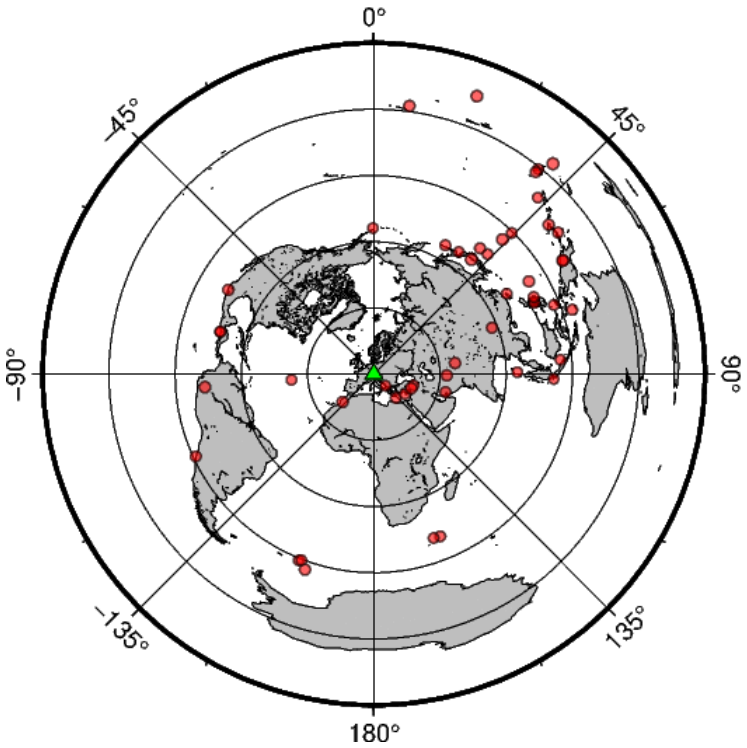

Figure 5.13: The location of 48 selected earthquakes (red circle) detected by ROMY (green triangle) and G-ring (about 200 km NE of ROMY) that are used for the study, plotted on a ROMY centered polar-projection map.

cially ROMY and frequent split-mode operation states (= no data), as well as instrumental glitches occurring during events as a result of mode jumps and instrumental drifts. A polar distribution of epicenters of the selected, useful events is shown in Figure 5.13. Most events are located in a backazimuth range of 0 to 90° (= south-western Pacific area) with respect to ROMY.

Figure 5.14 shows as an example data for an M_w 6.8 event on April 05, 2024 (11:03:15 UTC), with the data used to estimate the peak amplitude is shaded in blue. Each trace is zero-padded, bandpass filtered with in 6th-octave frequency bands and an absolute peak amplitude is determined using the 95th percentile. For each event, the amplitude spectra are computed using an FFT. Since the focus is on the vertical rotation rate, catalog-based theoretical backazimuths are used to rotate into a ZRT coordinate system and use the transverse acceleration of FUR and WET for further analysis. For the example event, these amplitudes are shown in the lower panel of Figure 5.14.

Median values for peak amplitudes estimated in the time domain are shown with a 60 % confidence interval for vertical rotation rate of ROMY and G-ring in Figure 5.16a and for transverse acceleration FUR and WET in Figure 5.15a. Statistical values for the spectral amplitudes and ratios are shown for accelerations in Figure 5.17 and for rotation rate in Figure 5.18.

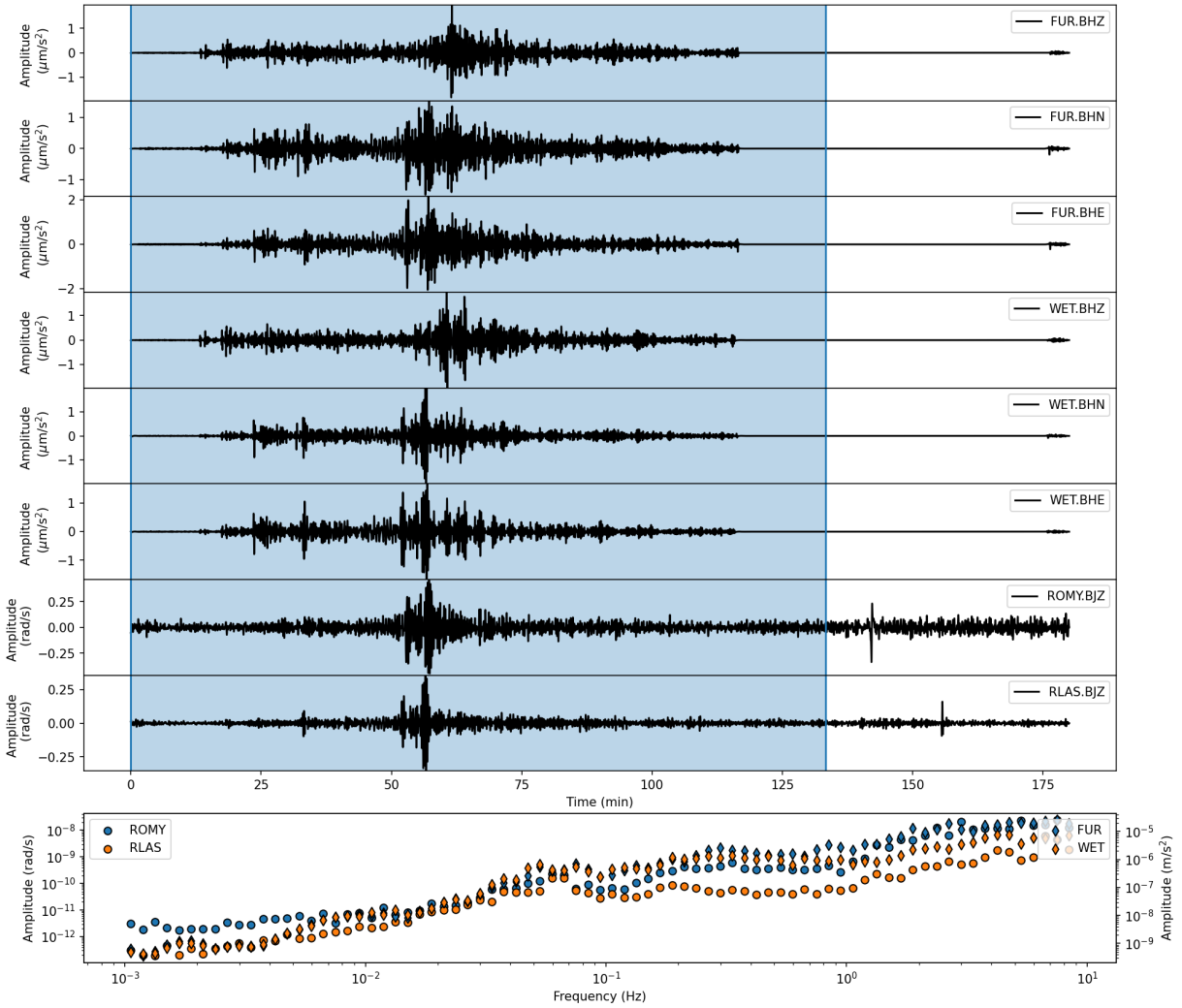

Figure 5.14: Upper panel: Three hour traces of an exemplary event are shown for all component of seismometers BW.FUR and BW.WET and vertical components of ring lasers BW.ROMY and BW.RLAS (G-ring). Blue shaded area indicates data that is used for further analysis. Lower panel: Peak amplitudes estimated as a 95 percentile in 6th-octave frequency bands.

The ratio for transverse acceleration between 1 mHz and 100 mHz is approximately 1 before it increases towards higher frequencies. Above 1 Hz, the ratio is between 10 and 20. This might also be related to a generally higher level of anthropogenic noise around the site of FUR.

When comparing the vertical rotation rate of ROMY and the G-ring, a level of about 1 prad s^{-1} between 1 mHz and 10 mHz is approached. This is a resolution limit and therefore mostly noise rather than seismic energy. Moreover, most events are not expected to provide significant seismic energy in this frequency band. Conclusions for frequencies below 10 mHz

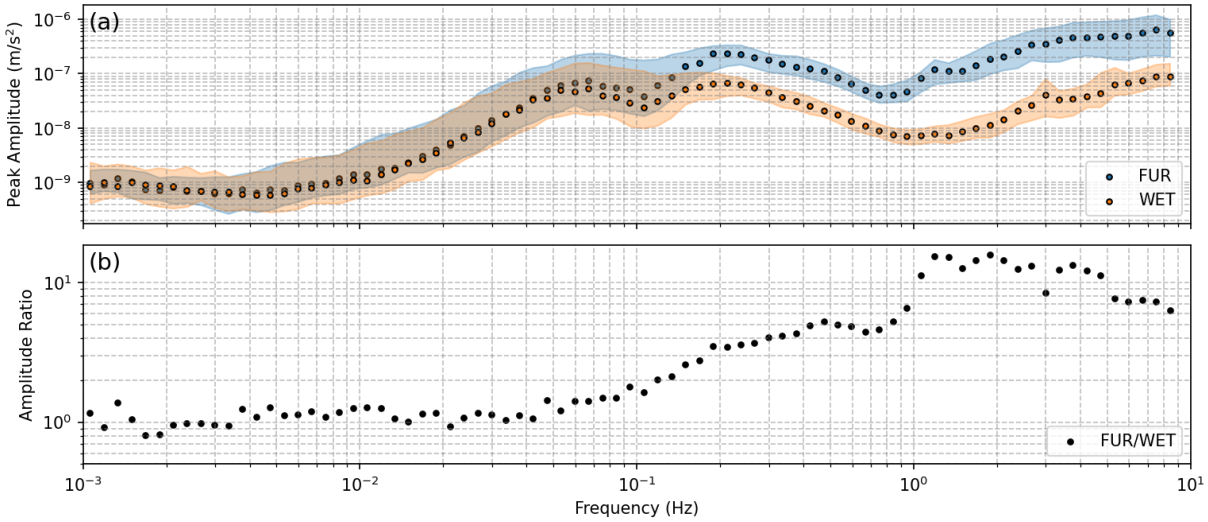

Figure 5.15: (a) Median values of peak amplitudes of all events (circles) for 6th-octave frequency band and 60 % confidence interval (shaded) for transverse accelerations of GR.FUR and GR.WET. (b) FUR-to-WET ratio of median values of peak amplitudes.

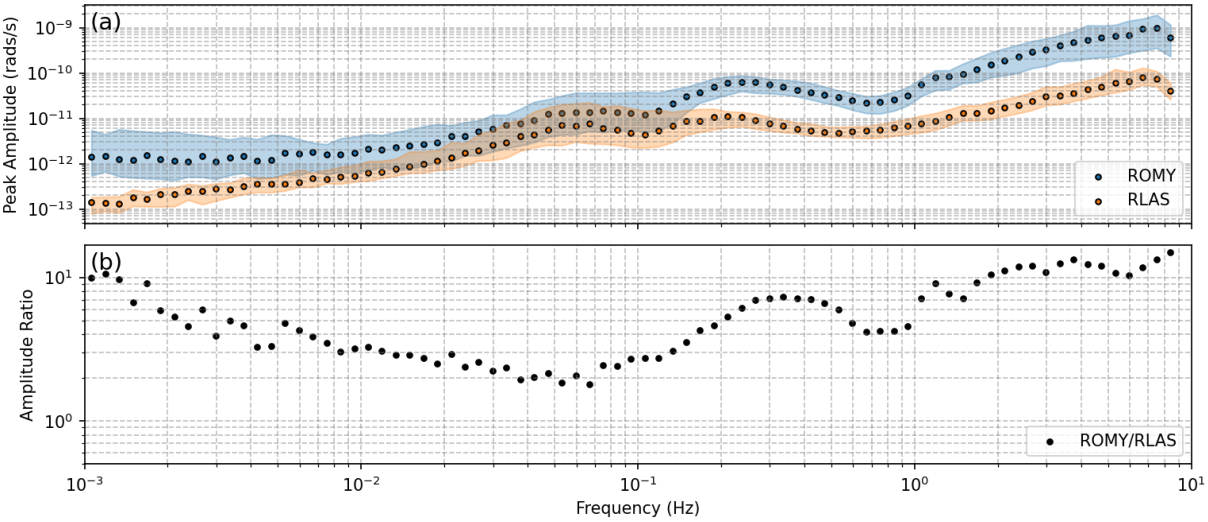

Figure 5.16: (a) Median values of peak amplitudes of all events (circles) for 6th-octave frequency band and 60 % confidence interval (shaded) for transverse accelerations of BW.ROMY and BW.RLAS. (b) ROMY-to-RLAS ratio of median values of peak amplitudes.

are therefore not reliable.

Between 10 mHz and 100 mHz the teleseismic earthquake signal content is dominant and a rotation rates at ROMY are larger by a factor of 2 to 3 (Fig. 5.16). For frequencies above 0.1 Hz, the difference in signal energy increases for both acceleration and rotation

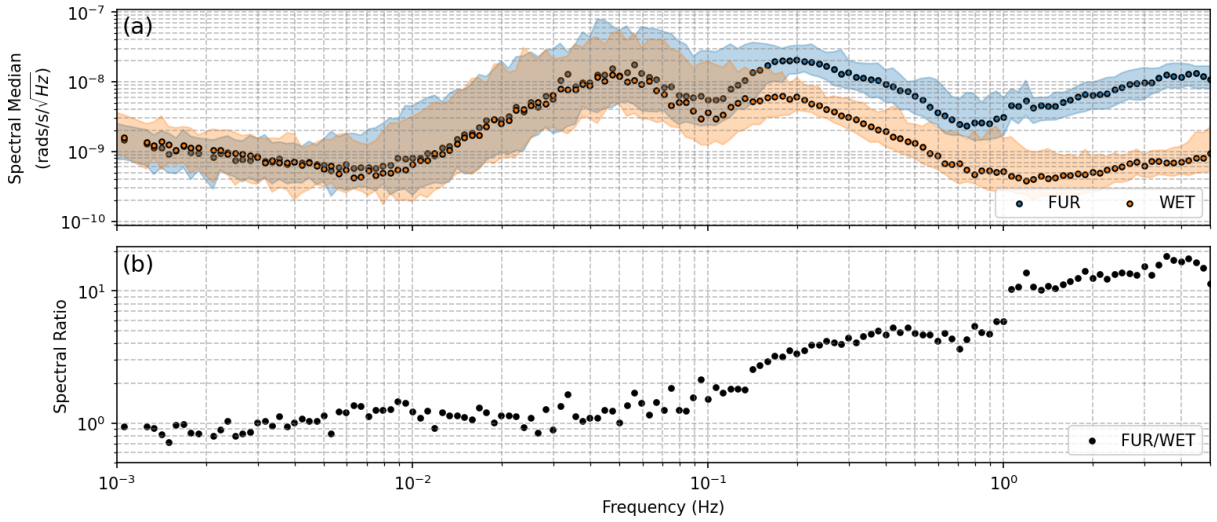

Figure 5.17: (a) Median values of amplitude spectra of all events (circles) and 60% confidence interval (shaded) for transverse accelerations of GR.FUR and GR.WET. (b) FUR-to-WET ratio of median values of amplitude spectra.

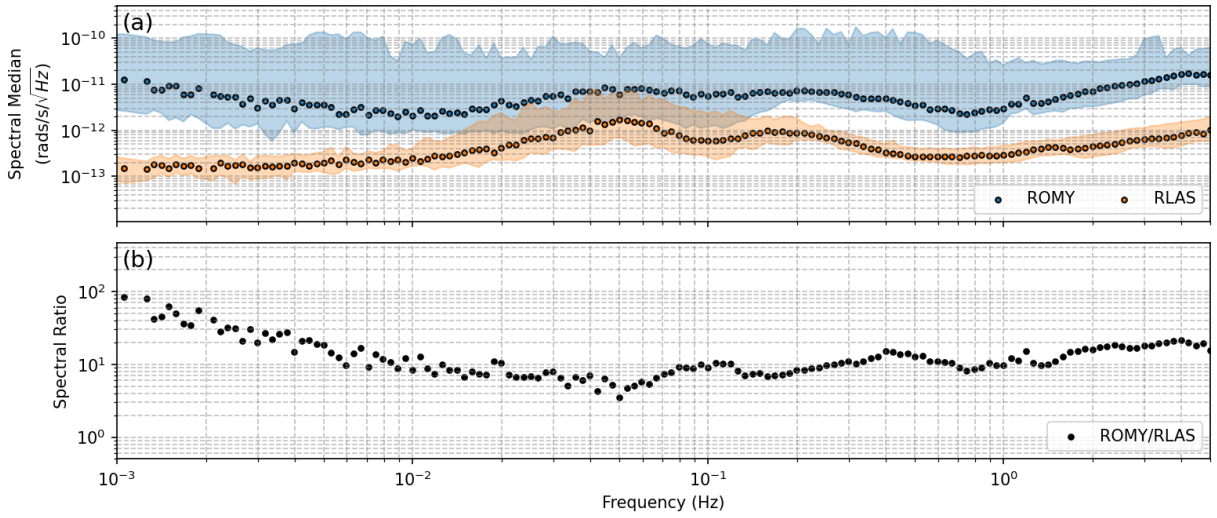

Figure 5.18: (a) Median values of amplitude spectra of all events (circles) and 60% confidence interval (shaded) for vertical rotation rate of BW.ROMY and BW.RLAS (G-ring). (b) ROMY-to-RLAS ratio of median values of amplitude spectra.

rate, indicating amplification effects, most likely due to the local sedimentary subsurface structure. The G-ring is mounted on top of crystalline rock, whereas ROMY is located in the pre-alpine sedimentary basin, which could be attributed to local amplification effects. No significant effect of directivity, as far as the non-uniform earthquake distribution permits (see Fig. 5.13).

Preliminary Conclusions and Outlook

The previously reported observation of amplitude differences between G-ring and ROMY for SH-type waves is supported by the preliminary results of this event-based analysis. A factor of 2 to 3 between 0.01 Hz to 0.1 Hz in rotation rate is identified, which is not present in the acceleration data. At higher frequencies >0.1 Hz, amplification effects, most likely due to the sedimentary nature of the subsurface, are also present for acceleration. A pronounced directivity effect for amplifications is not evident. Whether the cause lies in the data processing cannot be excluded at present, but is considered unlikely. A detailed simulation of the entire processing chain for ROMY has been initiated, but not yet finished.

A 2D or even 3D simulation of teleseismic events with a refined velocity model at the location of the G-ring and ROMY based on the respective geological setting, is required to model the observed difference in rotational amplitude. A detailed site characterization could potentially be used to correct for the local site effects to the benefit of teleseismic observations.

5.3 Atmospheric Pressure and Ground Deformation

A mechanical seismometer is an acceleration sensor that is sensitive to inertial acceleration, such as that caused by seismic waves, and to gravitational acceleration, caused by the redistribution of mass in the atmosphere above the sensor. These contributions cannot be distinguished due to the equivalence principle. A third contribution originates from tilting the sensor, which results in a coupling of the gravitational acceleration to the tilted components, thus tilt-coupled acceleration. Tilt-coupled acceleration for inertial seismometers is a first-order effect for the horizontal components and a second-order effect for the vertical component, where the contributions are not constructively aligned.

A dominant contribution of local tilt deformation of the Earth's surface is attributed to atmospheric pressure loading, especially for frequencies below 10 mHz (Zürn et al. 2007, Tanimoto & Li 2020, Zürn et al. 2022). Several months of direct observations of all three components of ground tilt provided by ROMY allow redundant compliance estimation of air pressure and tilt and eventually a discrimination between tilt and other contributions to the seismic noise floor at low frequencies (<10 mHz).

5.3.1 ROMY and Air Pressure Modelling

Zürn et al. (2007) modelled these effects on a seismometer for a homogeneous half-space, including contributions of gravitational attraction, tilt-coupled acceleration and inertial acceleration. An approach to model the tilt θ motion introduced by atmospheric pressure loading was proposed and tested by Zürn et al. (2007). This model consists of a linear combination of co-located barometric pressure records and the Hilbert transform thereof (Zürn et al. 2007):

$$\theta(t) = a \cdot P(t) + b \cdot H\{P(t)\} \ . \tag{5.4}$$

The local pressure represents tilts due to local elastic deformation at the sensor location as a response to barometric loading (LDT = Local Deformation Tilts), often associated with 'cavity effects' or local heterogeneities (Zürn et al. 2007). The Hilbert transform of the barometric pressure is referred to as travelling wave tilt (TWT = Travelling Wave Tilt) and approximates the spatial pressure gradient (Zürn et al. 2007). A correlation of the respective waveforms is visually recognizable (see Fig. S.18).

Several months of data from ROMY and the co-located STS-2 broadband seismometer FUR are analyzed to estimate the linear coefficients of Equation 5.4 and validate their temporal stability. Figures 5.19 and 5.20 present the results of the analysis for the different components of FUR and ROMY, respectively.

Table 5.1: Median and confidence interval (upper and lower quartile) of the estimated linear coefficients a and b (Eq. (5.4)) for FUR and ROMY.

FUR	a_Z	a_N	a_E	b_Z	b_N	b_E
upper quartile	–	32.3	14.2	–	6.0	3.9
median	–	26.8	12.6	–	3.5	2.2
lower quartile	–	19.6	10.9	–	1.6	1.0
ROMY						
upper quartile	9.3	77.0	64.0	32.3	388.8	230.7
median	3.3	47.4	43.2	26.6	253.5	148.0
lower quartile	1.5	24.0	26.5	17.9	159.7	90.0

The coefficients of Equation 5.4 are estimated using a multi-variate regression with a RANSAC approach on three hours of data, with one hour overlap, for all components of ROMY (2024-03-01 to 2024-09-30) and the horizontal components of FUR (2024-01-01 to 2024-07-31), using barometric pressure observations from FFBI. These coefficients are considered compliance, or the response of the ground to atmospheric pressure loading. Tilting motion is expected on the horizontal components, while rotation around a vertical axis (SH-type waves) should be of subordinate relevance. The variance reduction (Eq. 3.5) and the zero-lag cross-correlation (CC) coefficient are used to validate the barometric model. Higher correlation in the waveform mostly results in a high variance reduction ($> 50\,\%$).

Estimating model coefficients for many data periods is more robust than focusing on exemplary case studies only. However, longer time series include data periods of reduced atmospheric activity that are of little significance to the modelling approach. Therefore,

only coefficient estimates with a CC coefficient above 0.7 and with a time lag below 120 s are considered to derive a median coefficient with a confidence interval (Tab. 5.1).

With regard to FUR, many data periods yield a high variance reduction, in particular for the north component (Fig. 5.19b). The coefficients appear to converge and be stable over time with higher values for a, thus a ratio (a/b) above one. A ratio of about 9 is obtained between the median coefficients for a_N (26 nrad hPa^{-1}) and b_N (3 nrad hPa^{-1}) for the north component and of about 6 between a_E (12 nrad hPa^{-1}) and b_E (2 nrad hPa^{-1}) for the east component. Maximum CC coefficients are found at zero lag time, which is expected for a physical elastic deformation model with no time delay. Excitation of SH-type waves (recorded by the vertical component of ROMY) by barometric pressure is not expected, but is observed and therefore included in this analysis. For the vertical component, a significant variance reduction is achieved less often than for the horizontal components. The variation in lag time for maximum CC coefficients also indicates a poor

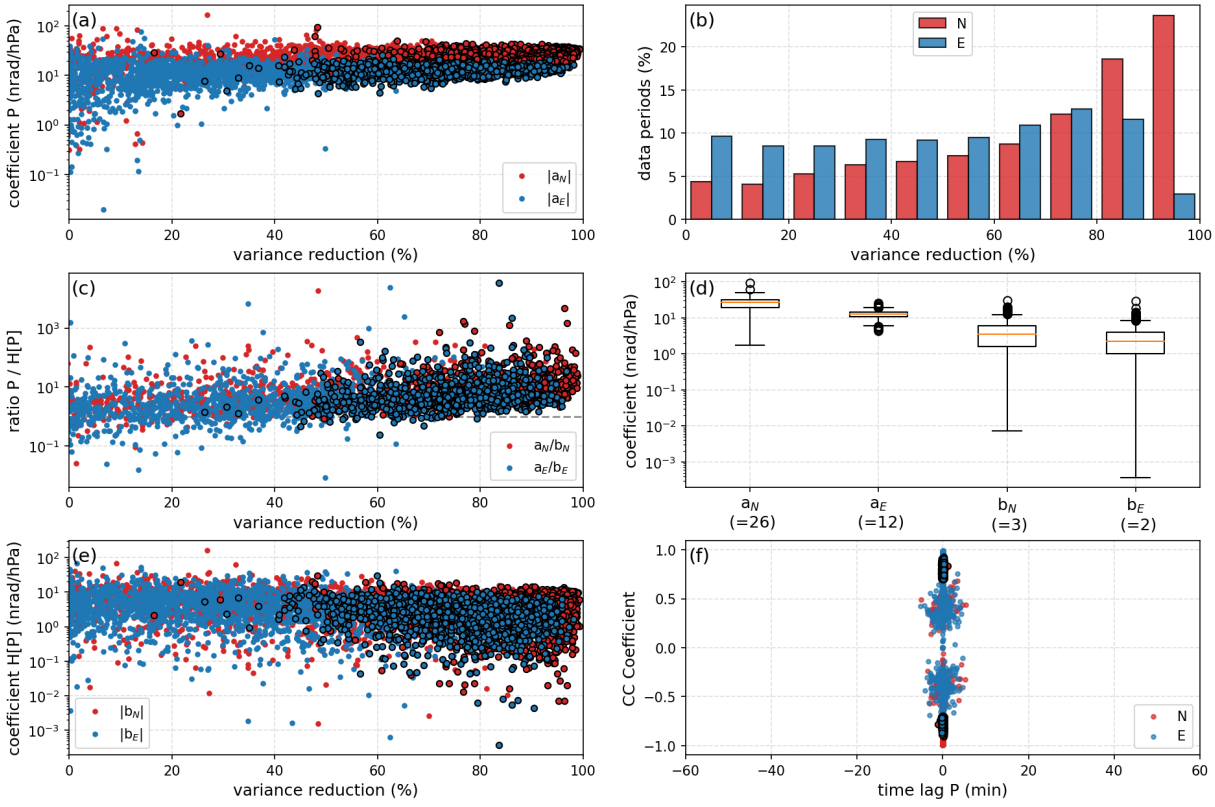

Figure 5.19: Estimates for linear coefficients $|a|$ and $|b|$ (Eq. (5.4)) each for three hours data periods of the north (red) and east (blue) component of FUR (2024-01-01 to 2024-07-31) are shown in (a) and (e), while their ratio (a/b) is presented in (c). (b) A histogram of data periods by achieved variance reduction. (d) Statistical coefficient estimates based on data periods with cross-correlation coefficients above 0.7 (= estimates with black edge). (f) Maximal cross-correlation coefficients versus time lag.

model for the vertical component. The coefficient estimates for the horizontal components of ROMY appear to converge for the considered dataset, yielding a ratio below one and thus higher coefficients for the TWT. The estimated compliance of $a_N = 47\,\mathrm{nrad\,hPa^{-1}}$ and $a_E = 43\,\mathrm{nrad\,hPa^{-1}}$ are similar, while $b_N = 253\,\mathrm{nrad\,hPa^{-1}}$ and $b_E = 147\,\mathrm{nrad\,hPa^{-1}}$ are different by a factor of 1.7.

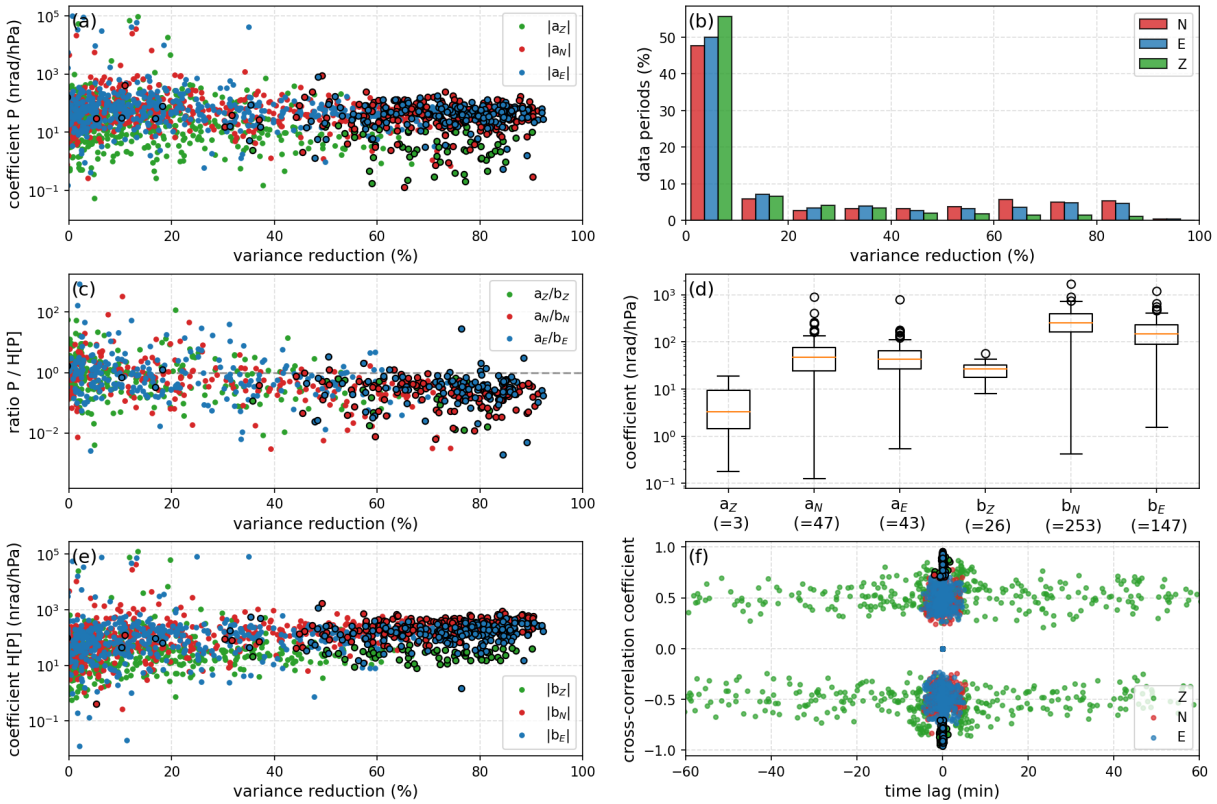

Figure 5.20: Estimates for linear coefficients $|a|$ and $|b|$ (Eq. (5.4)) each for three hours data periods of the vertical (green), north (red) and east (blue) component of ROMY (2024-03-01 to 2024-09-30) are shown in (a) and (e), while their ratio (a/b) is presented in (c). Estimates with (b) A histogram of data periods by achieved variance reduction. (d) Statistical coefficient estimates based on data periods with cross-correlation coefficients above 0.7 (= estimates with black edge). (f) Maximal cross-correlation coefficients versus time lag.

5.3.2 Spatial Pressure Gradient

By using the recorded pressure at the barometer array (see Fig. 2.17) and the methodology for ADR (Spudich & Fletcher 2009) using pressure as the vertical channel input, a gradient can be computed for a north and east direction. As for ADR, this assumes a homogeneous, rigid baseplate beneath the entire array (Spudich et al. 1995).

Figure 5.21 presents an example of the derived spatial pressure gradient for frequencies

between 0.5 mHz to 10 mHz on 2024-10-27, with peak-to-peak pressure variations of about 10 Pa to 15 Pa. The east component has about half the amplitude of the north component. This results in a mostly north-south oriented pressure gradient (Fig. 5.21e).

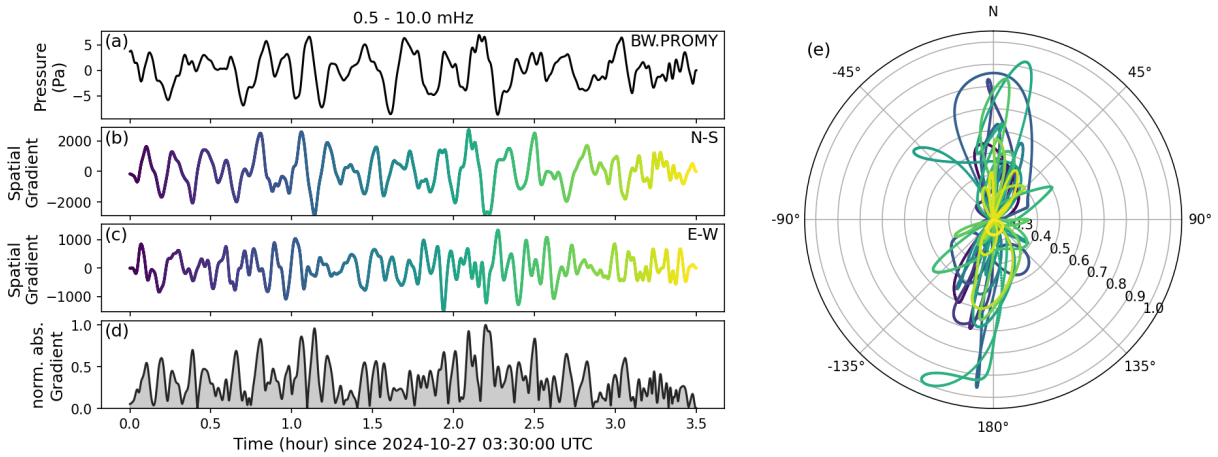

Figure 5.21: Exemplary spatial pressure gradients for barometer array around ROMY on 2024-10-27. (a) Barometric pressure changes at ROMY and derived spatial pressure gradients (b) in north-south and (c) east-west direction. (d) A normalized absolute pressure gradient is shown. (e) Polar plot of the combined pressure gradient with respect to north. Data are bandpass filtered between 0.5 mHz to 10 mHz.

Currently, the gradient estimate is based on merely six stations, with only one station located towards north and north-east. Adding more barometer stations would allow for a more homogeneous distribution and increase the aperture (currently about 4.2 km). This could improve the spatial gradient estimation and provide a larger frequency range. At the same time, the pressure wavefield is less coherent at higher frequencies, consequently increasing the complexity of the gradients. This would weaken the underlying assumptions. Therefore, the underlying assumptions for the ADR computation, with respect to plane waves and a rigid baseplate, may no longer hold.

5.3.3 Tilt Correction

By observing pure tilt motion with high sensitivity, tilt-coupled contributions from accelerometers could be removed (e.g., Bernauer et al. 2020b, Lin et al. 2022). This is particularly valuable for ocean-bottom seismometer installations, being severely affected by oceanic compliance (e.g., Lindner et al. 2017).

The potential for tilt correction is assessed for exemplary data of ROMY and FUR on 2024-10-27 (see Fig. 5.22). Atmospheric-induced tilt contributions are modelled using the barometric model (Eq. (5.4)) with the Hilbert transform as a proxy for the spatial pressure gradient (= MH) and with the derived gradient using the barometer array (= MG). FUR

accelerations are converted to tilt by dividing by $9.81\,\mathrm{m\,s^{-2}}$, assuming that the dominant signal below 10 mHz is tilt-induced.

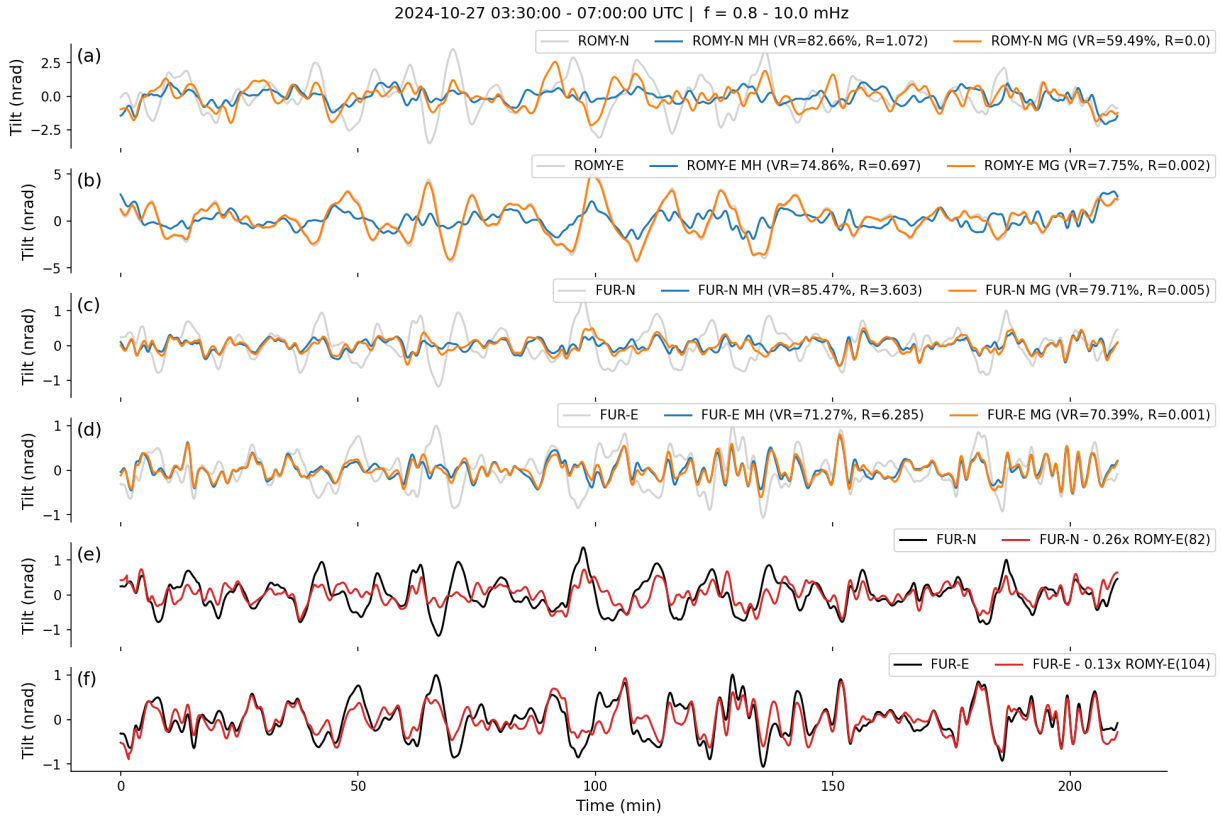

Figure 5.22: Tilt removal for ROMY and FUR using a barometric model based on local barometric pressure and the Hilbert transform thereof (= MH) and on local barometric pressure and the derived spatial gradient (= MG). Tilt observed the (a) north and (b) east component of ROMY (gray) and the residuals after correction with MH (blue) and MG (orange) are shown. Horizontal acceleration for the (c) north and (d) east component of FUR is converted to tilt by dividing with $9.81\,\mathrm{m\,s^{-2}}$. Tilt of FUR is reduced by subtracting by direct tilts of ROMY scaled linearly and shifted in time (red) for (e) north and (f) east. VR=variance reduction; R=ratio of pressure over gradient.

A high variance reduction of more than 70 % is achieved with MH for both components of ROMY and FUR. For FUR, MG gives similar, however, slightly lower variance reductions. For ROMY, however, the difference between the models is large, in particular for the east component, where MG achieves a reduction of only 7.75 %, while MH achieves 74.86 %. A comparison in the frequency domain reveals reductions of several dB up to about 20 db, especially at lower frequencies (< 3 mHz) (see Fig. S.20).

In order to effectively reduce tilt observations of FUR using ROMY data, a scaling of 0.26 and 0.13 as well as a time shift of 82 s and 104 s must be applied to the north and east component, respectively (Fig. 5.22e and 5.22f). The seismic stations FUR is located

about 10 m distance apart in a seismic underground vault, generally considered as co-located sensor, however, likely experiencing different 'cavity effects', as demonstrated for instruments at slightly different locations by Zürn et al. (2022).

5.3.4 Air Pressure Compliance Function

The compliance of barometric pressure and ground motions is estimated as a function of frequency. Hourly PSDs are computed for each ground motion sensor and local barometer using a multitaper approach, and median PSD values are estimated for 12^{th}-octave frequency bands. seismo-barometric scatter plots (ground motion versus barometric pressure), as shown in Figure 5.23, reveal a linear increase in ground motion background level above a minimum power in barometric pressure. Single scatter points with low coherence at high pressure power and low ground motion power are commonly related to distortions in air pressure (e.g., during maintenance work), that are not captured by the applied outlier-exclusion-criteria (see Fig. 5.23).

Coherence values per frequency band between ground motion and pressure are used as a selection criterion (COH $>$ 0.8) for the linear orthogonal distance regression. Hereby, a uniform relation between ground motion and pressure is assumed and only the intercept is fitted. Uncertainties are determined by performing multiple regressions on randomly sampled subsets (80 % of the samples) and computing a median and a 90 % confidence interval. Compliance functions for three components of ground acceleration observed by the seismic stations FUR and BFO (Black Forest Observatory) are shown in Figure 5.24. Tilt motions by ROMY's tiltmeter, ROMYT, are converted to accelerations using the gravitational acceleration ($g = 9.81\,\mathrm{m\,s^{-2}}$). The compliance function obtained for rotation rate from ROMY is integrated to tilt by scaling with $(2\pi \mathrm{f})^{-1}$.

The compliance for the vertical component (Z) of BFO and FUR is, as expected, lower than the corresponding compliance for horizontal components by a factor of about 10 and 15, respectively. Slightly different compliance is estimated for the north (N) and east (E) components of FUR and BFO. The seismometer at BFO is installed in a former underground mine in stiff, crystalline rock, while the STS-2 seismometer of FUR is located in an underground vault adjacent to the ROMY structure on top of several kilometers of sediments.

Both components of the tiltmeter ROMYT reveal a similar compliance function as the one of the north component of FUR. This is to be expected, since the inertial tiltmeter ROMYT is a long period seismometer. All horizontal components of the instruments at the site of the ROMY appear to converge to comparable compliance values above 10 mHz between 500 $\mathrm{nm\,hPa^{-1}}$ to 1000 $\mathrm{nm\,hPa^{-1}}$. For long periods, below 10 mHz, the compliance functions of different instruments and their components diverge.

The estimated compliance functions can be used to obtain a low noise level for ROMY, specific to its site characteristics. For this purpose, the compliance functions are multiplied by the lower bound (2.5 %) of the PSDs for barometric pressure as observed at the ROMY

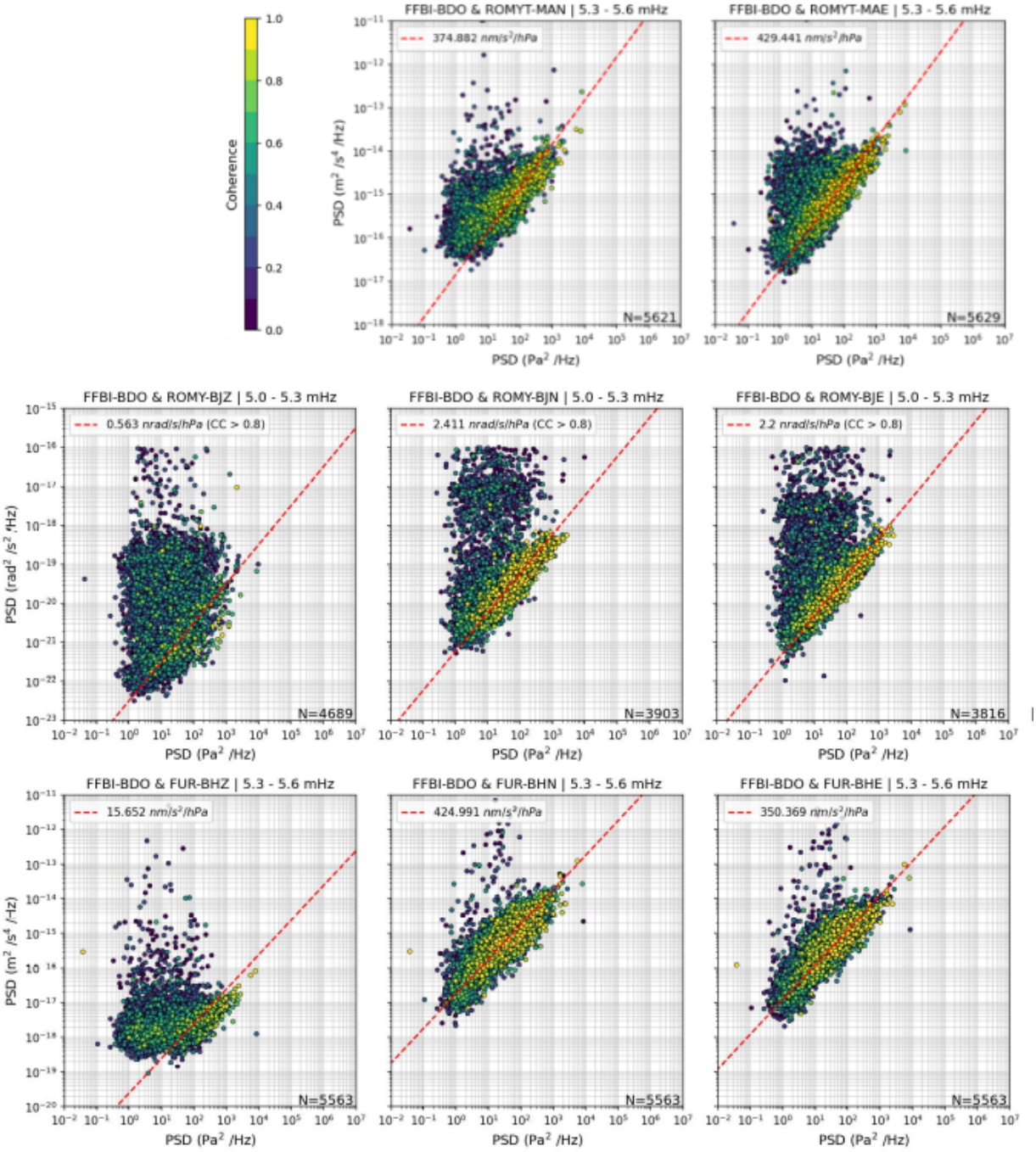

Figure 5.23: Exemplary seismo-barometric scatter plots for all components (Z, N and E) of tiltmeter ROMYT (upper row), ring laser ROMY (central row) and seismometer FUR (bottom row). Data is color-coded based on the corresponding coherency values.

site (see Fig. 2.16). The estimated limit is about 30 dB to 50 dB above the RLNM for transverse rotations (Brotzer et al. 2023). It seems that the horizontal components of ROMY are limited by this pressure-imposed limit for long periods.

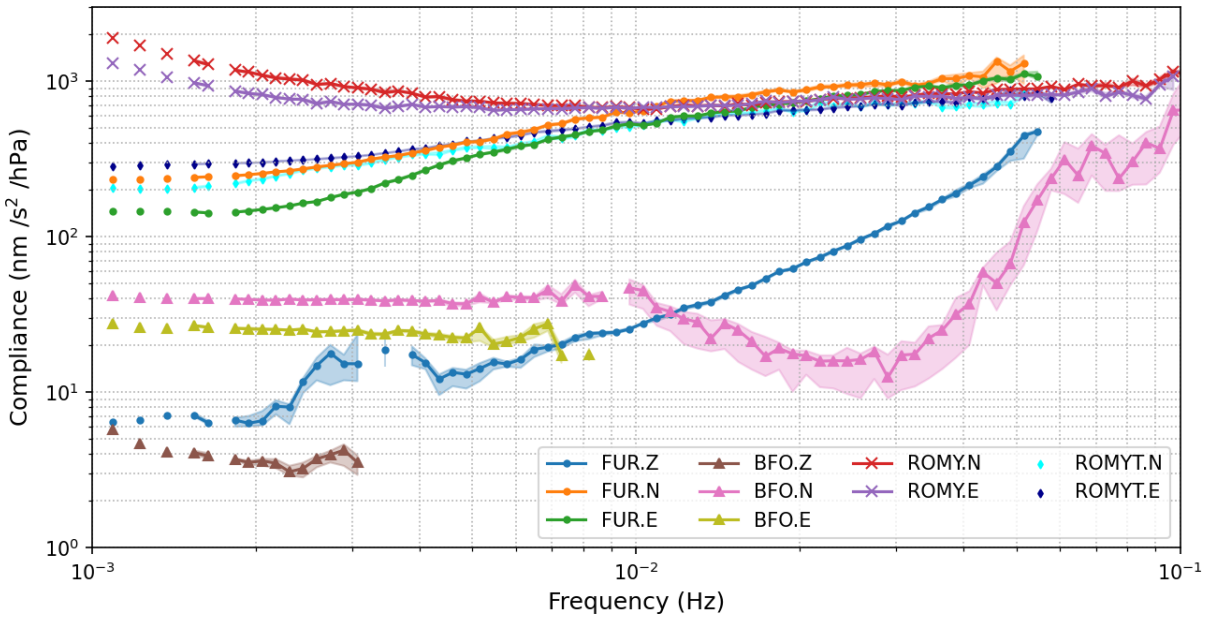

Figure 5.24: Estimated median compliance per 12^{th}-octave frequency band for seismometer FUR and BFO, tiltmeter ROMYT and ring laser ROMY. Rotation rates of ROMY are integrated to tilt and tilt converted to acceleration by scaling with a gravitational acceleration of $9.81\,\mathrm{m\,s^{-1}}$.

For comparison purposes, the low noise model for the horizontal accelerations by Berger et al. (2004), based on data from the Global Seismic Network (GSN), is converted to tilt by diving with the common gravitational acceleration of $9.81\,\mathrm{m\,s^{-2}}$. This assumes pure tilts below 10 mHz and would indicate a limit at around $10^{-23}\,\mathrm{rad^2\,s^{-2}\,Hz^{-1}}$ and thus about 30 dB above the RLNM (Fig. 5.25). The difference to the estimated low noise limit for ROMY may be due to the sedimentary structure beneath ROMY, which allows for a greater pressure-induced deformation and thus a higher background level of rotational motion. A contribution of pressure-induced instrumental effects (see Sec. 3.2) may also contribute. This should be re-evaluated when the optical resonators of the RLGs of ROMY are actively stabilized.

Preliminary Conclusions and Outlook

A strong, low-frequency tilt-induced contribution is observed for the horizontal components of the seismometer FUR. At times this leads to a variance reduction of more than 90 % when corrected with a linear barometric model, in particular valid for the north component. Estimation of the linear model coefficients statistically indicates a temporal invariance of

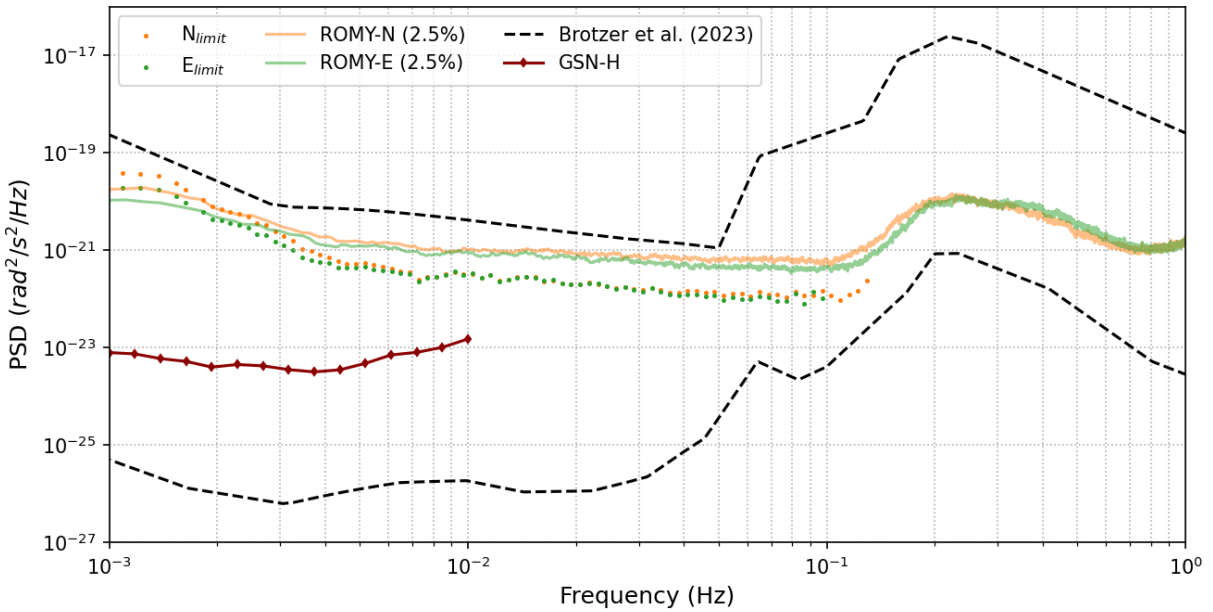

Figure 5.25: Estimated low noise level for ROMY's horizontal components imposed by pressure-induced tilts (N_{limit} and E_{limit}). The 2.5-percentile of PSDs computed for ROMY's north (orange) and east (green) component are shown. The rotational low/high noise model by Brotzer et al. (2023) are shown for reference. The low noise model for the horizontal accelerations by Berger et al. (2004) based on data of the global seismic network (GSN) is converted to tilt by scaling with $9.81\,\mathrm{m\,s^{-2}}$ and shown for frequencies below 10 mHz.

these compliance coefficients. For FUR, higher compliance coefficients are obtained with respect to the local barometric pressure, suggesting at dominant 'cavity effect'.

The available dataset of direct tilt observations from ROMY allows to constrain the compliance values for tilt directly. However, due to periods of insufficient data quality (see Sec. 2.2), less usable data are available for the analysis. The model coefficients can be statistically determined and yield a ratio of compliance values below one, hence with a dominant contribution of the spatial pressure gradient, in contrast to FUR. Peak variance reductions above 80 % can be achieved with the barometric model.

Compliance functions are estimated that support a linear relation between barometric pressure and ground rotation, as expected with strong compliance for horizontal components. These might be amplified at the location of ROMY and FUR sites due to the sedimentary nature of the subsurface, allowing for more deformation as a result of barometric loading. Compared to the compliance functions estimated for the BFO site, located in solid rock, the compliance functions for ROMY and FUR yield an increase toward higher frequencies and are thus more consistent with those modelled based on a two-layer subsurface structures (Kenda et al. 2020). The compliance functions can be used to estimate the low noise level for ROMY's horizontal components imposed by pressure-induced tilts at low frequencies.

In order to advance this study, the effects of deformation caused by barometric pressure loading should be simulated with a local 3D model. The derived characteristic compliance functions could be more closely related to the specific local site characteristics. The origins of SH-type waves, possibly excited by atmospheric gravity waves interacting with the topography, could be investigated by including the local topography in the model. Observations of the existing or potentially extended barometer array could serve as input data for such simulations. An orientation could be a simulation done for the G-ring by Gebauer et al. (2012).

5.4 Seismic Source Tracking

Using seismic observations to track natural events that generate seismic signals, such as avalanches (e.g., Pérez-Guillén et al. 2019), storms (e.g., Davy et al. 2014), tectonic ruptures (e.g., Krüger & Ohrnberger 2005) or anthropogenic sources, such as traffic Riahi & Gerstoft (2015), Yuan et al. (2021), is of relevance and has been widely tested, developed and applied. Moreover, 6 DoF observations can be used as a polarization filter for different wave types of the seismic wavefield (e.g., Sollberger et al. 2020) and thus enable to locate sources for Rayleigh and Love type waves separately. The high self-noise level of portable sensors such as the blueSeis-3A (see Sec. 4.2) limits the applicability of 6 DoF processing using ambient seismic noise, such as the seismic microseism. High-sensitivity 6 DoF observations of ROMY, allow to demonstrate the feasibility and potential of 6 DoF processing, which will become available as soon as portable rotation sensors with sufficient sensitivity are developed.

5.4.1 Microseism Tracking

The primary and secondary microseism peaks originate from energy transfer between the oceans and the solid Earth, while the mechanism for the secondary microseism is a non-linear oceanic wave-wave interaction, the primary microseism is caused by the interaction of oceanic infragravity waves with coasts or bathymetric features in the ocean (e.g., Longuet-Higgins & Jeffreys 1950, Hasselmann 1963, Tanimoto & Anderson 2023) The identification of seismic microseism source locations caused by the interaction of ocean waves and seafloor or coasts has been successfully demonstrated with seismic arrays (e.g., Hillers et al. 2012), as well as fiber-optic cables (DAS) (e.g., Xiao et al. 2022). Single-station 6 DoF observations provide a similar potential, while the combination of several distributed 6 DoF stations, replacing seismic arrays, would significantly increase the accuracy (e.g., Yuan et al. 2021).

Figures S.21 and S.22 present power spectral densities (PSDs) computed hourly based on a multitaper approach for acceleration records of GR.FUR and rotation rate observed by BW.ROMY, respectively. The dominant peak of the secondary microseism is evident in all components of FUR (0.1 Hz to 0.3 Hz), but also the weaker peak of the primary microseism (0.05 Hz to 0.1 Hz), is also visible. Both weaken gradually in power towards summer in the Northern Hemisphere. The lower frequency of the slope of the secondary

microseism peak appears more turbulent, depending on the oceanic source activity. Only minor gaps are visible for FUR, while ROMY still reveals many time periods of poor data quality, resulting in data gaps. The corresponding PSDs are rejected for this analysis based on maintenance logs and predefined thresholds. The most continuous observations of the secondary microseism peak are available for the vertical component. The secondary microseism features are very similar for accelerations and rotation rate observations (see Fig. S.21 and Fig. S.22). A clear peak for the secondary microseism band is recognizable in the median PSD of all components for ROMY.

In order to identify the dominant source locations for the microseisms of Love and Rayleigh waves, backazimuth estimations are performed as described in Section 4.2. Waveforms are bandpass filtered between 7 s to 10 s period (0.1 Hz to 0.14 Hz) in order to capture the secondary microseism peak. Moving time windows of 20 s with an overlap of 90 % are used. Average backazimuths are obtained for one-hour time intervals using Gaussian density kernels of estimates with cross-correlation values above 0.5. This allows a standard deviation to be assigned to the dominant backazimuth estimate. A current weakness of the implementation is the artificial discontinuity between 0° and 360°, which distorts the density kernel for peaks near the edges of the scale, thus north. An example of the results for a one-hour interval on 2024-03-07 is shown in Figure S.23 of the supplementary materials.

For validation purposes, the backazimuth is also estimated using the seismic array f-k processing method, hereafter referred to as beamforming. The results are based on the vertical components of the seismic array stations and therefore sensitive to SV-polarized motion. This should be extended to three component beamforming.

Hourly estimates with uncertainties for the observation period between 2024-02-01 and 2024-10-31 using four different approaches are shown in Figure 5.26.

There seems to be an increased uncertainty for the backazimuth estimates for all methods during the summer months compared to the winter months in the Northern Hemisphere, indicating less pronounced or distant sources for seismic microseisms during summer (see Fig. 5.27). For the early months of 2024, a dominant backazimuth of around 300° can be observed. For Love waves, however, the dominant backazimuth seems to be at around 250°. In October, the dominant backazimuth appears to re-emerge after the summer months of more distributed directions.

This is visualized by plotting all moving window estimates as angular histograms in 5° bins weighted by the computed CC coefficient (Fig. 5.28). There are no CC coefficients for the beamforming estimates, therefore no weights were applied. The dominant direction of Love waves is west-south-west (235° to 270°), while for the Rayleigh wave grid search approach most estimates point towards west-north-west (270° to 315°). The covariance approach is also based on SV-polarized waves and points to the west. The beamforming distribution is most consistent with the Rayleigh wave grid search approach, but tends to be more unidirectional than the other approaches.

A systematic drift away from the dominant backazimuth direction is observed for all applied

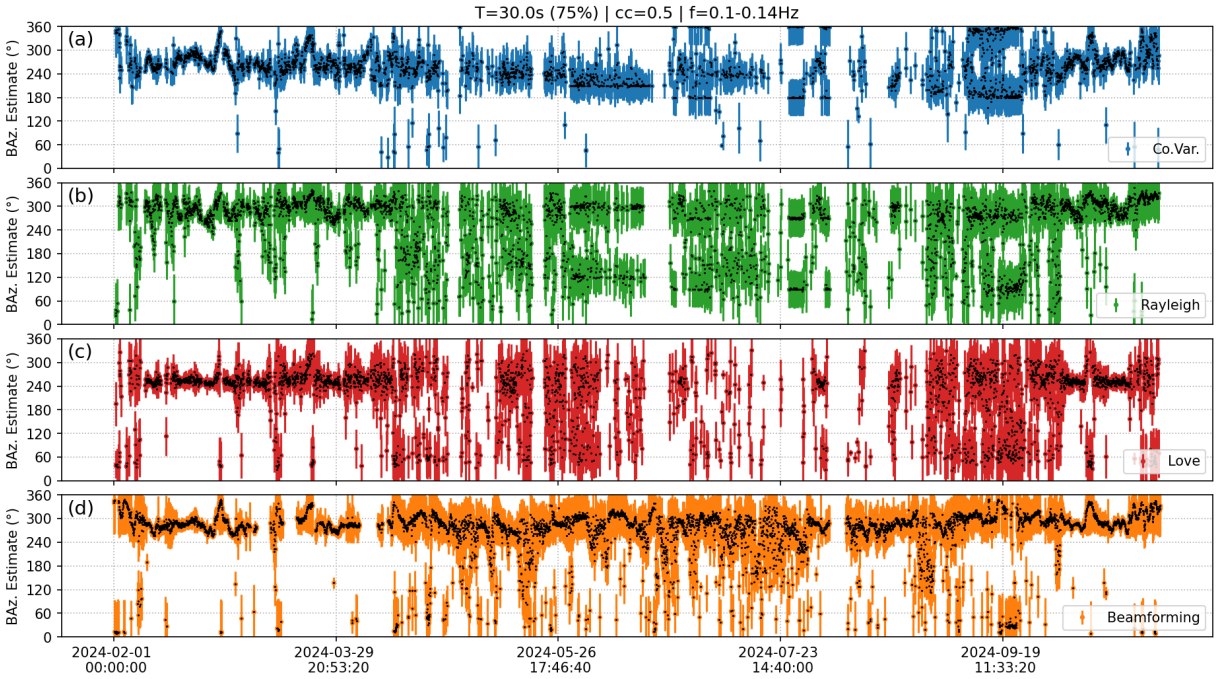

Figure 5.26: Hourly backazimuth estimates for the secondary microseism peak (0.1 Hz to 0.14 Hz) are shown with uncertainties between 2024-02-01 to 2024-10-31. Backazimuths are estimated using a (a) Rayleigh covariance, (b) Rayleigh polarization grid search, (c) Love polarization grid search method as well as (d) f-k array beamforming approach, using vertical ground motions, as reference.

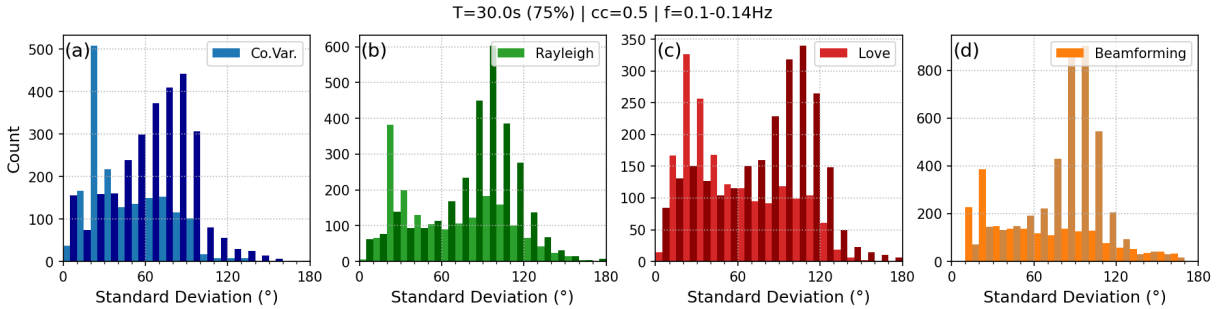

Figure 5.27: Uncertainties of hourly backazimuth estimates between 2024-02-01 and 2024-10-31 are compared, being separated by summer (2024-03-21 to 2024-09-20) in dark colors and not summer in light colors. Backazimuths estimates based on a (a) Rayleigh covariance, (b) Rayleigh polarization grid search, (c) Love polarization grid search method as well as (d) f-k array beamforming approach are compared.

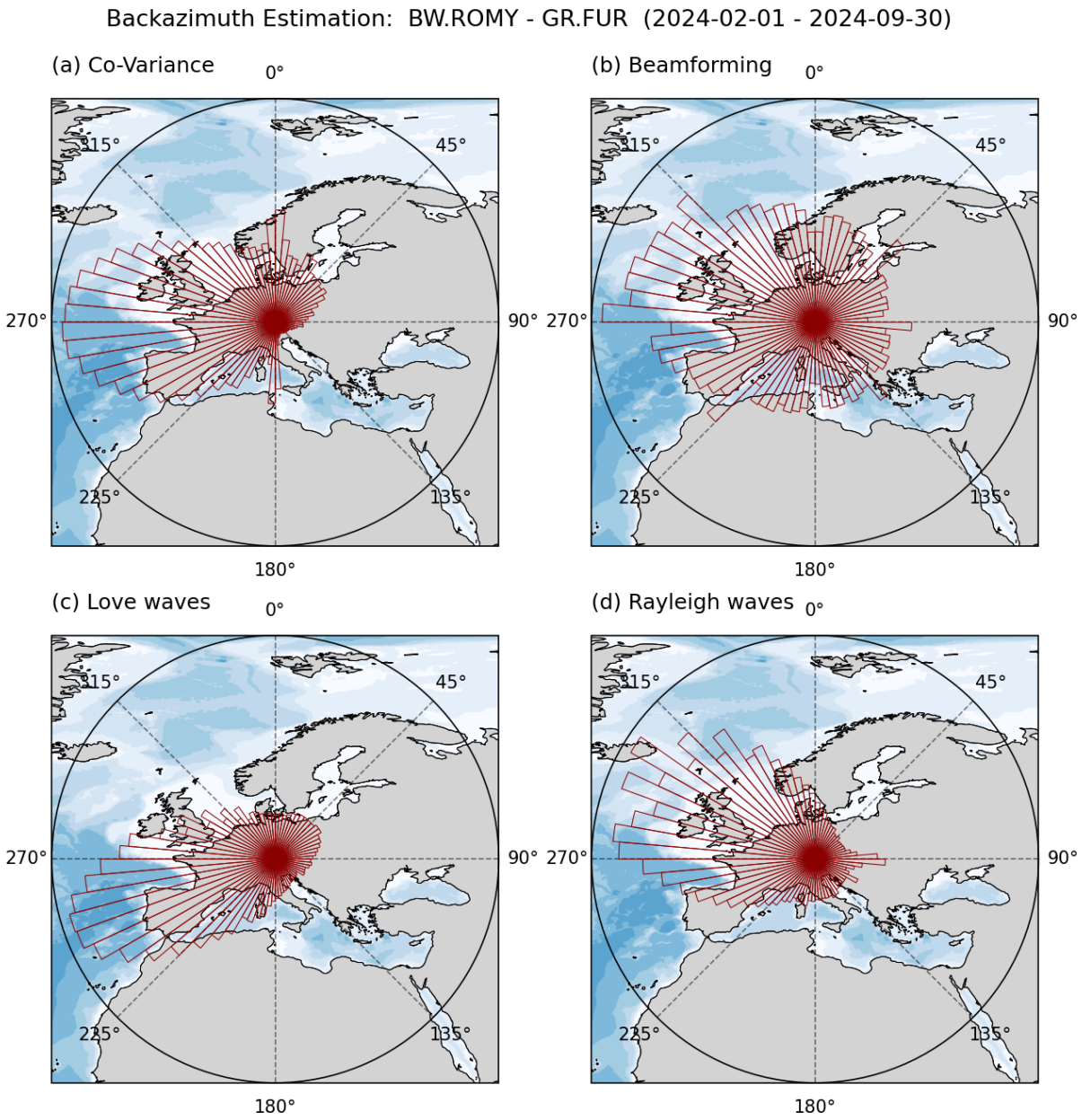

Figure 5.28: Backazimuth directions are estimated for secondary microseism peak (6 s to 11 s period) between 2024-02-01 and 2024-09-30 and plotted as angular histograms weighted with cross-correlation coefficients (CC) above 0.5 and centered on the location of ROMY. Backazimuths are estimated using a (a) Rayleigh covariance, (b) Rayleigh polarization, (c) Love polarization approach, as well as based on a (d) f-k array beamforming method using vertical ground motion. Bathymetry data is provided by (Natural Earth 2024).

methods during the last week of February in 2024 as shown in Figure 5.29. For Rayleigh polarized waves, the backazimuth first deviates about 60° south until 2024-02-26, before the drift reverses and drifts northwards to about 350°. From 2024-02-29 onwards, the dominant backazimuth direction matches the previous one of about 300°. The uncertainties increase with the northward drift, however, this seems to indicate a moving source of dominant microseism energy, likely a storm in the Northern Atlantic.

As microseism generation is linked to oceanic wave activity, thus sea surface wave significant height (SWH) measurements, obtained by satellite altimetry, are often used as an observational proxy to constrain source regions. Daily maximum SHWs from satellite measurements are available (CMEMS 2024) and compared with daily histograms of backazimuth estimates based on the covariance approach for the period of strong location drift (Fig. 5.30). It is understood that secondary microseisms are generated by a non-linear interaction of oceanic surface waves (e.g., Longuet-Higgins & Jeffreys 1950, Hasselmann 1963, Tanimoto & Anderson 2023). The dominant backazimuth directions, indicated by the weighted histograms, generally point towards the area of maximum SWH. A mismatch is observed for 2024-02-22 (Fig. 5.30c). On February 26, 2024, there are two areas of pronounced SHW, with the backazimuth estimate pointing to the closer but weaker area north of Spain (Fig. 5.30g).

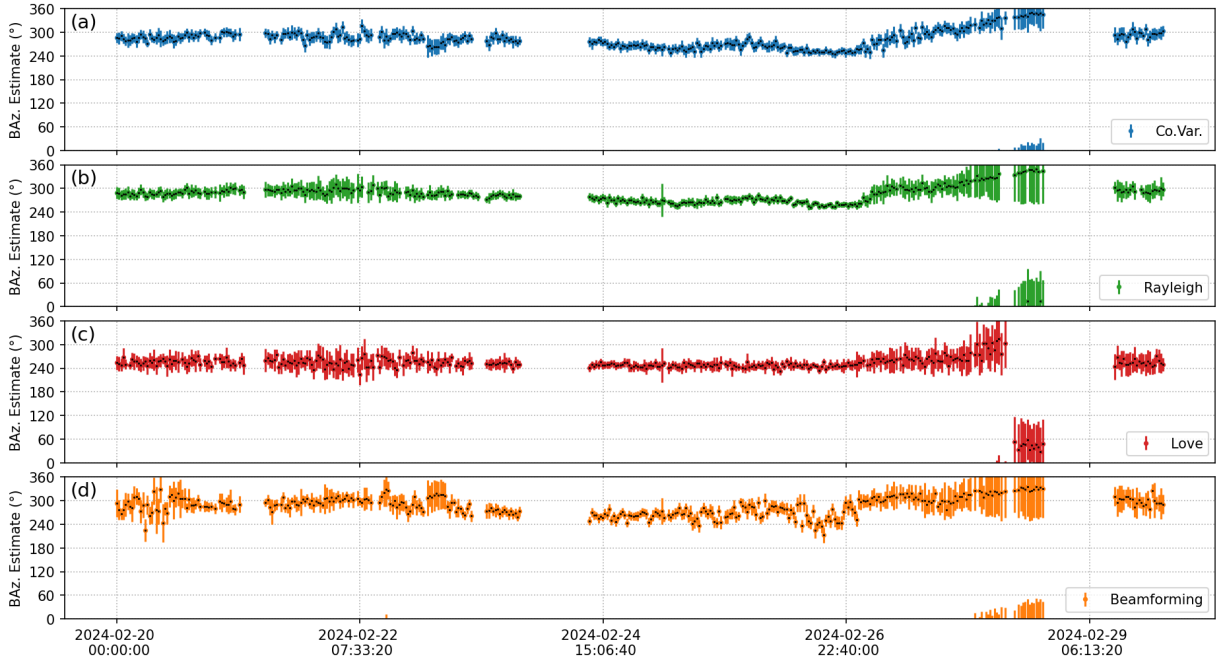

Figure 5.29: Backazimuth estimates for secondary microseism peak (7 s to 10 s period) are shown as half-hourly maximum-likelihood peaks and error bars for a storm event (2024-02-20 to 2024-03-01. Backazimuths are estimated using a (a) tangent, (b) Rayleigh polarization, (c) Love polarization methods as well as (d) f-k array beamforming based on the vertical component.

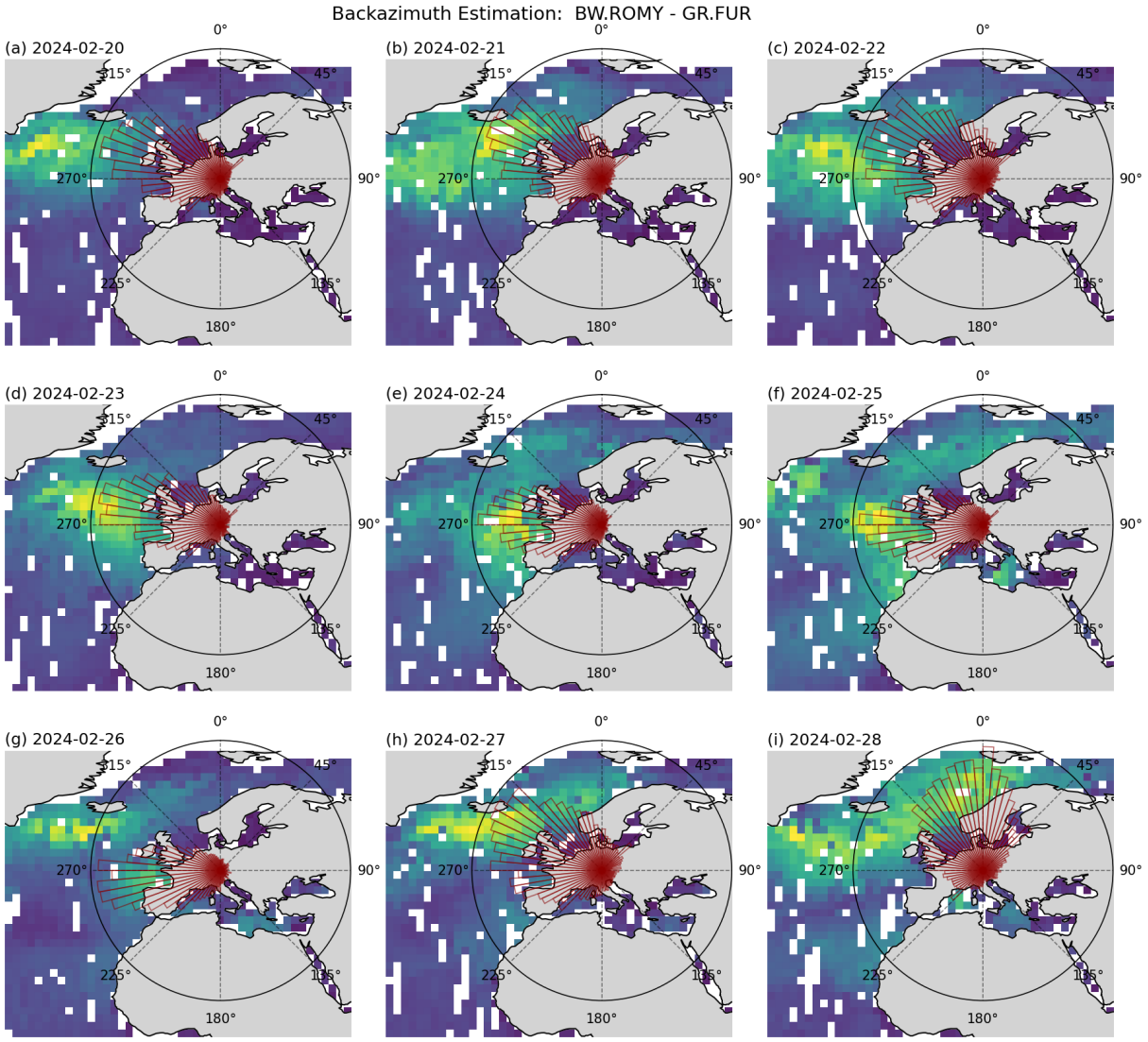

Figure 5.30: Daily angular histograms of backazimuth estimates weighted by cross-correlation coefficients based on the Rayleigh covariance approach between 2024-02-20 and 2024-02-28. In the background, the daily maximal sea surface wave significant height (SWH) in the northern Atlantic is shown, based on satellite data (CMEMS 2024).

A study by Hadziioannou et al. (2012) used rotational data of G-ring and obtained a dominant backazimuth direction around 300° for Love waves. Similar source directions are obtained for secondary microseism in a study based on seismic arrays across Europe (Juretzek & Hadziioannou 2016). A difference in source direction for the secondary microseism for Love and Rayleigh waves is not identified here (Juretzek & Hadziioannou 2016). An apparent difference in source region for Love and Rayleigh waves should therefore be verified with future longer time series.

5.4.2 Tractor Tracking

In Section 4.2, backazimuth estimation based on 6 DoF observations is applied to local and regional earthquakes. Here, 6 DoF data of ROMY are used to track a tractor working in a neighboring field (see Fig. 5.31a and 5.31b).

This is certainly an unusual application on a very small scale, but it demonstrates the range of applications for seismic source tracking. The feasibility of tracking vehicles along a busy, nearby road north of ROMY with 6 DoF data has already been demonstrated by Yuan et al. (2021). Therefore, this is just an extended example to demonstrate the level of detail that can be achieved.

The example shows transient signals associated with the tractor working in the adjacent fields (see Figs. 5.31c and 5.31d). The amplitude and cross-correlation value increase during the day, indicating that the tractor is gradually approaching ROMY. The backscatter estimated backazimuth in Figure 5.31d shows a reoccurring east-west pattern (about 90° to 270°) with an interruption, likely related to reversing, in between. During a break, presumably a lunch break around noon local time, car traffic north of ROMY dominates the signals.

Preliminary Conclusions and Outlook

The secondary microseisms are recorded by the RLGs of ROMY and 6 DoF methods for backazimuth estimation seem promising to locate source regions for Love and Rayleigh waves individually, with a single station. A difference for Love and Rayleigh wave source regions may be discernible. Ideally, data and simulations, are required to further constrain the observations. Therefore, any interpretation at this time should be considered preliminary.

Yuan et al. (2021) suggest that having more, distributed 6 DoF stations would improve the accuracy of the source tracking. The only additional station would be G-ring, providing observations of a vertical component, thus SH-wave observations. The antenna formed by the two stations would be limited in resolution due to the proximity of ROMY and G-ring.

In the case of the tractor tracking, it is still unresolved how an extended, large-scale sensor such as ROMY is able to properly record rotation rates at very high frequencies ($> 10\,\mathrm{Hz}$) and thus successfully track nearby sources to the presented detail.

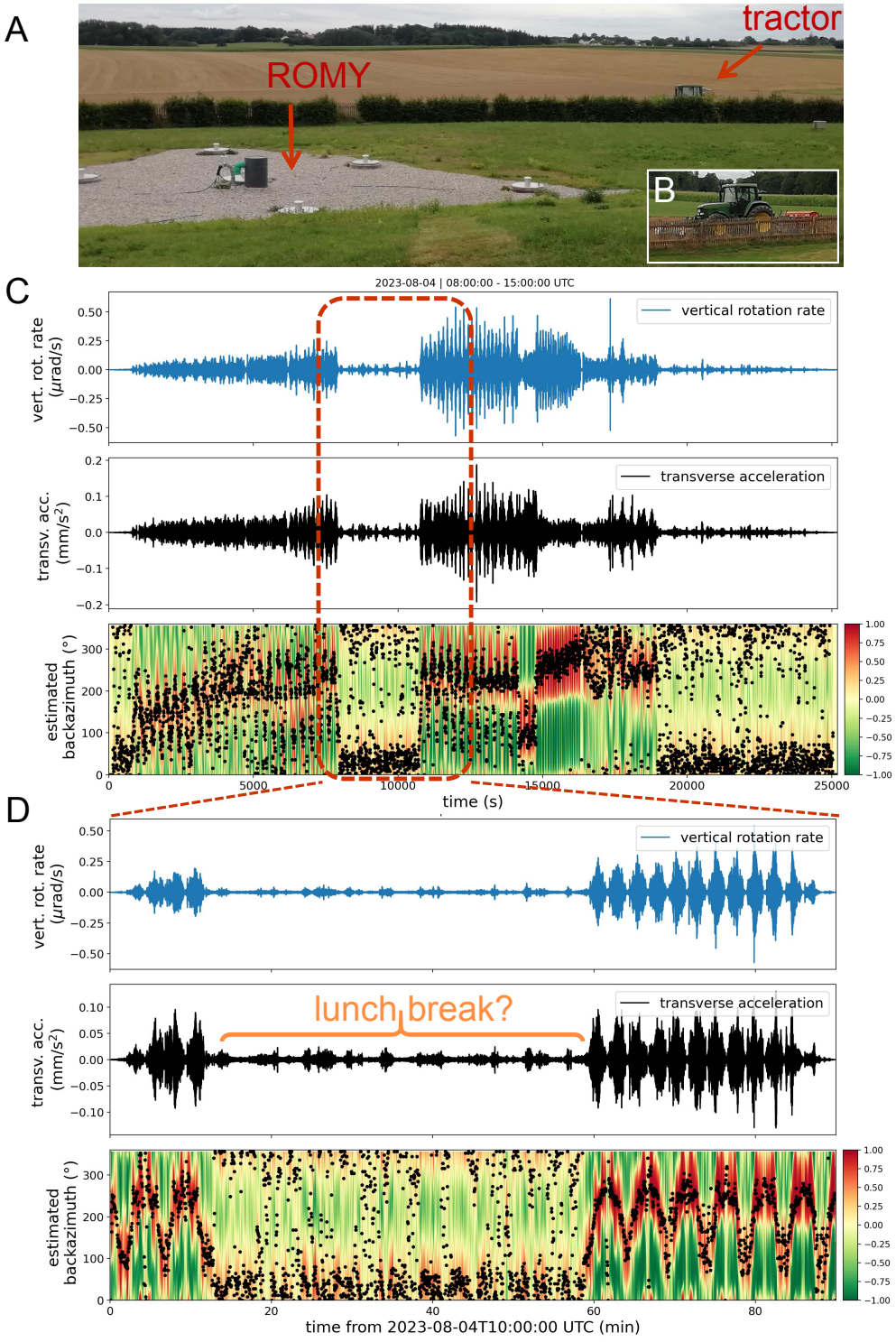

Figure 5.31: Tractor tracking with ROMY data. **A** Image of ROMY and the tractor on the adjacent fields. **B** Close-up image of the tractor with equipment. **C** Waveforms for vertical rotation rate (upper) and transverse acceleration (center)on 2024-08-04, between 08:00 and 15:00 UTC. Estimated backazimuths color-coded by cross-correlation values (lower). **D** Zoom-in starting at 12:00 LT including the presumable 'lunch break'.

Chapter 6

Conclusions and Outlook

This thesis covers various topics related to the instrumental characteristics of the ring laser array ROMY and the contribution of 6 DoF observations to seismology. The key findings are summarized and an outlook on further improvements of the unique instrument ROMY and on the potential of research projects to address open scientific questions is given.

As ROMY is a prototype with a unique design, a profound understanding of the sensor's characteristics in its environment is essential. The long-term stability of ROMY's heterolithic rings is currently limited by geometric deformation of the optical resonator, which manifests itself as a drift in the Sagnac frequency. A network of sensors has been assembled and implemented to study and quantify the instrumental effects of ROMY due to environmental influences. Temperature-induced deformation of the optical resonator has the strongest influence on the stability, while out-of-plane deformation is partially attributed to deformation induced by barometric pressure loading on the access shafts.

A set of video cameras was used to capture the beam positions at different corners, allowing the monitoring of the beam walk caused by deformation at the resonator corners. Long-term drifts of beam displacement over 74 days show a large dynamic in the beam walk, amounting to about 100 µm out-of-plane and 340 µm in-plane. In the presence of strong, short-term temperature perturbations ($> 1\,^{\circ}\mathrm{C}$), the deformation rate can be as high as 90.9 µm/°C, as observed for RV. In addition, an experiment to monitor the free-spectral range (FSR) was carried out to provide a record of the perimeter change of RZ. By tracking the 12^{th} FSR, a perimeter change of the order of $7\,\mu\mathrm{m\,d^{-1}}$ can be derived. These deformations contribute to frequent mode-jumps or split-mode operating regimes, thus compromising the operational stability. In order to overcome these geometrical instabilities, an active resonator stabilization system has to be designed and implemented. The backscatter error for ROMY's rings contributes to short-term drifts of about 1 mHz to 2 mHz. In the future, monobeam detection to apply a backscatter correction should be the default for all rings.

An automatic quality assessment algorithm was developed to evaluate the ring laser data. This made it possible to quantify the performance and optimize the RLGs towards higher uptime and improved quality. In this context, a ROMY monitor was installed at the observatory, which displays current data from the sensor network installed within ROMY as well as a quality analysis to enable rapid operational assessment in near real-time.

With the deployment of a blueSeis-3A rotation sensor at the Piñon Flat Observatory in Southern California, the first permanent 6 DoF station was established. One year of data allowed the successful application of 6 DoF processing techniques to a local and regional seismic event with sufficient signal-to-noise ratio. However, the observation and processing of smaller events is currently limited by the sensor performance. A newly introduced, empirical scaling relation for rotation rates provides guidance for similar experimental setups in the future.

A first rotational low noise model (RLNM) for the Earth was derived from a known model for translational ground motions, known relations, and a set of model-based, globally distributed, phase velocity curves. The RLNM was validated using existing observations from ADR and RLGs. A separate low noise level for vertical and transverse rotations, in particular for low frequencies, could not be excluded.

Most portable sensors that are currently available or under development still have a self-noise level above the RLNM. However, sensors based on a mechanical beam balance setup appear to be close to resolving the secondary microseism peak. In this context, the presented RLNM serves as a valuable benchmark for instrument development. The model can be further validated and refined in the future with additional data from more high-sensitive rotation sensors.

The validity of the presented RLNM for transverse rotations towards longer periods remained an open question. Moreover, the low noise limits of accelerometers imposed by pressure-induced tilts for long periods are not yet fully understood. This motivated the installation of a microbarometer station at ROMY, as well as a barometric array around ROMY, to harness its unique ability to provide direct, horizontal ground rotations and investigate the pressure-induced tilts and the low noise limits at long periods. Estimation of compliance coefficients allows pressure-induced ground tilts to be modelled and variance reductions for observed tilts of more than 90 % at certain times to be obtained. Observations over several months allowed to derive compliance functions to constrain a low noise limit characteristic for ROMY's site imposed by pressure-induced ground rotations.

As a result of continuous supervision and frequent maintenance work, ROMY has been successfully operated with three RLGs for over one year. Implemented and tested hardware upgrades for the RLGs of ROMY have been documented and elaborated. Currently, the horizontal ring of ROMY is equipped with an enhanced instrumental setup.

The following technical upgrades are suggested within the scope of a next major revision of ROMY:

- The installation of electrical grounding strips in each access shaft to connect all electrical devices and enclosures to a common ground. This might reduce electronic noise and crosstalk, thereby improving signal quality.
- The development and installation of an active temperature stabilization system for each access shaft to compensate for the seasonal temperature trend. A reduction of the remaining temperature-driven resonator deformation might be achieved in this way. The aim should be to stabilize the temperature at the millikelvin level at around 22 °C room temperature. The existing passive thermal insulation will reduce heating efforts and seasonal temperature variations will be mitigated.
- All rings should be equipped in the same way as RZ, including large-aperture photodiodes (10 x10 mm active area, e.g. Hamamatsu C10439-03) in combination with ADT units for reliable monobeam detection and a double detection for Sagnac signal in order to reduce common-mode noise. Moreover, Koester prisms for beam combination should be mounted on a micrometer translation stage and prism mount for precise manual alignment. Also, sufficient video cameras or better quadrant photodiodes for beam walk tracking are recommended.
- A sophisticated resonator stabilization system is required to counteract geometric deformation of the resonator. This could be based on an FSR stabilization scheme or an ultra-stable external frequency reference using multiple piezo actuators to adjust the geometric at the corners along two degrees of freedom.

In the future, the creation of a digital twin of ROMY, involving a detailed local site model, could help to constrain the observations discussed in Section 5, such as local site amplification characteristics or pressure-induced ground deformation. A more complete understanding of the local site effects could help to distinguish between local and remote contributions to the 6 DoF observations, useful for instance for the source location of different wave types. In addition, ROMY could provide the first observations of the Earth's horizontal rotational free oscillations, given sufficient excitation during a large earthquake.

In conclusion, ROMY is an unprecedented instrument that has already provided unique observations to answer open scientific questions and could help to answer more in the future. However, in order to harness ROMY's full potential, more time and effort will be needed to technically upgrade the instrument and keep it operating at peak performance to provide the required continuous data for seismological and eventually geodetic observations.

Bibliography

Abreu, R., Durand, S., Rost, S. & Thomas, C. (2023), 'Deep Earth rotational seismology', *Geophysical Journal International* **234**(3), 2365–2374. https://doi.org/10.1093/gji/ggad245.

Agnew, D. (2010), '6-Earth Tides', *Treatise Geophys* **3**, 163.

Agnew, D. C. & Wyatt, F. K. (2003), 'Long-Base Laser Strainmeters: A Review'.

Aki, K. & Richards, P. G. (2002), *Quantitative seismology*, University Science Books, Sausalito, California.

Anderson, R., Bilger, H. R. & Stedman, G. E. (1994), '"Sagnac" effect: A century of earth-rotated interferometers', *American Journal of Physics* **62**(11), 975–985. https://doi.org/10.1119/1.17656.

Ardhuin, F., Gualtieri, L. & Stutzmann, E. (2015), 'How ocean waves rock the earth: Two mechanisms explain microseisms with periods 3 to 300 s', *Geophysical Research Letters* **42**(3), 765–772. https://doi.org/10.1002/2014GL062782.

Aronowitz, F. (1971), 'The laser gyro', *Laser applications.* **1**, 133–200.

Bamforth, P., Chisholm, D., Gibbs, J. & Harrison, T. (2008), 'Properties of concrete for use in eurocode 2'.

Basti, A., Beverini, N., Bosi, F., Carelli, G., Ciampini, D., Di Virgilio, A. D. V., Fuso, F., Giacomelli, U., Maccioni, E., Marsili, P., Passeggio, G., Porzio, A., Simonelli, A. & Terreni, G. (2021), 'Effects of temperature variations in high sensitivity Sagnac gyroscope'.

BayernNetz (2001), 'BayernNetz', Department of Earth and Environmental Sciences, Geophysical Observatory, University of Munich. International Federation of Digital Seismograph Networks. www.fdsn.org/networks/detail/BW/. doi.org/10.7914/SN/BW. https://doi.org/10.7914/SN/BW.

Belfi, J., Beverini, N., Bosi, F., Carelli, G., Cuccato, D., De Luca, G., Di Virgilio, A., Gebauer, A., Maccioni, E., Ortolan, A., Porzio, A., Saccorotti, G., Simonelli, A. & Terreni, G. (2017), 'Deep underground rotation measurements: GINGERino ring laser

gyroscope in Gran Sasso', *Review of Scientific Instruments* **88**(3), 034502. https://doi.org/10.1063/1.4977051.

Belfi, J., Beverini, N., Carelli, G., Di Virgilio, A., Maccioni, E., Saccorotti, G., Stefani, F. & Velikoseltsev, A. (2012), 'Horizontal rotation signals detected by "g-pisa" ring laser for the m w= 9.0, march 2011, japan earthquake', *Journal of Seismology* **16**, 767–776. https://doi.org/https://doi.org/10.1007/s10950-012-9276-9.

Berger, J., Davis, P. & Ekström, G. (2004), 'Ambient earth noise: a survey of the global seismographic network', *Journal of Geophysical Research: Solid Earth* **109**(B11). https://doi.org/10.1029/2004JB003408.

Bernauer, F., Behnen, K., Wassermann, J., Egdorf, S., Igel, H., Donner, S., Stammler, K., Hoffmann, M., Edme, P., Sollberger, D., Schmelzbach, C., Robertsson, J., Paitz, P., Igel, J., Smolinski, K., Fichtner, A., Rossi, Y., Izgi, G., Vollmer, D., Eibl, E. P. S., Buske, S., Veress, C., Guattari, F., Laudat, T., Mattio, L., Sèbe, O., Olivier, S., Lallemand, C., Brunner, B., Kurzych, A. T., Dudek, M., Jaroszewicz, L. R., Kowalski, J. K., Bońkowski, P. A., Bobra, P., Zembaty, Z., Vackář, J., Málek, J. & Brokesova, J. (2021), 'Rotation, Strain, and Translation Sensors Performance Tests with Active Seismic Sources', *Sensors* **21**(1), 264. https://doi.org/10.3390/s21010264.

Bernauer, F., Garcia, R. F., Murdoch, N., Dehant, V., Sollberger, D., Schmelzbach, C., Stähler, S., Wassermann, J., Igel, H., Cadu, A., Mimoun, D., Ritter, B., Filice, V., Karatekin, O., Ferraioli, L., Robertsson, J. O. A., Giardini, D., Lecamp, G., Guattari, F., Bonnefois, J.-J. & De Raucourt, S. (2020a), 'Exploring planets and asteroids with 6DoF sensors: Utopia and realism', *Earth, Planets and Space* **72**(1), 191. https://doi.org/10.1186/s40623-020-01333-9.

Bernauer, F., Wassermann, J., Guattari, F., Frenois, A., Bigueur, A., Gaillot, A., de Toldi, E., Ponceau, D., Schreiber, U. & Igel, H. (2018), 'BlueSeis3A: Full Characterization of a 3C Broadband Rotational Seismometer', *Seismological Research Letters* **89**(2A), 620–629. https://doi.org/10.1785/0220170143.

Bernauer, F., Wassermann, J. & Igel, H. (2012), 'Rotational sensors — A comparison of different sensor types', *Journal of Seismology* **16**, 595–602. https://doi.org/10.1007/s10950-012-9286-7.

Bernauer, F., Wassermann, J. & Igel, H. (2020b), 'Dynamic tilt correction using direct rotational motion measurements', *Seismological Research Letters* **91**(5), 2872–2880. https://doi.org/10.1785/0220200132.

Bernauer, M., Fichtner, A. & Igel, H. (2012), 'Measurements of translation, rotation and strain: new approaches to seismic processing and inversion', *Journal of Seismology* **16**(4), 669–681. https://doi.org/10.1007/s10950-012-9298-3.

Beyreuther, M., Barsch, R., Krischer, L., Megies, T., Behr, Y. & Wassermann, J. (2010), 'Obspy: A python toolbox for seismology', *Seismological Research Letters* **81**(3), 530–533. https://doi.org/10.1785/gssrl.81.3.530.

Bońkowski, P., Bobra, P., Zembaty, Z. & Jędraszak, B. (2023), 'Experimental analysis of stiffness identification of damaged reinforced concrete beams with directly measured rotational modes (preprint)'. https://doi.org/10.2139/ssrn.4552257.

Bosi, F., Cella, G., Di Virgilio, A., Ortolan, A., Porzio, A., Solimeno, S., Cerdonio, M., Zendri, J. P., Allegrini, M., Belfi, J., Beverini, N., Bouhadef, B., Carelli, G., Ferrante, I., Maccioni, E., Passaquieti, R., Stefani, F., Ruggiero, M. L., Tartaglia, A., Schreiber, K. U., Gebauer, A. & Wells, J.-P. R. (2011), 'Measuring gravitomagnetic effects by a multi-ring-laser gyroscope', *Physical Review D* **84**(12), 122002. https://doi.org/10.1103/PhysRevD.84.122002.

Brotzer, A., Bernauer, F., Schreiber, K. U., Wassermann, J. & Igel, H. (2021), 'Automated Quality Assessment of Interferometric Ring Laser Data', *Sensors* **21**(10), 3425. https://doi.org/10.3390/s21103425.

Brotzer, A., Igel, H., Stutzmann, E., Montagner, J., Bernauer, F., Wassermann, J., Widmer-Schnidrig, R., Lin, C., Kiselev, S., Vernon, F. & Schreiber, K. U. (2023), 'Characterizing the Background Noise Level of Rotational Ground Motions on Earth', *Seismological Research Letters* . https://doi.org/10.1785/0220230202.

Brune, J. N. & Oliver, J. (1959), 'The seismic noise of the Earth's surface', *Bulletin of the Seismological Society of America* **49**(4), 349–353. https://doi.org/10.1785/BSSA0490040349.

Chen, C., Wang, Y., Sun, L., Lin, C., Wei, Y., Liao, C., Lin, B. & Qin, L. (2023), 'Six-component earthquake synchronous observations across taiwan strait: Phase velocity and source location', *Earth and Space Science* **10**(12). https://doi.org/10.1029/2023ea003040.

Chow, B., Wassermann, J., Schuberth, B. S. A., Hadziioannou, C., Donner, S. & Igel, H. (2019), 'Love wave amplitude decay from rotational ground motions', *Geophysical Journal International* **218**(2), 1336–1347. https://doi.org/10.1093/gji/ggz213.

CMEMS (2024), 'Global ocean l4 significant wave height from nrt satellite measurements', CLS (France). E.U. Copernicus Marine Service Information (CMEMS). Marine Data Store (MDS). https://doi.org/10.48670/moi-00176. Last Accessed: 2024-10-30.

Cochard, A., Igel, H., Schuberth, B., Suryanto, W., Velikoseltsev, A., Schreiber, U., Wassermann, J., Scherbaum, F. & Vollmer, D. (2006), Rotational motions in seismology: theory, observation, simulation, *in* 'Earthquake source asymmetry, structural media and rotation effects', Springer, pp. 391–411. https://doi.org/10.1007/3-540-31337-0_30.

Davy, C., Barruol, G., Fontaine, F. R., Sigloch, K. & Stutzmann, E. (2014), 'Tracking major storms from microseismic and hydroacoustic observations on the seafloor', *Geophysical Research Letters* **41**(24), 8825–8831. https://doi.org/10.1002/2014GL062319.

Deen, M., Stutzmann, E. & Ardhuin, F. (2018), 'The earth's hum variations from a global model and seismic recordings around the indian ocean', *Geochemistry, Geophysics, Geosystems* **19**(10), 4006–4020. https://doi.org/10.1029/2018GC007478.

Donner, S. (2021), 'Rotational ground motion measurements for regional seismic moment tensors: A review', *Advances in Geophysics* **62**, 141–186. https://doi.org/10.1016/bs.agph.2021.06.002.

Donner, S., Bernauer, M. & Igel, H. (2016), 'Inversion for seismic moment tensors combining translational and rotational ground motions', *Geophysical Journal International* **207**(1), 562–570. https://doi.org/10.1093/gji/ggw298.

Donner, S., Igel, H., Hadziioannou, C. & the Romy group (2018), Retrieval of the seismic moment tensor from joint measurements of translational and rotational ground motions: Sparse networks and single stations, *in* 'Moment Tensor Solutions', Springer International Publishing, pp. 263–280. https://doi.org/10.1007/978-3-319-77359-9_12.

Donner, S., Lin, C., Hadziioannou, C., Gebauer, A., Vernon, F., Agnew, D. C., Igel, H., Schreiber, U. & Wassermann, J. (2017), 'Comparing Direct Observation of Strain, Rotation, and Displacement with Array Estimates at Piñon Flat Observatory, California', *Seismological Research Letters* **88**(4), 1107–1116. https://doi.org/10.1785/0220160216.

Donner, S., Mustać, M., Hejrani, B., Tkalčić, H. & Igel, H. (2020), 'Seismic moment tensors from synthetic rotational and translational ground motion: Green's functions in 1-d versus 3-d', *Geophysical Journal International* **223**(1), 161–179. https://doi.org/10.1093/gji/ggaa305.

ECCS (2015), *ECCS-European Convention for Constructional Steelwork. Design of steel structures: eurocode 3: design of steel structures, part 1-1: general rules and rules for buildings*, John Wiley & Sons.

Friedrich, A., Krüger, F. & Klinge, K. (1998), 'Ocean-generated microseismic noise located with the Gräfenberg array', *Journal of Seismology* **2**(1), 47–64. https://doi.org/10.1023/A:1009788904007.

Gebauer, A., Schreiber, K. U., Klügel, T., Schön, N. & Ulbrich, U. (2012), 'High-frequency noise caused by wind in large ring laser gyroscope data', *Journal of Seismology* **16**(4), 777–786. https://doi.org/10.1007/s10950-012-9283-x.

Gebauer, A., Tercjak, M., Schreiber, K. U., Igel, H., Kodet, J., Hugentobler, U., Wassermann, J., Bernauer, F., Lin, C.-J., Donner, S., Egdorf, S., Simonelli, A. & Wells, J.-P. R. (2020), 'Reconstruction of the Instantaneous Earth Rotation Vector with Sub-Arcsecond Resolution Using a Large Scale Ring Laser Array', *Physical Review Letters* **125**(3), 033605. https://doi.org/10.1103/PhysRevLett.125.033605.

GEOSCOPE (1982), 'Geoscope, french global network of broad band seismic stations', GEOSCOPE, French Global Network of broad band seismic stations. Institut de physique du globe de Paris (IPGP) and École et Observatoire des Sciences de la Terre de Strasbourg (EOST). FDSN Network Code G. https://doi.org/10.18715/GEOSCOPE.G.

GRSN (1976), 'German Regional Seismic Network (GRSN)', Bundesanstalt für Geowissenschaften und Rohstoffe (BGR). International Federation of Digital Seismograph Networks. www.fdsn.org/networks/detail/GR/. https://doi.org/10.25928/MBX6-HR74.

GSN (1986), 'Global seismograph network - iris/ida', Global Seismograph Network - IRIS/IDA. Scripps Institution of Oceanography. International Federation of Digital Seismograph Networks. https://www.fdsn.org/10.7914/SN/II.

GSN (2014), 'Global Seismograph Network (GSN - IRIS/USGS)', Global Seismograph Network (GSN - IRIS/USGS). Albuquerque Seismological Laboratory/USGS.International Federation of Digital Seismograph Networks. https://doi.org/10.7914/SN/IU.

Gualtieri, L., Bachmann, E., Simons, F. J. & Tromp, J. (2021), 'Generation of secondary microseism love waves: effects of bathymetry, 3-d structure and source seasonality', *Geophysical Journal International* **226**(1), 192–219. https://doi.org/10.1093/gji/ggab095.

Gualtieri, L., Stutzmann, E., Juretzek, C., Hadziioannou, C. & Ardhuin, F. (2019), 'Global scale analysis and modelling of primary microseisms', *Geophysical Journal International* **218**(1), 560–572. https://doi.org/10.1093/gji/ggz161.

Guattari, F., Toldi, E. d., Garcia, R. F. & Mimoun, D. (2019), Fiber optic gyroscope For 6-component planetary seismology, *in* 'International Conference on Space Optics — ICSO 2018', Vol. 11180, SPIE, pp. 2867–2884. https://doi.org/10.1117/12.2536207.

Guéguen, P. & Astorga, A. (2021), 'The torsional response of civil engineering structures during earthquake from an observational point of view', *Sensors* **21**(2), 342. https://doi.org/10.3390/s21020342.

Guéguen, P., Guattari, F., Aubert, C. & Laudat, T. (2020), 'Comparing direct observation of torsion with array-derived rotation in civil engineering structures', *Sensors* **21**(1), 142. https://doi.org/10.3390/s21010142.

Hadziioannou, C., Gaebler, P., Schreiber, U., Wassermann, J. & Igel, H. (2012), 'Examining ambient noise using colocated measurements of rotational and translational motion',

Journal of Seismology **16**(4), 787–796. https://doi.org/10.1007/s10950-012-9288-5.

Haned, A., Stutzmann, E., Schimmel, M., Kiselev, S., Davaille, A. & Yelles-Chaouche, A. (2016), 'Global tomography using seismic hum', *Geophysical Journal International* **204**(2), 1222–1236. https://doi.org/10.1093/gji/ggv516.

Hasselmann, K. (1963), 'A statistical analysis of the generation of microseisms', *Reviews of Geophysics* **1**(2), 177–210. https://doi.org/10.1029/RG001i002p00177.

Hillers, G., Graham, N., Campillo, M., Kedar, S., Landès, M. & Shapiro, N. (2012), 'Global oceanic microseism sources as seen by seismic arrays and predicted by wave action models', *Geochemistry, Geophysics, Geosystems* **13**(1). https://doi.org/10.1029/2011GC003875.

Huang, B.-S. (2003), 'Ground rotational motions of the 1999 Chi-Chi, Taiwan earthquake as inferred from dense array observations', *Geophysical Research Letters* **30**(6). https://doi.org/10.1029/2002GL015157.

Hurst, R. B., Mayerbacher, M., Gebauer, A., Schreiber, K. U. & Wells, J.-P. R. (2017), 'High-accuracy absolute rotation rate measurements with a large ring laser gyro: establishing the scale factor', *Applied Optics* **56**(4), 1124–1130. https://doi.org/10.1364/AO.56.001124.

Hurst, R. B., Rabeendran, N., Schreiber, K. U. & Wells, J.-P. R. (2014), 'Correction of backscatter-induced systematic errors in ring laser gyroscopes', *Applied Optics* **53**(31), 7610–7618. https://doi.org/10.1364/AO.53.007610.

Hurst, R. B., Stedman, G. E., Schreiber, K. U., Thirkettle, R. J., Graham, R. D., Rabeendran, N. & Wells, J.-P. R. (2009), 'Experiments with an 834m2 ring laser interferometer', *Journal of Applied Physics* **105**(11), 113115. https://doi.org/10.1063/1.3133245.

Ichinose, G. A., Ford, S. R. & Mellors, R. J. (2021), 'Regional Moment Tensor Inversion Using Rotational Observations', *Journal of Geophysical Research: Solid Earth* **126**(2), e2020JB020827. https://doi.org/10.1029/2020JB020827.

Igel, H., Bernauer, M., Wassermann, J. & Schreiber, K. U. (2014), Seismology, rotational, complexity, *in* R. A. Meyers, ed., 'Encyclopedia of Complexity and Systems Science', Springer, Berlin, Heidelberg, pp. 1–26. https://doi.org/10.1007/978-3-642-27737-5_608-1.

Igel, H., Cochard, A., Wassermann, J., Flaws, A., Schreiber, U., Velikoseltsev, A. & Pham Dinh, N. (2007), 'Broad-band observations of earthquake-induced rotational ground motions', *Geophysical Journal International* **168**(1), 182–196. https://doi.org/10.1111/j.1365-246X.2006.03146.x.

Igel, H., Nader, M.-F., Kurrle, D., Ferreira, A. M., Wassermann, J. & Schreiber, K. U. (2011), 'Observations of Earth's toroidal free oscillations with a rotation sensor: The 2011 magnitude 9.0 Tohoku-Oki earthquake', *Geophysical Research Letters* **38**(21). https://doi.org/10.1029/2011GL049045.

Igel, H., Schreiber, K. U., Gebauer, A., Bernauer, F., Egdorf, S., Simonelli, A., Lin, C.-J., Wassermann, J., Donner, S., Hadziioannou, C., Yuan, S., Brotzer, A., Kodet, J., Tanimoto, T., Hugentobler, U. & Wells, J.-P. R. (2021), 'ROMY: A multicomponent ring laser for geodesy and geophysics', *Geophysical Journal International* **225**(1), 684–698. https://doi.org/10.1093/gji/ggaa614.

Igel, H., Schreiber, U., Flaws, A., Schuberth, B., Velikoseltsev, A. & Cochard, A. (2005), 'Rotational motions induced by the M8. 1 Tokachi-oki earthquake, September 25, 2003', *Geophysical Research Letters* **32**(8). https://doi.org/10.1029/2004GL022336.

Jaroszewicz, L. R., Kurzych, A., Krajewski, Z., Kowalski, J. K. & Teisseyre, K. P. (2016), 'Fosrem: Fibre-optic system for rotational events and phenomena monitoring: Construction, investigation and area of application', *Seismic Behaviour and Design of Irregular and Complex Civil Structures II* pp. 49–64. https://doi.org/10.1007/978-3-319-14246-3_5.

Juretzek, C. & Hadziioannou, C. (2016), 'Where do ocean microseisms come from? a study of love-to-rayleigh wave ratios', *Journal of Geophysical Research: Solid Earth* **121**(9), 6741–6756. https://doi.org/10.1002/2016JB013017.

Keil, S., Wassermann, J. & Igel, H. (2021), 'Single-station seismic microzonation using 6c measurements', *Journal of Seismology* **25**(1), 103–114. https://doi.org/10.1007/s10950-020-09944-1.

Kenda, B., Drilleau, M., Garcia, R. F., Kawamura, T., Murdoch, N., Compaire, N., Lognonné, P., Spiga, A., Widmer-Schnidrig, R., Delage, P., Ansan, V., Vrettos, C., Rodriguez, S., Banerdt, W. B., Banfield, D., Antonangeli, D., Christensen, U., Mimoun, D., Mocquet, A. & Spohn, T. (2020), 'Subsurface Structure at the InSight Landing Site From Compliance Measurements by Seismic and Meteorological Experiments', *Journal of Geophysical Research: Planets* **125**(6), e2020JE006387. https://doi.org/10.1029/2020JE006387.

Kislov, K. & Gravirov, V. (2021), 'Rotational seismology: Review of achievements and outlooks', *Seismic Instruments* **57**(2), 187–202. https://doi.org/10.3103/S0747923921020262.

Krüger, F. & Ohrnberger, M. (2005), 'Tracking the rupture of the Mw = 9.3 Sumatra earthquake over 1,150 km at teleseismic distance', *Nature* **435**(7044), 937–939. https://doi.org/10.1038/nature03696.

Laske, G., Masters, G., Ma, Z. & Pasyanos, M. (2013), 'Update on CRUST1.0 - A 1-degree global model of Earth's crust: EGU general assembly 2013', *Geophys. Res. Abstr.* **15**, EGU2013–2658.

Lay, T. & Wallace, T. C. (1995), *Modern global seismology*, Elsevier.

Le Pape, F., Craig, D. & Bean, C. J. (2021), 'How deep ocean-land coupling controls the generation of secondary microseism love waves', *Nature Communications* **12**(1), 2332. https://doi.org/10.1038/s41467-021-22591-5.

Leugoud, R. & Kharlamov, A. (2012), 'Second generation of a rotational electrochemical seismometer using magnetohydrodynamic technology', *Journal of Seismology* **16**(4), 587–593. https://doi.org/10.1007/s10950-012-9290-y.

Li, Z. & van der Baan, M. (2017), 'Tutorial on rotational seismology and its applications in exploration geophysics', *GEOPHYSICS* **82**(5), W17–W30. https://doi.org/10.1190/geo2016-0497.1.

Liao, C.-M., Hicke, K., Bernauer, F., Igel, H., Hadziioannou, C. & Niederleithinger, E. (2022), 'Multi-sensor measurements on a large-scale bridge model', *5. Brückenkolloquium: Fachtagung für Beurteilung, Planung, Bau, Instandhaltung und Betrieb von Brücken* p. 223.

Lin, C.-J., Huang, H.-P., Pham, N. D., Liu, C.-C., Chi, W.-C. & Lee, W. H. K. (2011), 'Rotational motions for teleseismic surface waves', *Geophysical Research Letters* **38**(15). https://doi.org/10.1029/2011GL047959.

Lin, C.-J., Ku, C.-S., Chi, T.-C., Huang, B.-S., Huang, H.-H. & Liu, C.-C. (2022), 'Correcting the background tilt signal of the horizontal seismometer using a rotation sensor', *Seismological Research Letters* **93**(3), 1564–1572. https://doi.org/10.1785/0220210185.

Lindner, F., Wassermann, J., Schmidt-Aursch, M. C., Schreiber, K. U. & Igel, H. (2017), 'Seafloor ground rotation observations: Potential for improving signal-to-noise ratio on horizontal OBS components', *Seismological Research Letters* **88**(1), 32–38. https://doi.org/10.1785/0220160051.

Longuet-Higgins, M. S. & Jeffreys, H. (1950), 'A theory of the origin of microseisms', *Philosophical Transactions of the Royal Society of London. Series A, Mathematical and Physical Sciences* **243**(857), 1–35. https://doi.org/10.1098/rsta.1950.0012.

Macek, W. M. & Davis, D. T. M. J. (1963), 'Rotation Rate Sensing with Traveling-Wave Ring Lasers', *Applied Physics Letters* **2**(3), 67–68.

Marty, J., Doury, B. & Kramer, A. (2021), 'Low and High Broadband Spectral Models of Atmospheric Pressure Fluctuation', *Journal of Atmospheric and Oceanic Technology* **38**(10), 1813–1822. https://doi.org/10.1175/JTECH-D-21-0006.1.

McCann, J. J., Winterflood, J., Ju, L. & Zhao, C. (2021), 'A multi-orientation low-frequency rotational accelerometer', *Review of Scientific Instruments* **92**(6), 064503. https://doi.org/10.1063/5.0047069.

McLeod, D., Stedman, G., Webb, T. & Schreiber, U. (1998), 'Comparison of standard and ring laser rotational seismograms', *Bulletin of the Seismological Society of America* **88**(6), 1495–1503. https://doi.org/10.1785/BSSA0880061495.

Megies, T., Beyreuther, M., Barsch, R., Krischer, L. & Wassermann, J. (2011), 'ObsPy–What can it do for data centers and observatories?', *Annals of Geophysics* **54**(1), 47–58. https://doi.org/10.4401/ag-4838.

Nader, M., Igel, H., Ferreira, A., Al-Attar, D., Wassermann, J. & Schreiber, K. (2015), 'Normal mode coupling observations with a rotation sensor', *Geophysical Journal International* **201**(3), 1482–1490. https://doi.org/10.1093/gji/ggv082.

Natural Earth (2024), Open Source Dataset on Bathymetry by Natural Earth. https://www.naturalearthdata.com/. Last Accessed: 2024-10-30.

Nishida, K., Kawakatsu, H., Fukao, Y. & Obara, K. (2008), 'Background Love and Rayleigh waves simultaneously generated at the Pacific ocean floors', *Geophysical Research Letters* **35**(16). https://doi.org/10.1029/2008GL034753.

Noe, S., Yuan, S., Montagner, J.-P. & Igel, H. (2022), 'Anisotropic elastic parameter estimation from multicomponent ground-motion observations: a theoretical study', *Geophysical Journal International* **229**(2), 1462–1473. https://doi.org/10.1093/gji/ggac006.

Ortolan, A., Belfi, J., Bosi, F., Di Virgilio, A., Beverini, N., Carelli, G., Maccioni, E., Santagata, R., Simonelli, A., Beghi, A. et al. (2016), The GINGER project and status of the GINGERino prototype at LNGS, *in* 'Journal of Physics: Conference Series', Vol. 718, IOP Publishing, p. 072003. https://doi.org/https://10.1088/1742-6596/718/7/072003.

Pancha, A., Webb, T. H., Stedman, G. E., McLeod, D. P. & Schreiber, K. U. (2000), 'Ring laser detection of rotations from teleseismic waves', *Geophysical Research Letters* **27**(21), 3553–3556. https://doi.org/10.1029/2000GL011734.

Patterson, Tom. Kelso, N. V. (2012), 'World urban areas, landscan, 1:10 million', *North American Cartographic Information Society* . https://doi.org/https://geo.nyu.edu/catalog/stanford-yk247bg4748.

Perron, V., Hollender, F., Mariscal, A., Theodoulidis, N., Andreou, C., Bard, P., Cornou, C., Cottereau, R., Cushing, E. M., Frau, A., Hok, S., Konidaris, A., Langlaude, P., Laurendeau, A., Savvaidis, A. & Svay, A. (2018), 'Accelerometer, Velocimeter Dense-Array, and Rotation Sensor Datasets from the Sinaps@ Postseismic Survey (Cephalonia 2014–2015 Aftershock Sequence)', *Seismological Research Letters* **89**(2A), 678–687. https://doi.org/10.1785/0220170125.

Peterson, J. R. (1993), 'Observations and modeling of seismic background noise', *U.S. Geological Survey – Open-File Report* pp. 93–322. https://doi.org/10.3133/ofr93322.

Poppeliers, C. & Evans, E. V. (2015), 'The effects of measurement uncertainties in seismic-wave gradiometry', *Bulletin of the Seismological Society of America* **105**(6), 3143–3155. https://doi.org/10.1785/0120150043.

Pritsch, B., Schreiber, K. U., Velikoseltsev, A. & Wells, J.-P. R. (2007), 'Scale-factor corrections in large ring lasers', *Applied Physics Letters* **91**(6), 061115. https://doi.org/10.1063/1.2768639.

Pérez-Guillén, C., Tsunematsu, K., Nishimura, K. & Issler, D. (2019), 'Seismic location and tracking of snow avalanches and slush flows on Mt. Fuji, Japan', *Earth Surface Dynamics* **7**(4), 989–1007. https://doi.org/10.5194/esurf-7-989-2019.

Rau, G. C., Eulenfeld, T., Howe, D., Rietbroek, R., Gosselin, J.-S., Staniewicz, S. & TaylorDixonHD (2022), 'hydrogeoscience/pygtide: Pygtide v0.7.1'. https://doi.org/10.5281/zenodo.6673581.

Riahi, N. & Gerstoft, P. (2015), 'The seismic traffic footprint: Tracking trains, aircraft, and cars seismically', *Geophysical Research Letters* **42**(8), 2674–2681. https://doi.org/10.1002/2015GL063558.

Ross, M. P., van Dongen, J., Huang, Y., Zhou, H., Chowdhury, Y., Apple, S. K., Mow-Lowry, C. M., Mitchell, A. L., Holland, N. A., Lantz, B., Bonilla, E., Engl, A., Pele, A., Griffith, D., Sanchez, E., Shaw, E. A., Gettings, C. & Gundlach, J. (2023), 'A vacuum-compatible cylindrical inertial rotation sensor with picoradian sensitivity', *Review of Scientific Instruments* **94**(9). https://doi.org/10.1063/5.0167283.

Ross, M. P., Venkateswara, K., Hagedorn, C. A., Gundlach, J. H., Kissel, J. S., Warner, J., Radkins, H., Shaffer, T. J., Coughlin, M. W. & Bodin, P. (2017), 'Low-frequency tilt seismology with a precision ground-rotation sensor', *Seismological Research Letters* **89**(1), 67–76. https://doi.org/10.1785/0220170148.

Ross, Z. E., Hauksson, E. & Ben-Zion, Y. (2017), 'Abundant off-fault seismicity and orthogonal structures in the san jacinto fault zone', *Science advances* **3**(3), e1601946. 10.1126/sciadv.1601946.

Sagnac, G. (1913), 'L'éther lumineux démontré par l'effet du vent relatif d'éther dans un interféromètre en rotation uniforme', *CR Acad. Sci.* **157**, 708–710.

Saito, M. (1988), 'Disper80: A subroutine package for calculation of seismic normal-mode solution', *Seismological Algorithm* . https://doi.org/10.3124/segj.64.127.

Salvermoser, J., Hadziioannou, C., Hable, S., Krischer, L., Chow, B., Ramos, C., Wassermann, J., Schreiber, U., Gebauer, A. & Igel, H. (2017), 'An Event Database for Rotational Seismology', *Seismological Research Letters* **88**(3), 935–941. https://doi.org/10.1785/0220160184.

Sbaa, S., Hollender, F., Perron, V., Imtiaz, A., Bard, P.-Y., Mariscal, A., Cochard, A. & Dujardin, A. (2017), 'Analysis of rotation sensor data from the SINAPS@ Kefalonia (Greece) post-seismic experiment—link to surface geology and wavefield characteristics', *Earth, Planets and Space* **69**(1), 124. https://doi.org/10.1186/s40623-017-0711-6.

SCEDC (2013), 'Global ocean l4 significant wave height from nrt satellite measurements', Southern California Earthquake Data Center (SCEDC). Caltech. Dataset. https://doi.org/10.7909/C3WD3xH1. Last Accessed: 2023-05-15.

Schmelzbach, C., Donner, S., Igel, H., Sollberger, D., Taufiqurrahman, T., Bernauer, F., Häusler, M., Van Renterghem, C., Wassermann, J. & Robertsson, J. (2018), 'Advances in 6c seismology: Applications of combined translational and rotational motion measurements in global and exploration seismology', *Geophysics* **83**(3), 53–69. https://doi.org/10.1190/geo2017-0492.1.

Schreiber, K. U., Gebauer, A., Igel, H., Wassermann, J., Hurst, R. B. & Wells, J.-P. R. (2014), 'The centennial of the Sagnac experiment in the optical regime: From a tabletop experiment to the variation of the Earth's rotation', *Comptes Rendus. Physique* **15**(10), 859–865. https://doi.org/10.1016/j.crhy.2014.10.003.

Schreiber, K. U., Klügel, T., Velikoseltsev, A., Schlüter, W., Stedman, G. E. & Wells, J.-P. R. (2009), 'The Large Ring Laser G for Continuous Earth Rotation Monitoring', *Pure and Applied Geophysics* **166**(8), 1485–1498. https://doi.org/10.1007/s00024-004-0490-4.

Schreiber, K. U., Kodet, J., Hugentobler, U., Klügel, T. & Wells, J.-P. R. (2023a), 'Variations in the Earth's rotation rate measured with a ring laser interferometer', *Nature Photonics* **17**(12), 1054–1058. https://doi.org/10.1038/s41566-023-01286-x.

Schreiber, K. U., Stedman, G. E., Igel, H. & Flaws, A. (2006b), Ring laser gyroscopes as rotation sensors for seismic wave studies, *in* 'Earthquake source asymmetry, structural media and rotation effects', Springer, pp. 377–390. https://doi.org/https://doi.org/10.1007/3-540-31337-0_29.

Schreiber, K. U., Velikoseltsev, A., Rothacher, M., Klügel, T., Stedman, G. E. & Wiltshire, D. L. (2004), 'Direct measurement of diurnal polar motion by ring laser gyroscopes', *Journal of Geophysical Research: Solid Earth* **109**(B6). https://doi.org/https://doi.org/10.1029/2003JB002803.

Schreiber, K. U. & Wells, J.-P. R. (2013), 'Invited Review Article: Large ring lasers for rotation sensing', *Review of Scientific Instruments* **84**(4), 041101–041101–26. https://doi.org/10.1063/1.4798216.

Schreiber, K. U., Wells, J. P. R. & Stedman, G. E. (2008), 'Noise processes in large ring lasers', *General Relativity and Gravitation* **40**(5), 935–943. https://doi.org/10.1007/s10714-007-0584-2.

Schreiber, U., Igel, H., Cochard, A., Velikoseltsev, A., Flaws, A., Schuberth, B., Drewitz, W. & Müller, F. (2006a), The GEOsensor Project: Rotations — a New Observable for Seismology, *in* 'Observation of the Earth System from Space', Springer, Berlin, Heidelberg, pp. 427–443. https://doi.org/10.1007/3-540-29522-4_28.

Schreiber, U. & Wells, J.-P. (2023b), *Rotation Sensing with Large Ring Lasers: Applications in Geophysics and Geodesy*, Cambridge University Press. https://doi.org/https://doi.org/10.1017/9781108524933.

Singh, S., Capdeville, Y. & Igel, H. (2020), 'Correcting wavefield gradients for the effects of local small-scale heterogeneities', *Geophysical Journal International* **220**(2), 996–1011. https://doi.org/10.1093/gji/ggz479.

Sollberger, D. (2023), 'solldavid/twistpy: Twistpy - first release'. https://doi.org/10.5281/zenodo.8124030.

Sollberger, D., Greenhalgh, S. A., Schmelzbach, C., Van Renterghem, C. & Robertsson, J. O. (2018), '6-C polarization analysis using point measurements of translational and rotational ground-motion: Theory and applications', *Geophysical Journal International* **213**(1), 77–97. https://doi.org/10.1093/gji/ggx542.

Sollberger, D., Heimann, S., Bernauer, F., Eibl, E. P., Donner, S., Hadziioannou, C., Igel, H., Yuan, S. & Wassermann, J. (2023), Twistpy: An open-source python toolbox for wavefield inertial sensing techniques, *in* 'EGU General Assembly Conference Abstracts', pp. EGU–7563. https://doi.org/10.5194/egusphere-egu23-7563.

Sollberger, D., Igel, H., Schmelzbach, C., Edme, P., Van Manen, D.-J., Bernauer, F., Yuan, S., Wassermann, J., Schreiber, U. & Robertsson, J. O. A. (2020), 'Seismological Processing of Six Degree-of-Freedom Ground-Motion Data', *Sensors* **20**(23), 6904. https://doi.org/10.3390/s20236904.

Spudich, P. & Fletcher, J. B. (2008), 'Observation and prediction of dynamic ground strains, tilts, and torsions caused by the Mw6.0 2004 Parkfield, California, earthquake and aftershocks, derived from UPSAR array observations', *Bulletin of the Seismological Society of America* **98**(4), 1898–1914. https://doi.org/10.1785/0120070157.

Spudich, P. & Fletcher, J. B. (2009), 'Software for Inference of Dynamic Ground Strains and Rotations and Their Errors from Short Baseline Array Observations of Ground

Motions', *Bulletin of the Seismological Society of America* **99**(2B), 1480–1482. https://doi.org/10.1785/0120080230.

Spudich, P., Steck, L. K., Hellweg, M., Fletcher, J. & Baker, L. M. (1995), 'Transient stresses at Parkfield, California, produced by the M7.4 Landers earthquake of June 28, 1992: Observations from the UPSAR dense seismograph array', *Journal of Geophysical Research: Solid Earth* **100**(B1), 675–690. https://doi.org/10.1029/94JB02477.

Stedman, G. E. (1997), 'Ring-laser tests of fundamental physics and geophysics', *Reports on Progress in Physics* **60**(6), 615–688. https://doi.org/10.1088/0034-4885/60/6/001.

Stedman, G., Li, Z. & Bilger, H. (1995), 'Sideband analysis and seismic detection in a large ring laser', *Applied Optics* **34**(24), 5375–5385. https://doi.org/10.1364/AO.34.005375.

Stutzmann, E., Ardhuin, F., Schimmel, M., Mangeney, A. & Patau, G. (2012), 'Modelling long-term seismic noise in various environments', *Geophysical Journal International* **191**(2), 707–722. https://doi.org/10.1111/j.1365-246X.2012.05638.x.

Suryanto, W., Igel, H., Wassermann, J., Cochard, A., Schuberth, B., Vollmer, D., Scherbaum, F., Schreiber, U. & Velikoseltsev, A. (2006), 'First comparison of array-derived rotational ground motions with direct ring laser measurements', *Bulletin of the Seismological Society of America* **96**(6), 2059–2071. https://doi.org/10.1785/0120060004.

Takeo, M. (2009), 'Rotational Motions Observed during an Earthquake Swarm in April 1998 Offshore Ito, Japan', *Bulletin of the Seismological Society of America* **99**(2B), 1457–1467. https://doi.org/10.1785/0120080173.

Tanimoto, T. & Anderson, A. (2023), 'Seismic noise between 0.003 Hz and 1.0 Hz and its classification', *Progress in Earth and Planetary Science* **10**(1), 56. https://doi.org/10.1186/s40645-023-00587-7.

Tanimoto, T., Hadziioannou, C., Igel, H., Wasserman, J., Schreiber, U. & Gebauer, A. (2015), 'Estimate of Rayleigh-to-Love wave ratio in the secondary microseism by colocated ring laser and seismograph', *Geophysical Research Letters* **42**(8), 2650–2655. https://doi.org/10.1002/2015GL063637.

Tanimoto, T. & Li, Y. (2020), 'Nature of Low-Frequency, Atmosphere-Generated Seismic Noise', *Journal of Geophysical Research: Solid Earth* **125**(7), e2020JB019423. https://doi.org/10.1029/2020JB019423.

Tanimoto, T., Lin, C.-J., Hadziioannou, C., Igel, H. & Vernon, F. (2016), 'Estimate of Rayleigh-to-Love wave ratio in the secondary microseism by a small array at piñon Flats Observatory, California', *Geophysical Research Letters* **43**(21), 11–173. https://doi.org/10.1002/2016GL071133.

Todd, K. (2020), 'toddkarin/global-land-mask: Release of version 1.0.0'. https://doi.org/10.5281/zenodo.4066722.

Trani, L., Koymans, M., Atkinson, M., Sleeman, R. & Filgueira, R. (2017), 'Wfcatalog: A catalogue for seismological waveform data', *Computers & Geosciences* **106**, 101–108. https://doi.org/10.1016/j.cageo.2017.06.008.

Trifunac, M. D. (2009), 'The role of strong motion rotations in the response of structures near earthquake faults', *Soil Dynamics and Earthquake Engineering* **29**(2), 382–393. https://doi.org/10.1016/j.soildyn.2008.04.001.

UCSD (2014), 'Piñon Flats Observatory Array', University of California San Diego (UCSD). International Federation of Digital Seismograph Networks. www.fdsn.org/networks/detail/PY/. https://doi.org/10.7914/sn/py.

van Driel, M., Wassermann, J., Nader, M. F., Schuberth, B. S. A. & Igel, H. (2012), 'Strain rotation coupling and its implications on the measurement of rotational ground motions', *Journal of Seismology* **16**(4), 657–668. https://doi.org/10.1007/s10950-012-9296-5.

Venkateswara, K., Hagedorn, C. A., Gundlach, J. H., Kissel, J., Warner, J., Radkins, H., Shaffer, T., Lantz, B., Mittleman, R., Matichard, F. & Schofield, R. (2017), 'Subtracting tilt from a horizontal seismometer using a ground-rotation sensor', *Bulletin of the Seismological Society of America* pp. 709–717. https://doi.org/10.1785/0120160310.

Venkateswara, K., Paros, J., Bodin, P., Wilcock, W. & Tobin, H. J. (2021), 'Rotational seismology with a quartz rotation sensor', *Seismological Research Letters* **93**(1), 173–180. https://doi.org/10.1785/0220210171.

Wassermann, J., Bernauer, F., Shiro, B., Johanson, I., Guattari, F. & Igel, H. (2020), 'Six-axis ground motion measurements of caldera collapse at kīlauea volcano, hawai'i—more data, more puzzles?', *Geophysical Research Letters* **47**(5). https://doi.org/10.1029/2019GL085999.

Wassermann, J., Braun, T., Ripepe, M., Bernauer, F., Guattari, F. & Igel, H. (2022), 'The use of 6DOF measurement in volcano seismology – A first application to Stromboli volcano', *Journal of Volcanology and Geothermal Research* **424**, 107499. https://doi.org/10.1016/j.jvolgeores.2022.107499.

Wassermann, J., Lehndorfer, S., Igel, H. & Schreiber, U. (2009), 'Performance test of a commercial rotational motions sensor', *Bulletin of the Seismological Society of America* **99**(2B), 1449–1456. https://doi.org/10.1785/0120080157.

Waxler, R. & Gilbert, K. E. (2006), 'The radiation of atmospheric microbaroms by ocean waves', *The Journal of the Acoustical Society of America* **119**(5), 2651–2664. https://doi.org/10.1121/1.2191607.

Widmer-Schnidrig, R. & Zurn, W. (2009), 'Perspectives for Ring Laser Gyroscopes in Low-Frequency Seismology', *Bulletin of the Seismological Society of America* **99**(2B), 1199–1206. https://doi.org/10.1785/0120080267.

Xiao, H., Tanimoto, T., Spica, Z. J., Gaite, B., Ruiz-Barajas, S., Pan, M. & Viens, L. (2022), 'Locating the Precise Sources of High-Frequency Microseisms Using Distributed Acoustic Sensing', *Geophysical Research Letters* **49**(17), e2022GL099292. https://doi.org/10.1029/2022GL099292.

Xu, P., Shu, Y., Niu, X., Liu, J., Yao, W. & Chen, Q. (2019), 'High-rate multi-GNSS attitude determination: experiments, comparisons with inertial measurement units and applications of GNSS rotational seismology to the 2011 tohoku mw9.0 earthquake', *Measurement Science and Technology* **30**(2), 024003. https://doi.org/10.1088/1361-6501/aaf987.

Yuan, S., Gessele, K., Gabriel, A.-A., May, D. A., Wassermann, J. & Igel, H. (2021), 'Seismic Source Tracking With Six Degree-of-Freedom Ground Motion Observations', *Journal of Geophysical Research: Solid Earth* **126**(3), e2020JB021112. https://doi.org/10.1029/2020JB021112.

Yuan, S., Simonelli, A., Lin, C.-J., Bernauer, F., Donner, S., Braun, T., Wassermann, J. & Igel, H. (2020), 'Six degree-of-freedom broadband ground-motion observations with portable sensors: Validation, local earthquakes, and signal processing', *Bulletin of the Seismological Society of America* **110**(3), 953–969. https://doi.org/10.1785/0120190277.

Zembaty, Z., Bernauer, F., Igel, H. & Schreiber, K. U. (2021), 'Rotation Rate Sensors and Their Applications', *Sensors* **21**(16), 5344. https://doi.org/10.3390/s21165344.

Zembaty, Z., Kokot, S. & Bobra, P. (2016), Application of Rotation Rate Sensors in Measuring Beam Flexure and Structural Health Monitoring, *in* Z. Zembaty & M. De Stefano, eds, 'Seismic Behaviour and Design of Irregular and Complex Civil Structures II', Springer International Publishing, Cham, pp. 65–76. https://doi.org/10.1007/978-3-319-14246-3_6.

Zou, D. (2021), Ring laser gyroscopes: using optical frequency to vary the scale factor, PhD thesis, University of Canterbury.

Zürn, W., Exß, J., Steffen, H., Kroner, C., Jahr, T. & Westerhaus, M. (2007), 'On reduction of long-period horizontal seismic noise using local barometric pressure', *Geophysical Journal International* **171**(2), 780–796. https://doi.org/10.1111/j.1365-246X.2007.03553.x.

Zürn, W., Forbriger, T., Widmer-Schnidrig, R., Duffner, P. & Ringler, A. T. (2022), 'Modelling tilt noise caused by atmospheric processes at long periods for several horizontal seismometers at BFO—a reprise', *Geophysical Journal International* **228**(2), 927–943. https://doi.org/10.1093/gji/ggab336.

Supplementary Material

Supplementary Figures for Section 2

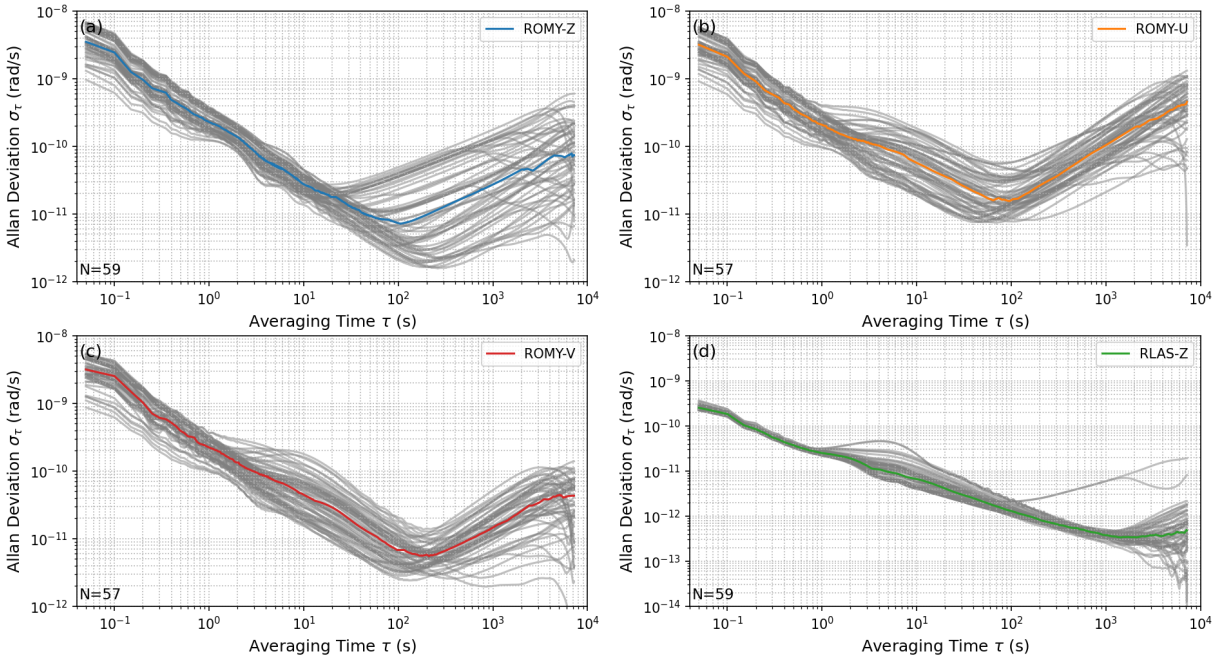

Figure S.1: Statistical Allan deviation for (a) RZ, (b) RU, (c) RV and (d) G-ring (= RLAS). Each overlapping Allan deviation is computed using for 4 h intervals with 50 % overlap between 2024-04-20 and 2024-04-25, while corrupt data periods are ignored. The median for each averaging time is colored.

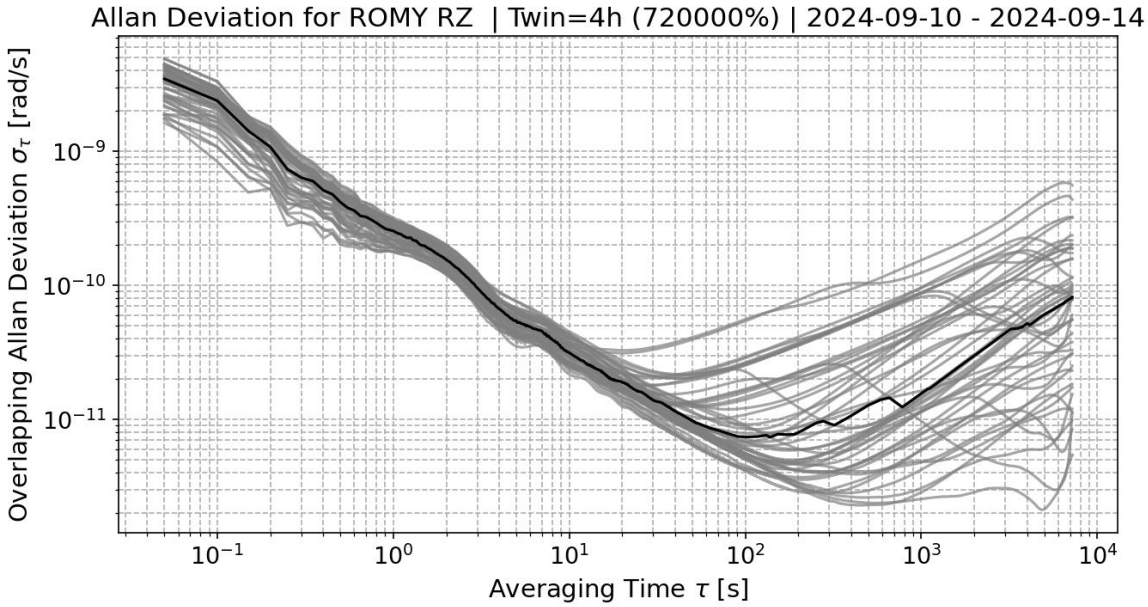

Figure S.2: Statistical overlapping Allan deviations for RZ in a phase-locked multi-mode regime for 4 h windows with 50 % overlap between 2024-09-10 and 2024-09-14 (gray) and a median value for each averaging time (black).

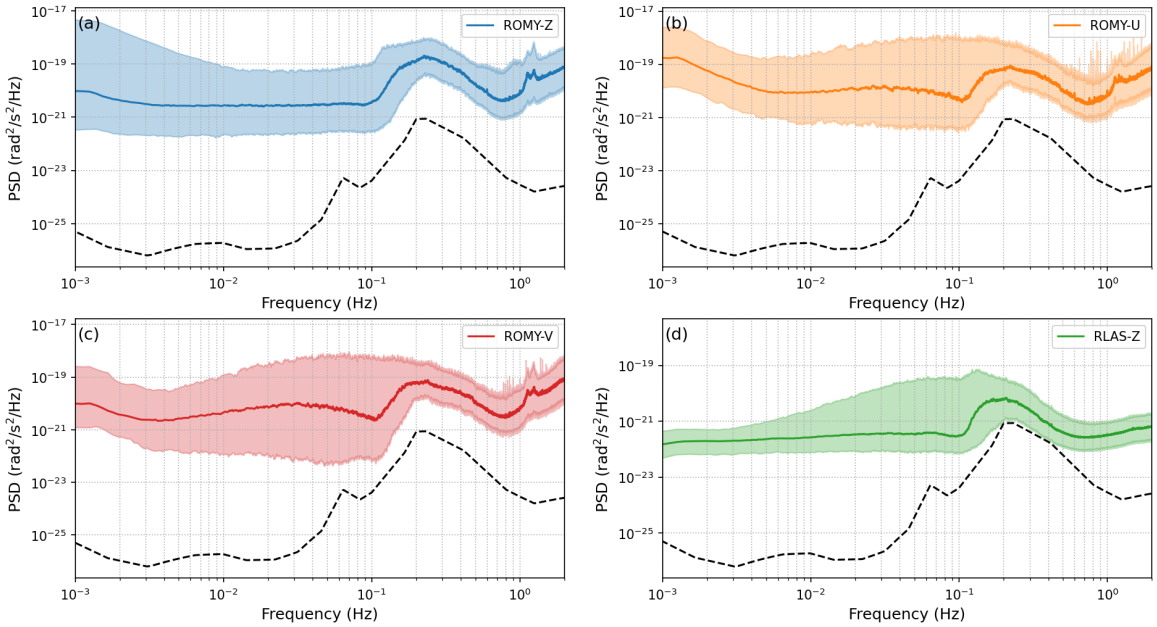

Figure S.3: Median PSDs with a 95 % confidence interval are shown for (a) RZ, (b) RU, (c) RV and (d) G-ring (RLAS). The RLNM is shown for reference (Brotzer et al. 2023).

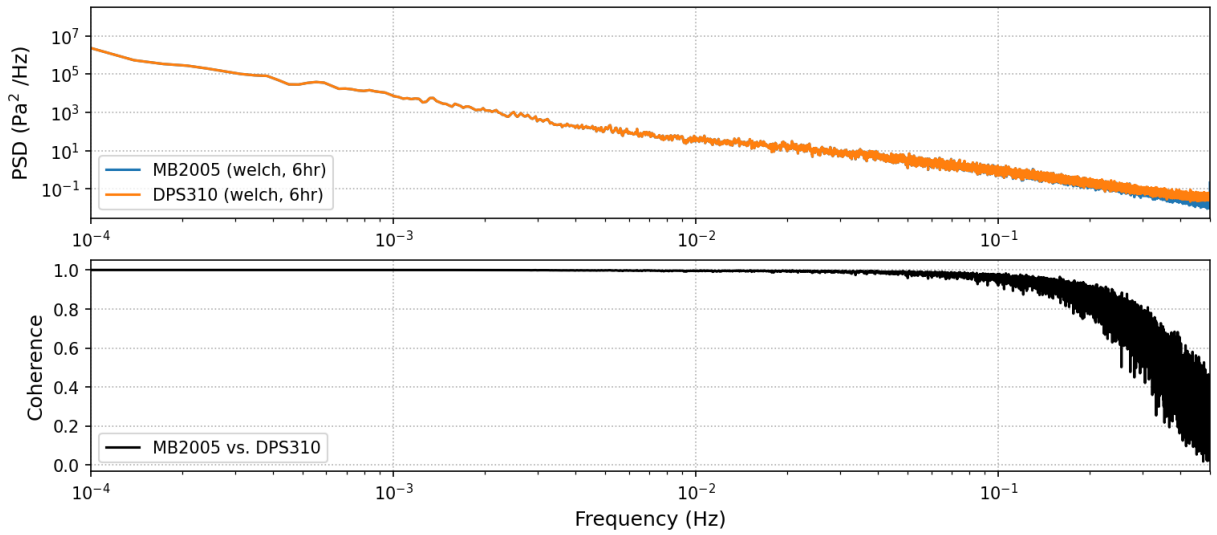

Figure S.4: A comparison of MB2005 barometer and digital pressure sensor DPS310 in terms of power spectral density (PSD) functions (top panel) and signal coherence (bottom panel) is shown.

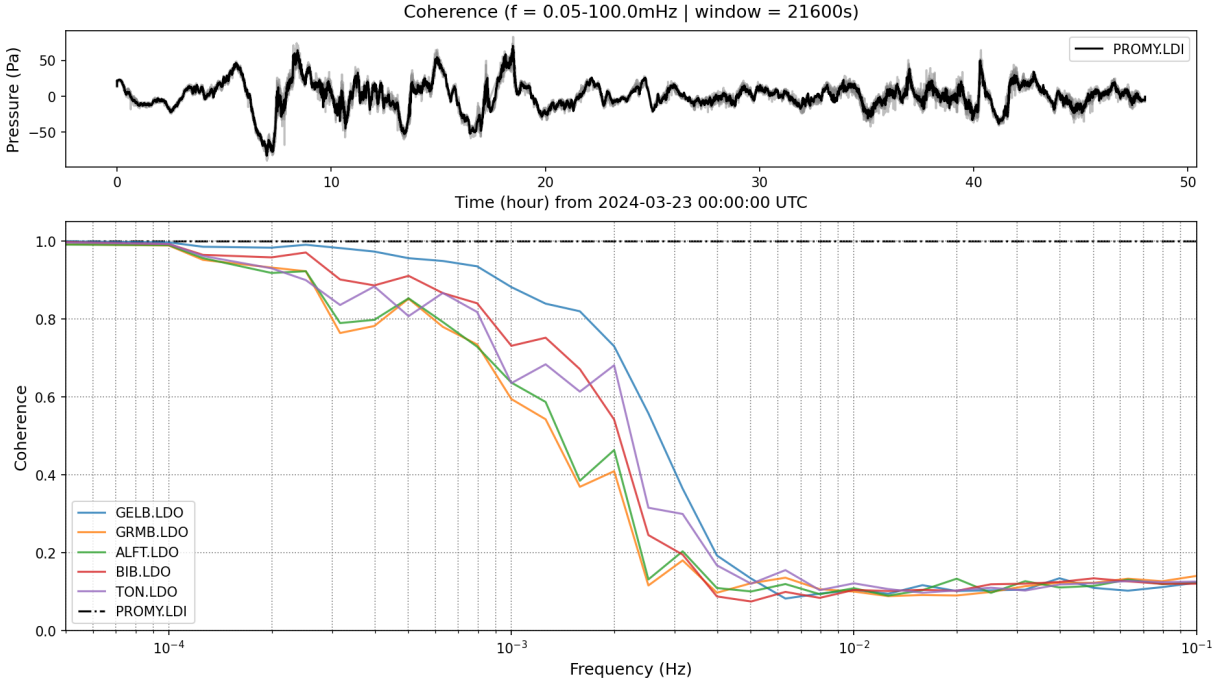

Figure S.5: Bandpass filtered (0.05 - 100 mHz) traces of all barometer stations for two days (gray) and reference station BW.PROMY (black) (top panel). Coherence of barometer records with respect to reference BW.PROMY (bottom panel).

Supplementary Figures for Section 3.2

Table 1: Video cameras used for beam tracking by IDS Imaging Development Systems with model type, sensor size and resolution specifications. RLG and shaft, by means of cardinal direction, specify at which ring resonator and access shaft the camera was deployed.

Code	Model	Sensor Size (H x W)	Pixel Size (μm)	Resolution (MPx)	RLG	Shaft
IDS00	UI-1240LE-NIR-GL	2748 x 3840	1.67	10.0	RU	NW
IDS01	UI-1490LE-M-GL	1024 x 1280	5.30	1.31	RZ	S
IDS03	UI-1490LE-M-GL	1024 x 1280	5.30	1.31	RZ	S
IDS05	UI-1490LE-M-GL	1024 x 1280	5.30	1.31	RZ	NW
IDS07	UI-1490LE-M-GL	1024 x 1280	5.30	1.31	RV	S

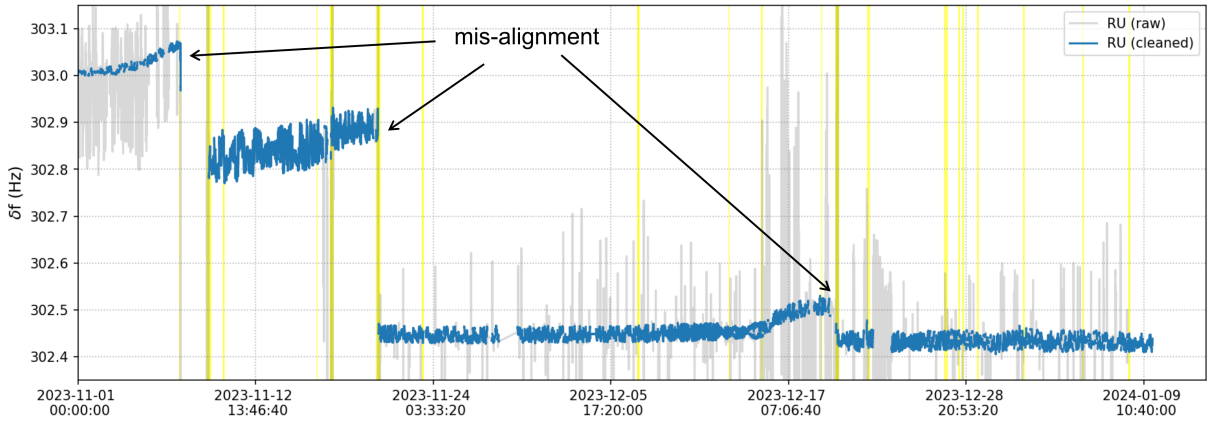

Figure S.6: Long-term Sagnac frequency time series for RU between 2023-11-01 and 2024-01-10 (gray) and without MLTI sequences (blue). Misalignment episodes of the optical resonator that required manual re-alignment are marked. Yellow bars indicate time periods of maintenance work.

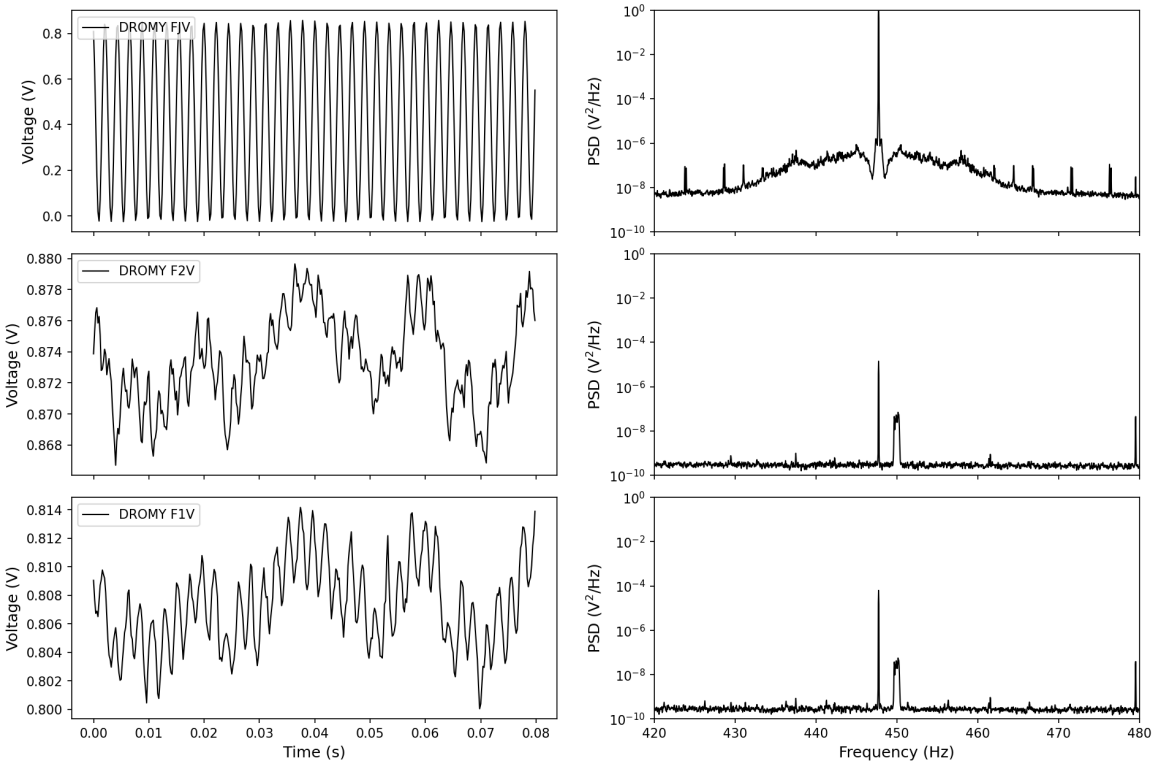

Figure S.7: Unfiltered time series of the Sagnac signal and both monobeams (left panels) and corresponding power spectral densities as a zoom-in on the Sagnac frequency of RV at about 447.7 Hz. All PSDs are normalized to the Sagnac peak of FJV.

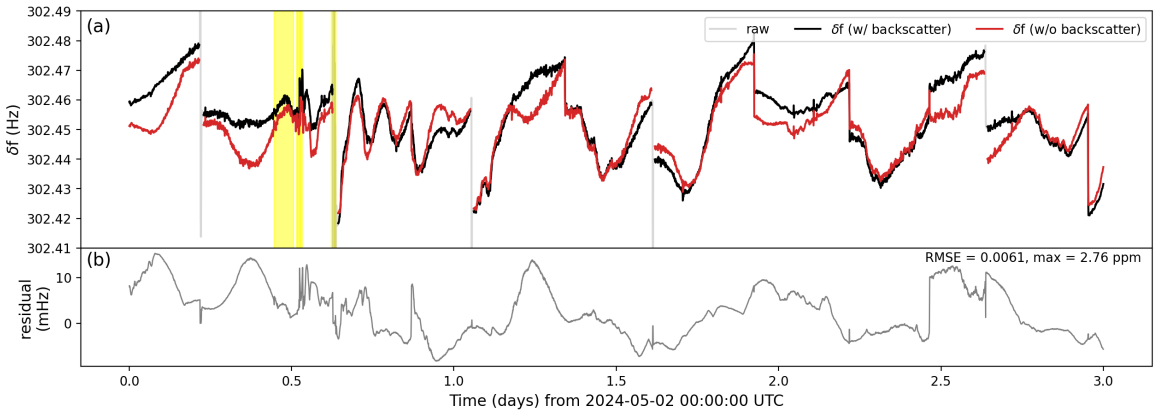

Figure S.8: (a) The time series for ROMY's northern ring (RU) of the raw Sagnac frequency (gray), the processed Sagnac frequency by removing MLTI launches and a Sagnac frequency with a backscatter correction applied (red). In panel (b) the difference is shown for the time series with and without backscatter contribution. Yellow bars indicate times of maintenance work.

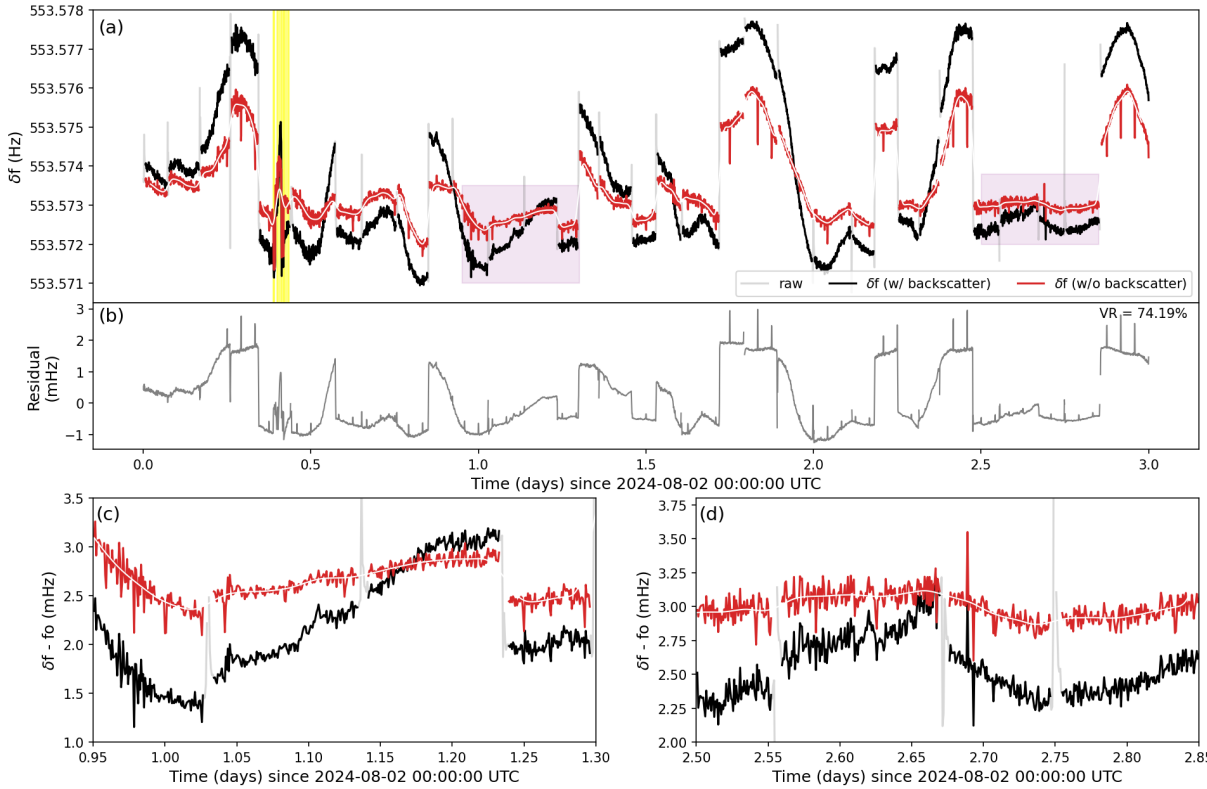

Figure S.9: (a) The time series for ROMY's horizontal ring (RZ) of the raw Sagnac frequency (gray), the processed Sagnac frequency by removing MLTI launches (black) and with a backscatter correction applied (red). In panel (b) the difference is shown for the time series with and without backscatter contribution. (c) and (d) each present data zoom-in on the purple shaded time intervals in (a). Yellow, vertical lines indicate maintenance periods.

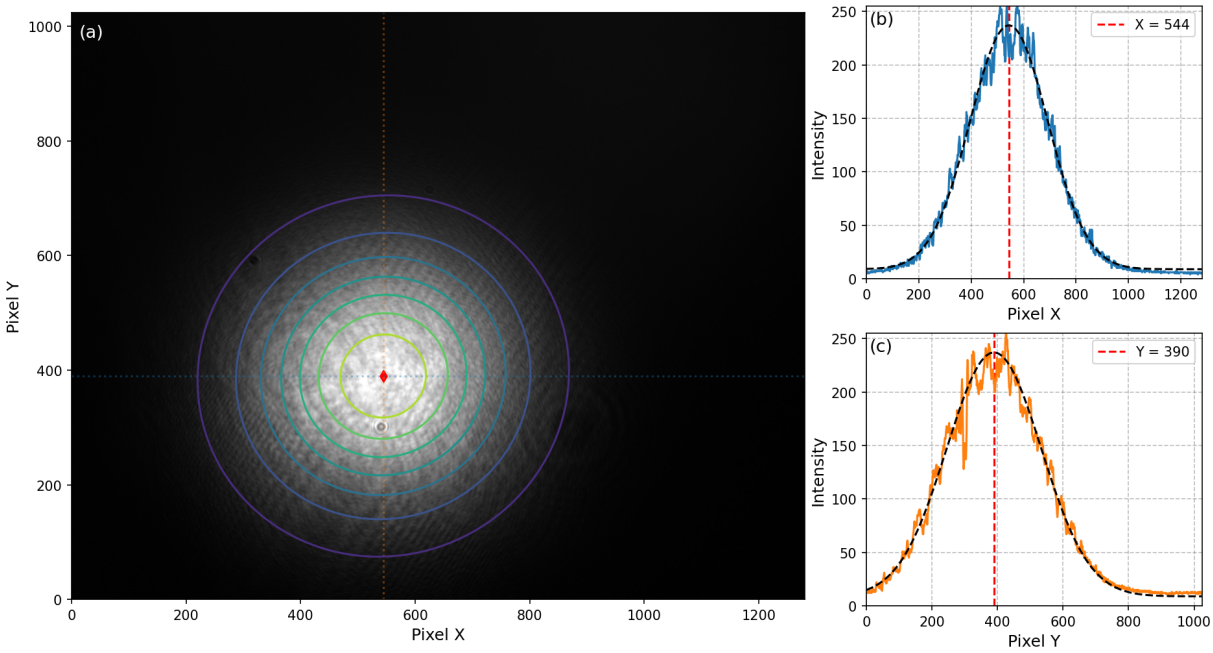

Figure S.10: (a) Example image of IDS camera for mono beam of horizontal ring (RZ) on 2024-05-06 22:36:04 UTC. 2D Gaussian fit is indicated as overlay with colored lines and the Gaussian peak (red diamond) at (x, y) = (554, 390). (b) and (c) show cross-section in x- and y-direction respectively, crossing the Gaussian peak (red, dashed line). The respective 1D Gaussian fit is shown (black, dashed line).

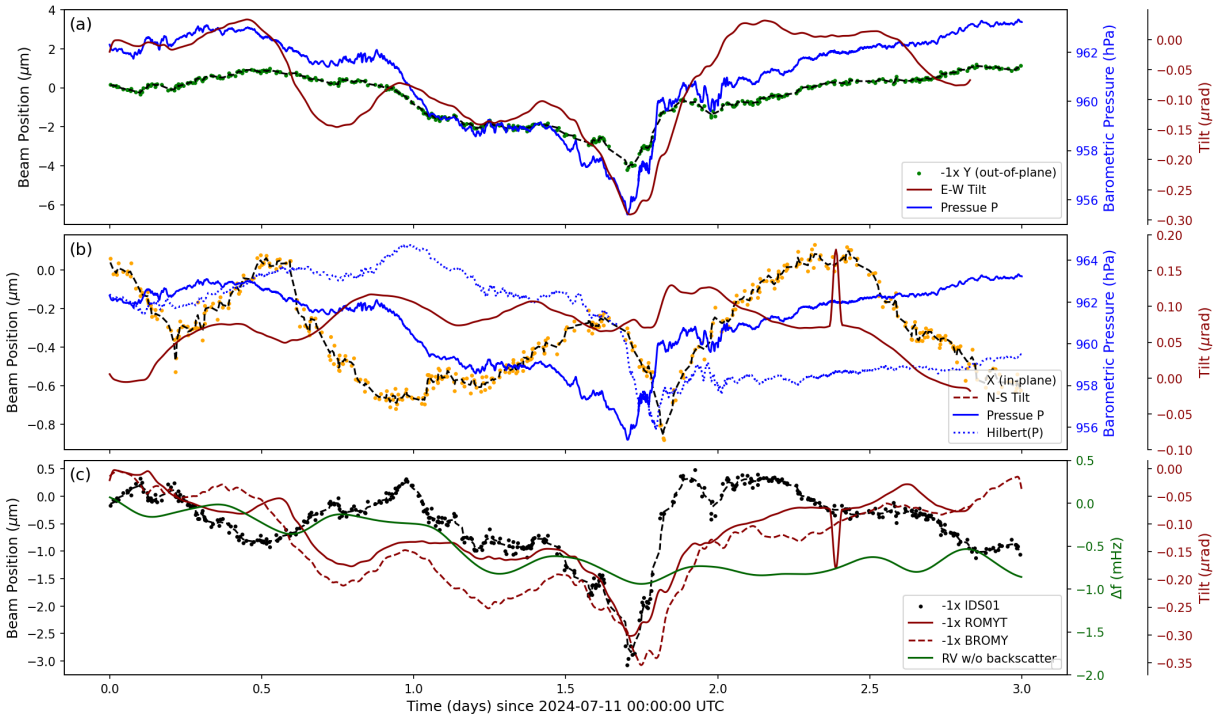

Figure S.11: Beam position of RZ is shown (a) in reversed y-direction (= out-of-plane) and (b) in x-direction (= in-plane) from 2024-07-11 to 2024-07-14. Outliers have been removed. The absolute barometric pressure (solid blue) as well as the Hilbert transform of the barometric pressure (dotted blue) are plotted. Tilt observations of a tiltmeter located next to the resonator corner ($\simeq$50 cm distance) are shown as N-S (dashed red) and E-W (solid red) tilt, respectively. (c) Comparison of the absolute beam displacement ($\sqrt{X^2+Y^2}$) of IDS01, the absolute tilt ($\sqrt{N^2+E^2}$) for ROMYT (solid) and BROMY (dashed) as well as the 6 hour moving average of the Sagnac frequency of RV without backscatter.

Supplementary Figures for Section 4.1

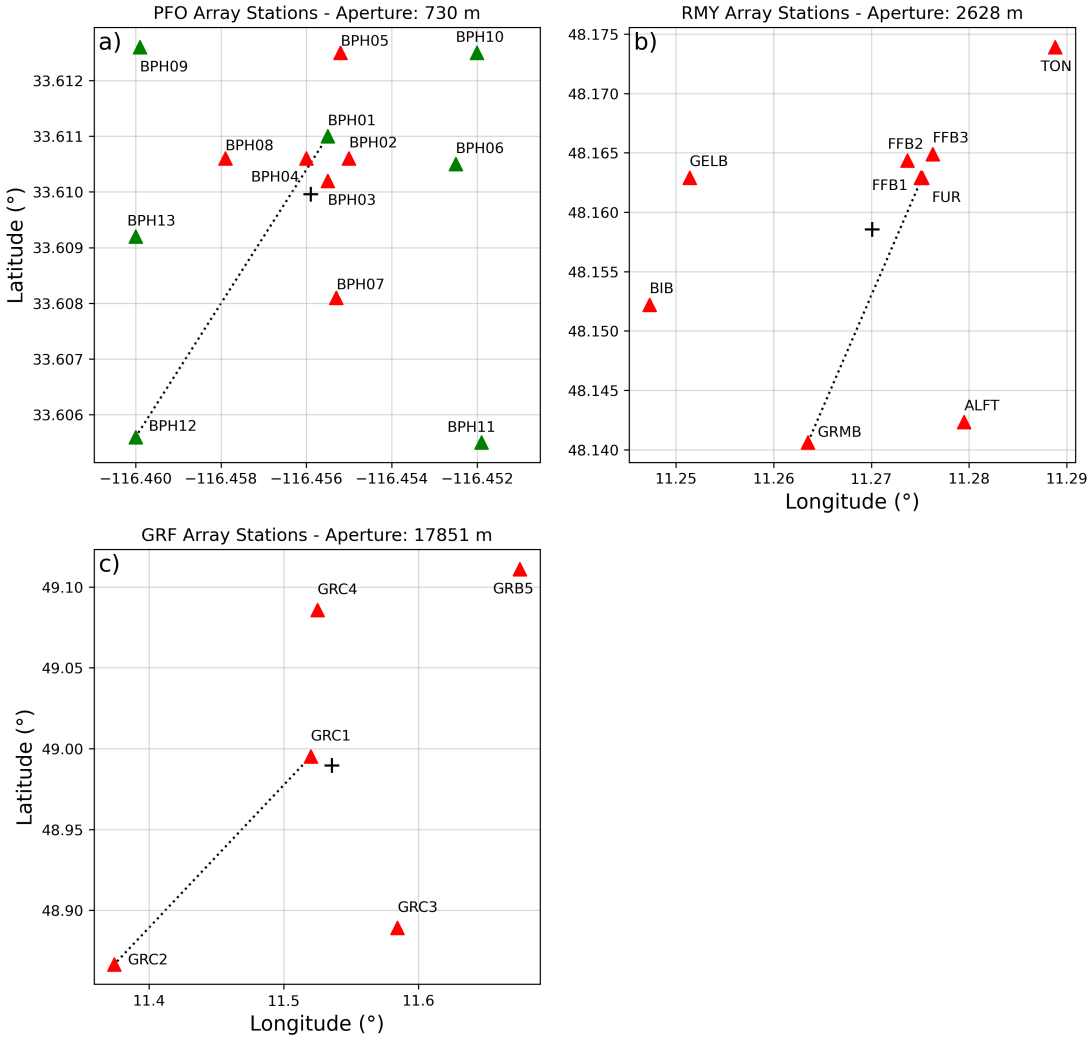

Figure S.12: Shown are locations of the seismic stations of **a)** the Piñon Flat Observatory (PFO) array and the employed subset of seven stations (green), **b)** the ROMY array (RMY) with an inner (FUR, FFB1, FFB2 and FFB3) and outer (FUR, GELB, TON, ALFT, BIB, GRMB) array as well as **c)** a subset of five stations of the German Gräfenberg array (GRF), which are used for computations of array-derived rotations (ADR). The cross symbol indicates the centroid location of the array, respectively. Dotted lines indicate the maximal aperture of each array: PFO = 730 m; RMY = 2 628 m; GRF = 17 851 m.

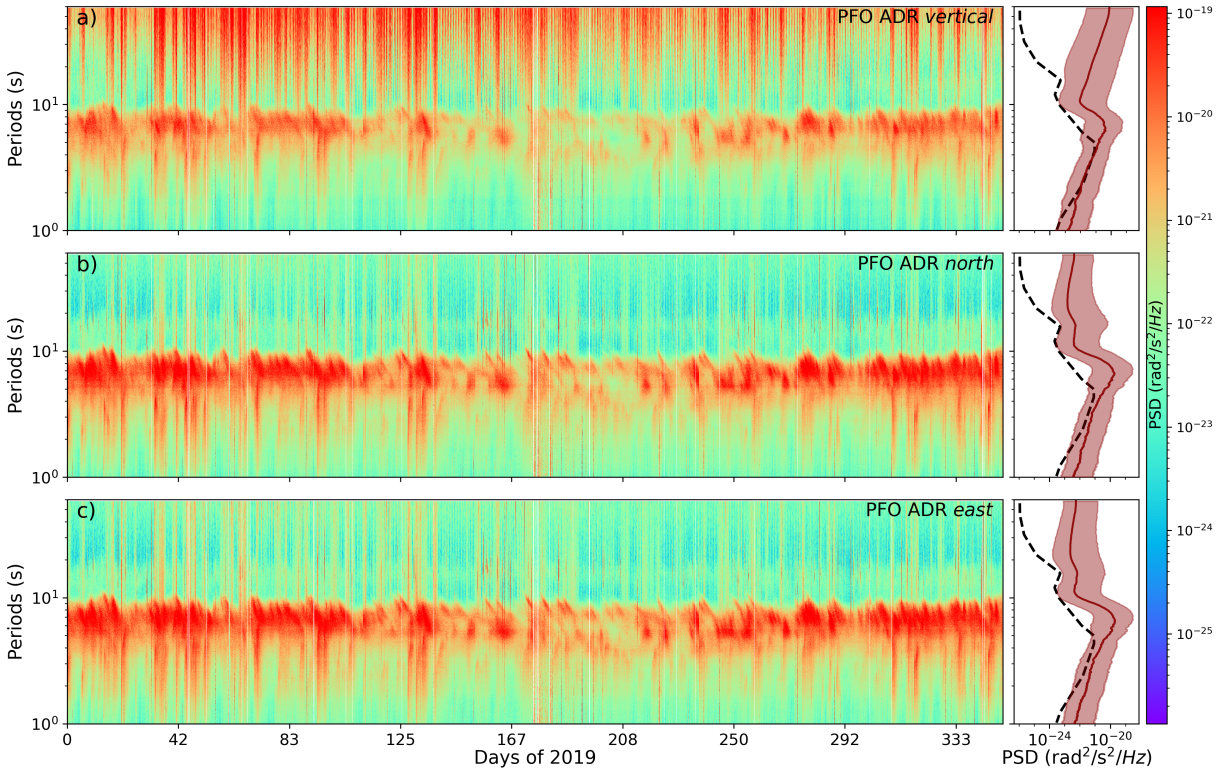

Figure S.13: The left panels show hourly power spectral densities for 2019 of the **a)** vertical, **b)** north and **c)** east component of array-derived rotations (ADR) at a subset of stations of the Piñon Flat Observatory (PFO) in California, USA. The right panel represents the median of all PSDs (red, solid) with a 95% confidence interval (red shade). The black, dashed line represents the Rotational Low Noise Model (RLNM).

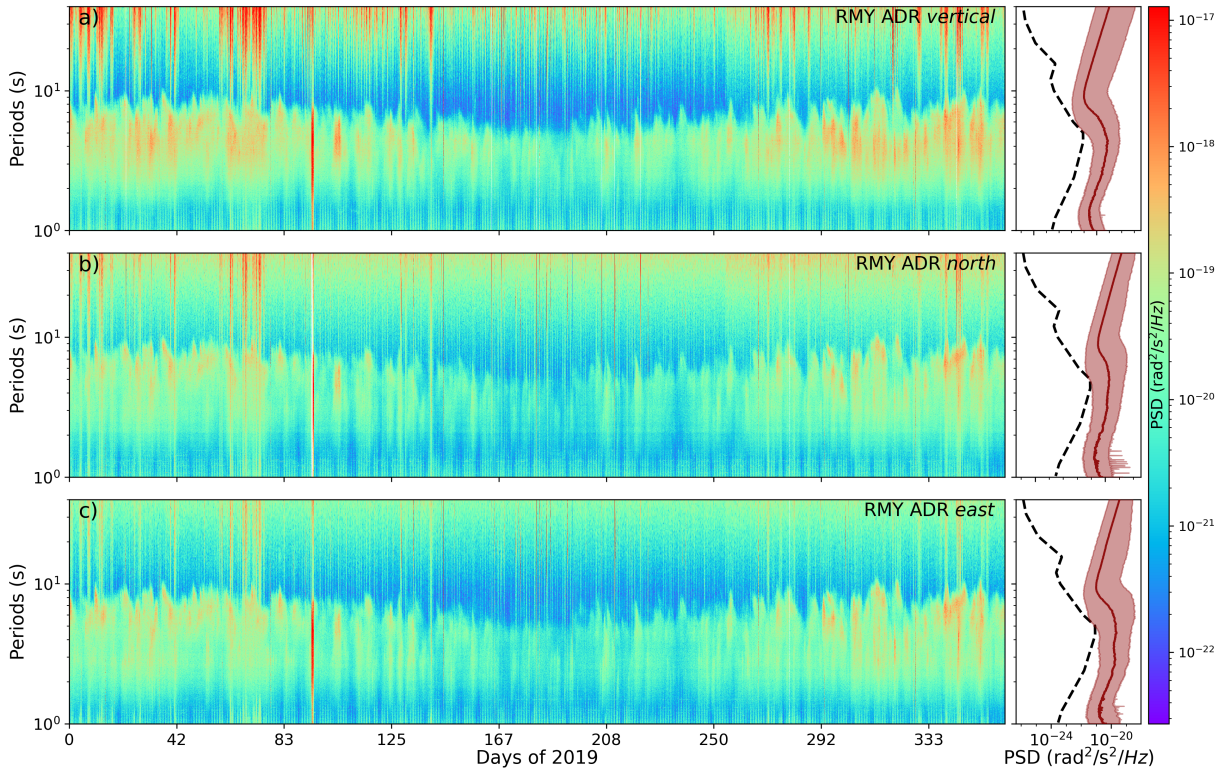

Figure S.14: The left panels show hourly power spectral densities for 2019 for the **a)** vertical, **b)** north and **c)** east component of array-derived rotations (ADR) for the inner subarray of the ROMY array (RMY) in Fürstenfeldbruck, Germany. The right panel represents the median of all PSDs (red, solid) with a 95% confidence interval (red shade). The black, dashed line represents the Rotational Low Noise Model (RLNM).

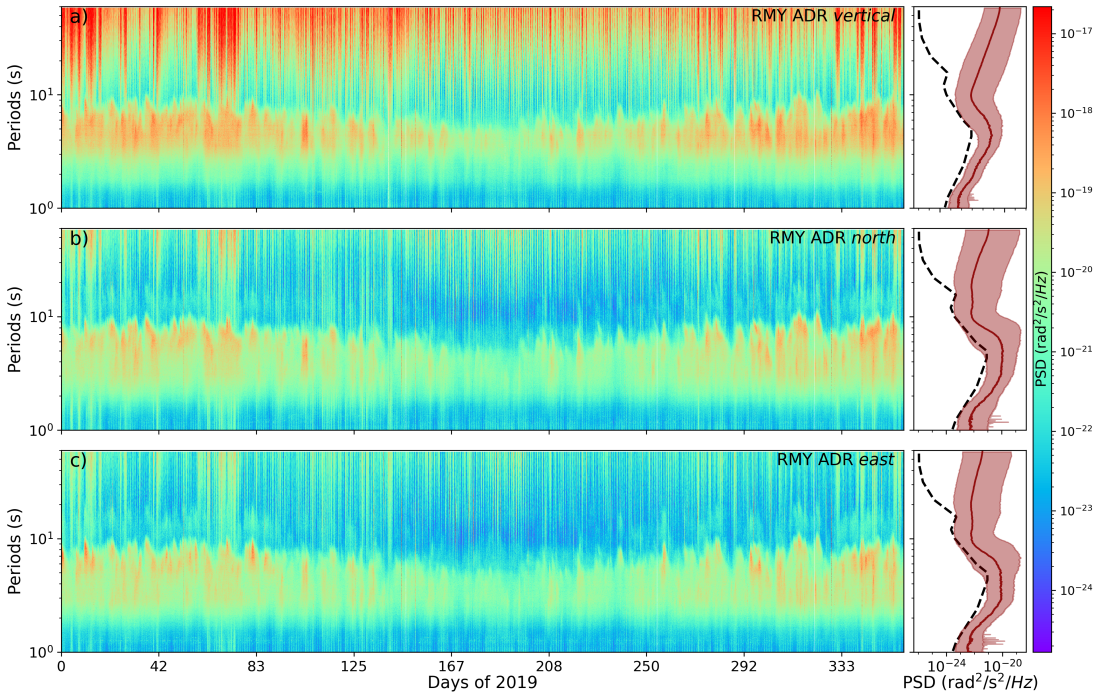

Figure S.15: The left panels show hourly power spectral densities for 2019 for the **a)** vertical, **b)** north and **c)** east component of array-derived rotations (ADR) for the outer subarray of the ROMY array (RMY) in Fürstenfeldbruck, Germany. The right panel represents the median of all PSDs (red, solid) with a 95% confidence interval (red shade). The black, dashed line represents the Rotational Low Noise Model (RLNM).

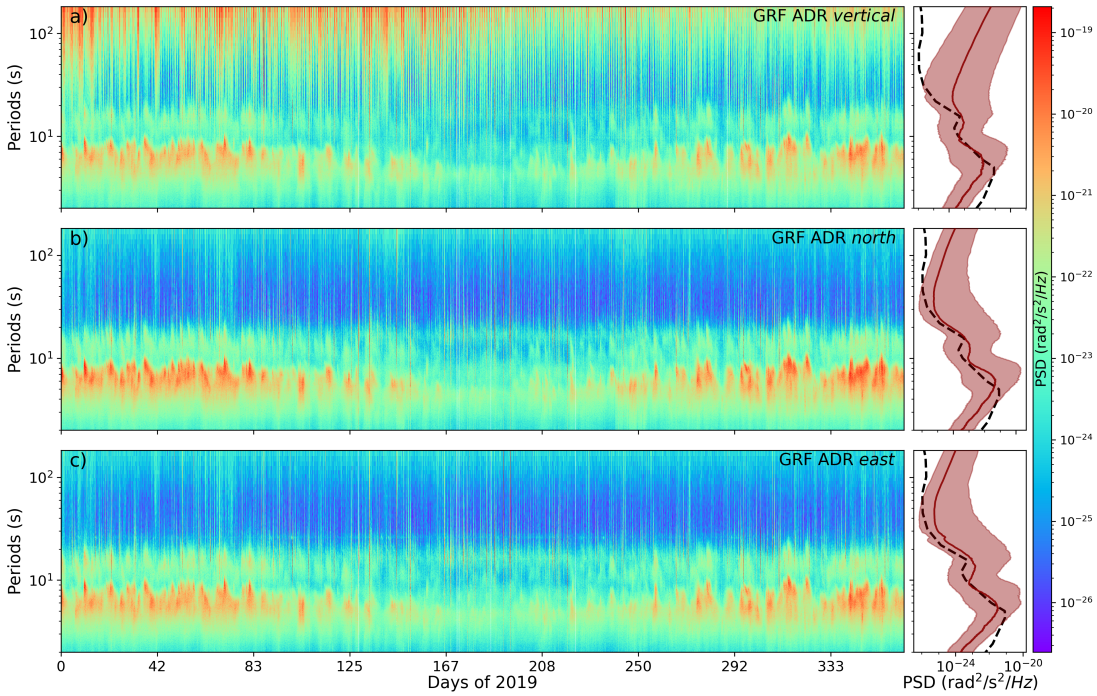

Figure S.16: The left panels show hourly power spectral densities for 2019 for the **a)** vertical, **b)** north and **c)** east component of array-derived rotations (ADR) at a subset of stations of the Gräfenberg array (GRF) in Germany. The right panel represents the median of all PSDs (red, solid) with a 95% confidence interval (red shade). The black, dashed line represents the Rotational Low Noise Model (RLNM).

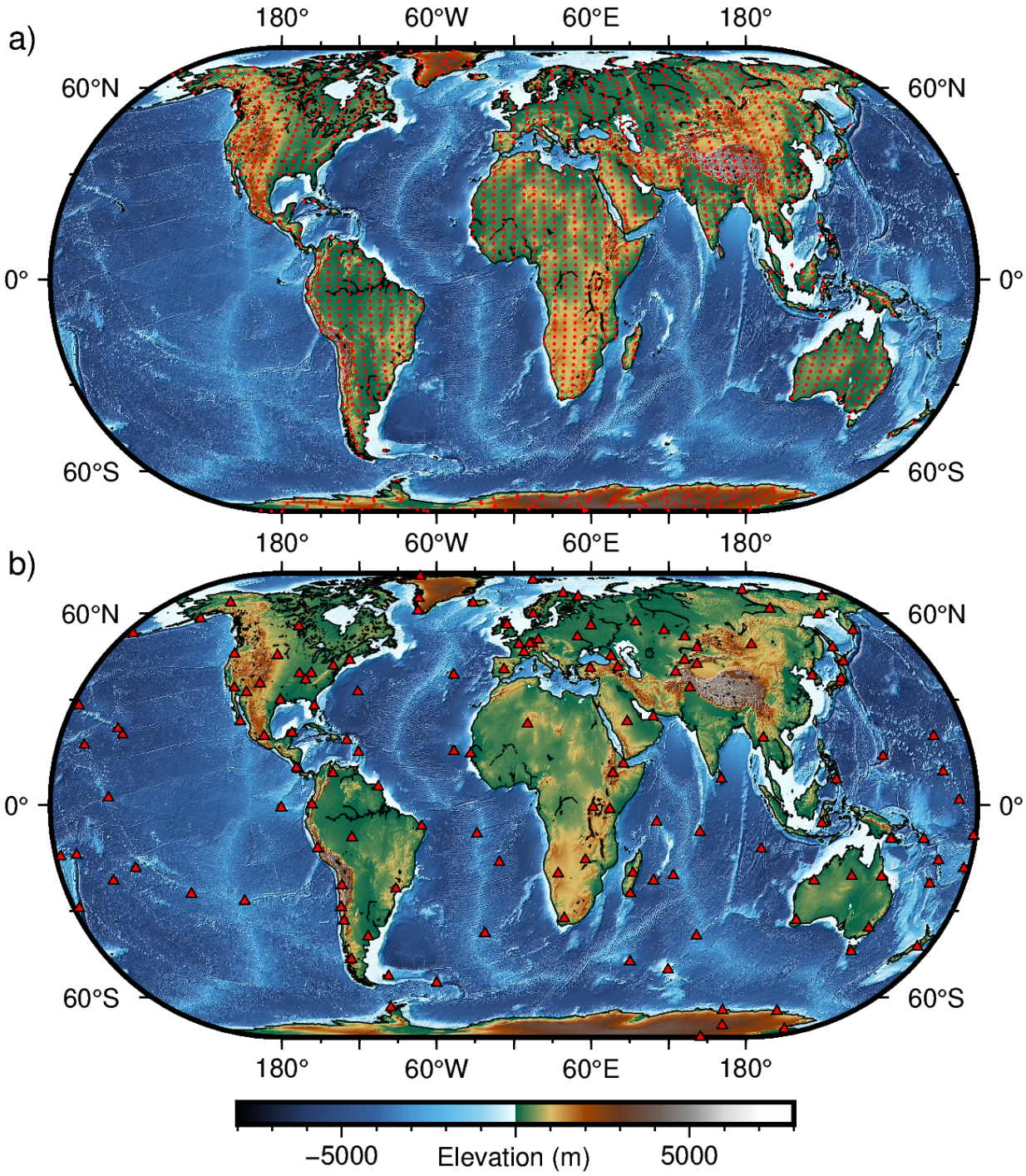

Figure S.17: **a)** shows the revised sampling locations of the CRUST1.0 model in order to extract dispersive Rayleigh phase velocity curves on continents only. **b)** shows a set of globally distributed seismic stations belonging to several seismic networks used for the statistical single station validation.

Translation to Rotation - Supplement of Section 4.1

We want to infer the relations of rotational rate and translational acceleration for seismic ground motions in an x-y-z-coordinate system. An infinitesimal vector rotation rate $\vec{\Omega}(\vec{r},t)$ in linear elasticity can be expressed as:

$$\dot{\vec{\Omega}}(\vec{r},t) = \frac{1}{2}\,\frac{\partial}{\partial t}\,\left(\vec{\nabla}\times\vec{u}(\vec{r},t)\right) = \frac{1}{2}\begin{pmatrix}\partial_x\\ \partial_y\\ \partial_z\end{pmatrix}\times\begin{pmatrix}\partial_t u_x\\ \partial_t u_y\\ \partial_t u_z\end{pmatrix} = \frac{1}{2}\begin{pmatrix}\partial_y\partial_t\ u_z - \partial_z\partial_t\ u_y\\ \partial_z\partial_t\ u_x - \partial_x\partial_t\ u_z\\ \partial_x\partial_t\ u_y - \partial_y\partial_t\ u_x\end{pmatrix}, \tag{1}$$

with $\vec{r} = [x,y,z]^T$.

Love waves

For SH-polarized type waves (Love waves), we assume a plane wave for the displacement field propagating in x-direction: $\vec{u}(x,t) = [0,\ A\ sin(\omega t - k_x x),\ 0]^T$. The second derivative in time, the acceleration field $\ddot{\vec{u}}(x,t)$, results to:

$$\ddot{\vec{u}}(x,t) = [0,\ -A\ \omega^2\ sin(\omega t - k_x x),\ 0]^T, \tag{2}$$

while the rotation rate $\dot{\vec{\Omega}}(x,t)$ is given by:

$$\dot{\vec{\Omega}}(x,t) = [0,\ 0,\ 0.5\ A\ \omega\ k_x\ sin(\omega t - k_x x)]^T. \tag{3}$$

Relating the transverse acceleration $\ddot{u}_T$ and vertical rotation rate $\dot{\Omega}_Z$ reveals:

$$\frac{\ddot{u}_T(x,t)}{\dot{\Omega}_Z(x,t)} = \frac{-\ A\ \omega^2\ \sin(\omega t - k_x x)}{0.5\ A\ \omega\ k_x\ \sin(\omega t - k_x x)} = -2\frac{\omega}{k_x} = -2\ c_L \quad \Rightarrow \quad \dot{\Omega}_Z = -\frac{1}{2}\ \frac{\ddot{u}_T}{c_L}, \tag{4}$$

with c_L being the apparent Love wave phase velocity.

Rayleigh waves

For elliptical SV-polarized type waves (Rayleigh waves), we assume a plane wave for the displacement field propagating in x-direction at zero depth: $\vec{u}(x,t) = [-0.42\ A\ k_x\ sin(\omega t - k_x x),\ 0,\ 0.62\ A\ k_x\ cos(\omega t - k_x x)]^T$, following Lay & Wallace (1995). The second derivative in time, the acceleration field $\ddot{\vec{u}}(x,t)$, can be written as:

$$\ddot{\vec{u}}(x,t) = [0.42\ A\ k_x\ \omega^2\ sin(\omega t - k_x x),\ 0, -0.62\ A\ k_x\ \omega^2\ cos(\omega t - k_x x)]^T. \tag{5}$$

Cochard et al. (2006) infer at the free surface, using a traction-free boundary condition, the following equations from Hooke's law:

$$\frac{\partial u_x}{\partial z} = \frac{-\partial u_z}{\partial x} \quad \text{and} \quad \frac{\partial u_y}{\partial z} = \frac{-\partial u_z}{\partial y} \quad \text{and} \quad \frac{\partial u_z}{\partial z} = \frac{-\lambda}{\lambda + 2\mu}\ \left(\frac{\partial u_x}{\partial x} + \frac{\partial u_y}{\partial y}\right), \tag{6}$$

with λ and μ being the Lame parameters. Using these equations in combination with equation (1) an expression for the rotation rate at the free surface perpendicular to the propagation direction, here along the y-axis, caused by Rayleigh waves is given by:

$$\dot{\Omega}_y = -\frac{\partial \dot{u}_z}{\partial x} = -0.62\ A\ k_x^2\ \omega\ cos(\omega t - k_x x), \tag{7}$$

stated by Cochard et al. (2006) and also used in Lin et al. (2011). Relating the vertical acceleration $\ddot{u}_z$ and transverse rotation rate $\dot{\Omega}_y$ then yield:

$$\frac{\ddot{u}_Z(x,t)}{\dot{\Omega}_T(x,t)} = \frac{-0.62\ A\ k_x\ \omega^2\ \cos(\omega t - k_x x)}{-0.62\ A\ \omega\ k_x^2\ \cos(\omega t - k_x x)} = \frac{\omega}{k_x} = c_R \quad \Rightarrow \quad \dot{\Omega}_T = \frac{\ddot{u}_Z}{c_R}, \tag{8}$$

with c_R being the apparent Rayleigh wave phase velocity. A detailed explanation can also be found in Lin et al. (2011).

Supplementary Figures for Section 5

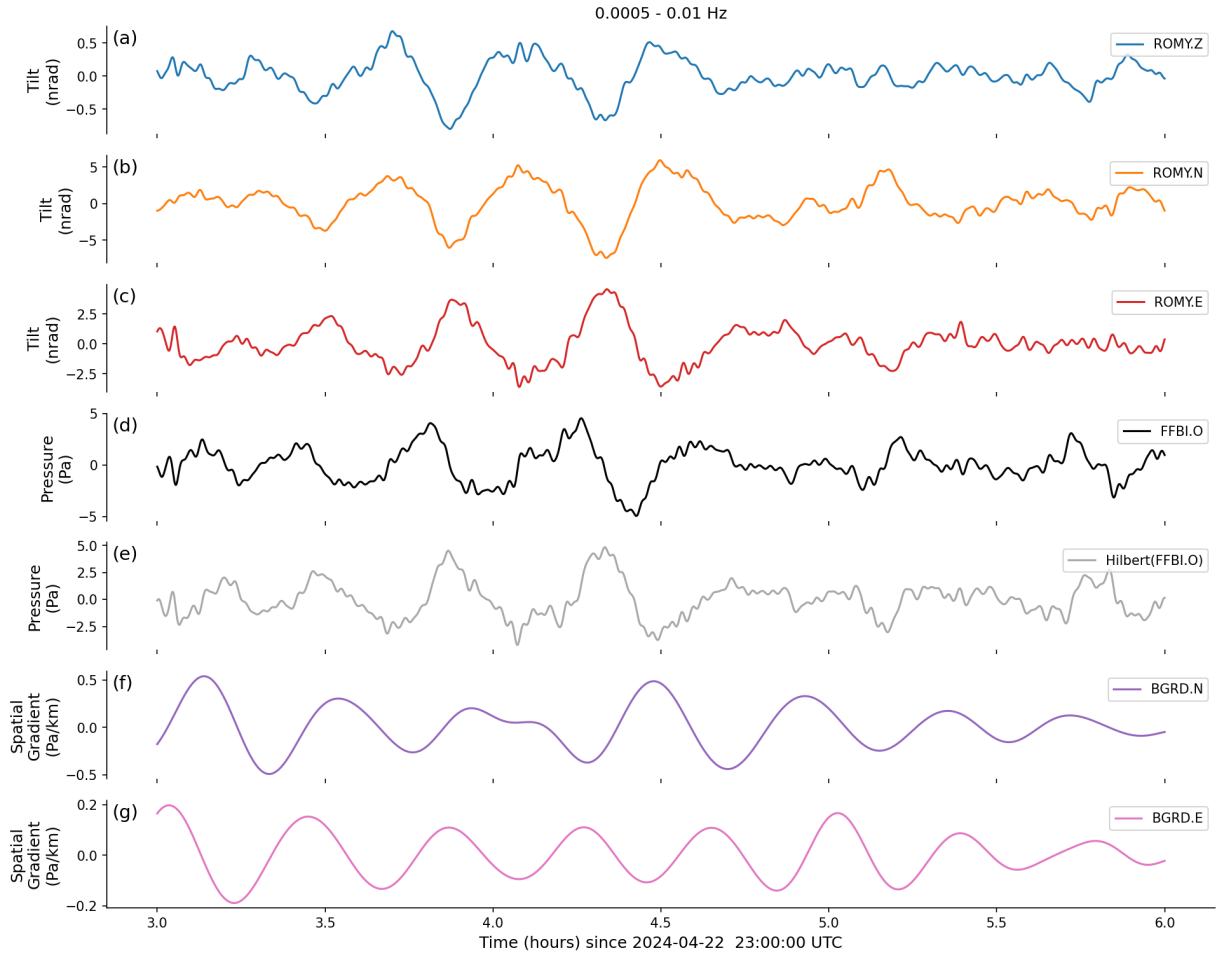

Figure S.18: Tilt of ROMY for (a) Z, (b) N and (c) E component (in nanoradian), respectively. (d) Barometric pressure of FFBI (MB2005) and (e) the Hilbert transform of the barometric pressure. (f) Northward and (g) eastward spatial pressure gradient derived from the barometer array. All traces are band-pass filtered between 0.5 mHz and 10 mHz.

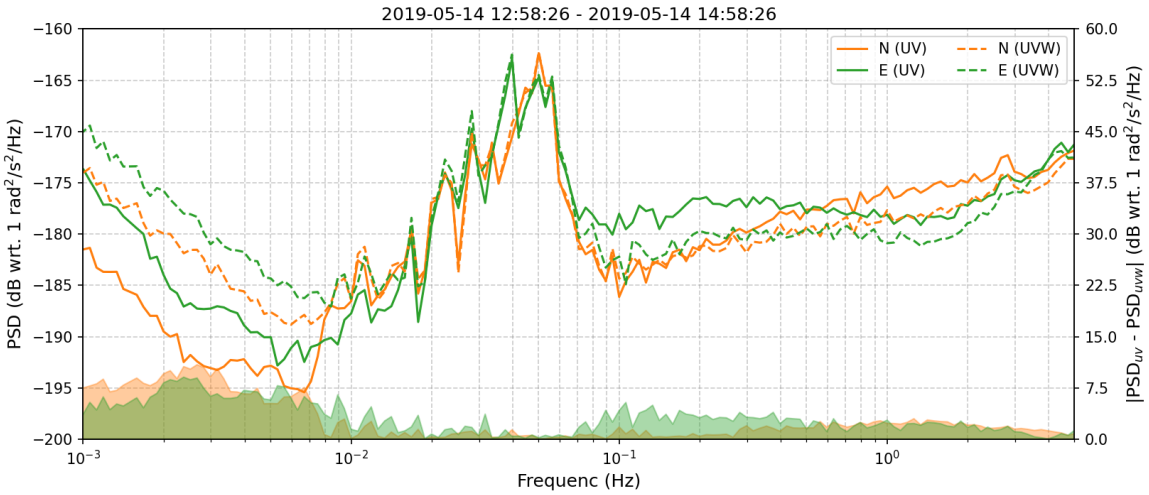

Figure S.19: Power spectral densities for north and east based on a multitaper approach and averaged in 12^{th} octave bands for the M_w 7.5 earthquake on 2019-05-14. North and east is reconstructed using the U-V-W and a reduced U-V system. A second y-axis shows the spectral differences in decibels.

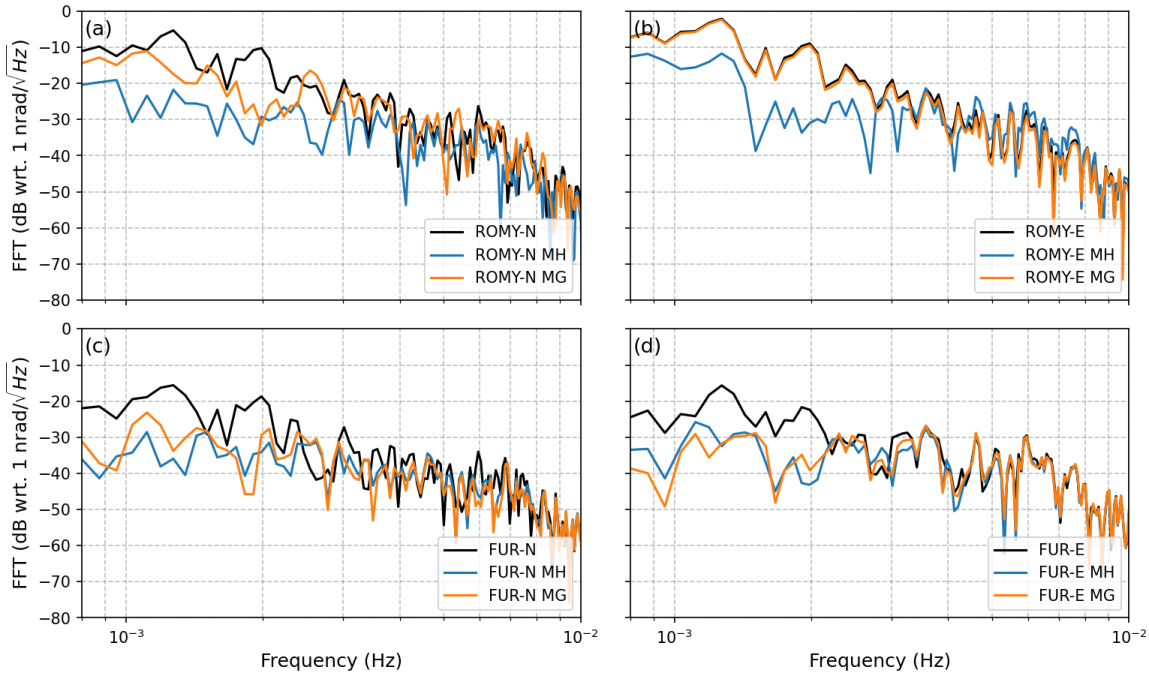

Figure S.20: Spectra of the tilt observations of ROMY and FUR (black) compared to the reduced data using a barometric model based on local barometric pressure and the Hilbert transform thereof (= MH) and on local barometric pressure and the derived spatial gradient (= MG).

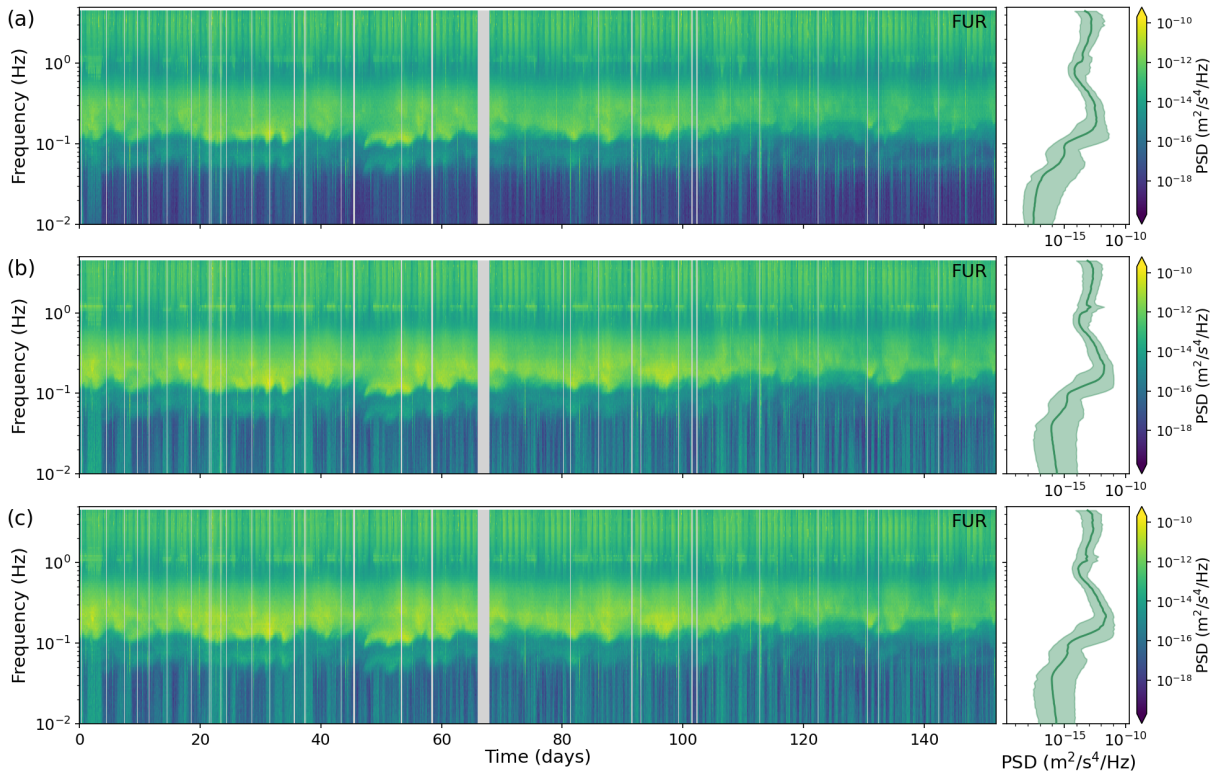

Figure S.21: Hourly PSDs for three components(a) Z, (b) north and (c) east of GR.FUR are shown over time 152 days (2024-01-01 to 2024-05-31). the side panels show a projection onto the y-axis as median (solid) and a 90 % confidence interval (shaded). Rejected data is replaced by gray bars.

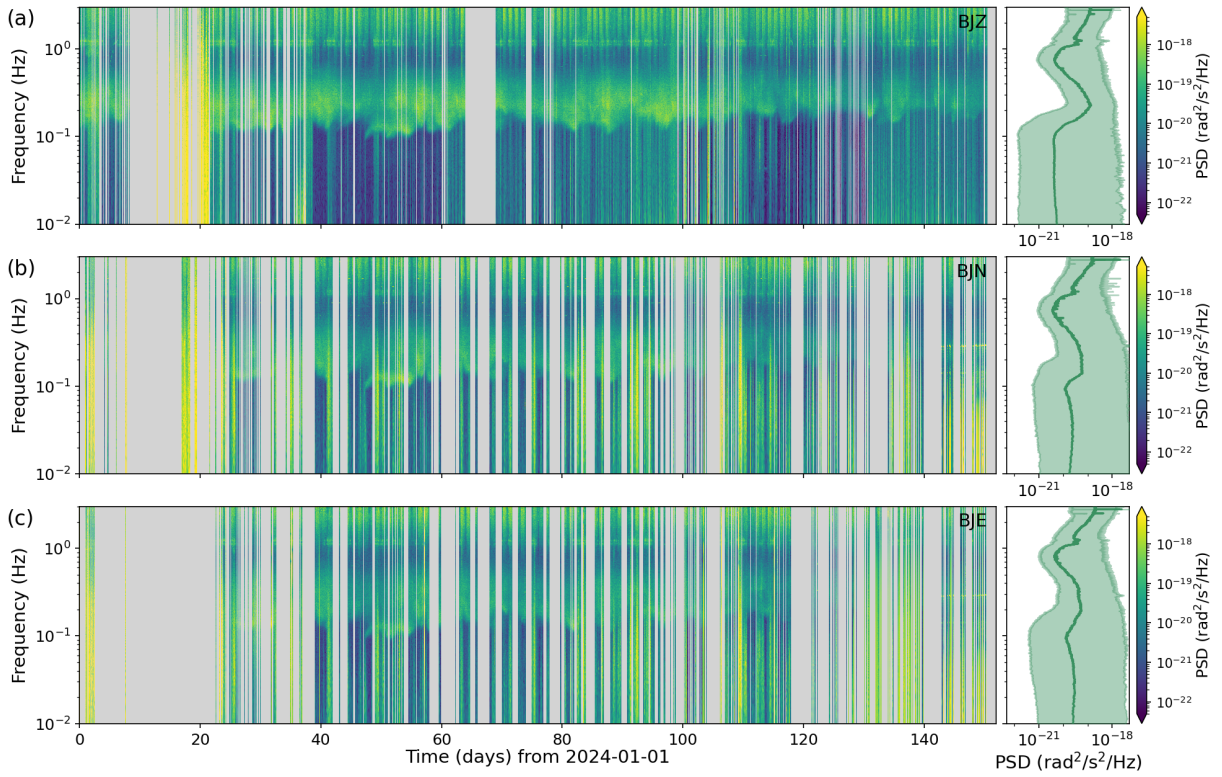

Figure S.22: Hourly PSDs for three components (a) Z, (b) north and (c) east of BW.ROMY are shown over time 152 days (2024-03-01 to 2024-05-31). the side panels show a projection onto the y-axis as median (solid) and a 90 % confidence interval (shaded). Rejected data is replaced by gray bars.

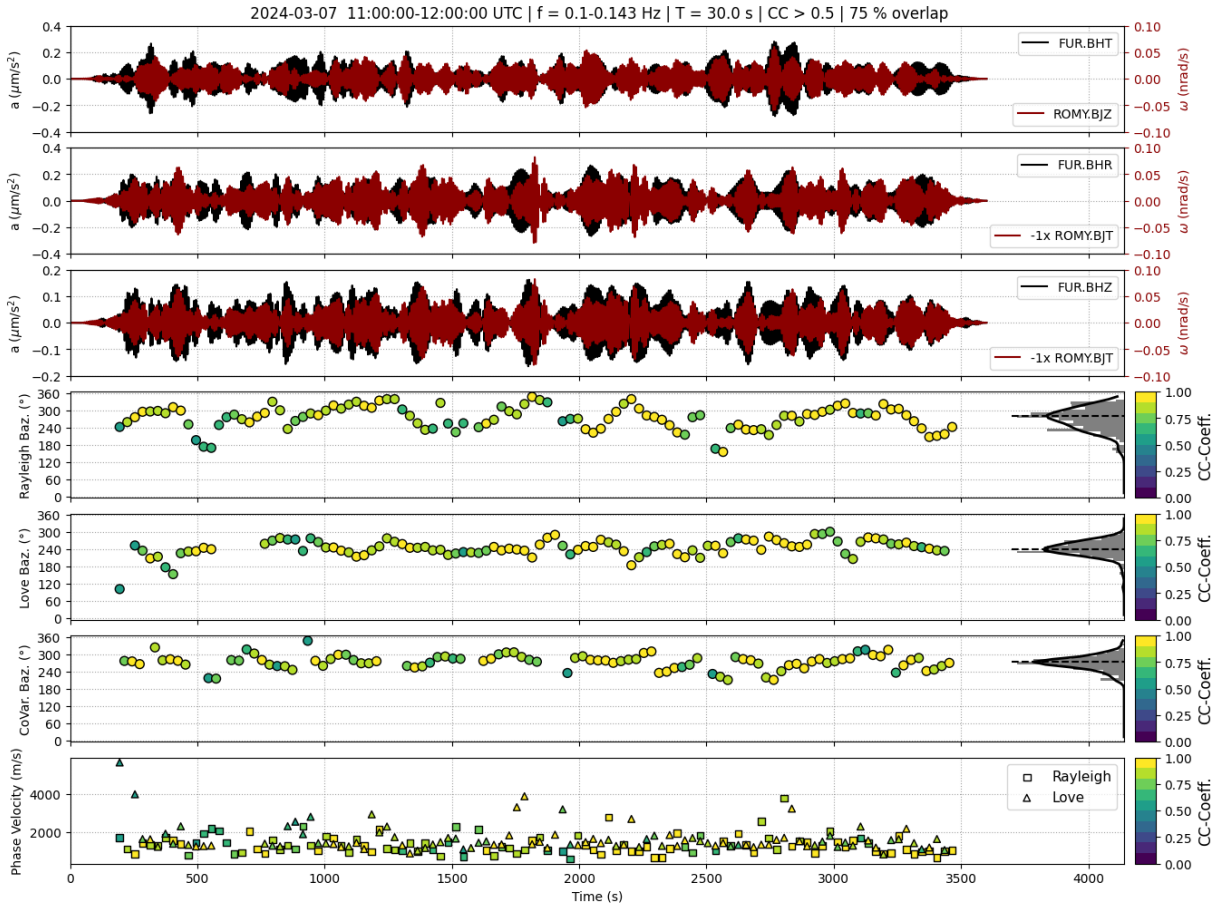

Figure S.23: Panels 1-3 show different combinations of acceleration and rotation rate band-pass filtered between 7 s and 10 s period on 2024-03-07 (11:00 - 12:00 UTC). Panels 4-6 show estimates of backazimuths color-coded by cross-correlation coefficients using a Rayleigh wave polarization, a Love wave polarization and a SV wave co-variance methods. Histograms of the estimates and Gaussian kernel distributions are plotted on the right y-axis. Panel 7 shows estimates for Love and Rayleigh wave phase velocities.